CRANFIELD UNIVERSITY

THOMAS KRIECHBAUMER

FIELD-BASED MEASUREMENT OF HYDRODYNAMICS ASSOCIATED WITH ENGINEERED IN-CHANNEL STRUCTURES: THE EXAMPLE OF FISH PASS ASSESSMENT

SCHOOL OF ENERGY, ENVIRONMENTAL TECHNOLOGY AND AGRIFOOD

Doctor of Philosophy
Academic Year: 2012 - 2016

Supervisors: Monica Rivas Casado, Kim Blackburn, Andrew Gill
March 2016

CRANFIELD UNIVERSITY

SCHOOL OF ENERGY, ENVIRONMENTAL TECHNOLOGY AND AGRIFOOD

Doctor of Philosophy

Academic Year 2012 - 2016

THOMAS KRIECHBAUMER

FIELD-BASED MEASUREMENT OF HYDRODYNAMICS ASSOCIATED WITH ENGINEERED IN-CHANNEL STRUCTURES: THE EXAMPLE OF FISH PASS ASSESSMENT

Supervisors: Monica Rivas Casado, Kim Blackburn, Andrew Gill

March 2016

ABSTRACT

The construction of fish passes has been a longstanding measure to improve river ecosystem status by ensuring the passability of weirs, dams and other in-channel structures for migratory fish. Many fish passes have a low biological effectiveness because of unsuitable hydrodynamic conditions hindering fish to rapidly detect the pass entrance. There has been a need for techniques to quantify the hydrodynamics surrounding fish pass entrances in order to identify those passes that require enhancement and to improve the design of new passes. This PhD thesis presents the development of a methodology for the rapid, spatially continuous quantification of near-pass hydrodynamics in the field. The methodology involves moving-vessel Acoustic Doppler Current Profiler (ADCP) measurements in order to quantify the 3-dimensional water velocity distribution around fish pass entrances. The approach presented in this thesis is novel because it integrates a set of techniques to make ADCP data robust against errors associated with the environmental conditions near engineered in-channel structures. These techniques provide solutions to (i) ADCP compass errors from magnetic interference, (ii) bias in water velocity data caused by spatial flow heterogeneity, (iii) the accurate ADCP positioning in locales with constrained line of sight to navigation satellites, and (iv) the accurate and cost-effective sensor deployment following pre-defined sampling strategies. The effectiveness and transferability of the methodology were evaluated at three fish pass sites covering conditions of low, medium and high discharge. The methodology outputs enabled a detailed quantitative characterisation of the fish pass attraction flow and its interaction with other hydrodynamic features. The outputs are suitable to formulate novel indicators of hydrodynamic fish pass attractiveness and they revealed the need to refine traditional fish pass design guidelines.

Keywords:

Acoustic Doppler Current Profiler, attraction flow, eco-hydraulics, fish pass attractiveness, flow measurement, Global Navigation Satellite System, radio-control boat, river monitoring, stereo vision, Total Station, visual odometry

Measurement is the first step that leads to control and eventually to improvement. If you can't measure something, you can't understand it. If you can't understand it, you can't control it. If you can't control it, you can't improve it.

– H. James Harrington (1929 - Present)

ACKNOWLEDGEMENTS

Throughout the time of the PhD project, I have had support from numerous people, thanks to whom the past years of research have been a fascinating experience. Here, I would like to take the opportunity to acknowledge them.

My first thanks go to the funders of my PhD research: the Environment Agency (particularly Nick Everard and Ros Wright) and the Engineering and Physical Research Council (EPSRC). Without their financial support this project would not have been possible.

A particularly great thank you to my supervisors, Monica Rivas Casado, Kim Blackburn and Andrew Gill, who offered guidance and support throughout the project. I am truly grateful and have enjoyed the many inspiring discussions, the exciting hours in the field and the invaluable training in the engineering lab. A large thank you also to Nick Everard from the Environment Agency for the great support during data collection and for helping to make my research relevant to practice. Likewise, I am very grateful to Toby Breckon from Durham University, who supervised my work on stereo visual odometry for ADCP platforms.

I would also like to thank the other members of my thesis committee: subject advisors Jenny Mant and (later) Toby Waine, as well as the independent committee chairs Paul Shore and (later) Kumar Patchigolla. Their constructive comments during the thesis review meetings have been valuable.

For the support during data collection in the field, I would like to thank the Hydrometry and Telemetry team from the Environment Agency, particularly Rob Davies, Gary Bywater, Steven Baker and Mark Golding. Thank you also to Adam Piper from the Zoological Society of London, Chris Bainger and Oliver Roden from the Environment Agency for the help in the field and for providing valuable information on the study sites. I also gratefully acknowledge Simon Stranks from Cranfield University for technical help during work in the engineering lab.

I am grateful to Leica Geosystems, particularly Shane O'Regan, for the provision of equipment, which was vital to the project. I acknowledge the

provision of data on river discharge from the National River Flow Archive (NRFA) and GNSS correction data from the British Isles continuous GNSS Facility (BIGF).

On a personal note, I thank my friends and family for their support during the last three years. Thank you to Waltraud and Josef for providing me with a great place to work and live during the final months of the project. I thank my parents Elfi and Franz and my brother Stefan for the emotional support throughout my studies and the wonderful times during their visits in England.

Last but not least, I am forever grateful to you, Anna, for bravely following me to England and for being by my side, wherever life takes us.

TABLE OF CONTENTS

ABBREVIATIONS

2D	2-dimensional
3D	3-dimensional
ADCP	Acoustic Doppler Current Profiler
ADV	Acoustic Doppler Velocimeter
BT	Bottom Tracking
CEP	Circular Error Probable
CFD	Computational Fluid Dynamics
DC	Direct Current
DOP	Dilution Of Precision
EA	Environment Agency
EDM	Electronic Distance Meter
EGNOS	European Geostationary Navigation Overlay Service
EKF	Extended Kalman Filter
ESC	Electronic Speed Controller
EU	European Union
GNSS	Global Navigation Satellite System
GPS	Global Positioning System
GUI	Graphical User Interface
HEP	Hydro-Electric Plant
IDE	Integrated Development Environment
IDW	Inverse Distance Weighting
IGS	International GNSS Service
IMU	Inertial Measurement Unit
INS	Inertial Navigation System
IP	Ingress Protection
IPOS	Intensity Periodicity Orientation Scale
ISR	Interrupt Service Routine
LED	Light Emitting Diode
LiPo	Lithium Polymer
LM	Levenberg Marquardt
LS-PIV	Large Scale Particle Image Velocimetry
MEMS	Micro Electro-Mechanical System

NiMH	Nickel Metal Hydrate
NTP	Network Time Protocol
OLS	Ordinary Least Squares
OS	Ordnance Survey
PbAc	Lead Acid
PIV	Particle Image Velocimetry
PPK	Post Processed Kinematic
PRN	Pseudo Random Noise
PWM	Pulse-Width Modulation
RANSAC	Random Sample Consensus
RC	Radio-Control
RF	Radio Frequency
RFID	Radio Frequency Identification
RSS	Radio Signal Strength
RTC	Real-Time Clock
RTK	Real-Time Kinematic
S.D.	Standard Deviation
S.E.	Standard Error
SBAS	Space Based Augmentation System
SBC	Single Board Computer
SGBM	Semi-Global Block Matching
SLAM	Simultaneous Localisation and Mapping
SSH	Secure Shell
SVP	Strain-Velocity-Pressure
TOA	Time Of Arrival
TS	Total Station
UK	United Kingdom
US	United States
USB	Universal Serial Bus
USGS	United States Geological Survey
UTM	Universal Transverse Mercator
WFD	Water Framework Directive
WGS84	World Geodetic System 1984

WLAN	Wireless Local Area Network

Chapter 1

INTRODUCTION

1.1 Research background

The rapid growth in world population and global economic development are causing ever-increasing demands on rivers and other surface waters (MEA, 2005; WWAP, 2015). The necessary efficient management and conservation of water resources rely on a better understanding of how human interventions influence the hydrodynamics and morphology of rivers and how these in turn affect the functionality of river ecosystems. Over the past few decades, all major developments improving our understanding of fluvial processes have been underpinned by field-based research and measurement (Sukhodolov, 2015). Thus, the advancement of the technologies and methodologies used to obtain data from the field can be a crucial step towards better informed river management (Muste et al., 2012).

Within fluvial hydraulics and related disciplines, the accurate characterisation of fluid motion (hydrodynamics) in river channels has been a longstanding and inherently complex problem (Nikora & Roy, 2012; Sukhodolov, 2015). In the 20th century, *in situ* measurements of river hydrodynamics were dominated by the mechanical current meter, an intrusive instrument that uses the force of water rotating a propeller to measure point water velocities. Only within the last two decades, the availability of cheap computing power, electronics and sensor technology have enabled the development of non-intrusive digital continuous (time and space) flow measurement instrumentation that has revolutionised the *in situ* characterisation of river hydrodynamics (Muste et al., 2012).

Despite these developments, the accurate, spatially continuous characterisation of hydrodynamics at the reach scale remains a complex task, particularly if measurements are taken in the immediate vicinity of engineered in-channel structures, such as weirs, dams or fish passes. While the hydrodynamics induced by in-channel structures can be of particular relevance in the assessment of their ecological and hydromorphological effects, the environmental conditions associated with these structures pose several limitations to reliable water velocity measurements. These limitations range from errors in digital signal processing of acoustic measurement devices,

caused by highly turbulent and spatially complex hydraulics, to practical difficulties of safe sensor deployment and accurate spatial data referencing. The PhD research presented in this thesis was concerned with the development and assessment of solutions to some of these data quality issues. The research was underpinned by a cross-disciplinary approach that transferred emerging techniques from the domains of electronics and mobile robotics to the environmental sciences. The techniques and equipment developed within the PhD research contribute to a range of river management tasks that rely on field-based hydrodynamics data. Herein, the techniques were used specifically to address the problem of fish passage at anthropogenic in-channel structures; a longstanding river management problem that has gained increased attention in recent years because of international legislation driving improvements to river ecosystem status (EC, 2000, 2007; Katopodis & Williams, 2012).

1.1.1 The problem of fish passage

Riverine fish migrate because of a separation in time and space of optimal habitats for reproduction, growth and survival during different life stages (Northcote, 1998). Diadromous fish, i.e. species that migrate between fresh and marine waters (e.g. Atlantic salmon, *Salmo salar* and European eel, *Anguilla anguilla*), rely on the longitudinal continuity of river systems. However, also potamodromous fish, i.e. species whose migration occurs entirely within freshwater (e.g. brown trout, *Salmo trutta* morpha *fario* and *lacustris,* and barbel, *Barbus barbus*) migrate distances varying from a few meters to hundreds of kilometres to reach reproduction and feeding zones (Larinier, 2001).

Thousands of engineered in-channel structures have led to the fragmentation of many of the large river systems across the globe (Nilsson et al., 2005). In smaller rivers, low-head structures, such as gauging weirs and culverts, pose significant barriers to the movement of aquatic organisms (Ovidio & Philippart, 2002; Vowles et al., 2013). The negative effects of obstructions in rivers on migrating fish include delays in the migration to upstream spawning grounds or downstream habitats, increased exposure to predators, environmental stress

and injury (Larinier, 1998, 2001; Odeh & Orvis, 1998; Scruton et al., 2008), as well as subsequent negative consequences on freshwater and related ecosystems (Meyer et al., 2007). On almost every continent, river obstructions have led to a decline or even the extinction of migratory fish populations (Hatry et al., 2013). To restore the longitudinal connectivity of river ecosystems, obstructions can be removed or devices that facilitate the free passage of fish over, through or around the structure can be installed. These devices are referred to as fish passes (Armstrong et al., 2010).

The installation of fish passes has been a longstanding river restoration measure, with the first fish passes in Europe built in the mid-18th century (Katopodis & Williams, 2012). However, the mere installation of a fish pass does not necessarily ensure river connectivity; rather, the construction of fish passes goes hand in hand with the problem of assessing their biological effectiveness. Already in the 1860s, Francis (1870, cited in Katopodis & Williams, 2012) visited sites of salmon passes in the United Kingdom (UK) and found that most of these did not work well because of poor hydraulic conditions that caused salmon not to pass. Relative to the large number of fish passes constructed around the globe, very few have been evaluated (Schmutz et al., 1998). In a qualitative review of the scientific literature on fish passage monitoring from 1960 to 2008, Roscoe & Hinch (2010) identified only 96 articles on post fish pass construction monitoring, 30% of which had been carried out in Europe. Noonan et al. (2012) complemented the study of Roscoe & Hinch (2010) by reviewing the efficiency of fish passes, where monitoring had been conducted and published from 1960 to 2011. They found average upstream passage efficiencies of 61.7% for salmonids and 21.1% for non-salmonids and average downstream passage efficiencies of 74.6% and 39.6%. The insights from fish pass monitoring studies reveal the core problems of fish passage research:

i. The majority of current fish pass facilities do not achieve their primary conservation goal of restoring the connectivity of freshwater ecosystems (Bunt et al., 2012; Noonan et al., 2012), and

ii. the quantity and quality of available data from fish pass monitoring studies are insufficient for the proposal of reliable guidelines for fish pass design (Bunt et al., 2012).

Successful enhancements and design of fish passes rely on an improved understanding of the environmental, fish pass structural, and biological variables affecting fish passage (Castro-Santos et al., 2009). There is increasing evidence that the hydrodynamic conditions around the pass entrance (near-pass hydrodynamics) are one of the major factors influencing fish passage success in the upstream (Bunt et al., 2012; Burnett et al., 2014; Larinier, 2002a) and downstream directions (Nestler et al., 2008; Odeh & Orvis, 1998). These hydrodynamics, reflected in water velocities, acceleration, turbulence and discharge, affect the so called fish pass attractiveness, which determines the ability of fish to rapidly locate the fish pass entrance when approaching the migration barrier (Larinier, 2002; Williams et al., 2012; see Chapter 2). It has been argued that an improved understanding of the response of migratory fish species to these hydrodynamics is a key requirement and one of the most important challenges for the development of guidelines for successful fish passes (Castro-Santos et al., 2009; Nestler et al., 2008; Sprankle, 2005; Williams et al., 2012).

The low biological effectiveness of many fish passes is related to the dominance of unrealistic fish passage criteria and design guidelines based on studies under uniform hydraulic conditions. Recently, there have been calls for a paradigm shift towards an “eco-hydraulic approach” to fish pass assessment (Vowles et al., 2013). Its purpose is to develop realistic pass design guidelines that incorporate the complex hydraulic conditions in rivers as well as fish behaviour under natural conditions. The implementation of the eco-hydraulic approach requires technological advancement on two levels (Lacey et al., 2012; Vowles et al., 2013):

i. the availability of techniques to precisely measure fish positions and relevant variables of fish behaviour when they approach a migration barrier in the field, and

ii. tools and methodologies for the accurate field-based quantification of hydrodynamic variables of fish-ecological importance at relevant spatial and temporal scales.

1.1.2 Importance of measuring near-pass hydrodynamics

The PhD research presented herein addressed the second requirement for eco-hydraulic fish pass assessment as outlined in Section 1.1.1. Specifically, the research was concerned with the development of a methodology for the rapid and relatively low-cost *in situ* quantification of the 3-dimensional (3D) distribution of water velocities near fish passes and the derivation of hydrodynamic metrics potentially explaining fish pass attractiveness from these flow maps.

The usefulness of such a methodology to fish passage research and river management is manifold:

(i) It can be used for the rapid field-based assessment of fish pass attractiveness related to hydrodynamics prior to more time-consuming and expensive fish pass monitoring. Thereby, fish passes requiring enhancements to their attractiveness can be rapidly identified and, if needed, prioritised for further studies.

(ii) It can be used to complement fish pass monitoring involving fish tagging and/or tracking. As such, the methodology contributes to a more comprehensive strategy towards fish pass assessment; one that involves not only the quantification of fish passage success, but also its explanation through environmental variables in order to inform effective improvements to fish pass design.

(iii) It can be applied as part of scientific studies aiming to improve our understanding of fish behaviour towards the real, complex hydrodynamics found in rivers.

Summarising these points, the methodology developed in this research can contribute to a more informed and efficient use of resources invested in fish pass monitoring, more reliable pass design guidelines and the necessary

transfer of previously laboratory-based studies into the field. Thereby, it addresses the need for methods to assess the ecological effects of hydromorphological alterations in rivers, which has been emphasised in recent environmental policies (see Section 1.1.4).

1.1.3 Complexity of measuring near-pass hydrodynamics

Despite recognition of the relevance of near-pass hydrodynamics in the overall process of fish passage, only a few studies have attempted to quantify the spatially continuous distribution of water velocities near fish pass entrances. These studies mostly deployed 2-dimensional (2D) or 3D numerical hydrodynamic modelling (Andersson et al., 2012; Johnson et al., 2009; Lindberg et al., 2013; Nestler et al., 2008; Piper et al., 2015) or physical modelling with flow simulation at laboratory scale (Scruton et al., 2002, 2008). Successful *in situ* measurements of near-pass hydrodynamics have been rare and limited to spatially discontinuous point velocity data (e.g. Piper et al., 2012).

Digital flow measurement devices have opened up novel opportunities for the *in situ* quantification of near-pass hydrodynamics. The technology principles of these devices include acoustics, electromagnetics and imaging (Muste et al., 2012). The suite of currently marketed instruments ranges from high precision point measurement devices with spatio-temporal resolutions sufficiently high to resolve 3D velocities and natural turbulence at scales <1 cm (e.g. Acoustic Doppler Velocimeters, ADVs; García et al., 2005; Lane et al., 1998), to devices that instantaneously capture the 2D flow field over large areas of interest (e.g. Large Scale Particle Image Velocimetry, LS-PIV; Jodeau et al., 2008; Muste et al., 2008).

The instrument at the core of the research within this thesis is the Acoustic Doppler Current Profiler (ADCP), which has been attributed great potential in eco-hydraulic fish pass research (Shields & Rigby, 2005; Vowles et al., 2013). The ADCP was invented in the late 1970s by modifying a marine Doppler navigation sonar (Rowe & Young, 1979). Since the development of broadband ADCP technology in the early 1990s, ADCPs have been increasingly used for

discharge measurements in rivers (Gordon, 1996). By resolving the Doppler shift in acoustic signals transmitted and received via multiple transducers, vessel-mounted, downward-looking ADCPs instantaneously measure 3D water velocity vectors in multiple depths along the vertical water column without having to physically traverse the instrument. Vessel-mounted ADCPs can be manoeuvred along a trajectory of interest, such as a river cross section, to obtain a 2D snapshot representation of the water velocities and depths along the track (see Figure 1-1).

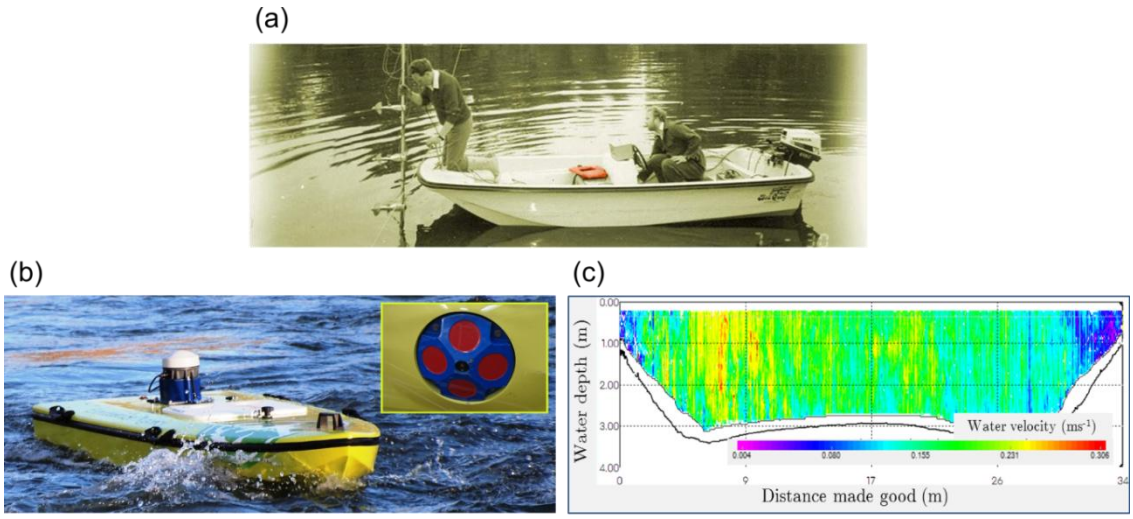

Figure 1-1. Examples of historic and modern flow measurement (photographs provided by Nick Everard, EA); (a) Point velocity measurement with a mechanical current meter in the 1980s; (b) Continuous flow measurement with an ADCP deployed from an ARC-Boat radio-control platform; the inlay plot shows the face of a 1,200 kHz RioGrande ADCP mounted on the ARC-Boat; (c) Typical data display of a cross-sectional water velocity distribution measured with an ADCP in a single river crossing

If the same trajectory is sampled repeatedly, the distribution of the temporally averaged water velocity can be estimated (Gunawan et al., 2010; Muste et al., 2004b). The interpolation of such data in 3D space yields a spatially continuous map of 3D velocities for an area, or river reach, of interest. Hydrodynamics quantification of such kind have rarely been available prior to ADCP application (Muste et al., 2012).

The usefulness of ADCPs in quantifying 3D hydrodynamics at reach scale has been demonstrated in numerous studies, resulting in new insights into river

hydrodynamics and associated morphology, such as the detailed characterisation of 3D flow fields of dunes (Parsons et al., 2005), confluences (Parsons et al., 2007), bifurcations (Szupiany et al., 2012) and bends (Vermeulen et al., 2015) in large rivers, the response of river hydrodynamics to tidal cycles (Dinehart & Burau, 2005a, 2005b), or the 3D flow structures leading to bedrock incision in canyons (Venditti et al., 2014). Moreover, ADCPs and expertise in their deployment are widely available within national river monitoring agencies. For example, the United States Geological Survey (USGS) conducts more than 50% of all discharge measurements that can be made from a boat, cableway or bridge with an ADCP (Muste et al., 2012) and since 2003, the ADCP has been the primary instrument for mobile river discharge measurements by the Environment Agency (EA) of England (pers. comm., EA Evidence Directorate, Nick Everard). Thus, an ADCP-based methodology for the rapid quantification of near-pass hydrodynamics has the advantage of a potentially fast uptake in practice.

However, from previous studies, several ADCP data quality issues are known, which are particularly distinct in (but not exclusive to) the environmental conditions frequently surrounding engineered in-channel structures. These issues include bias in water velocity readings due to spatial flow heterogeneity, incorrect velocities caused by temporary changes in the local magnetic field biasing the ADCP compass readings, discontinuous data caused by loss of the ADCP Bottom Tracking (BT) signal and incorrectly localised data due to the unavailability of Global Navigation Satellite Systems (GNSS; see Chapter 3 for a detailed review of these and other relevant sensor limitations). These issues are accompanied by practical difficulties of deploying a sensor within the rough surface waters associated with flow obstacles, particularly in non-wadeable rivers. Additionally, the specific instrument setup of the ADCP as a profiler and its specific spatial and temporal measurement resolutions make it difficult to link ADCP-measured hydrodynamics to ecological processes (Shields & Rigby, 2005).

From these problems arise two requirements for useful near-pass hydrodynamics quantification with ADCPs:

(i) to increase the accuracy and availability of ADCP data collected in the complex hydraulic and environmental conditions associated with engineered in-channel structures, and

(ii) to link ADCP-measured hydrodynamics to fish pass attractiveness.

These are the core research aspects and gaps in knowledge addressed in this research project.

1.1.4 Legal Background

Legal frameworks worldwide make specific consideration of fish passage to improve river ecosystem status. One of the most prominent is the European Union (EU) Water Framework Directive (WFD; EC, 2000), which requires member states to promote efforts towards free fish migration in European rivers. The EU WFD (Art. 4) set the targets of good ecological and chemical status of surface waters, to be achieved by 2015 and, where extensions to this deadline are applied, by no later than 2027. Annex V of the WFD specifically states river continuity as a hydromorphological quality element supporting the achievement of a good ecological status. Therefore, EU member states are required to resolve human-made barriers to fish migration that significantly alter the fish species composition and abundance. The number of affected barriers is vast; for example, in England and Wales alone, there are around 26,000 potential obstructions to fish migration (NASCO, 2015), 3,000 of which were estimated to require resolution if the targets of the WFD and other EU regulation (specifically, the EU Eel Regulation; EC, 2007) were to be achieved (Environment Agency, 2009).

In a recent assessment, the European Commission found that the approach taken by EU member states to achieve the environmental targets of the WFD was “clearly not sufficient […] for most water bodies” (EC, 2015). The assessment report stated that hydromorphological changes were a main factor causing these shortcomings and emphasised the need for methods of

monitoring and assessment to identify situations, where hydrological alterations prevent the achievement of good ecological status. The methodology developed in this research contributes towards achieving the targets of the WFD by raising our understanding of fish passage and ultimately informing the design of biologically effective fish pass facilities.

1.2 Aim and objectives

Based on the research background outlined above, the research aim and objectives were set up as follows.

1.2.1 Overall research aim and question

The aim of this research project was to define an effective and practicable methodology for the measurement of hydrodynamic indicators of fish pass attractiveness in non-wadeable rivers.

The re-formulation of this aim resulted in the overarching research question:

At the current state and availability of technology, is it possible to define an effective and practicable methodology for the measurement of hydrodynamic indicators for fish pass attractiveness in non-wadeable rivers?

1.2.2 Objectives

The aim was accomplished through the following research objectives:

(1) to identify a set of hydrodynamic metrics indicating fish pass attractiveness,
(2) to identify the state of the art of ADCP-based quantification of hydrodynamics in rivers and the most relevant sensor limitations to such measurements near engineered in-channel structures,
(3) to enhance ADCP measurements near engineered in-channel structures in terms of accuracy, availability and practicability of sensor deployment,
(4) to assess the effect of the spatio-temporal ADCP data sampling strategy on the flow field quantification near fish passes,

(5) to evaluate the suitability of the improved ADCP-based near-pass hydrodynamics quantification to derive hydrodynamic descriptors based on those identified in objective (1) at a range of sites with different fish pass types and discharge conditions, and

(6) to synthesise the findings from objectives (1) to (5) into a methodology for the ADCP-based near-pass hydrodynamics quantification and a methodology appraisal in terms of effectiveness, practicability and transferability.

1.3 Thesis layout

The thesis is divided into thematic **parts** and **chapters**. Figure 1-2 shows the four thematic parts and eight chapters of the thesis along with the associated research objectives.

The reviews presented in Part I have underpinned the requirement and methods of the experimental, mainly field-based, research presented in Parts II and III. In Part IV, the research findings have been synthesised and future research and technical development requirements have been highlighted. The chapters of Parts II & III (Chapters 4 to 7) follow the structure typical for original research articles in peer-reviewed specialist journals, covering the sections “Methods” as well as “Results and Discussion”. This has facilitated publication of parts of the research (see Appendix B). Each of these chapters starts by defining a list of three to five tasks fulfilled within that chapter to accomplish the associated research objective(s).

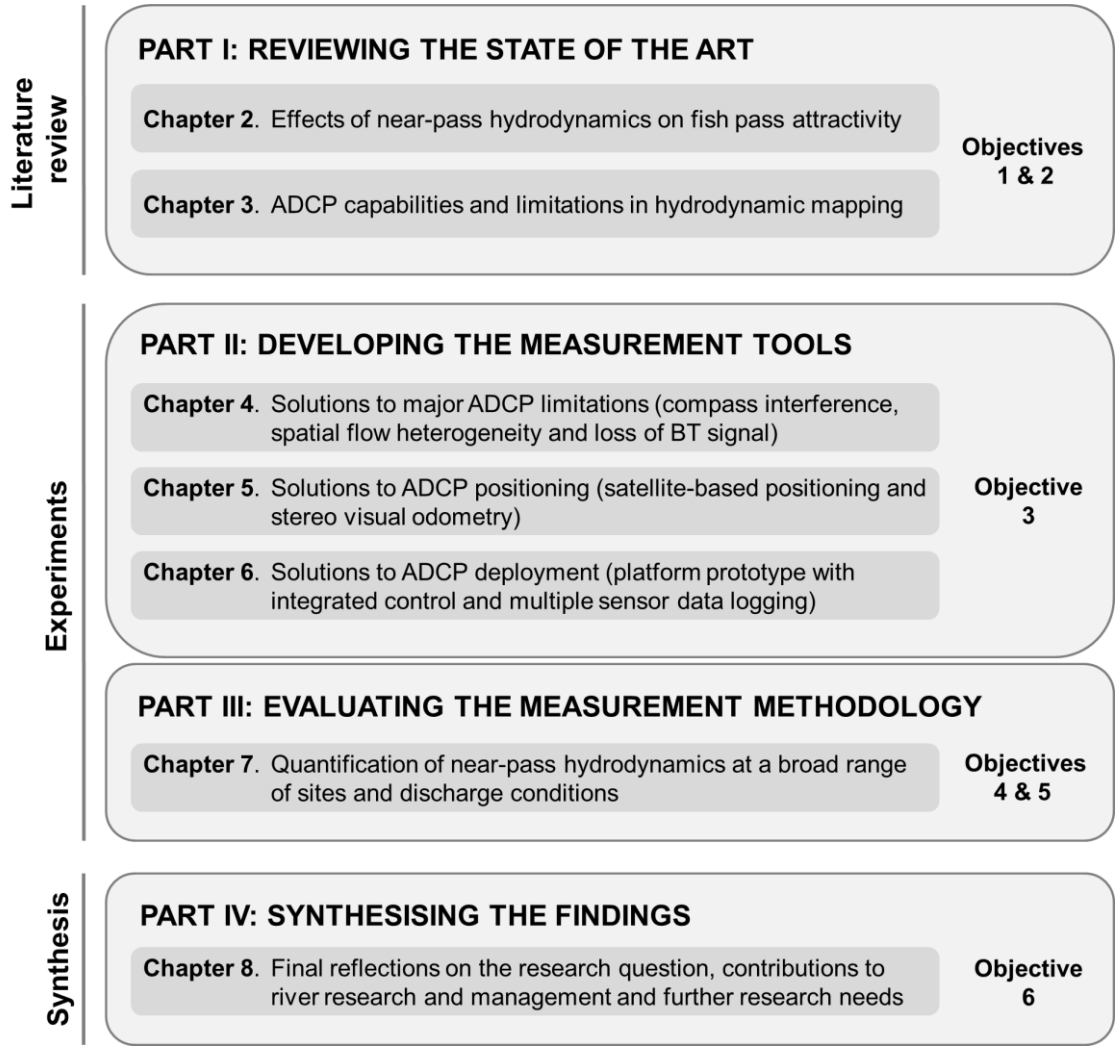

Figure 1-2. Thesis structure in relation to the research objectives

1.3.1 Part I – reviewing the state of the art

Part I of the thesis provides a detailed review of the state of knowledge on fish behaviour towards hydrodynamics (**Chapter 2**) and the state of the art of measuring river hydrodynamics with ADCPs (**Chapter 3**). The review has been structured into two chapters because of the interdisciplinary nature of the PhD research. In particular, the research aim (see Section 1.2.1) required elaboration of both (i) *what* to measure, and (ii) *how* to measure. The former concerned the fundamental question, *Which hydrodynamic variables indicate fish pass attractiveness?*. This question is associated with the research field of eco-hydraulics and grounded in fish behavioural biology and physiology. The latter concerned the question, *How should ADCPs be used in hydrodynamic*

mapping applications and can they deliver reliable results within the complex hydraulic conditions associated with fish passes?. This question relates to the research around flow measurement instrumentation and is grounded in the operational principles and inherent limitations of ADCPs. The identification of the most relevant ADCP limitations required particular attention because ADCPs used on rivers had not been designed for the purpose of hydrodynamic mapping, but for discharge measurement. Moreover, some of the potential errors in ADCP data can be particularly pronounced in the environmental conditions associated with engineered in-channel structures (see Section 1.1.3).

The reviews presented in Part I of the thesis resulted in:

(i) a set of hydrodynamic descriptors found to potentially indicate fish pass attractiveness (presented in Section 2.6), and

(ii) a set of errors in ADCP data that were found to substantially limit ADCP measurements near fish passes, along with potential solutions (presented in Section 3.4).

Based on a synopsis of both reviews, a methodology for the ADCP-based quantification of near-pass hydrodynamics has been proposed in the final section of Chapter 3 (Section 3.5). The author of the thesis encourages the reader to direct particular attention towards this section, because it outlines the approach towards the methodology implementation and evaluation presented in Parts II and III of the thesis.

1.3.2 Part II – developing the measurement tools

Part II of the thesis covers the development and assessment of techniques that increase the accuracy, availability and practicability of ADCP measurements near fish passes. It formed the largest part of the research presented herein, because of the overwhelming evidence from previous studies on the numerous, relevant ADCP errors associated with the environmental conditions near engineered in-channel structures and the lack of reliable and/or cost-effective solutions to some of these problems. The techniques developed in Part II of the

thesis form an integral part of the methodology for ADCP-based near-pass hydrodynamics quantification proposed in Part I.

The study presented in **Chapter 4** assessed a set of techniques to increase the robustness of ADCP data against errors associated with the environmental conditions near engineered in-channel structures. This involved:

(i) a novel technique to reduce temporary errors in the ADCP-internal compass (e.g. from interference with ferromagnetic on-site materials),
(ii) a recently suggested post-processing method to reduce the effects from violations of the flow homogeneity assumption inherent to conventional ADCP data processing, and
(iii) the ADCP positioning and boat velocity measurement via a target tracking tachymeter integrating electronic distance and angular measurement (Total Station; TS) as an alternative to GNSS.

The suggested techniques were integrated on a Radio-Control (RC) ADCP platform and demonstrated downstream of a weir with a vertical slot fish pass. Their effects on selected metrics describing the near-pass hydrodynamics were assessed statistically.

The study presented in **Chapter 5** addressed one of the major challenges of ADCP measurements in small to medium sized rivers: the accurate sensor positioning and data localisation in areas with limited line of sight to GNSS satellites. The error of GNSS-based ADCP positioning was quantified during five data collection campaigns covering three different fish pass sites in the UK and a wide range of environmental site conditions. Based on a review of alternative positioning systems, stereo visual odometry from the domain of mobile robotics was assessed in a detailed statistical analysis as a novel, low-cost solution for ADCP positioning in GNSS-denied locales.

Chapter 6 covers the development of an ADCP platform prototype addressing the need for a platform with an on-board system for multiple-sensor data logging and integrated propulsion control as well as sufficiently small and light to enable single-person deployment. The enhanced platform electronics were

needed, firstly, to facilitate the integration of the ADCP with external sensors as part of the techniques developed in Chapters 4 and 5, and secondly, to provide the basis for future features of platform autonomy supporting the accurate implementation of pre-defined sampling strategies. Moreover, the availability of a small-sized platform contributed to the overall research aim by making the application of the proposed methodology for near-pass hydrodynamics quantification cheaper, supporting its wide-spread uptake in practice.

The performances of the techniques and equipment presented in Part II of the thesis were essentially uncertain prior to their field-based assessment. It was due to this uncertainty that some of the techniques could be considered ready for use within the methodology evaluation in Part III, whereas others required further research beyond the scope of the thesis.

1.3.3 Part III – evaluating the measurement methodology

Part III of the thesis has been covered in **Chapter 7**. Building on the methodology proposed in Part I and the technical developments in Part II, the chapter presents the evaluation of the ADCP-based quantification of near-pass hydrodynamics at a range of sites. These covered three different types of fish passes as well as conditions of low, medium and high discharge, enabling an assessment of the methodology transferability and its limits related to the environmental on-site conditions. The methodology was evaluated regarding its suitability to identify common qualitative descriptors of near-pass hydrodynamics and to quantify indicators for fish pass attractiveness identified or proposed in Part I of the thesis. Moreover, the chapter presents an analysis of the effects of the spatio-temporal ADCP sampling strategy on the obtained near-pass hydrodynamics quantification. The analysis informed the efficient methodology implementation, which, given time constraints, can be considered key to the methodology uptake in practice.

1.3.4 Part IV – synthesising the findings

Chapter 8 synthesises the findings of the research presented in the thesis. It summarises the methodology developed in the PhD research and provides

recommendations for its implementation based on the research findings. This is followed by a methodology appraisal in terms of effectiveness, practicability and transferability, providing an answer to the research question stated in Section 1.2. Finally, the chapter highlights contributions of the PhD research beyond the context of fish passage and requirements for future research.

Chapter 2

A REVIEW OF THE ROLE OF NEAR-PASS HYDRODYNAMICS IN THE BARRIER PASSAGE OF UP- AND DOWNSTREAM MIGRATING FISH

2.1 Introduction

The development of a measurement methodology requires clear knowledge of *what* variables to measure, prior to setting out *how* to measure them. Achievement of the PhD research aim (see Section 1.2) was thus reliant on a clear understanding of the question: *Which hydrodynamic variables indicate fish pass attractiveness?*

This question was addressed by means of a literature review, the findings of which are presented in this chapter. Thereby, **objective 1** of the PhD research was addressed (see Section 1.2):

to identify a set of hydrodynamic metrics indicating fish pass attractiveness.

2.1.1 Definition of key terms and review scope

In this research, fish pass (also referred to as fishway or fish ladder) was defined as:

- “any form of conduit, channel, lift, other device or structure which facilitates the free passage of migrating fish over, through or around any dam or other obstruction, whether natural or man-made, in either an upstream or a downstream direction” (Armstrong et al., 2010).

Fish pass attractiveness (or attractivity) was defined as:

- the characteristic of a fish pass that enables migratory fish to find the entrance to the pass with as little delay to the migration as possible (Armstrong et al., 2010; Baras et al., 1994; Larinier, 2002a). The concept can be applied both to the entrance at the downstream end of the pass (for upstream passage) and the upstream end (for downstream passage).

The scope of the PhD research and thus of the review presented herein was restricted to those fish pass characteristics that are reflected in the hydrodynamics surrounding the pass entrance. Specifically, the term “near-pass hydrodynamics” (also “near-field hydraulics“; Bunt et al., 2012) was defined as:

- the motion of water, reflected in water velocity, turbulence or any flow patterns, surrounding the entrance to a fish pass at its up- or downstream end (based on Williams et al., 2012).

The scope was based on the evidence from previous studies showing the near-pass hydrodynamics to be a key factor influencing the ability of fish to find the entrance to a pass, and the attraction to the pass to be a crucial stage in the overall process of successful fish passage (see Section 2.2).

2.1.2 Chapter outline

The remainder of this chapter is structured as follows: **Section 2.2** defines the role of near-pass hydrodynamics and fish pass attractiveness within the overall process of fish pass assessment. Thereby, it relates the research presented in the thesis to previous, established methods and concepts of fish pass assessment. **Section 2.3** summarises qualitative descriptions of near-pass hydrodynamic conditions known to support or deteriorate fish pass attractiveness. **Sections 2.4** and **2.5** present the evidence on fish response towards near-pass hydrodynamics based on basic fish behavioural research conducted under controlled conditions in the laboratory and studies of fish pass monitoring in the field, respectively. In accordance with objective 1 of the research (see Section 1.2), particular emphasis was put on the metrics used to describe the hydrodynamics encountered by the fish. Finally, **Section 2.6** presents a framework for categorising the hydrodynamic metrics potentially explaining fish pass attractiveness and discusses the implications of the literature review on the methodology developed to quantify near-pass hydrodynamics.

2.2 Near-pass hydrodynamics within the concept of fish pass assessment

The near-pass hydrodynamics form one of several factors potentially influencing the performance of a fish pass. In order to define the role of near-pass hydrodynamics within the concept of fish passage, and to locate the contribution

of this PhD thesis within fish passage research, a general framework of fish pass assessment has been developed (see Figure 2-1).

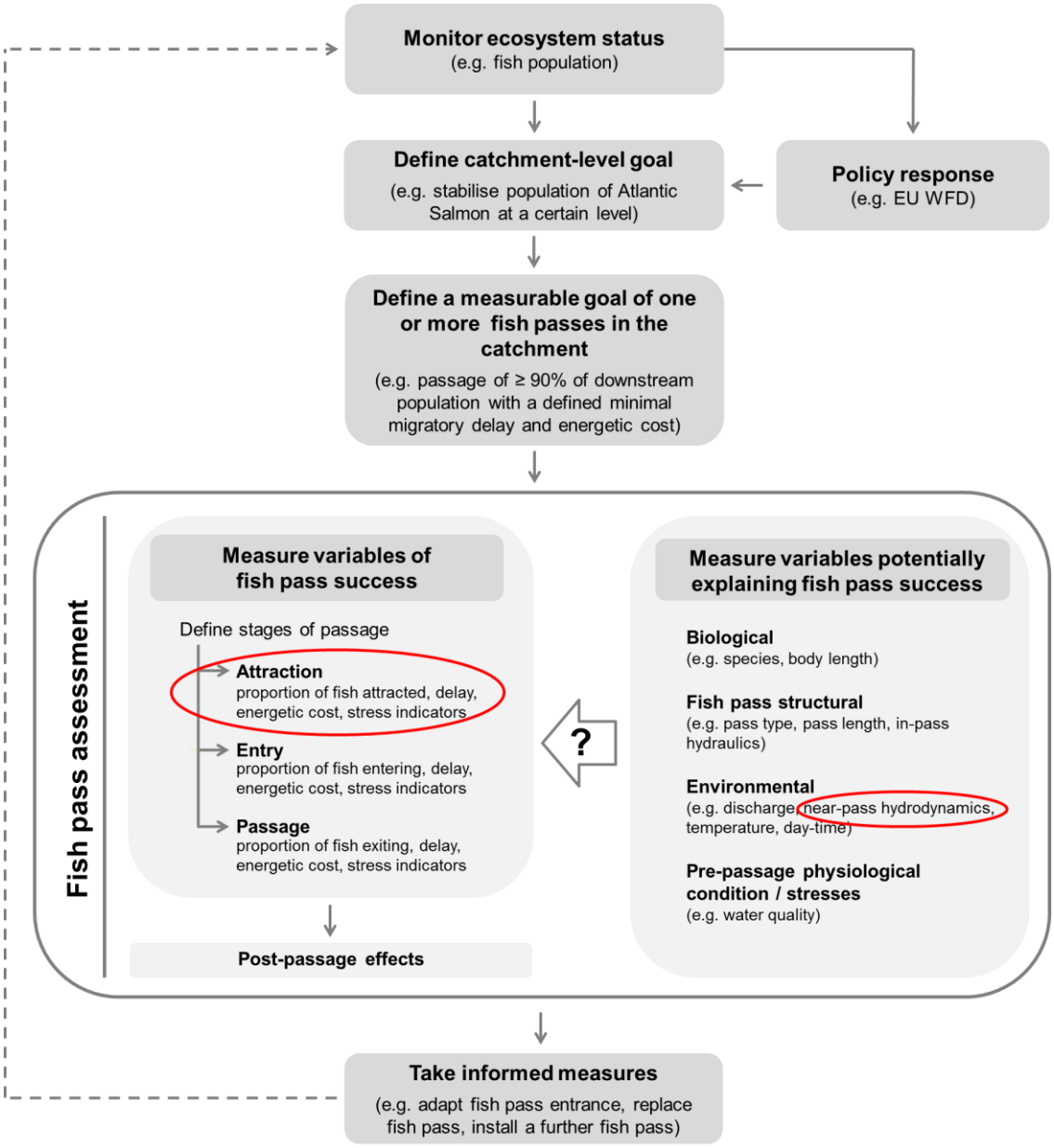

Figure 2-1. Conceptual framework of fish pass assessment; the elements of primary concern to this PhD research are highlighted in red.

Comprehensive fish pass assessment requires the purpose and goal of the fish pass under study to be clearly defined (Castro-Santos et al., 2009; Roscoe & Hinch, 2010). This goal may be related to a conservation target for the overall catchment, informed by the status of fish populations based on population

monitoring and motivated by environmental policies like the EU WFD (see Section 1.1.4). Quantitative fish pass assessment requires the goal to be measureable (Castro-Santos et al., 2009). The measure of total passage efficiency is regarded as the “gold standard” in evaluating fish passes (Cooke & Hinch, 2013). It is a measure of the proportion of migrating fish of a particular species attempting to pass a barrier relative to the number of fish that actually pass successfully (Bunt et al., 2012; Travade & Larinier, 2002).

For diadromous fish, a passage efficiency of 90 to 100% (Lucas & Baras, 2001) or passage of the whole population (Larinier, 1998) are generally considered necessary. The most stringent concepts demand “transparent” migration, i.e. passage without delay, stress or injury that might affect upstream migration (Castro-Santos et al., 2009; Larinier, 2002b). The stringency of this concept is based on the insight that in modified rivers, fish may encounter a large number of migration barriers with cumulative effects on energy expenditure and migratory delay (Armstrong et al., 2010; Castro-Santos et al., 2009; Caudill et al., 2007). Some fish species that migrate from the sea to riverine breeding habitats (referred to as anadromous fish; e.g. Atlantic salmon and Pacific salmon, *Oncorhynchus spp.*) do not feed during their upstream migration, but depend entirely on their energetic reserves acquired at sea to complete migration, gonad development and spawning (Lucas & Baras, 2001; Scruton et al., 2007). There is evidence to suggest that exhaustive depletion of energetic resources during upstream migration compromises reproductive success and thus can result in dramatic reductions in the population of these species (Castro-Santos & Haro, 2003). Also the downstream migrating juvenile fish of many anadromous species have a limited time window within which to reach the sea before losing the physiological capabilities required to survive in freshwater. Therefore, high passage efficiencies at all structures with minimal delay to migration is vital for the population of these species (Castro-Santos & Haro, 2003; Larinier, 1998). In contrast, a fish pass targeted at resident species may be designed to prevent population fragmentation, a goal that can already be achieved if the pass is used by a smaller proportion of individuals (Larinier, 1998).

The overall process of fish passage can be separated into the arrival at the pass entrance (“attraction” or “guidance”), the decision to enter (“entry”) and the exit of the fish pass after successful passage (“passage” or “exit”; Bunt et al., 2012; Castro-Santos et al., 2009; see Figure 2-1). Accordingly, the measure of total fish passage efficiency can be categorised into (1) attraction efficiency, (2) entrance efficiency and (3) passage efficiency (Bunt et al., 2012). Various different definitions have been used for these measures (Kemp & O’Hanley, 2010). The attraction efficiency can be defined based on criteria related to space and/or time. In the context of fish pass assessment by radio-tagging and fish tracking, Bunt et al. (2012) defined it as the proportion of fish tagged and released that are subsequently located within less than about 3 m from the fish pass entrance or at the base of a barrier to fish movement and close enough to a fish pass entrance for fish to detect the attraction flow (i.e. the jet of water issued from the fish pass entrance). Alternatively, the attraction efficiency can be defined with regards to the individual fish as the number of approaches an individual makes before eventually entering a fish pass and the time it takes the individual to do so (Kemp & O’Hanley, 2010). The entrance efficiency describes the proportion of tagged fish attracted to a fish pass that actually enters the structure (Evans et al., 2008; Noonan et al., 2012). The passage efficiency can be defined as the proportion of fish entering a pass that successfully ascend and exit the pass (e.g. Bunt et al., 1999). In quantitative fish pass assessments it is frequently attempted to measure some or all of these components through radio-telemetry, where the movement patterns of individual fish attempting to pass a barrier are tracked (Bunt et al., 2012; Travade & Larinier, 2002).

Fish pass assessment that determines not only the performance of a pass, but also informs effective modifications to enhance the performance, requires to describe covariates potentially explaining the measured attraction, entrance and passage efficiencies (Castro-Santos et al., 2009). The covariates involve biological factors (e.g. fish species, fish body length), factors related to the fish pass structure (e.g. fish pass type, length, slope), environmental factors (e.g. near-pass hydrodynamics, light conditions, water temperature) and the

physiological conditions of the fish before attempting to pass a barrier (Roscoe & Hinch, 2010; see Figure 2-1).

As indicated in Figure 2-1, the near-pass hydrodynamics form an environmental factor potentially explaining the attraction of fish to a pass. The methodology for near-pass hydrodynamics quantification developed in the PhD research can thus be used to complement fish pass assessment (see also Section 1.1.2), but cannot be used to substitute the measurement of variables of fish pass success, such as the attraction efficiency, as this requires fish marking or tagging (Cooke & Hinch, 2013).

Finally, there may be interaction between the covariates of fish pass success, the understanding of which is important to define effective strategies for enhancing hydrodynamic fish pass attractiveness. For example, the extent of the flow issued from the fish pass and attracting fish to its location depends on the slope and other design characteristics of the fish pass structure (see Section 2.5.1). If the relationship between near-pass hydrodynamics, fish pass structure and pass attractiveness is understood, even small modifications in pass design can, in some cases, substantially improve passage success (Scruton et al., 2002, 2008; see Section 2.5.2.2). The methodology developed in this research contributes towards this understanding and thus to improved fish pass design.

2.3 Qualitative guidelines for near-pass hydrodynamics

Larinier (2002a) provided descriptions of predominantly qualitative nature or ‘rules of thumb’ for favourable and unfavourable near-pass hydrodynamic conditions and these guidelines have become part of national and international fish pass design manuals (e.g. Armstrong et al., 2010; FAO, 2002). Many of his recommendations relate to the extent and direction of the attraction flow in relation to other flow patterns forming downstream of migration barriers.

2.3.1 Attraction flow

The attraction flow should be detectable by fish approaching a pass at the greatest possible distance from the pass entrance (Larinier, 2002a). The extent of the attraction flow depends on the momentum (i.e. discharge multiplied by velocity) of the water jet. Thus, it is essential to create sufficiently high discharge and water velocities at the fish pass entrance, while ensuring compatibility with the swimming capabilities of all targeted species and life stages. Larinier (2002a) suggested a minimum water velocity of 1 ms^{-1} for most species and an optimal range in the order of 2 to 2.4 ms^{-1} for salmonids and other large migrating fish (see also Section 2.4.1). Further, he recommended a discharge through the fish pass of about 1 to 5% of the total river discharge in fish migration periods, whereby higher volumes may be necessary during low flow conditions. According to Williams et al. (2012), 5 to 10% are typical discharges through fish passes at dams in the United States (US), UK and France.

Also downstream passage depends on hydrodynamic cues guiding fish to or repelling them from the entrance of a bypass channel (see Section 2.4.3). For Hydro-Electric Plants (HEPs) in the US, Odeh & Orvis (1998) stated a minimum flow through bypass channels for downstream passage of 2 to 5% of the turbine capacity, depending on the fish guidance device in use.

2.3.2 Competing flows

According to Larinier (2002a), the attraction flow must remain distinct in the downstream channel; it must not be masked by other flow patterns in the tailwater with which it cannot compete, such as hydraulic jumps, eddies, recirculation zones or competing flows from turbines. Where competing flows are issued from turbines or spillways, an attraction flow directed parallel or only at a slight angle to the direction of the main river flow is favourable to a jet directed perpendicular to the channel flow, which may not persist far downstream. Moreover, the formation of recirculation cells or static water zones

downstream of a barrier should be avoided to prevent fish getting trapped in them (see Figure 2-2).

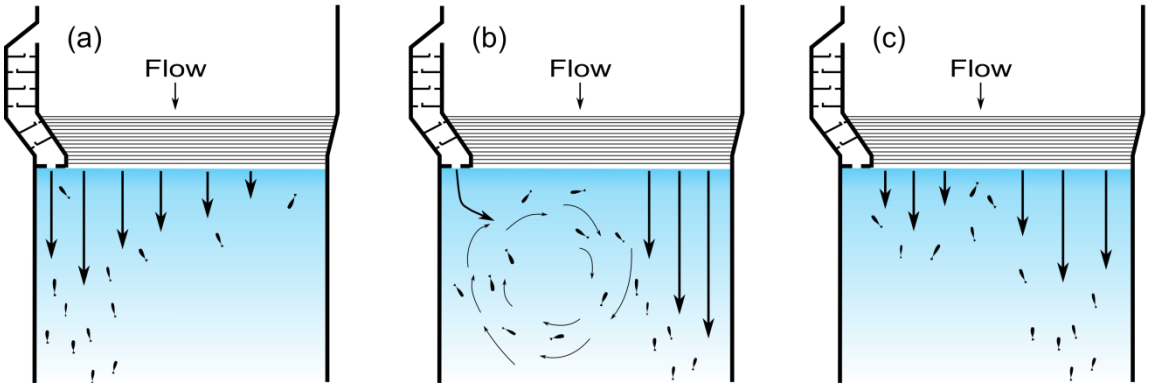

Figure 2-2. Three scenarios of near-pass hydrodynamics downstream of a weir with a fish pass installed on the right river bank (based on Baek & Kim, 2014; Larinier, 2002a); the arrows indicate the water velocity magnitudes and directions, the drawings are not to scale; (a) Optimal conditions with strong attraction flow towards the pass entrance; (b) Strong competing flow over the left bank of the weir, forming a recirculation zone that is masking the pass entrance; (c) Very little attraction flow from the pass and static water zones masking the pass entrance

2.3.3 Fish pass location and fish migration pathways

The relevance of hydrodynamic features near fish passes depends on their location in relation to the fish pass entrance and the pathways that fish are likely to use when approaching a barrier. Larinier (2002a) suggested that the pass entrance should be located on or near the river bank rather than in the middle of an obstruction, as fish (especially salmonids and shad) tend to migrate along the edges of the main water body in order to take advantage of lower water velocities in these areas, particularly during conditions of high discharge. Hinch et al. (2002) validated this behaviour by tracking upstream migrating pink salmon, *Oncorhynchus gorbuscha*, and sockey salmon, *O. nerka;* and Sprankle (2005) observed the behaviour for upstream migrating American shad, *Alosa sapidissima*. Adult upstream migrants tend to move as far as possible upstream and to swim against the main current (positive rheotaxis) when encountering the increasing velocities induced by the flow discharged from dams. They avoid areas of low velocities (FAO, 2002; Williams et al., 2012; see also Karppinen et al. (2002) and Lundqvist et al. (2008) validating this behaviour for Atlantic

salmon, and Arnekleiv & Kraabol (1996) for brown trout). Consequently, the pass entrance should be located as close as possible to the most upstream point reachable by migrating fish and oriented such that fish moving against the current can enter the pass as directly as possible (Larinier, 2002a; Williams et al., 2012). This is another reason why attraction flows oriented parallel to the main river flow are considered more favourable than those oriented perpendicular. It is critical to identify the points or lines up to which certain fish species and life stages are able to swim; the so called “blockage zones” or “hydraulic barriers” (Larinier, 2002a). These may correspond to the physical migration barrier or the location of water velocities too high to pass or extreme turbulence (Larinier, 2002a). This implies that the optimal entrance location varies for species with different swimming capabilities and development stage, e.g. small coarse fish may require fish pass entrances further downstream in calmer and less turbulent zones, whereas for salmonid species the optimal entrance may be further upstream and closer to turbines (if an HEP forms the migration barrier).

In contrast to their adult upstream migrating counterparts, downstream migrating salmon smolts tend to move towards the area in the river channel with the highest flow velocities and avoid zones of water velocity acceleration or deceleration (Coutant & Whitney, 2000; Svendsen et al., 2007; Williams et al., 2012), a behaviour that has been confirmed in laboratory-based studies (see Section 2.4.3). These preferences may be explained by a behavioural strategy to avoid migratory delays, increased susceptibility to predation and physical injury, while minimising energy use (Enders et al., 2009; Kemp et al., 2005).

2.3.4 Final remarks on qualitative guidelines

Some of the hydrodynamic features mentioned by Larinier (2002a), such as the direction and spatial extent of the attraction flow in relation to competing flows, eddies and recirculation zones, might be identifiable on maps visualising the spatial distribution of water velocities around the pass entrance. Such visualisations could thus provide a useful starting point in the assessment of near-pass hydrodynamics. The survey area to be covered would have to reach

sufficiently close to the fish pass entrance for the attraction flow to be discernible and ideally cover the full width of the river channel in order to identify potentially competing flows or hydraulic barriers as described by Larinier (2002a). In a second step, quantitative descriptors of these and other hydrodynamic features could be derived from the flow maps (see also Section 2.6). The availability of such quantitative descriptors from previous fish behavioural and fish pass monitoring studies has been reviewed in the following sections.

2.4 Evidence from fish behavioural studies

2.4.1 Water velocity magnitude and fish swimming capability

Traditionally, fish pass design guidelines regarding the pass length and maximum water velocities within the structure have been based on estimates of fish swimming speed and endurance (e.g. Bell, 1990; Clay, 1995). Several authors (e.g. Beach, 1984; Beamish, 1978; Bell, 1990) suggested categories of fish swimming speeds and classifications of speed-endurance relationships (see Appendix A.1). These relationships have been obtained either empirically in forced swimming experiments under controlled laboratory conditions (e.g. Bainbridge, 1958; Clough & Turnpenny, 2001; Nikora et al., 2003) or theoretically, based on physiological capabilities in the light of limited energy stores (e.g. Beach, 1984). For some UK fish species, the swimming capabilities as a function of fish size and temperature, as derived from empirical studies, can be obtained from the software SWIMIT v. 3.3 (Jacobsaquatic, 2006).

Even though the highest water velocities can be assumed to occur within the fish pass or at its entrance (and thus affect the entry and passage stages; see Section 2.2), measures of fish swimming performance can also be relevant within the stage of attraction to the pass. Firstly, they can help to identify whether the water velocities within certain areas near the pass exceed the maximum swimming speed of targeted fish species or life stages and thus form hydraulic barriers that affect the pathways fish are physically able to use when

approaching a pass (see Section 2.3.3). Secondly, the water velocity magnitudes encountered within competing flows (such as flows issued from turbines of HEPs; see Section 2.5.3.1) can be put in relation to the energy fish use when approaching a migration barrier multiple times before locating the fish pass (Scruton et al., 2007).

The traditional estimates of fish swimming performance have recently been criticised for not considering the effects of the inherently complex flow conditions in natural river channels (Vowles et al., 2013). Several authors have promoted the development of new criteria and indices that incorporate the effects of turbulence on fish swimming performance and enable more realistic fish pass assessments (Lacey et al., 2012; Lupandin, 2005; Tritico & Cotel, 2010; Vowles et al., 2013).

2.4.2 Turbulence

Turbulence has been defined as "*chaotic vortical flows of multiple strengths and sizes superimposed onto a mean flow velocity*" (Liao, 2007). The turbulence descriptors used in the literature on fish swimming behaviour are numerous (see for example the review by Wilkes et al., 2013). By introducing the IPOS framework, Lacey et al. (2012) attempted to structure the scientific discussion and to facilitate the transfer of results from laboratory-based fish behavioural studies to field conditions. The framework postulates that the effect of turbulence on fish depends on the Intensity (I), Periodicity (P), Orientation (O) and the spatial Scale (S) of the turbulence structure (see Table 2-1). Depending on these parameters as well as on the body and fin morphology, fish may be attracted to or repelled by turbulence (Liao, 2007).

Table 2-1. The IPOS framework (Lacey et al., 2012)

Intensity	**Periodicity**	**Orientation**	**Scale**
Turbulence intensity	Predictability	Axis of eddy rotation	Eddy length scale
Turbulent kinetic energy	Energy spectra	Direction of dominant	Eddy diameter
Reynolds shear stress		fluctuation	Reynolds number
Vorticity			

The effect of turbulence on fish are manifested either in (1) displacement, i.e. an alteration of fish body motion relative to the Earth frame of reference or (2) kinematics, i.e. changes in the fish body shape through active motion or passive deformation relative to the fish frame of reference (Liao, 2007). A crucial factor determining whether fish experience displacement or show kinematics is the spatial scale of the vortical flows relative to the fish size (Liao, 2007; Odeh et al., 2002; Pavlov et al., 2008; Figure 2-3).

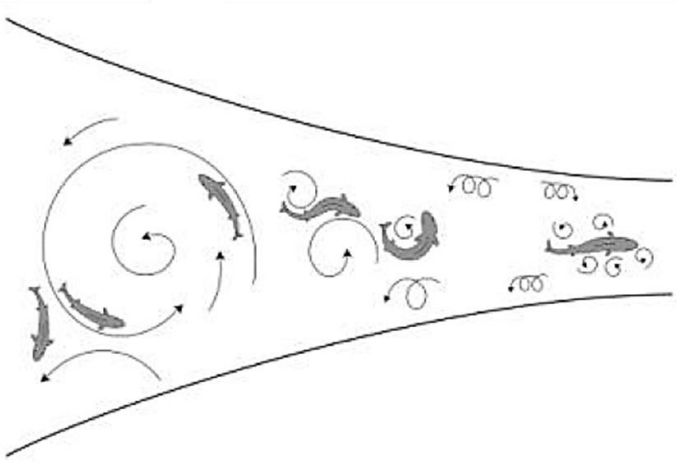

Figure 2-3. Variety of spatial turbulence scales in rivers (Odeh et al., 2002)

Generally, fish are attracted to turbulent flows if the spatio-temporal velocity fluctuations remain steady and predictable and if fish can maintain stability (Liao, 2007). Coutant (1998) proposed that juvenile downstream migrating salmonids could be guided through dam forebays and towards the entrance of bypasses by a trail of mild turbulence and increased flow velocity relative to the surrounding flow. This “trail of turbulence” should simulate the hydrodynamic features of natural, unimpounded rivers in a narrow path.

Liao et al. (2003b, 2003a) confronted rainbow trout, *Oncorhynchus mykiss*, with vortices forming a Kármán street generated by flow passing a D-section cylinder. The fish synchronised their body motion to the vortex shedding

frequency to adopt a unique pattern of axial motion termed Kármán gate. This finding supported the hypothesis that fish can tune their swimming behaviour in order to reduce muscle activity and potentially energy cost, subject to an appropriate background turbulence level and ratio of vortex diameter to fish body length.

On the other hand, unpredictable wide fluctuations in velocity can also increase the energy expenditure from swimming (Enders et al., 2003) and reduce maximum fish swimming speeds (Lupandin, 2005; Tritico & Cotel, 2010). Turbulence can disorient fish and shear forces at extremely high levels, such as near turbine blades, can even physically damage fish (Odeh et al., 2002).

Enders et al. (2003) confronted individual juvenile Atlantic salmon (mean weight of 10 g) with four types of turbulent conditions and measured the energy expenditure of fish swimming by means of respirometry. The swimming cost increased 1.3 times and 1.6 times as the turbulence intensity (expressed as the Standard Deviation, S.D., of the streamwise velocity, σ_u) increased from 0.05 to 0.08 ms^{-1} while keeping fixed mean streamwise velocities of 0.18 and 0.23 ms^{-1}, respectively. These results suggested that fish swimming cost models should incorporate velocity S.D. in addition to mean flow velocities.

Nikora et al. (2003) quantified the swimming velocity of inanga, *Galaxias maculatus*, in two flumes with smooth and rough walls, respectively, with the latter generating increased turbulence intensity. The effects of turbulence on the swimming performance of inanga were found to be negligible. Nikora et al. (2003) explained that the most likely reason for this unexpected result was that the mechanics of fish-turbulence interactions depended not only on the turbulence intensity, but also on the spectrum of spatial turbulence scales in relation to fish size. This hypothesis was later tested by Lupandin (2005) and Tritico and Cotel (2010). Lupandin (2005) measured the critical velocities, i.e. the minimum current velocity at which fish begin to be carried away by the water flow (Pavlov, 1989), for 214 European perch, *Perca fluviatilis*, with body lengths ranging from 0.03 to 0.12 m, along with water velocity, relative turbulence intensity and spatial turbulence scale, in an experiment in the Volga River. The

relative turbulence intensity (TI) is frequently quantified for each velocity component as (Wilkes et al., 2013):

$$TI_u = \sigma_u/\bar{u} \qquad TI_v = \sigma_v/\bar{v} \qquad TI_w = \sigma_w/\bar{w} \tag{2-1}$$

where σ_u, σ_v, σ_w are the S.D. and $\bar{u}$, $\bar{v}$, $\bar{w}$ are the temporal averages of the streamwise, cross-stream and vertical velocity components, respectively. Lupandin (2005) obtained 1-dimensional velocity measurements with a mechanical current meter, so that it is unclear which velocity component was captured. The spatial turbulence scale was quantified as the one-dimensional time correlation of the flow rate L, which is an indicator of the mean vortex size, and quantified as:

$$L = t_0^* \bar{u} \tag{2-2}$$

where t_0^* is the time interval after which the coefficient of flow rate correlation decreases to zero (also referred to as zero-correlation time). The TI was found to significantly influence the critical velocity and, depending on the fish body length, there seemed to be a threshold turbulence scale L_{thr} above which the critical velocity would decrease. Lupandin (2005) described this relationship as

$$L_{thr} = 0.66 * TL \tag{2-3}$$

meaning that the critical velocity started to decrease when the turbulence reached spatial scales above two thirds of the fish body length.

Using Particle Image Velocimetry (PIV) to quantify turbulent eddies, Tritico & Cotel (2010) found that the stability and the 2-minutes critical swimming speed (i.e. V_{crit} defined in Appendix A.1, with time intervals of 2 minutes) of creek chub, *Semotilus atromaculatus*, decreased in turbulent conditions depending on eddy diameter, the axis of eddy orientation and the vorticity. Eddies were identified as local minima and maxima of vorticity following Drucker & Lauder (1999). The vorticity, ω, provides a measure of turbulence intensity and is defined as twice the angular velocity, i.e. the rate of rotation of a fluid at a point (Wilkes et al., 2013). For each eddy, the eddy diameter d_e, and thus the circular

eddy area, was quantified such that the eddy circulation (angular momentum per unit mass) was maximal. The relatively small sample of seven creek chub showed that this species experiences stability challenges if the largest (95th percentile) eddy diameters within the eddy distribution reached 76% of the total fish body length. Under conditions involving eddies larger than this, losses in postural control were 230% more frequent and lasted 24% longer in flow fields dominated by horizontal eddies than in conditions dominated by vertical eddies of the same diameter. The resulting reductions in the 2-minutes critical swimming speed ranged up to 22% relative to a control treatment with minimal turbulence.

The relevance of intraspecies variation in swimming behaviour towards hydrodynamics was emphasised by the results of Hockley et al. (2014). In a laboratory-based experiment, they confronted 60 female (mean ± standard length of 21.3 ± 3.5 mm) and 51 male (16.2 ± 1.3 mm) guppies, *Poecilia reticulata*, with a heterogeneous flow field generated by hemispherical boulders in an open channel flume. Based on densely spaced point velocity measurements with an ADV, the turbulence intensity in the flow field around the boulders was quantified in terms of the turbulent kinetic energy (TKE) and turbulent shear stress (Reynolds stress; RS). The former was defined as:

$$TKE = 0.5 * (u_{RMS}^2 + v_{RMS}^2 + w_{RMS}^2) \quad \textbf{(2-4)}$$

where $\{u_{RMS,} v_{RMS,} w_{RMS}\}$ are the root mean square of the instantaneous velocity fluctuations $\{u', v', w'\}$ around the temporally averaged velocity (see also Equation (2-10)). The Reynolds stress in the planes uv, uw and vw was defined as:

$$RS_{uv} = |\rho\overline{u'v'}|; \qquad RS_{uw} = |\rho\overline{u'w'}|; \qquad RS_{vw} = |\rho\overline{v'w'}| \quad \textbf{(2-5)}$$

where ρ is the density of water. The results showed that habitat preferences in terms of water velocity and turbulence intensity varied with fish size, sex and physiological condition (a sub-sample of guppies had been infected with parasites prior to the trial). Even though the study by Hockley et al. (2014)

focused primarily on fish microhabitat selection, the presence of intraspecies variation in swimming behaviour is relevant also to fish passage. Differences in fish body morphology and pre-passage physiological conditions may cause variation in preferences towards near-pass hydrodynamics not only between, but also within fish species.

2.4.3 Spatial velocity gradients

There is evidence to suggest that migratory fish actively seek migration pathways to increase their chance of survival (Williams et al., 2012). They can detect and react to small changes in water velocity and the resulting pressure differences via a network of mechanosensory organs called neuromasts that are distributed along their lateral line (Figure 2-4; Bleckmann, 1986; Dijkgraaf, 1963; Floyd et al., 2007; Liao, 2007).

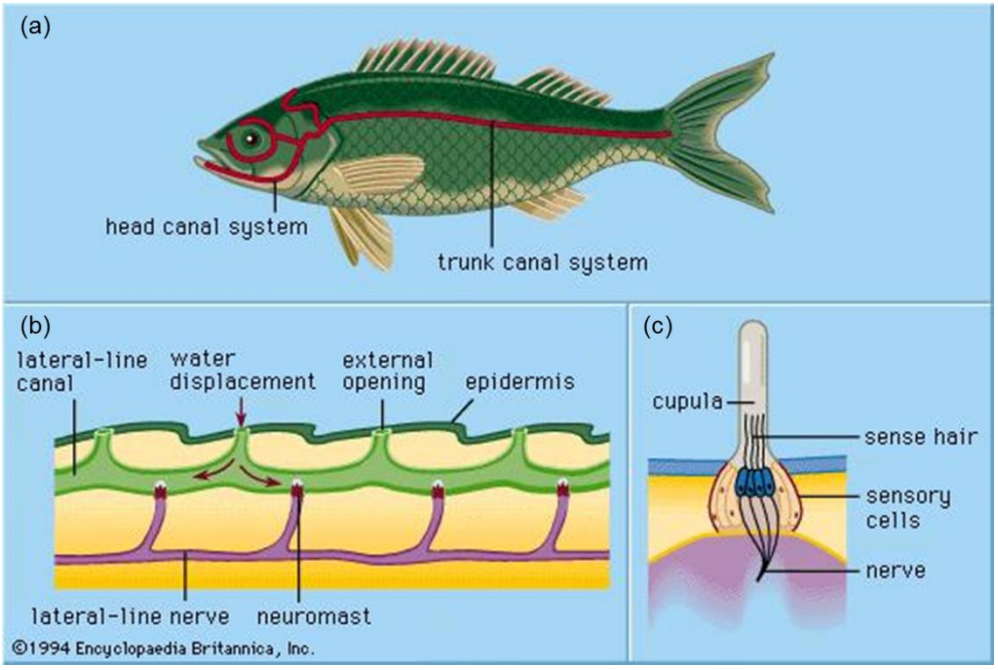

Figure 2-4. Lateral line system of a fish (Zug, 2015); (a) Bodily location of lateral lines; (b) Longitudinal section of a canal; (c) Superficial neuromast

An early study on the effect of flow acceleration on downstream migrants was conducted by Haro et al. (1998). In a flume study, they compared the passage rates and behaviour of Atlantic salmon smolts (mean fork length of 0.19 m) over two types of weirs: a sharp crested weir with rapid flow acceleration of around

2 $ms^{-1}m^{-1}$ and a new weir design with a uniform spatial flow acceleration of 1 $ms^{-1}m^{-1}$. Smolts showed higher overall passage rates and earlier passage after release at the weir with less rapid flow acceleration (89.7% passage rate after 180 min) than at the sharp crested weir (74.3%). The vast majority of smolts approached the weir tail first (exhibiting positive rheotaxis) and turned to negative rheotaxis where the velocities became too high to maintain position. Moreover, Haro et al. (1998) identified a "critical reaction point" at a flow velocity of 2.25 ms^{-1} over the weir, where smolts either continued to pass the weir or showed a burst movement upstream in order to avoid entrainment.

More recently, some studies (e.g. Enders et al., 2009, 2012; Russon & Kemp, 2011; Vowles & Kemp, 2012) quantified the avoidance behaviour of downstream migrants under laboratory conditions, where the fish response could be observed and the hydrodynamic conditions could be measured at high spatial and temporal resolutions. These studies recorded the spatial velocity gradient (SVG) across the Total Length of the fish body (TL), the response velocity (V_R) and/or the response type. The SVG was quantified as:

$$SVG = \frac{\left|V_{T,Head} - V_{T,Tail}\right|}{TL} \quad \textbf{(2-6)}$$

where $V_{T,Head}$ and $V_{T,Tail}$ are the resultant water velocities at the fish head and tail, respectively, at the time of the avoidance response. The resultant water velocity V_T at any point in the flume was defined as

$$V_T = \sqrt{\overline{V_x}^2 + \overline{V_y}^2 + \overline{V_z}^2} \quad \textbf{(2-7)}$$

where $\overline{V_x}$, $\overline{V_y}$ and $\overline{V_z}$ are the temporally averaged velocities in the x, y and z directions of a 3D Cartesian coordinate system. V_R was defined as the highest water velocity at the fish body at the time of the avoidance response.

For wild Chinook salmon, *Oncorhynchus tshawytscha*, smolts (mean TL ± S.D. of 15 ± 2.3 cm) encountering accelerating flow, Enders et al. (2009, 2012) found an average SVG of 1.23 $cms^{-1}cm^{-1}$ and an average V_R of 29.6 cms^{-1}. Both parameters exhibited a wide range across the 120 fish recorded: 0.01 to

7.94 $cms^{-1}cm^{-1}$ for SVG and 4.4 to 132.0 cms^{-1} for V_R. There were no statistically significant effects of fish body length, flow conditions (three discharge scenarios were tested) or water temperature on SVG.

For hatchery reared brown trout (mean TL ± S.D. of 24.2 ± 2.1 cm), Vowles & Kemp (2012) recorded an average SVG threshold of about 0.4 $cms^{-1}cm^{-1}$. Inter-specific differences and/or a more cautious strategy of farmed fish on encountering abrupt hydraulic conditions for the first time may explain the differences in these results to those by Enders et al. (2009, 2012).

The majority of both Chinook salmon and brown trout in these studies encountered the velocity gradient head first (negative rheotaxis). A switch to positive rheotaxis was the most common avoidance response type. Neither Enders et al. (2009) nor Vowles & Kemp (2012) studied the effects of acclimatisation on the avoidance response towards accelerating flow. However, in a similar experiment with farmed yearling brown trout, Russon & Kemp (2011) found that the number of approaches to an orifice weir in a flume had no significant effect on the passage behaviour and response to flow acceleration. Previous studies had indicated that fish may need to become acquainted to the hydrodynamic conditions near fish passes before entering and passing (Gowans et al., 1999; Laine, 1995; Nestler et al., 2008).

In another flume experiment, Enders et al. (2012) confronted wild Chinook salmon smolts with decelerating flow. Smolts actively avoided areas of decelerating flow with SVG above ca. 1 $cms^{-1}cm^{-1}$ by swimming into the main current, whereby the swimming speed increased with the SVG encountered.

In all of the studies mentioned above, fish were monitored individually. The potential effects of the presence of other fish and schooling behaviour on the avoidance response were not captured. In natural settings, smolts may migrate in groups, affect and/or mimic each other's behaviour (Haro et al., 1998; Kemp et al., 2006). For example, in a study by Johnson et al. (2009) the majority of all yearling salmonids observed with an acoustic imaging device (DIDSON) at The Dalles Dam on the Columbia River (Washington State, US) were schools of

three or more fish. Moreover, positive rheotactic behaviour was exhibited more often by fish schools than by fish swimming alone.

The number of species whose response to velocity gradients has been studied is limited. A transfer of the critical SVG from one to another species is not straightforward, e.g. downstream migrating adult European eel may respond little to velocity gradient, but rather to structure (thigmotactic behaviour) when encountering migration barriers (Russon & Kemp, 2011; see Section 1.6.2.2 for an opposing finding by Piper et al., 2015).

2.4.4 Total hydraulic strain and the Strain-Velocity-Pressure hypothesis

Nestler et al. (2008) explained the swim path selection of downstream migrating juvenile salmon at dams by a set of deterministic behavioural rules that relate fluvial geomorphology and hydrodynamics with fish sensory biology. This set of rules was summarised as the Strain-Velocity-Pressure (SVP) hypothesis (Goodwin, 2004; see Table 2-2). It considered three hydrodynamic variables: (1) total hydraulic strain (THS), a turbulence surrogate that combines hydraulic variables regarded as turbulence precursors, (2) water velocity magnitudes with the resulting flow streamlines, and (3) depth as an indicator of hydrostatic pressure.

Table 2-2. SVP hypothesis (Goodwin, 2004; Nestler et al., 2008)

1.	Follow the flow (i.e. streamlines, not necessarily the direction of increasing water velocity).
2.	If elevated total hydraulic strain associated with a wall-bounded flow gradient (caused by friction resistance at the channel boundaries) is detected, then swim into the direction of increasing water velocity.
3.	If elevated total hydraulic strain associated with a free-shear flow gradient (caused by form resistance at in-channel boulders, debris and other flow obstacles) is detected, then swim into the direction of decreasing water velocity. Alternatively, an emigrant can swim against the flow to move back upstream of the obstruction.
4.	If an elevated change in depth (hydrostatic pressure) is detected, swim in the direction of acclimatised depth.

THS is a measure of the overall velocity shear and is computed as the sum of the absolute values of each spatial velocity gradient in 3D space (Nestler et al., 2008):

$$THS = \left|\frac{\Delta V_x}{\Delta x}\right| + \left|\frac{\Delta V_x}{\Delta y}\right| + \left|\frac{\Delta V_x}{\Delta z}\right| + \left|\frac{\Delta V_y}{\Delta x}\right| + \left|\frac{\Delta V_y}{\Delta y}\right| + \left|\frac{\Delta V_y}{\Delta z}\right| + \left|\frac{\Delta V_z}{\Delta x}\right| + \left|\frac{\Delta V_z}{\Delta y}\right| + \left|\frac{\Delta V_z}{\Delta z}\right| \quad \textbf{(2-8)}$$

where ΔV_x, ΔV_y and ΔV_z are the changes in the velocity components along the the x, y and z directions.

To define whether fish detect an increase in THS, Nestler et al. (2008) applied the Weber-Fechner Law, which states that animals only detect a change in stimulus intensity if it exceeds the background intensity to which the animal is acclimated by a threshold corresponding to the "just noticeable difference". Acclimatisation of fish to the high-energetic flow conditions at migration barriers may lead to a change in this threshold with time, as found for example by Piper et al. (2015) for downstream migrating European eel approaching an area of increased flow acceleration (see Section 2.5.2.2).

Nestler et al. (2008) tested the SVP hypothesis at three dams (the Lower Granite, The Dalles and Wanapum Dams on the Snake, Lower Columbia and Mid-Columbia rivers in Washington State, US). The hydrodynamic variables were quantified through a Computational Fluid Dynamics (CFD) model that captured the 3D steady state flow field. The generated flow map was overlaid with paths of acoustically tagged downstream migrating salmon. The results showed that the SVP hypothesis was a reasonable approximation to the strategy of downstream migrants in complex flow fields such as near dams or other migration barriers. Graphical analysis showed that the spatial distribution of velocities and THS served well to explain the recorded swim paths of tagged fish. Moreover, it provided a means to explain the higher passage rates at a

removable spillway weir (78%) compared to a surface bypass collector (44%) at the Lower Granite Dam.

In a study on salmonid behaviour near surface flow outlets at The Dalles Dam, Johnson et al. (2009) also found the water velocities to be associated with swimming behaviour and THS to be correlated with fish swimming efforts, which confirmed the SVP hypothesis.

2.4.5 Final remarks on fish behavioural studies

Odeh et al. (2002) hypothesised that there would be an optimal level of turbulence serving as migratory cues and allowing fish to reduce energetic swimming cost. Some of the studies on turbulence effects, but also on water velocity gradients, showed large spreads over the respective fish study samples (e.g. Enders et al., 2009, 2012; Hockley et al., 2014). Thus, for a given species, the optimal level of hydrodynamic conditions may be a range rather than a threshold and may be subject to intraspecific differences. The presence of intraspecific differences in fish behaviour towards hydrodynamic conditions would be consistent with the argument that this behaviour is interrelated with the conditions found in the 'natural' surrounding of the fish (e.g. Nestler et al., 2008; see Section 2.4.4). For example, Skorobogatov et al. (1996) found that two groups of juvenile roach, *Rutilus rutilus*, originating from a reach of the River Volga dominated by stagnant flow and a stream-like part of the Upper Volga, respectively, showed differences in their preferences for water velocity magnitudes and turbulence. This suggests that generalisations of the results presented in this section should be carefully considered before being made.

While the maximum water velocity magnitudes in relation to fish swimming capabilities have been of major interest in previous research related to upstream passage (Section 2.4.1), the fish response towards spatial water velocity gradients has been studied predominantly in the context of downstream passage. This may be explained by the fact that downstream migrants move with the flow and thus, relative to upstream migrants, rely less on swimming ability for successful barrier passage, but more on behavioural capabilities

towards hydrodynamic variation (Williams et al., 2012). Nonetheless, Williams et al. (2012) stated that they “believe” that also upstream migrants “seek specific cues from flow and water velocity gradients” to actively choose migration pathways. This view was based on decades of observations on upstream migrants and experience from field-based fish pass monitoring studies (Williams et al., 2012).

2.5 Evidence from field-based fish pass monitoring

2.5.1 Literature reviews of fish pass monitoring studies

In their review of fish pass monitoring studies from 1960 to 2011, Noonan et al. (2012) identified only twelve studies (out of 122) that assessed the attraction efficiency and eleven that assessed the entrance efficiency, with average efficiency estimates of 65.1% (Standard Error, S.E., of 7.6) and 39.6% (S.E. of 8.1), respectively. They found that both the attraction and the entrance efficiencies were significantly negatively related to the slope of the fish pass and positively, but not significantly, related to the length of the fish pass. Moreover, the water velocity within a fish pass was positively correlated with the total upstream passage efficiency, which they explained by the stronger attraction flow.

Bunt et al. (2012) conducted a meta-analysis of attraction and passage efficiency of fish passes using data from 19 selected[1] peer-reviewed scientific papers and consultancy reports, covering 35 fish passes at 28 locations in six countries and 26 fish species. They found that for all fish pass types covered (pool/weir, vertical slot, Denil and nature-like passes) the attraction efficiency varied broadly. While pool/weir (range of 29 to 100%, mean of 77%), vertical slot (range of 0 to 100%, mean of 63%) and Denil (range of 21 to 100%, mean

[1] Bunt et al. (2012) considered 116 peer-reviewed scientific papers and consultant reports and selected only those studies that (i) detected fish both near the entrance to and at the exit of the fish pass, (ii) studied fish actively migrating during a single spawning season, and (iii) evaluated fish behaviour under natural conditions.

of 61%) passes showed similar average attraction efficiencies, the average attractiveness of nature-like passes was notably lower (range of 0 to 100%, mean of 48%). They explained that this may be due to the frequently low discharge through nature-like fish passes and the resulting poor attraction flow. Bunt et al. (2012) noticed that the attraction of fish to a pass entrance was mostly affected by the entrance location and configuration as well as by the near-field hydraulics and that many fish passes appeared to have entrances that were poorly located or produced insufficient attraction flow to compete with other currents. Nonetheless, they did not include these factors in their quantitative analysis of covariates influencing fish pass efficiency. The study by Bunt et al. (2012) suggested that the most important biological factors driving attraction and passage efficiency were whether the monitored species was anadromous or potamodromous as well as the thermal tolerance of species (warm-water or cool-water adapted).

Based on a review of fish passage in France, Larinier (1998) concluded that most cases of inefficient passage facilities were the result of a lack of attraction flow due to poorly located entrances or insufficient water discharge.

2.5.2 Case studies of fish pass assessment with measurements of near-pass hydrodynamics

2.5.2.1 Upstream passage

Piper et al. (2012) studied the effects of plunging and streaming flow on the attraction of upstream migrating European eel to elver passes at an intertidal weir on the River Stour in East Anglia, UK. Over a period of 78 days, they captured 14,732 eels at four elver passes in different locations across the weir (right bank, centre right, centre left, left bank) and with alternating attraction flow treatments close to the pass entrances (plunging and streaming). The majority of the captured eels chose the plunging flow treatment over the streaming flow treatment (69% and 31%, respectively) and the passes located at the channel sides above those in the centre (90% and 10%, respectively). Piper et al. (2012) used an ADV to record water velocity time series (60 seconds at 50 Hz) 0.2 m

from the water surface and 0.2 m from the river bed at distances from 0.05 to 5 m from the pass entrance. This allowed the quantification of the spatial extent and intensity of both flow treatments. Close to the water surface the plunging flow treatment caused increased water velocities detectable beyond the background flow for 3 m downstream of the pass entrance, whereas the streaming flow treatment was detectable for only 1 m at the water surface and stronger just above the river bed. Upstream migrating eels had previously been found to exhibit strong rheotactic behaviour (Knights & White, 1998) and the early life stages are predominantly surface-oriented when actively swimming in the intertidal zone (Tesch, 2003). The increased near-surface velocity and the flow disturbance at the water surface are possible explanations for the higher attraction to passes with plunging flow treatment (Piper et al., 2012).

Andersson et al. (2012) used a CFD model to estimate water velocities and turbulence intensities downstream of the Stornorrfors power plant in the River Umeälven in Sweden. To inform the construction of a fish pass, they simulated the jet water issuing from fish passes with different entrance locations and angles. Lindberg et al. (2013) combined the hydrodynamic model outputs with the results from a study that monitored the occurrence and positions of Atlantic salmon approaching the tailrace channel of the hydropower plant using a hydroacoustic system and radio-telemetry. The detected areas of fish aggregation were overlaid with maps of turbulence intensities and water velocities derived from the hydrodynamic model. This revealed a coincidence of fish detections with areas of turbulence intensities between 0.6 and 0.8[2]. It was argued that the preference of Atlantic salmon for these areas may have been due to a reduced energy expenditure during upstream migration because of turbulence energy exploitation as described in Liao et al. (2003; see Section 2.4.2). Following the assumption that the optimal fish pass entrance is located where migrating fish aggregate and where the attraction flow reaches as many fish as possible, the study also revealed a suitable location and attraction flow for the planned fish pass.

[2] It is unclear how turbulence intensity was defined in Lindberg et al.(2013).

2.5.2.2 Downstream passage

The study by Scruton et al. (2002, 2008) illustrated the high importance of the hydraulic conditions in the vicinity of barriers to downstream migration. They evaluated the efficiency of a louver and bypass system in guiding downstream migrating Atlantic salmon smolts and kelts to the entrance of a bypass at the Grand Falls-Windsor HEP on the Exploits River in Newfoundland, Canada. Fish movements immediately upstream of the dam were monitored through various capturing and tracking techniques over a period of seven years involving a plant refurbishment and modifications of the guidance system to improve the hydraulics near the bypass entrance. In the first two years of the study period, guidance efficiencies were very low (23%). Radio telemetry to track smolt movement through discrete reception zones along the louver revealed that smolt guidance was lost in areas associated with unfavourable hydraulic conditions, in particular strong velocity decelerations at the bypass entrance. A physical model of the power canal, louver line and bypass at a scale of 1:25 was used to identify locations of poor hydraulic conditions and to test a variety of modifications, such as different louver angle, changes of the bottom contour in the power canal and the installation of a ramp or curved wall into the bypass entrance. During the physical flow simulations, the water velocities within the model were measured with a Nixxon Streamflo velocity meter and dye was used to map eddy patterns for qualitative photographic and video documentation. This confirmed that the locations of the worst hydraulic conditions (wide spatial and temporal fluctuations in water velocities) coincided with those of the greatest loss in smolt guidance. Subsequently, relatively small changes in the guidance system, e.g. related to the louver angle, and the removal of old penstock abutments, improved the hydraulic conditions and led to a strongly improved guidance efficiency of 65%.

Piper et al. (2015) studied the behaviour of downstream migrating adult European eel in relation to hydrodynamics (quantified through a 2D CFD model calibrated through data from a vessel-mounted ADCP) in the forebay of a redundant hydropower intake on the River Stour, Dorset, UK. A sample of 40 eel were tracked through the forebay, using acoustic and passive integrated

transponder telemetry. These tracks were overlaid onto maps of flow streamlines and flow acceleration (both based on the depth-averaged water velocities) for two hydrodynamic treatments involving unrestricted flow with low acceleration and constricted flow with high acceleration near the intake. The flow acceleration was defined as (Piper et al., 2015):

$$a(x,y) = \sqrt{a_x^2 + a_y^2} \quad \textbf{(2-9)}$$

where $a_x = V_x(\Delta V_x/\Delta x) + V_y(\Delta V_x/\Delta y)$ and $a_y = V_x(\Delta V_y/\Delta x) + V_y(\Delta V_y/\Delta y)$ are the components of acceleration in the x and y directions of a 2D plane. The results showed that eel exhibit avoidance responses (switch of body orientation followed by escape back upstream) when encountering high flow acceleration (comparable to those found for salmonids; see Section 2.4.3). In conditions of lower flow acceleration, eel predominantly showed a behaviour described as 'exploratory' (switch of body orientation followed by lateral movement perpendicular to the streamwise direction) and moved closer to the intake before switching orientation than during high acceleration. Before entering the distorted flow field, eel followed pathways close to the channel banks with a tendency to align with the flow streamlines. Eel appeared to acclimatise to the conditions as the number of approaches increased before passage through the intake. Physical contact with the bar rack at the intake was of little relevance to the recorded avoidance response, which is in contrast to laboratory-based studies of eel behaviour (e.g. Russon & Kemp, 2011; see Section 2.4.3).

2.5.3 Case studies of fish pass assessment without measurements of near-pass hydrodynamics

2.5.3.1 Upstream passage

Gowans et al. (1999) monitored the movements of 39 adult Atlantic salmon approaching a pool-and-orifice fish pass at the Pitlochry Dam on the River Tummel in Scotland. All tagged fish that approached the dam ascended the fish pass. However, the majority of salmon visited the pass entrance more than once before ascending, with a maximum of up to ten visits per fish. In total, less

than half of the visits at the fish pass entrance resulted in pass entry. Gowans et al. (1999) explained this by the relatively low discharge from the fish pass and possible difficulties of salmon to orient towards the flow issued from the pass entrance with a mean velocity of 2.4 ms^{-1}. The time between the first detection/visit at the dam and the entrance of the fish pass was 14.8 days on average and ranged from 36 min to 66 days for all tagged fish. The site had previously been assessed in a study by Webb (1990), where only five out of eleven tagged salmon passed the barrier. Gowans et al. (1999) argued that the improvement in passage efficiencies might have been due to fish screens inserted along the dam tailrace after the study by Webb (1990). These might have reduced the counter attraction flow from the turbines, enabling salmon to locate the pass entrance more easily. Gowans et al. (1999) recorded the mean water velocity immediately at the entrance of the fish pass; direct measurements of the near-pass hydrodynamics were, however, not reported.

Several studies described the attraction of upstream migrating salmonids to tailraces of HEPs rather than the fish pass entrance, so called “false attraction”, a problem that can lead to migratory delays up to several weeks (e.g. Scruton et al., 2007; Smith et al., 1997; Thorstad et al., 2003; Webb, 1990). For Arctic grayling, *Thymallus arcticus*, Fleming & Reynolds (1991) found that migratory delays of only three days can lead to reduced spawning success. Scruton et al. (2007) monitored the movements of Atlantic salmon approaching the tailrace of the Grand Falls-Windsor HEP on the Exploits River, Newfoundland, Canada. The turbines of the plant and their tailrace channels were located nearly perpendicular to the main river flow and a fish pass was located closer to the dam further upstream. 20 out of 21 tagged fish approaching the study zone were attracted to the tailrace area. Turbine discharge was found to be the primary factor causing false attraction to the tailrace, whereas river discharge did not have a significant influence. The number of visits before moving further upstream towards the fish pass or again downstream ranged between 1 and 21 with the majority (66.7%) entering the tailrace 2 to 10 times. With 0.87 hours, the average cumulative residence time in the tailrace per fish was short, but some individuals showed residence times of more than 24 hours.

2.5.3.2 Downstream passage

Scruton et al. (2008) used radio telemetry to study the guidance efficiency of a surface spill bypass system at the Bishop Falls HEP on the Exploits River in Newfoundland, Canada, for Atlantic salmon smolts and kelts over a period of three years. The guidance efficiency was defined as the proportion of the released fish that were detected in the bypass. Smolts showed efficiencies of around 60-70% and kelts of more than 90% throughout the study period. Smolts showed relatively long residence times in the forebay before entering the bypass (average resident times from 19.9 to 39.2 hours in the three years) or being passed through the turbines (30.0 to 57.5 hours). Scruton et al. (2008) argued that the turbulence in the power plant forebay could disorient smolts and diminish their ability to maintain position. In contrast, Salmon kelt are stronger swimmers, thus they were able to better navigate through the turbulent waters of the forebay.

2.5.4 Final remarks on field-based monitoring studies

The evidence from fish pass monitoring studies of the past decades underlines the importance of near-pass hydrodynamics to fish pass attractiveness. In the majority of studies that found the near-pass hydrodynamic conditions to be a major factor influencing the attraction efficiency, these conditions were not quantified. It may be argued that these studies would have benefitted from such quantification in order to explain the measured efficiency and to inform effective measures for its improvement. The rarity of near-pass hydrodynamics quantification in previous fish pass monitoring studies may be explained by the lack of a methodology enabling such quantification with relatively little time and monetary resources, a gap that the PhD research presented in this thesis attempted to fill.

The few published fish pass monitoring studies that quantified near-pass hydrodynamic variables chose a variety of approaches to do so, including CFD modelling (Andersson et al., 2012; Lindberg et al., 2013; Nestler et al., 2008; Piper et al., 2015), physical modelling and flow simulation (Scruton et al., 2002, 2008) as well as in-field measurements (Piper et al., 2012). The ADCP-based

methodology developed here complements these previous methods. It has the potential to be quicker, computationally less intensive than CFD modelling and to require less monetary resources than physical modelling, particularly due to the use of equipment that is widely available within national agencies (see also Section 1.1.3).

2.6 Implications on the methodology for near-pass hydrodynamics quantification

The literature review revealed several hydrodynamic indicators used in fish behavioural studies related to fish passage. The variety of metrics indicates that there is a lack of standardised hydrodynamic indicators in fish passage research, a fact that has previously been criticised by others too, because it complicates the comparison of study results and the transfer of laboratory-based findings to the field (e.g. Lacey et al., 2012; Wilkes et al., 2013). Notably, various metrics have been introduced in the eco-hydraulics literature to describe spatial velocity gradients, such as THS and SVG. The return to common terminology established in fluid mechanics, where velocity gradients are described as shear strain rate, would facilitate the cross-disciplinary communication between hydraulics and ecology required in the field of eco-hydraulics. This might support the development of standardised hydrodynamic indicators in fish passage research.

The recent studies quantifying fish behaviour in relation to spatial or temporal changes in hydrodynamics were primarily concerned with downstream passage. The research on upstream passage has focused mainly on water velocity magnitudes based on fish swimming performance, whereas the effect of spatio-temporal variations in near-pass hydrodynamics has been limited to qualitative descriptions. As hypothesised in Section 2.3.4, a first step of near-pass hydrodynamics quantification could be to assess the spatially continuous distribution of water velocities near the fish pass entrance against these qualitative descriptions. In a second step, quantitative metrics potentially indicating fish pass attractiveness can be derived from these maps. The current

knowledge on the behaviour of upstream migrants is, however, insufficient to quantitatively relate such hydrodynamic metrics to fish pass attractiveness without additional biological data. Hence, this aspect was not a specific focus of the PhD research, but was considered in the application of the method outputs in the research synthesis (see Chapter 8).

2.6.1 Categorisation of hydrodynamic indicators

As shown in Chapter 3, the metrics used in fish behavioural research differ from those quantified in the ADCP-centred literature. A common framework capturing the fundamental variables of fluid motion was required to relate metrics from both research domains to each other. Such a framework was provided through the classical Reynolds decomposition, according to which the water velocity $\{u, v, w\}$ at any location and time is composed of a steady (temporally averaged) component $\{\bar{u}, \bar{v}, \bar{w}\}$ and a temporally fluctuating component $\{u', v', w'\}$ (e.g. Sotiropoulos, 2005):

$$m = \bar{m} + m' \qquad for\ m = \{u, v, w\} \tag{2-10}$$

The hydrodynamic metrics identified in the literature review can be categorised dependent on whether they are derived from $\{\bar{u}, \bar{v}, \bar{w}\}$ or $\{u', v', w'\}$ and their respective statistical and/or spatial distributions (see Table 2-3). This categorisation contributes to the aim of this PhD research by framing the systematic identification of instrument specifications and data sampling strategies required to quantify metrics of near-pass hydrodynamics (see Section 2.6.2).

Table 2-3. Hydrodynamic metrics used previously in relation to fish passage (see main text for the equations and the discovered effects of these metrics on fish behaviour)

Metric		Unit	Species studied	Reference
Metrics derived from spatial distribution of $\{\bar{u}, \bar{v}, \bar{w}\}$				
Flow streamlines		-	*Salmo salar*	Nestler et al., 2008
			Anguilla anguilla	Piper et al., 2015
Spatial velocity gradient	SVG	s^{-1}	*Salmo salar*	Enders et al.,2003
			Oncorhynchus tshawytscha	Enders et al., 2009, 2012
			Anguilla anguilla, Salmo trutta	Vowles and Kemp, 2011;
Total hydraulic strain	THS	s^{-1}	*Salmo spp.*	Nestler et al., 2008
Flow acceleration	a	ms^{-2}	*Anguilla anguilla*	Piper et al., 2015
Metrics derived from $\{u', v', w'\}$				
Turbulence intensity	$\sigma_{u,v,w}$,	ms^{-1}	*Salmo salar*	Enders et al. 2003
	TI	-	*Perca fluviatilis*	Lupandin, 2005
Turbulent kinetic energy	TKE	m^2s^{-2}	*Poecilia reticulata*	Hockley et al., 2014
Reynolds stress	$RS_{uv,uw,vw}$	Nm^{-2}	*Poecilia reticulata*	Hockley et al., 2014
Turbulence scale	L	m	*Perca fluviatilis*	Lupandin, 2005
Vorticity	ω	s^{-1}	*Semotilus atr.*	Tritico and Cotel, 2010
Eddy circulation	Γ_e	m^2s^{-1}	*Semotilus atr.*	Tritico and Cotel, 2010
Axis of eddy rotation		-	*Semotilus atr.*	Tritico and Cotel, 2010
Eddy diameter	d_e	m	*Semotilus atr.*	Tritico and Cotel, 2010

The lack of standardised hydrodynamic metrics in fish passage research, as found in this review, had to be considered in the development of the methodology for near-pass hydrodynamics quantification. Instead of selecting an isolated set of metrics (which, for upstream passage research was simply not available from previous biological studies), the methodology should enable the accurate quantification of the spatial and or statistical distributions of $\{\bar{u}, \bar{v}, \bar{w}\}$ and $\{u', v', w'\}$, from which numerous previous and (potentially) future

metrics could then be derived. Thereby, the methodology development followed an adaptive framework that considered the early stage of research on fish behaviour towards near-pass hydrodynamics and enabled the incorporation of future insights as the knowledge on this subject increased.

2.6.2 Methodology and instrument requirements

The first category of metrics described in Table 2-3 can be derived from a map of the spatial distribution of temporally averaged 3D water velocity components. In previous studies, this distribution has been estimated using steady-state CFD modelling (Andersson et al., 2012; Nestler et al., 2008; Piper et al., 2015) or spatially dense velocity measurements and subsequent interpolation to estimate velocities in unmeasured locations (Enders et al., 2009; Russon & Kemp, 2011; Vowles & Kemp, 2012). The reliable estimation of the mean velocity depends on a sufficiently large sample of velocity measurements at a given location to capture the temporal average (Nezu & Nakagawa, 1993). The spatial resolution of the velocity map should be based on the scales most relevant to the targeted fish species and life stage. The findings of some experiments (e.g. Lupandin, 2005; Tritico & Cotel, 2010) indicate that the spatial scale of particularly high importance is related to the fish body length. This is also reflected in the frequently used SVG metric that relies on the velocity variation at a scale as fine as the distance from the fish head to the fish tail (see Section 2.4.3).

The second category of metrics captures the temporal variation around the mean velocity and is typically derived from a time series of velocities measured in one point. The recording frequency (also referred to as digitisation rate) of the instrument determines the temporal scale of the estimated metrics and the susceptibility to measurement bias from aliasing effects (Bendat & Piersol, 2000; Nezu & Nakagawa, 1993). As outlined in Section 2.4.2, the magnitude and regularity of the velocity fluctuations around the mean (captured for example as TI) affect whether fish can exploit these fluctuations and reduce swimming cost (Liao et al., 2003a) or whether the fluctuations lead to increased swimming cost and reduced maximum swimming speeds (Enders et al., 2003; Lupandin, 2005; Tritico & Cotel, 2010). A complete understanding of the effect

of turbulence on fish passage relies on velocity recording frequencies sufficiently large to resolve the highest frequencies of velocity fluctuation in rivers. Enders et al. (2003) and Tritico & Cotel (2010) recorded velocities at frequencies of 25 Hz and 30 Hz, respectively. Wilkes et al. (2013) pointed out that this may not always be sufficient to resolve the highest frequency of velocity fluctuations present in rivers and emphasised the recent development of second generation ADVs capable of measuring velocities at up to 200 Hz.

In Chapter 3, the capabilities of ADCPs have been systematically reviewed against the requirements for measuring $\{\bar{u}, \bar{v}, \bar{w}\}$ and $\{u', v', w'\}$ at the spatial and temporal scales found to be biologically relevant.

2.7 Conclusions

Fish pass monitoring studies within the past decades have provided evidence for the high relevance of the near-pass hydrodynamic conditions to fish passage success, but there has been little effort to quantify these conditions in the field. Instead, insights on the effects of hydrodynamics on fish approaching migration barriers and fish passes have been obtained mainly from experiments under controlled hydraulic conditions simulated in the laboratory. Hydrodynamics beyond simple measures of velocity magnitudes have been considered only recently and in a relatively small number of studies. These mainly involved life stages and hydrodynamics associated with downstream passage, whereas in upstream passage research, near-pass hydrodynamics have been described mainly qualitatively and fish pass design has been guided by traditional measures relating maximum water velocity magnitudes to fish swimming speeds. The findings from decades of observations on upstream migrating fish indicate that also upstream migrants seek cues from spatial variations in velocities, a behaviour that is supported by the physiological capabilities of fish to detect water velocity variation along their lateral line. The hydrodynamic metrics used in laboratory-based eco-hydraulics studies have been categorised based on whether they are derived from the spatial distribution of temporally averaged water velocities or the temporal velocity fluctuations around the mean.

The accurate quantification of these velocity components at the spatial and temporal scales found to be relevant to migrating fish relies on the capabilities of the velocity measurement instrument and the sampling strategy used, which, for ADCPs, have been reviewed in Chapter 3.

Chapter 3

ADCP-BASED CHARACTERISATION OF NEAR-PASS HYDRODYNAMICS: AN ASSESSMENT OF STATE OF THE ART METHODS

3.1 Introduction

While the review in Chapter 2 has identified hydrodynamic metrics potentially indicating fish pass attractiveness, this chapter presents an assessment of whether and how these indicators can be quantified in the field using ADCPs. Some of the indicators have previously been quantified in laboratory-based studies using scaled-down flumes with controllable hydraulic conditions (see Section 2.4). Field-based data acquisition, on the other hand, is complicated by the limited ability to control the environmental measurement conditions, challenges of safe and accurate instrument deployment at pre-defined locations, and the requirement to cover larger survey areas. The development of an ADCP-based methodology for the field-based quantification of near-pass hydrodynamics relied on knowledge of how these challenges affected ADCPs and of the available techniques to reduce any detrimental effects on data quality.

This chapter covers a review of the capabilities of ADCPs to quantify hydrodynamics in rivers with a particular focus on measurements in environmental conditions associated with fish passes and other engineered in-channel structures. The measurement errors most relevant to the quantification of near-pass hydrodynamics were identified along with the available techniques to reduce their effects. Two primary outcomes were attempted with this review:

(i) a proposal for an ADCP-based methodology enabling the accurate quantification of hydrodynamic metrics identified in Chapter 2, and
(ii) the identification of the most relevant limitations to the methodology implementation.

Thereby, this chapter addressed **objective 2** of the PhD research (see Section 1.2):

to identify the state of the art of ADCP-based quantification of hydrodynamics in rivers and the most relevant sensor limitations to such measurements near engineered in-channel structures

3.1.1 Review scope

The review presented herein was based on scientific literature (peer-reviewed journal papers and government reports) evaluating the use of downward looking vessel-mounted ADCPs to quantify hydrodynamics in rivers. Studies involving ADCPs installed in fixed locations (e.g. as side-lookers along the river banks) were not considered because such instrument deployment would compromise the research aim of a practicable (low-cost and rapid to implement) methodology (see also Section 3.2.8).

3.1.2 Chapter outline

In what follows, **Section 3.2** introduces the measurement principles of ADCPs and ADCP deployment techniques, highlights limitations intrinsic to ADCP instrumentation and discusses their relevance to the quantification of near-pass hydrodynamics. **Section 3.3** reviews the data collection and processing strategies evaluated in previous studies to quantify hydrodynamics in rivers. Particular focus was put on the variables that underpin the near-pass hydrodynamic metrics identified in Chapter 2, specifically, the spatial distribution of temporally averaged velocities $\{\bar{u}, \bar{v}, \bar{w}\}$, and the temporal fluctuations around the mean velocity $\{u', v', w'\}$. Based on the review, **Section 3.4** describes those ADCP measurement errors, which can be particularly detrimental to the quality of ADCP data collected in the environmental conditions associated with fish passes and discusses potential solutions. **Section 3.5** synthesises the reviews presented here and in Chapter 2 by suggesting a methodology for the ADCP-based quantification of hydrodynamic indicators for fish pass attractiveness, while highlighting gaps in knowledge addressed within the subsequent parts of the PhD research.

3.2 Fundamentals of downward-looking ADCPs

ADCPs are acoustic instruments with a mono-static arrangement of typically three to four transducers, which transform electrical to acoustic energy (Gordon,

1996; Simpson, 2001; see Figure 3-1). Pulses of acoustic energy are transmitted from each transducer face into the water column along narrow beams and backscattered to the instrument by particulate matter (“scatterers”), such as sediment, biological matter or bubbles. The acoustic beams are spread at an angle α of usually 20 to 30 deg relative to the vertical. The measurements from at least three beams at a given depth are combined to derive a 3D velocity vector (see Section 3.2.4). This arrangement allows downward-looking ADCPs mounted on a stationary or mobile platform to use a single acoustic signal (called “ping”) to measure 3D water velocities in multiple depths along the vertical water column.

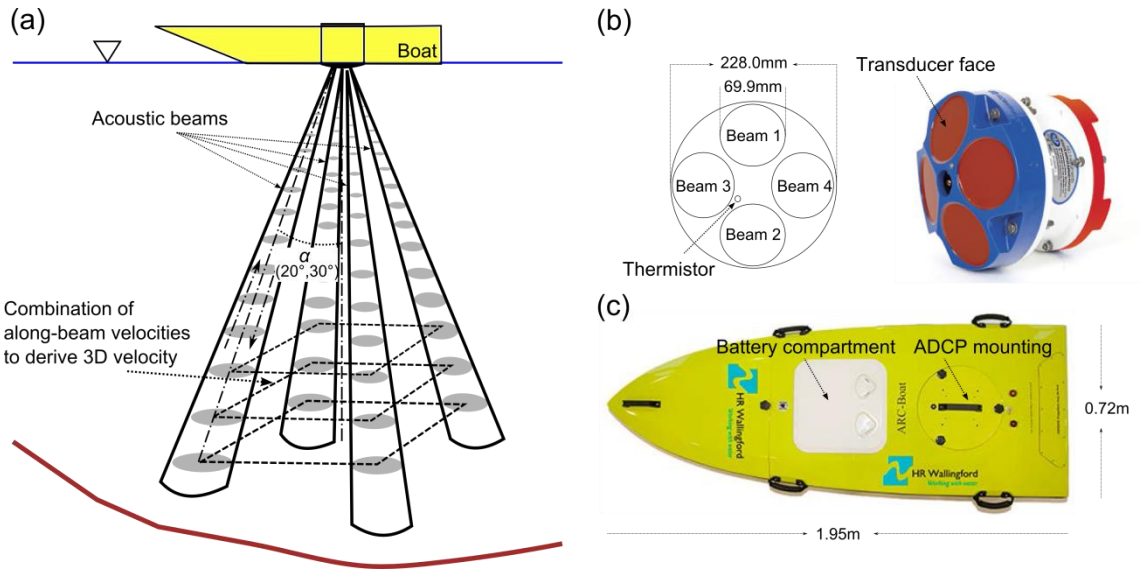

Figure 3-1. (a) Illustration of vessel-mounted downward-looking ADCP setup; $\boldsymbol{\alpha}$ stands for the beam spread angle against the vertical direction; the blue and brown lines denote the water surface and the river bed, respectively (based on Muste et al., 2004b); (b) Face view of a 1,200 kHz WorkHorse RioGrande ADCP (based on Teledyne RDI, 2007); (c) Top view on an ARC-Boat ADCP platform (HR Wallingford, 2015)

3.2.1 Measurement principles

A key assumption of ADCP technology is that the sound reflecting scatterers move at a speed and direction equal to the water (Gordon, 1996). The underlying principle of ADCP measurements is the Doppler shift principle, which

states that if a source of sound is moving relative to the sound receiver, there will be a shift between the transmitted and the received sound frequency. The frequency of the acoustic energy transmitted by an ADCP transducer is shifted once when received by the scatterers and a second time when received by the ADCP. Thus, the velocity of the water relative to the ADCP and along the acoustic beam p (referred to as "radial" or "along-beam" velocity), is calculated as (Gordon, 1996):

$$p = \frac{c(f_B - f_S)}{2f_S} \quad \textbf{(3-1)}$$

where c is the speed of sound in water, f_B is the sound frequency backscattered from the particles, and f_S is the sound frequency transmitted from the ADCP transducer.

The location of the measured water velocity along an acoustic beam is determined based on the duration until the sound is backscattered to the ADCP (provided that the beam spread angle, instrument draft and instrument pitch and roll are known; Gordon, 1996).

3.2.2 Resolving the Doppler shift

Since the invention of ADCPs (Rowe & Young, 1979; see Section 1.1.3) advancements in electronics and signal processing have enabled continuous improvements of the ADCP signal generation process and the methods used to resolve the Doppler shift. Since 1991, so called broadband ADCPs have been in use and have increased the precision of their narrowband predecessors by nearly one order of magnitude (Mueller & Wagner, 2009). Broadband ADCPs transmit complex acoustic signals consisting of multiple phase-coded pulse pairs and measure the phase shifts between their superimposed echoes using autocorrelation techniques (Gordon, 1996). The phase shift is proportional to the particle displacement relative to the ADCP, so that each phase shift measurement corresponds to an independent measurement of the radial velocity. Thus, the water velocities recorded by broadband ADCPs represent

the average of hundreds of measurements retrieved from a single or multiple broadband signals.

Most currently marketed ADCPs allow the user to select between different measurement modes or switch automatically between them (auto-adaptive configuration) based on the ambient flow conditions and depths (Mueller et al., 2013). These modes differ mainly in the characteristics of the acoustic signal (e.g. the number of pulses and the time lag between pulses) and affect the S.D. of the ADCP measurement error associated with Doppler noise, referred to as single ping S.D. For some ADCPs, estimates of the single ping S.D. for a given ADCP configuration can be obtained through the software PlanADCP (Teledyne RDI, 2009a). This software has been used in the planning of ADCP data collection campaigns presented in Parts II and III of the thesis and as an indicator of the uncertainty inherent to ADCP-based near-pass hydrodynamics quantification (see Section 8.3.1.2).

3.2.3 From relative to absolute velocities

Sections 3.2.1 and 3.2.2 covered water velocities relative to the ADCP, whereas the absolute velocities rely on a correction for the velocity of the platform ("boat velocity"), from which the rigidly mounted ADCP is deployed. The boat velocity can be estimated either via BT, where the Doppler shift in the acoustic signal reflected from the streambed is measured, or through an ADCP-external navigation system, usually GNSS. Provided that the streambed is stationary and in range, BT is considered the most accurate method, because it measures the boat velocity in the same coordinate system as the water velocities so that common errors cancel out during the correction (Rennie et al., 2002; Teledyne RDI, 2011). A navigation system is used if BT is unavailable or biased by a non-stationary streambed.

The assumption of a stationary streambed can be tested through so called moving-bed tests, where the boat velocity based on BT is compared to that based on a navigation system (Mueller et al., 2013) or assessed through other

procedures (Mueller & Wagner, 2007). To prevent ADCP measurement errors from river bed mobilisation immediately downstream of in-channel structures, such tests should be an integral part of the ADCP-based methodology for quantifying near-pass hydrodynamics. In turn, the methodology relies on the availability of an accurate ADCP positioning system to substitute boat velocities from biased BT signals (see Section 3.4.3).

3.2.4 From radial to 3D velocities

Measurements along at least three acoustic beams are required to resolve the 3D water velocity vector in a Cartesian coordinate system. Assuming a 4-beam ADCP with beams 1 and 2 in the x-z plane and beams 3 and 4 in the y-z plane (see Figure 3-2), the radial velocities p_1, p_2, p_3, and p_4, measured along these beams can be decomposed into velocities V_x, V_y and V_z in the respective directions $\{x, y, z\}$ of a Cartesian coordinate system aligned with the ADCP as (Mueller and Wagner, 2009):

$$V_x = \frac{(p_1 - p_2)}{2\sin(\alpha)} \qquad V_y = \frac{(p_4 - p_3)}{2\sin(\alpha)} \qquad V_z = \frac{(p_1 + p_2 + p_3 + p_4)}{4\cos(\alpha)} \qquad \textbf{(3-2)}$$

where α is the beam tilt angle relative to the vertical direction (see Figure 3-1).

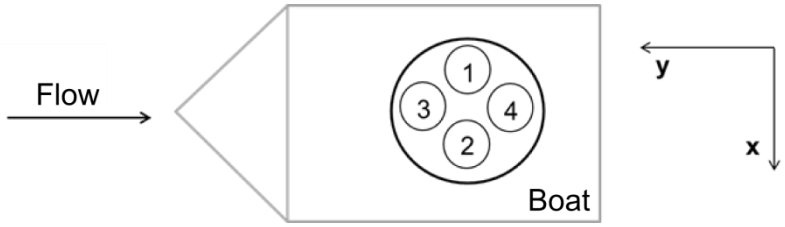

Figure 3-2. ADCP instrument coordinate system following the convention by Teledyne RDI (2010)

The conventional derivation of the 3D water velocity as shown in Equation (3-2) is based on the assumption that the water velocities of the volumes insonified by the three or four ADCP beams at a given horizontal depth layer do not significantly differ in magnitude or direction (Simpson, 2001). This is referred to

as flow homogeneity assumption (see Figure 3-3). Violations of the assumption can cause large errors in the ADCP-measured velocities (e.g. Nystrom et al., 2002; Richmond et al., 2015; Vermeulen et al., 2014) and are of particular concern to the research presented here because of the spatially complex hydraulic conditions associated with fish passes (see Section 3.4.1).

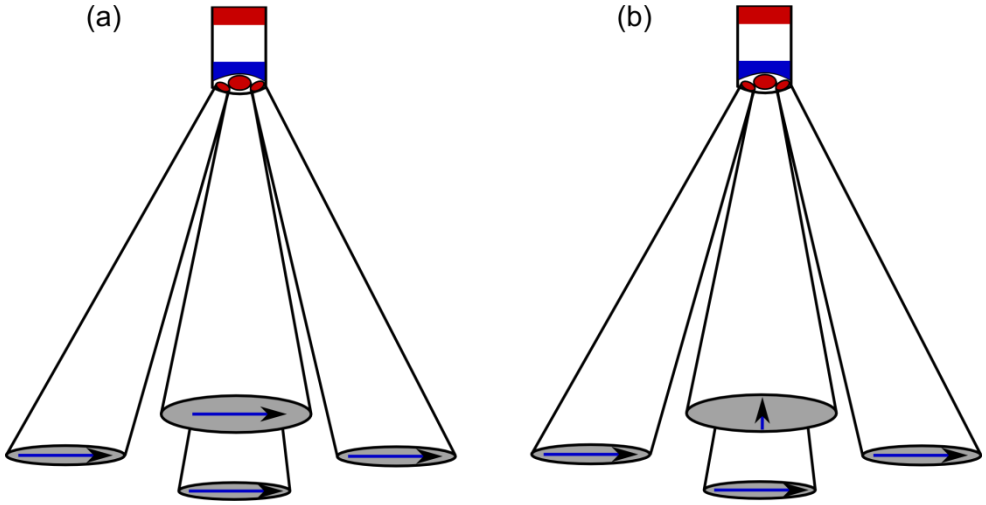

Figure 3-3. Illustration of homogeneous flow field (a) and non-homogeneous flow field (b); the arrows denote the water velocity direction within the insonified volumes (based on Simpson, 2001)

Moreover, the conventional ADCP data processing approach complicates the definition of the spatial resolution of the measured 3D velocities. These velocities represent the spatial averages of the velocities within three to four volumes of water, the spatial separation of which increases with depth. The size of the insonified volumes is determined by the (user-defined) vertical measurement resolution, measurement depth, beam geometry and the beam width at -3 dB, i.e. the spread of the main acoustic lobe (Rennie et al., 2002). The 3D water velocity vector derived from the radial velocities might be regarded as a spatial average over a cylindrically shaped volume enclosing the insonified sampling areas. The diameter of a circle enclosing the four beam footprints increases at a ratio of 0.76 m per 1 m increase in depth (calculated based on Rennie et al., 2002, for a 1,200 kHz RioGrande ADCP; see Figure 3-4).

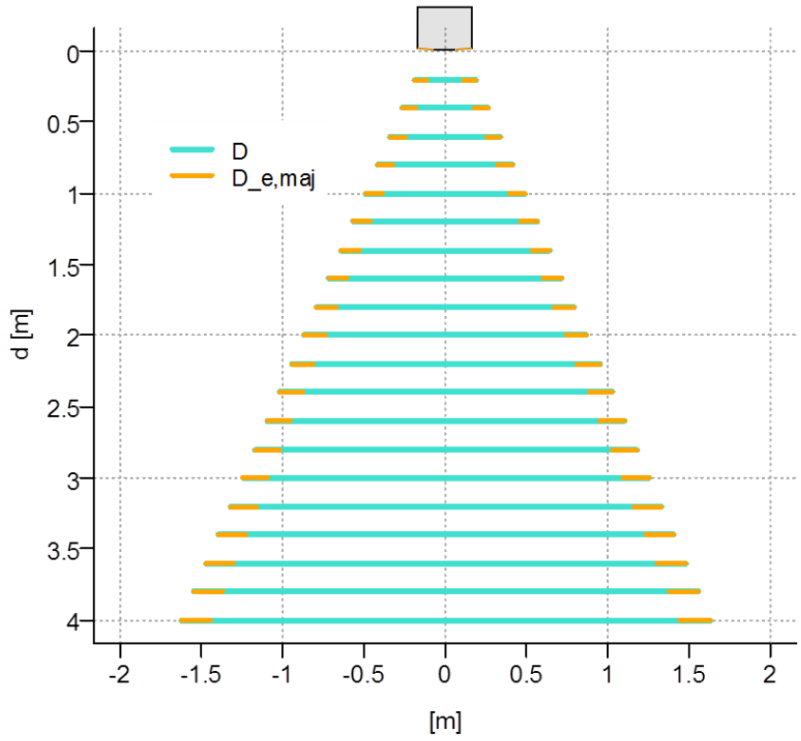

Figure 3-4. Length of the major axis of the quasi-elliptically shaped ADCP beam footprint ($\boldsymbol{D_{e,maj}}$) and the diameter of a circle enclosing the four single-beam footprints ($\boldsymbol{D}$), as a function of the distance of the measurement from the ADCP face ($\boldsymbol{d}$); shown for a 1,200 kHz RioGrande ADCP assuming a beam width at -3 dB of 1.5 deg (Teledyne RDI, 2002; computed based on Rennie et al., 2002)

Thus, the distance between the insonified areas is considerably larger than the body length of most upstream migrating fish in UK rivers, which compromises the capability of ADCPs to quantify hydrodynamics at the fine spatial scales believed to be most relevant to fish behaviour (see Section 2.6.2). Potential solutions to this fundamental problem have been covered as part of Section 3.4.1.

3.2.5 Defining bin, ensemble and transect

In common ADCP software, such as WinRiver II (Teledyne RDI, 2014a) and RiverSurveyor Live (SonTek, 2014a), the 3D water velocities measured along the vertical water column are displayed as a stack of bins referred to as “ensemble” (see Figure 3-5). The bin heights represent the vertical

measurement resolution and the bin widths relate to the boat distance travelled during the measurement. If a vessel-mounted ADCP is moved along a trajectory, e.g. a river cross section, a snapshot representation of the 2D water velocity distribution along the trajectory is obtained. This is referred to as “transect”.

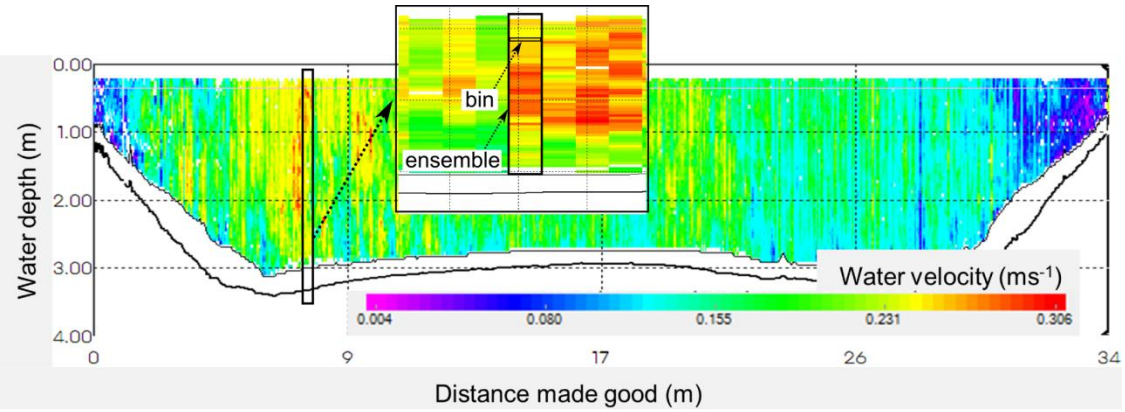

Figure 3-5. Transect display of a cross-sectional ADCP measurement in WinRiver II software with inlay plot to illustrate ensembles and bins

3.2.6 Non-measurable parts of the water column

The requirement of instrument submergence in the water as well as measurement biases near the instrument and near the streambed determine the minimum water depth required for ADCP deployment and the depth of the first measurement below the water surface (see Figure 3-6). ADCP measurements close to the water surface can be biased by transducer ringing effects and instrument induced flow disturbance. The former arises because of the mono-static instrument configuration, where the same transducer is used to transmit and receive acoustic energy. After the transmission of acoustic pulses, some time is required for the transducer to dampen before meaningful measurements can be obtained. Despite technological improvements that have reduced the distance below the instrument affected by ringing (e.g. low- or zero-blank transducers in the 1,200 kHz RioGrande ADCP), the measured velocities near the water surface require careful examination. CFD simulations (Mueller et al., 2007) and field experiments (Gartner & Ganju, 2002) have shown that the

velocities measured in the flow field immediately around the ADCP are biased low because the instrument induces flow patterns that violate the flow homogeneity assumption (see Section 3.2.4). In a laboratory experiment, Muste et al. (2010) found that the error expands about 1.5 times the ADCP head diameter into the water column. Moreover, the relative error, expressed as percentage of the actual flow velocity, decreases with increasing flow velocity, so that the error is more detrimental in shallow, slow flow conditions. For the 1,200 kHz RioGrande ADCP, Mueller & Wagner (2009) recommended discarding data within the first 0.25 m of the water column below the instrument.

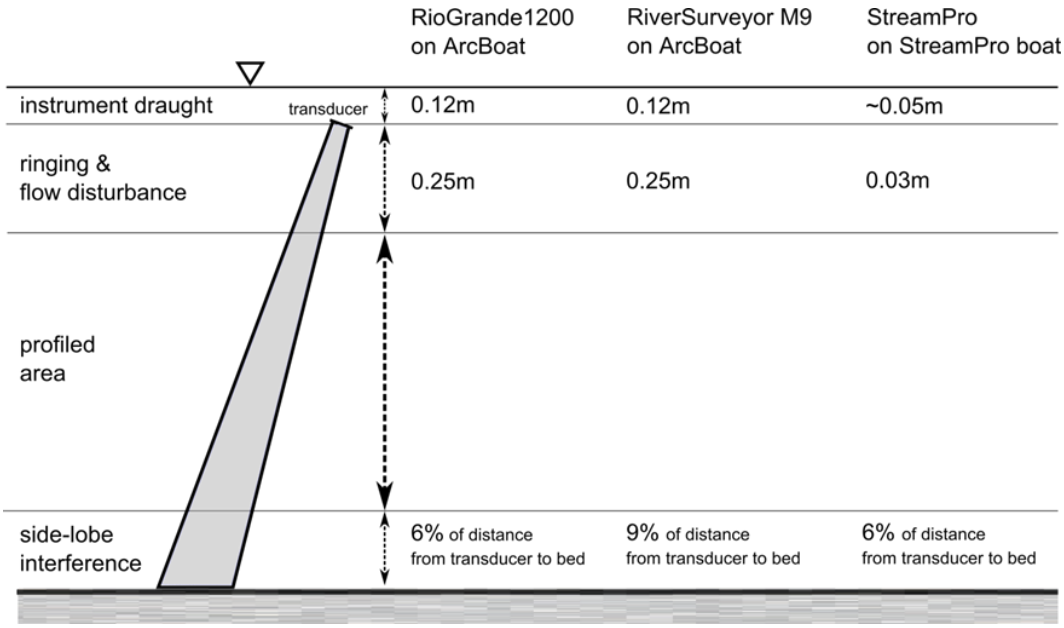

Figure 3-6. Non-measurable portions of the water column with examples for selected ADCP deployment configurations (based on Simpson, 2001); the extent of ringing effects and near-instrument flow disturbance are based on the default settings for the respective instruments and guidelines by Mueller & Wagner (2009).

Near the streambed, ADCP measurements are biased by interference from the backscatter of the low-intensity side-lobes, which are transmitted along with the main high-intensity beam, off the river bed. The percentage P_{max} of the distance from the ADCP head to the river bed that is not affected by side-lobe interference can be estimated as (Teledyne RDI, 2011):

$$P_{max} = 100\cos(\alpha) \quad \textbf{(3-3)}$$

Thus, P_{max} depends on the beam configuration and ranges from 94% for systems with a 20 deg beam angle to 87% for systems with a 30 deg beam angle (Teledyne RDI, 2011; see Figure 3-6).

The zones close to the water surface and the river bed are preferred by some, predominantly surface- or bottom-oriented migrating fish as highlighted in Chapter 2. Thus, the inability to measure water velocities in these locations limits the effectiveness of ADCP-based near-pass hydrodynamics quantification. Moreover, it precludes measurements in shallow areas (e.g. near the shore)and very shallow streams that may be preferred by some fish species. Various extrapolation methods have been suggested to estimate the velocities in non-measurable zones, most of which impose a trend to the data based on commonly accepted velocity-distribution laws for open channel flow (e.g. Mueller, 2013; Muste et al., 2004b; Simpson & Oltmann, 1993). These techniques are primarily used in the context of ADCP discharge measurements, where data are collected in straight river reaches with relatively uniform flow (Mueller & Wagner, 2009). The flow complexity induced by flow obstacles, however, is difficult to predict and may result in vertical velocity distributions that vary largely from laws describing idealised flow conditions, so that the applicability of extrapolation techniques for near-pass hydrodynamics quantification is questionable. Instead, complementary measurements from other instruments may be required to target those zones non-measurable by ADCPs (see Chapter 8).

3.2.7 ADCP models

The selection of a suitable ADCP model forms an important first step in ADCP-based quantification of near-pass hydrodynamics. The market provides numerous models that differ in the frequency of their acoustic signal, weight, size and measurement configuration, and thereby target different site conditions

in terms of the ranges of water depths and velocities covered. Table 3-1 compares key technical specifications of ADCP models by the two manufacturers that dominate the market sector of ADCPs for inland water resources in the US and UK (Teledyne RDI and Xylem Analytics with the brand name SonTek; as of 2015).

All ADCPs listed in Table 3-1 have manufacturer-stated accuracies (mean error) in water velocity measurements of ±0.002 ms^{-1}. Results of manufacturer-independent towing tank experiments (Oberg & Mueller, 2007; Oberg, 2002; Shih et al., 2000) showed that this error is slightly underestimated; e.g. for a Teledyne RDI 1,200 kHz ADCP using broadband technology, Oberg (2002) reported mean absolute errors in the measured depth-averaged water velocity ranging up to 0.0051 ms^{-1} and mean relative errors up to 1.2%. Table 3-1 also highlights the relatively low rate at which ADCPs record velocities; a specification that limits the capability of ADCPs to resolve hydrodynamic metrics based on fine-scale temporal velocity fluctuations (see Section 3.3.2). A possible explanation for the low recording frequency is the time required for the relatively complex internal processing of broadband ADCPs to resolve the Doppler shift in multiple depths (see Section 3.2.2).

For measurements in shallower rivers, the StreamPro ADCP and the RiverSurveyor M9 have the advantage of measuring very close to the water surface (see the profiling range for velocity measurements in Table 3-1; note that these areas may be affected by physical flow disturbance, see Section 3.2.6). The latter also offers auto-adaptive instrument configuration involving automatic switches between two sets of four high (3,000 kHz) and low (1,000 kHz) frequency transducers, as well as a 500 kHz vertical echo-sounder beam for depth measurement only. The RiverPro ADCP was released just towards the end of the project and therefore could not be considered in the instrument choice for this research.

Table 3-1. Comparison of commercial ADCP systems by the major manufacturers on the US and UK markets (SonTek, 2014b; Teledyne RDI, 2006a, 2009b, 2013, 2014b)

	Teledyne TRDI ADCPs				SonTek ADCPs	
	1,200 kHz RioGrande	**StreamPro**	**RiverRay**	**RiverPro**	**RiverSurveyor S5**	**RiverSurveyor M9**
Technical specifications						
Transducers						
Frequency (kHz)	1,200	2,000	600	1,200	3,000 (and 1,000)	3,000, 1,000 (and 500)
Number of transducers	4	4	4	4	5	9
Beam configuration	Janus 4 beam at 20° angle	Janus 4 beam at 20° angle	Phased array; Janus 4 beam at 30° angle	Janus 4 beam at 20° angle	Janus 4 beam at 25° angle; 1 vertical beam	Janus 4 beam at 25° angle; 1 vertical beam
Transducer head diameter (cm)	22.8	3.5	16.5	16.5	8.1	12.6
Weight in air (excluding batteries) (kg)	7.0	0.3	4.1	4.4	1.1	2.3
Data output rate (Hz)	1 – 2 (typical)	1	1 – 2 (typical)	1 – 2 (typical)	1	1
Velocity measurements						
Profiling range (velocity) (m/s)	±5 default, ±20 max	±5	±5 default, ±20 max	±5 default, ±20 max	±20	±20
Profiling range (depth)[a] (m)	0.3 – 25	0.1 - 2 (0.1 - 6 with optional upgrade)	0.4 - 60	0.2 - 25	0.06 - 5	0.06 - 40
Maximum number of cells/bins	128	20 (30 with upgrade)	typically 25; up to 200 possible	Typically 12 – 30; up to 200 possible	128	128
Cell/bin height (m)	0.05 – 2	0.02 – 0.1 (0.02 – 0.2 with upgrade)	minimum 0.1	0.02 - 5	0.02 – 0.5	0.02 - 4
Accuracy[b]	±0.25% of water velocity relative to ADCP; ±2mms^{-1}	±1% of water velocity relative to ADCP; ±2mms^{-1}	±0.25% of water velocity relative to ADCP ±2mms^{-1}	±0.25% of water velocity relative to ADCP ±2mms^{-1}	±0.25% of water velocity relative to ADCP ±2mms^{-1}	±0.25% of water velocity relative to ADCP ±2mms^{-1}
Resolution (mm/s)	1	1	1	1	1	1
Depth measurements						
Profiling range[a] (m)	0.5 – 30	0.1 - 7	0.3 - 70	0.15 - 120	0.2 - 15	0.2 - 80
Accuracy[b,c] (%)	±1	±1	±1	±1	±1	±1
Resolution (mm)	1	1	1	1	1	1
Bottom tracking						
Velocity range (m/s)	±9.5	n.a.	±9.5	±9	n.a.	n.a.
Depth range[a] (m)	0.5 – 30	0.1 - 7	0.4 - 100	0.15 - 35	n.a.	n.a.
Accuracy[b,c]	±0.25% of bottom velocity relative to ADCP	±0.25% of bottom velocity relative to ADCP	±0.25% of bottom velocity relative to ADCP	±0.25% of bottom velocity relative to ADCP	n.a.	n.a.
Resolution (mm/s)	1	1	1	1	n.a.	n.a.

[a] Assuming fresh water; actual range will depend on temperature and suspended solids concentration
[b] Note that the reported measurement accuracies are likely to be overestimated (Oberg, 2002; Shih et al., 2000).
[c] Assuming uniform water temperature and salinity profile

The methodology developed in the PhD research relied on the integration of external sensors (which were not supplied by ADCP manufacturers) and the possibility of exporting data that had undergone little instrument-internal processing. Among modern ADCPs for river measurements, this level of user access was possible only with the RioGrande ADCP. Therefore, this was the preferred ADCP model for the research presented in this thesis.

3.2.8 Deployment platforms

The location of relevant near-pass hydrodynamics in relation to the fish pass entrance is not known a priori, so that any quantification strategy will have to capture the hydrodynamics within a reach of interest, rather than at selected points. This can be achieved either through the installation of an array of fixed ADCPs (e.g. along the banks) or the use of a single ADCP deployed from a mobile vessel. Only the latter strategy allows for a methodology that is rapid to implement, relatively inexpensive and widely applicable at different fish pass sites.

Manned, tethered or RC platforms can be used for mobile ADCP measurements. The deployment of a sensor-carrying vessel in the rough surface waters associated with fish passes and other engineered in-channel structures involves practical difficulties. While the operation of manned vessels in close proximity to flow outlets of dams or weirs is limited by crew safety considerations (particularly during conditions of high discharge), tethered platforms require access to both river banks, limiting the sites where ADCP data collection is possible and complicating the implementation of pre-defined sampling strategies. RC platforms offer the advantage of high deployment safety and flexibility. In the literature, the potential of RC ADCP platforms in hydrodynamic mapping applications has rarely been noticed, with first empirical studies published only recently (Flener et al., 2015) or as a result of the PhD research presented in this thesis (Kriechbaumer et al., 2016). In practice, RC platforms have become a well-established tool for ADCP measurements in non-

wadeable rivers and at sites without nearby bridges or cableways for the deployment of tethered boats. For example, the EA employs over 30 RC ADCP platforms, which are in use every week for river discharge measurements, and increasingly, small scale surveys of bathymetry and velocity fields (pers. comm., EA Evidence Directorate, Nick Everard).

RC boats have self-contained motors and an RC system (typically in the 2.4 GHz frequency range) for boat manoeuvring. Table 3-2 compares the technical specifications of RC platforms marketed specifically for the purpose of ADCP measurements. Important characteristics of RC platforms are their dimensions, top speed, manoeuvrability and stability on the water, robustness of hull and propulsion system as well as endurance of the power system. Moreover, ease of transport to site and launching can be important criteria in practice.

For the purpose of the PhD research, a mono-hull RC boat was preferred to minimise the probability of entanglement in vegetation near river banks and to reduce alignment with the flow and platform yaw stability in complex surface flow conditions near fish passes. The choice of the 1,200 kHz RioGrande ADCP restricted the platform selection to the Q-Boat 1800(P) and the ARC-Boat (see Table 3-2). The latter was selected because of its dominance in the UK and the resulting availability for this project.

Table 3-2. RC ADCP boats available in the market (as of 2013; technical specifications are stated as provided by manufacturers; HR Wallingford, 2015; Oceanscience, 2011a, 2011b; Xylem Analytics UK, n.d.)

	HR Wallingford	Oceanscience		SonTek
Technical specifications	**ARC-Boat** 	**Q-Boat 1550T** 	**Q-Boat 1800(P)** 	**R2V2** 
ADCPs supported	Any instrument with diameter up to 0.23 m	RiverSurveyor S5 and M9 or StreamPro	Any instrument with diameter up to 0.23 m	RiverSurveyor S5 and M9
Hull				
Length (m)	1.95 (1.40 without detachable bow)	1.55	1.80	1.34
Width (m)	0.75	0.82 (0.45 if folded)	0.90	0.48
Total weight excl. ADCP (kg)	37.2	20	25	18.5
Material	Glass-reinforced plastic (GRP)	Polyethylene	UV resistant Acrylonitrile Butadiene Styrene (ABS)	Fibre-reinforced plastic (FRP)
ADCP draft (m)	0.12	0.10 - 0.15	0.10 - 0.15	0.12
Speed				
Top (ms^{-1})	5	2.3	1800: 1.8 1800P: 5	2.5
Cruising (ms^{-1})	n.a.	1.5	1800: 1 1800P: 4	Low gear: 1.5 High gear: 2.0
Propulsion	2 brushed DC motors Twin rudders and twin shrouded propellers	2 brushed DC motors	1 brushed DC outdrive (2 brushless DC outdrives for the 1800P)	2 brushless DC motors
Battery				
System	2 NiMH packs (24V, 10Ah each)	NiMH pack	1 NiMH pack (12V) (3 NiMH packs (24V) for 1800P)	1 lead-acid battery (12V)
Endurance(h) at cruising speed	up to 5	1.3	1 – 2 (0.75 - 2.3 for 1800P)	3

3.3 ADCP-based quantification of hydrodynamic metrics

This section reviews previous studies evaluating ADCPs for the quantification of hydrodynamic metrics indicating fish pass attractiveness or the variables that these metrics are derived from (see Section 2.6.1). The purpose of this review was to identify ADCP sampling strategies and data processing approaches

potentially suitable for the near-pass hydrodynamics quantification methodology developed in this research.

In the context of fish pass research, ADCPs have mostly been used to inform and/or validate hydrodynamic modelling (e.g. Andersson et al., 2012; Piper et al., 2015; Redeker & Morgenschweis, 2007). Reports of previous attempts to directly quantify the flow field near fish pass entrances with ADCPs have been rare (e.g. Johnson et al., 2009; Walton et al., 2012). Consequently, the review presented here involved literature beyond the context of fish pass research. It covered studies that informed the use of ADCPs to quantify:

(i) the variability of temporally averaged water velocities in 3D space, $\{\overline{u}, \overline{v}, \overline{w}\}$, and

(ii) the temporal velocity fluctuations around the mean, $\{u', v', w'\}$.

In Section 2.6.1 it was shown that these features describe the two categories of hydrodynamic indicators of fish pass attractiveness. The structure of this section follows this categorisation in order to facilitate the cross-disciplinary relation of metrics used in fisheries and ADCP-centred research.

3.3.1 Spatial variability of temporally averaged water velocities

Broadly, the strategies to quantify temporally averaged water velocities with ADCPs can be divided into fixed- and moving-vessel sampling (Muste et al., 2004a, 2004b). The continuous spatial distribution of the velocities can be obtained by spatially interpolating the mean velocities during post-processing (e.g. Jamieson et al., 2011; Tsubaki et al., 2012).

3.3.1.1 Fixed-vessel measurements

Continuous ADCP measurements at a fixed location have been shown to provide meaningful profiles of temporally averaged water velocities along the vertical water column (e.g. Barua & Rahman, 1998; González-Castro et al., 2000; Muste et al., 2004a; Sokoray-Varga et al., 2011; Szupiany et al., 2007). Such measurements rely on sufficiently long data collection times to capture the

temporal average and to limit the effects of randomly distributed measurement errors and instrument motion. Assessments of the minimum duration required have typically been based on plots of the mean velocity (e.g. Muste et al., 2004a; Sokoray-Varga et al., 2011; Szupiany et al., 2007) or its S.D. (Gunawan et al., 2010) versus time, to qualitatively assess the duration after which the mean velocity becomes insensitive to further data.[3] The results ranged from five (Stone & Hotchkiss, 2007) to 15 minutes (Barua & Rahman, 1998; see also Petrie et al., 2013, for a review of sampling lengths).

For two main reasons, this measurement approach is sub-optimal to quantify near-pass hydrodynamics:

(i) The relatively long measurement durations allow for only a few locations within an area of interest to be sampled within time limits, and the locations of near-pass hydrodynamic features of most relevance to fish pass attractiveness are not known *a priori*.

(ii) The approach assumes a static measurement position (Muste et al., 2004a; Petrie et al., 2010), which is practically difficult to achieve in the complex hydraulic conditions associated with in-channel structures. Moreover, the negative effect of deviations from a fixed position will increase with the spatial flow complexity at the measurement site.

3.3.1.2 Moving-vessel measurements

Due to natural flow variability, instrument noise and measurement errors, the instantaneous velocity profiles of a single ADCP transect measurement represent only a poor approximation of the temporally averaged flow velocity (Szupiany et al., 2007, 2009). In contrast, repeated transect measurements can provide mean velocity profiles as good as those from fixed-vessel measurements, as shown by Muste et al. (2004b) and Gunawan et al. (2010). In

[3] see González-Castro et al. (2000), for an alternative, quantitative approach based on the integral time scale

repeated transect measurements, the temporally averaged velocities are typically derived by projecting the ensembles of the different transects to a plane mesh fitted through the transect locations, and averaging the 3D velocities located within the same mesh cell (e.g. Dinehart & Burau, 2005a; Kim & Muste, 2012; Parsons et al., 2012). Muste et al. (2004b) compared the vertical velocity distribution obtained from moving-vessel transect measurements involving six river crossings with that from fixed-vessel measurements at a point along the sampled section. The deviations between the mean velocities obtained from these two methods were within ±20% and the mean vertical velocity profiles closely resembled each other.

Two major problems need to be addressed when estimating mean velocities from repeated transects. Firstly, the variability in the boat paths of different transects causes “spatial smearing”, potentially resulting in the loss of spatially dependent flow features (Jamieson et al., 2011). Technical aids can be used to minimise the boat path variability, e.g. winch and pulley systems were shown to be effective for tethered ADCP platforms (Gunawan et al., 2010), but rely on access to both river banks. For RC platforms, as used in the PhD research (see Section 3.2.8), the path variability might be reduced by visualising the platform track in real-time in relation to previous transects. Such a visualisation based on cm-level ADCP positioning has been developed as part of the PhD research (see Chapter 4). Alternatively, the variability might be reduced through an ADCP platform navigation system that enables autonomous repeated sampling along a pre-defined track. This solution relies primarily on a reliable positioning system and its integration with the platform control system, both of which have been addressed in this research (see Chapters 5 and 6).

Secondly, there is little guidance to *a priori* determine the number of transects required to capture the distribution of temporally averaged water velocities of a measurement section. Petrie et al. (2013b) found four cross-sectional transects to be suitable to identify general trends in the streamwise velocity component, but insufficient to describe the temporally averaged cross-stream velocities in bends of the lower Roanoke River (US). Muste et al. (2004b) suggested a

minimum of ten transects, with the actually required transect number depending on the site-specific turbulence conditions. However, the findings by Vermeulen et al. (2014) indicate that considerably less repeated transects are required to obtain a robust estimate of the mean velocity vector if their data processing approach is used instead of the conventional transect averaging procedure described above. They found that typically four to five transects were sufficient to obtain robust estimates of the mean velocity when taking measurements in the bend of the Mahakam river in Indonesia. The method by Vermeulen et al. (2014) fits a 3D velocity vector to a set of radial velocities sampled during repeated transect measurements and located within a user-defined water volume (see Section 3.4.1.1). The lower number of transects required would make the technique particularly suitable for near-pass hydrodynamics quantification and other studies mapping the spatial flow distribution of river reaches. In practice, such studies are often carried out under time constraint so that an increase in the number of transects per section comes at the cost of a decrease in the spatial density of the sampled sections. The latter can increase the error introduced by spatial velocity interpolation, particularly in spatially complex flow conditions (e.g. Jamieson et al., 2011; see Section 3.3.1.3). The PhD research presented in this thesis involved the first evaluation of the method by Vermeulen et al. (2014) near engineered in-channel structures (Kriechbaumer et al., 2016), including an assessment of the number of transects required to capture the temporally averaged velocity (see Chapters 4 and 7).

3.3.1.3 3D flow interpolation

Cross-sectional velocity distributions are not sufficient to understand the full flow structure in river reaches with complex bathymetry or near flow obstacles (Jamieson et al., 2011; Tsubaki et al., 2012). The estimation of the continuous spatial velocity distribution downstream of fish passes relies on spatial interpolation procedures to estimate the velocities in unmeasured locations. This involves two major questions concerning:

(i) the spatial density of the measurements, specifically the spacing of the sections sampled in moving-vessel measurements, and

(ii) the most suitable interpolation technique.

The former depends on the spatial flow complexity at a particular site (Jamieson et al., 2011). Rennie & Church (2010) estimated the spatial distribution of depth-averaged water velocities for a 5.5 km reach of the Fraser River in Canada. They sampled along single transects spaced 110 m apart on average, corresponding to about 25% of the channel width, and concluded that the overall uncertainty in the flow maps (expressed as kriging variance) was dominated by the error stemming from interpolation.

A denser spacing was chosen by Jamieson et al. (2011) who studied flow structures near two submerged wing dikes on the Lower Missouri River in the US. They interpolated single transect ADCP measurements with 5 to 20 m spacing, corresponding to 1% and 5% of the channel width, respectively. The accuracies of the velocity maps obtained from each spacing were evaluated through cross-validation, i.e. by comparing the ADCP-measured values with the interpolation results at the same locations (see also Section 7.2.4.2). The error showed little sensitivity to the transect spacing and the authors argued that the denser spacing led to little improvement to resolve the mean 3D flow field around the wing dikes relative to the coarser spacing. However, the derivation of more complex flow features, such as the location of vortex cores, was found to benefit from the denser transect spacing as it enabled a more spatially detailed analysis. Overall, the cross-validation error, represented as mean absolute percentage differences, ranged from 76-130% and 300-330% for streamwise and lateral flow velocities, respectively, depending on the interpolation parameters used. Jamieson et al. (2011) argued that these errors were not greater than the uncertainty from ADCP measurement errors and natural velocity fluctuations at the study site.

Based on the findings of these studies, it can be argued that the spatial interpolation of ADCP-measured velocities is suitable to estimate the spatial

velocity distribution of river reaches, but relies on a sufficiently dense section spacing to resolve hydrodynamic features at finer scales. Furthermore, it is remarkable that both Rennie & Church (2010) and Jamieson et al. (2011) implemented single transect measurement strategies. Jamieson et al. (2011) argued that the spatial variability in flow velocity may be just as large or larger than its temporal variability. This approach has not been followed in the PhD research, because:

(i) it would complicate the interpretation of the flow maps,

(ii) several studies have provided evidence on the necessity of repeated transect measurements to capture the temporally averaged velocity (see Section 3.3.1.2), and

(iii) the post-processing technique found to be most suitable for the conditions near fish passes (i.e. the technique by Vermeulen et al., 2014; see Section 3.4.1.1 and Chapter 4) can only be applied to repeated transect measurements.

To the author's knowledge, no previous study has assessed the effect of the section spacing when interpolating temporally averaged velocities derived from *repeated* transect measurements. This gap in knowledge has been addressed in the PhD research (see Chapter 7) in order to inform a suitable sampling strategy for the accurate quantification of near-pass hydrodynamics.

Numerous authors used ordinary kriging and thus followed a geostatistical approach to separately interpolate the ADCP-measured velocity components in 2D or 3D space (e.g. Jamieson et al., 2011; Rennie & Church, 2010; Rennie, 2012; Venditti et al., 2014). Earlier studies involved deterministic methods, such as Inverse Distance Weighting (IDW), but Dinehart & Burau (2005b) emphasised the need for more sophisticated flow interpolation procedures. Tsubaki et al. (2012) argued that neither kriging nor IDW interpolation on regular grids were suitable methods for estimating the mean 3D water velocity field from random ADCP surveys. Instead, they proposed an interpolation procedure involving averaging along the main flow direction (anisotropic

gridding) and continuity correction of the velocity distribution based on the fractional step method used in CFD. The procedure was shown to yield more accurate results than kriging and IDW interpolation for all three velocity components, provided that the point density along the ADCP track was high (e.g. due to high sampling frequencies and/or low vessel speeds).

While the potential superiority of the interpolation method by Tsubaki et al. (2012) is acknowledged here, its implementation and assessment against other techniques in the context of near-pass hydrodynamics mapping was beyond the scope of the PhD research, but is recommended for future studies (see Section 8.5.2). Instead, ordinary kriging interpolation in 3D space was used, because

(i) its suitability had been demonstrated in previous studies involving thorough assessments (Jamieson et al., 2011; Rennie & Church, 2010; Rennie, 2012; Venditti et al., 2014), and

(ii) the technique involves the computation of the kriging variance, which serves as an indicator of the uncertainty introduced through interpolation (Webster & Oliver, 2007), and thus provides a further measure to assess the accuracy of the estimated flow maps (e.g. Rennie & Church, 2010).

3.3.2 Temporal water velocity fluctuations around the mean

3.3.2.1 Instrument requirements

There are three fundamental requirements that instruments have to fulfil to capture the full spectrum of temporal water velocity fluctuations at a specific river site (Hinze, 1975; Muste et al., 2004a):

1) a probe size smaller than the smallest spatial turbulence scale present in the river, i.e. smaller than the Kolmogorov length scale η,
2) a sampling rate at least twice as high as the highest occurring turbulence frequency, $f_{inst} \geq 2f_{max}$ (Nyquist criterion), and
3) a sampling time sufficiently long to capture the mean flow velocity.

Several studies (e.g. Barua & Rahman, 1998; Muste et al., 2004a; Szupiany et al., 2007) have shown that ADCPs fulfil the third criterion if measurements are taken from fixed vessels for a sufficiently long time span. However, the volume of the smallest eddies present in most river flows is in the order of 1 mm^3 or less (Nezu & Nakagawa, 1993) and turbulence frequencies around 100 Hz are not unusual (Muste et al., 2004a). Thus, ADCPs do not meet the first two criteria stated above, because the ADCP single-beam sampling volume is much larger than the smallest scale turbulences present in rivers (see Section 3.2.4) and the recording frequency of typically 1-2 Hz (see Table 3.2.7) does not satisfy the Nyquist criterion. Moreover, the typical ADCP-internal averaging of multiple pings or sub-pings can bias the recorded temporal velocity fluctuations towards the mean (Nystrom et al., 2002) and violations of the flow homogeneity assumption have been shown to bias turbulence parameters derived from the ADCP-measured 3D velocity components (Barua & Rahman, 1998; Muste et al., 2004a; Nystrom et al., 2002).

Despite these apparent instrument limitations, the performance of ADCPs in quantifying measures of turbulence intensity has been assessed in laboratory experiments (Neary et al., 2013; Nystrom et al., 2002, 2007), through virtual ADCP measurements in flow conditions simulated through CFD (Tokyay et al., 2009) and during field measurements in river channels (Barua & Rahman, 1998; Demers et al., 2013; Muste et al., 2004a; Rennie & Church, 2010; Rennie, 2012; Vermeulen et al., 2011). All of these studies derived turbulence descriptors from time series of the radial velocities of single beams (1D) or the resolved streamwise, lateral or vertical velocity components (3D) obtained through fixed-vessel measurements.

3.3.2.2 Evidence from empirical assessments

In a laboratory experiment, Nystrom et al. (2002) compared the radial and the resolved streamwise velocities from an ADCP (600 kHz RioGrande ADCP with a bin height of 0.05 m and a recording frequency of around 5 Hz) with those from ADV measurements. Time series of the radial ADCP-measured velocities

were shown to depart largely from the ADV-recorded velocities measured within the ADCP single beam sampling volume. This was attributed to the instrument noise and the low spatial and temporal measurement resolution of ADCPs. A 44% error was found when comparing the S.D. of the radial velocities against the ADV measurements. The streamwise velocity time series was considerably noisier than the radial velocity series and the S.D. of the streamwise velocity was consistently overestimated throughout the vertical water column with errors up to 125%. The larger error was explained mainly by violations of the assumption of a homogeneous flow field and a magnification (error propagation) of the instrument noise when resolving the streamwise velocity from the radial velocities.

Tokyay et al. (2009) conducted virtual ADCP measurements on the outputs of an unsteady (time-dependent) CFD model. The findings from a comparison of turbulence intensity measures derived from the virtual ADCP measurements and the CFD model were consistent with those by Nystrom et al. (2002). The 3D turbulence intensity components represented as the root mean square velocity fluctuations of the streamwise, lateral and vertical velocities showed large errors over the entire depth of the water column.

Muste et al. (2004a) emphasised that results obtained in the laboratory can only partially be transferred to in-field measurements because the flow conditions and scales in laboratory flumes differ from those in natural rivers. They analysed ADCP measurements in the Upper Mississippi River and concluded that vessel-mounted ADCPs were suitable to accurately estimate turbulence intensities (represented as the S.D. of the streamwise velocity), provided adequate ADCP operation and post-processing. The study did, however, not include reference measurements, so that the estimated vertical distributions of turbulence intensity could only be compared to “textbook-like” profiles.

The literature provides examples of further ADCP-derived metrics describing temporal velocity fluctuations, specifically Reynolds stress (Nystrom et al., 2007; Stacey et al., 1999; Vermeulen et al., 2011) and turbulent kinetic energy

(Nystrom et al., 2007; Tokyay et al., 2009). Both of these measures are based on the temporal fluctuations of the radial velocities p' from multiple beams or the 3D velocity components $\{u', v', w'\}$, and thus are subject to the limitations outlined above.

There is sufficient evidence to suggest that ADCPs are currently not suitable to quantify hydrodynamic metrics based on the temporal velocity fluctuations around the mean. The main reasons for this are a sampling frequency far below the Nyquist frequency and violations of the flow homogeneity assumption. A further limitation arises from the oscillating vessel motion during the measurement period (Barua & Rahman, 1998). Some of these problems can be particularly pronounced in the complex hydraulic conditions associated with in-channel structures, so that accurate measurements of $\{u', v', w'\}$ cannot be assumed in these regions (Nystrom et al., 2002). Based on this evidence, the quantification of $\{u', v', w'\}$ has not been attempted in the PhD research.

3.3.3 Other hydrodynamic metrics

Shields & Rigby (2005) and Shields et al. (2003) presented some of the few studies attempting to quantify hydrodynamic metrics related to fish ecology with ADCPs. They showed that the indicators of hydrodynamic fish habitat quality suggested by Crowder & Diplas (2000, 2002) can be derived from densely spaced ADCP transect measurements. These indicators involve point- and area-measures of spatial velocity variation (see Table 3-3).

The first measure shown in Table 3-3 represents a generalised form of the SVG used in several laboratory-based fish behavioural studies (see Section 2.4.3). The latter two metrics, on the other hand, compactly capture the flow complexity over an entire vertical section (e.g. a cross section) or a horizontal plane at a specific depth. In the PhD research, they have been used as an area-based proxy for those hydrodynamic metrics based on the spatial variation in $\{\bar{u}, \bar{v}, \bar{w}\}$ (see Table 2-3). Specifically, they have been used to assess the effect of

various ADCP data quality enhancement techniques on this category of fish pass attractiveness indicators (see Chapter 4).

Table 3-3. Metrics of velocity gradients and flow circulation suggested by Crowder & Diplas (2000, 2002; modified from Shields & Rigby, 2005)

Metric	Description	Unit	Derivation from ADCP data
Velocity gradient between two points A measure of the amount of power expended by an organism in moving from one location (point 1) to another (point 2)	Spatial gradient of kinetic energy per unit mass and per unit distance	ms^{-2}	$\bar{V}\left\lvert\frac{V_{T,2}-V_{T,1}}{s}\right\rvert$ $\bar{V}=(V_{T,2}-V_{T,1})/2$ where s is the distance between points 1 and 2
Flow complexity in the vertical plane over an arbitrary area of interest	Weighted average of flow rotation in the vertical plane transverse to the channel	s^{-1}	$\frac{\Gamma_{ABS}}{A_{TOT}}=\frac{\sum\left\lvert\frac{\Delta V_z}{\Delta y}-\frac{\Delta V_y}{\Delta z}\right\rvert \Delta y\Delta z}{\sum \Delta y\Delta z}$ Shields & Rigby (2005) computed the measure for each transect across all bins.
Flow complexity in the horizontal plane over an arbitrary area of interest	Weighted average of flow rotation in the horizontal plane	s^{-1}	$\frac{\Gamma_{ABS}}{A_{TOT}}=\frac{\sum\left\lvert\frac{\Delta V_y}{\Delta x}-\frac{\Delta V_x}{\Delta y}\right\rvert \Delta x\Delta y}{\sum \Delta x\Delta y}$

3.4 ADCP measurements near engineered in-channel structures: major challenges and potential solutions

While Section 3.3 presented ADCP data sampling and processing approaches potentially useful for near-pass hydrodynamics quantification, this section highlights the various data quality issues that are particularly distinct in (but not exclusive to) such ADCP application, along with potential solutions. The few studies involving the use of ADCPs near fish pass entrances are dominated by reports on data quality issues. For example, Johnson et al. (2009) found the ADCP data collected near surface flow outlets at a large dam to be unusable because of violations of the spatial flow homogeneity assumption, and Walton et al. (2012) experienced frequent loss of BT resulting in discontinuous ADCP data downstream of a fish pass. Studies where ADCPs were used near other engineered in-channel structures such as groins (Jamieson et al., 2011, 2013) and hydrokinetic turbines (Neary et al., 2013) revealed further challenges potentially encountered in ADCP-based near-pass hydrodynamics quantification. This section reviews those limitations and highlights the solutions

implemented in the PhD research (see Chapters 4-6). For a comprehensive list and description of ADCP measurement errors, the reader is referred to González-Castro & Muste (2007) and Muste et al. (2004b).

3.4.1 Errors due to spatial flow heterogeneity

Nystrom et al. (2002) argued that the distance between the footprints of the ADCP beams (see Section 3.2.4) is comparable to the size of large-scale turbulence. Therefore, the assumption of a spatially homogeneous flow field could easily be violated in complex hydraulic conditions, such as those found in the vicinity of in-channel structures and fish passes. This resulting measurement bias can be particularly large as the depth of the measurement, and thus the distance between the individual ADCP beams, increases.

The literature provides a few examples where this error has limited or prevented the applicability of ADCPs near in-channel structures. Johnson et al. (2009) attributed unrealistic ADCP water velocities measured near surface flow outlets at a large dam and a strong disagreement of these with complementary 3D hydrodynamic model outputs to spatial flow inhomogeneity, rendering these ADCP data unusable. Similarly, Neary et al. (2013) found disagreement between ADCP- and ADV-measured 3D velocities and turbulence metrics measured close to a model hydrokinetic turbine in an open channel flume. Their interpretation that the error was caused by violations of the flow homogeneity assumption was later confirmed by Richmond et al. (2015) through numerical error simulation.

The literature review revealed two approaches to reduce the effect of this error:

(i) the post-processing strategy suggested by Vermeulen et al. (2014), and

(ii) the detection (and subsequent discarding) of biased 3D velocities based on indicators that can be derived from the ADCP data.

3.4.1.1 3D velocity derivation by Vermeulen et al. (2014)

Vermeulen et al. (2014) developed a technique that reduces the water volume for which homogeneous flow is required. The method uses a least squares procedure to estimate the 3D velocity vector that fits best to a set of radial velocities sampled during repeated cross-sectional measurements and located within the same 3D cell of a pre-defined mesh.

The set P consisting of N radial velocities is related to the mean water velocity Vvia a set Q of unit vectors describing the direction of the acoustic beams (Vermeulen et al., 2014):

$$P = QV \Leftrightarrow \begin{pmatrix} p_1 \\ \vdots \\ p_N \end{pmatrix} = \begin{pmatrix} q_1^T \\ \vdots \\ q_N^T \end{pmatrix} \quad \textbf{(3-4)}$$

The radial velocities are affected by temporal velocity variation, spatial velocity variation within the mesh cell, instrument noise and other errors. Their combined effect is captured in ϵ, so that:

$$P = QV + \epsilon \quad \textbf{(3-5)}$$

The velocity V is predicted such that the sum of squared errors $\hat{\epsilon}^T\hat{\epsilon}$ is minimised.

The method defines the mesh location as a straight line fitted to the instrument trajectory. The mesh cell dimensions are defined by the user and determine the volume for which spatially homogeneous flow is assumed. This is in contrast to conventional repeated transect processing, which involves the averaging of multiple 3D water velocity vectors, each of which is resolved independently from the three to four radial velocities measured at the same time (see Section 3.3.1.2). Thus, in conventional processing, the minimum size of the volume assumed to be homogeneous is fixed and determined by the ADCP beam spread and measurement depth.

A major question to be addressed concerns the sensitivity of the 3D velocity estimate to the user-defined cell dimensions and the trade-off between small cells to reduce effects from remaining spatial flow inhomogeneity, on the one hand, and a sufficiently large sample of radial velocities per cell to capture the temporally averaged velocities on the other hand. Moreover, as the method is relatively new, previous evaluations have been presented only for large rivers (e.g. in bends of the Makham River, Indonesia, with several hundreds of meters width; Vermeulen et al., 2014).

This thesis presents the first evaluation of the method by Vermeulen et al. (2014) near in-channel structures and on smaller rivers. Apart from the number of transects required to capture the temporally averaged velocities (see Section 3.3.1.2), particular emphasis was put on the effect of the user-defined cell dimensions on the resulting 3D velocity estimate.

3.4.1.2 Indicators of spatial flow heterogeneity

Although three transducers would be sufficient to resolve the 3D velocity vector, many ADCPs have a fourth beam to allow for calculation of the so called error velocity (e). In practice, the error velocity has been a widely used measure to assess the flow homogeneity assumption and to detect failure of one or more transducers (Mueller & Wagner, 2009; Teledyne RDI, 2010). It is defined as the difference between the vertical velocities derived from the radial velocity measurements of the two different pairs of opposing ADCP beams:

$$e = \frac{(p_1 + p_2)}{2\cos(\beta)} - \frac{(p_3 + p_4)}{2\cos(\beta)} = \frac{(p_1 + p_2 - p_3 - p_4)}{2\cos(\beta)} \quad \textbf{(3-6)}$$

An error velocity of zero is meant to indicate a homogeneous flow field and manufacturer-provided ADCP software (e.g. Teledyne RDI's WinRiver II) rejects measurements, where e exceeds a user-defined threshold.

For several reasons, the validity of the error velocity as an indicator for flow inhomogeneity or the velocity error resulting from it is questionable. In practice,

some small error velocity will always occur due to instrument noise (Simpson, 2001). Not all cases of flow inhomogeneity can be detected through the error velocity, for example when the flow heterogeneities do not affect the vertical water velocities or when the heterogeneity causes similar error magnitudes in the vertical velocity components derived from each beam pair (Gaeuman & Jacobson, 2005; Nystrom et al., 2002). Cook et al. (2007) suggested an alternative indicator (called homogeneity index HI), which overcomes the latter problem. However, also their indicator is solely based on differences in the vertical velocity components and thus unable to accurately indicate the severity of flow heterogeneities affecting mainly the horizontal velocities. Richmond et al. (2015) simulated ADCP measurements in the wake of hydrokinetic turbines and concluded that the error velocity can identify inhomogeneous flow, but cannot indicate the severity of the resulting velocity error.

The default maximum error velocity for data to be marked as "good" in WinRiver II is 1.50 ms^{-1} (Teledyne RDI, 2007). However, the literature lacks of an empirical functional relationship between e or HI and the magnitude of the bias in the 3D velocity. For the reasons outlined above, it is questionable whether an unambiguous functional relationship can be determined. Therefore, the use of these measures as sliding indices or in the form of thresholds, beyond which data are to be discarded, is effectively uninformed. For this reason, the use of indicators of spatial flow heterogeneity has not been included in the methodology defined in the PhD research. Instead, future research to thoroughly assess the validity of flow heterogeneity indicators is recommended.

3.4.2 Temporary bias in instrument heading data

A frequently encountered error in ADCP data stems from bias in the readings of the ADCP-internal fluxgate compass (Von Appen, 2015; Gaeuman & Jacobson, 2005; Marsden et al., 2003; Zhao et al., 2014). These readings are used to determine the transformation angle β, required to reference the instrument-aligned 3D velocities to the local ambient magnetic field (magnetic north) and, after correcting for the site-specific magnetic declination, to true north. When

the boat velocity correction (see Section 3.2.3) is based on navigation data from ADCP-external sensors (e.g. because of BT loss), the effect of moderate errors in β on the velocity components referenced to north can be large, as it depends on the magnitude and direction of the actual water velocity V_T, and the ADCP boat velocity B_T. For a ratio B_T/V_T of 1, an error in β of 10 deg can lead to a 17% error in the measured water velocity magnitude and an error of up to 20 deg in the water velocity direction (computed based on Gaeuman and Jacobson, 2005).

After on-site compass calibration, the remaining (and persistent) misalignments between true geographic north and compass north (referred to as compass calibration error) can be lower than ±0.5 deg (Gaeuman & Jacobson, 2005). Much larger compass errors can be caused by either (i) the presence of ferromagnetic materials inducing temporal changes in the local magnetic field, or (ii) large horizontal instrument acceleration leading to the physical displacement of movable parts within the compass (referred to as dynamic compass error). For example, Gaeuman & Jacobson (2005) reported dynamic compass errors up to 9 deg, caused by manually rattling the ADCP mount. Smooth platform manoeuvring can avoid this problem, but is complicated in rough surface water conditions, such as those found near some fish passes.

Little is known about the frequency and magnitude of ADCP compass errors caused by magnetic interference from on-site materials. Careful site selection can avoid this problem in ADCP discharge measurements (Mueller et al., 2013), but this is an inappropriate solution for hydrodynamic mapping studies, which are spatially bound to the reach of interest. Increased care must be taken when measuring near anthropogenic structures made from ferromagnetic materials (e.g. steel reinforced structures or steel sheet pilings along river banks). Moreover, occurrences of BT loss can be particularly frequent near flow obstacles due to increased water turbidity and turbulence, as, for example, experienced for ADCP measurements near a wing dike by Jamieson et al. (2011) or downstream of a fish pass by Walton et al. (2012). In such conditions, external navigation systems for boat velocity estimation are crucial to prevent

discontinuous ADCP data. This will increase the potential effect of instrument heading errors on the water velocity readings as outlined above.

To prevent biased ADCP heading data from ferromagnetic interference, Marsden et al. (2003) and Zhao et al. (2014) suggested the substitution of the ADCP-internal compass with an external gyrocompass and a GNSS compass, respectively. The latter computes heading based on the location data from two GNSS receivers with antennas spatially separated in the horizontal direction. The solution relies on continuous line of sight to a sufficiently large number of navigation satellites, which, near river banks or high in-channel structures may not be given (see Section 3.4.3 and Chapter 5). Both solutions bear relatively expensive equipment and the substitution of the ADCP-internal compass by any external heading sensor involves problems of orientation misalignments between the ADCP and the heading sensor (Zhao et al., 2014).

Therefore, in the PhD research an alternative, low-cost solution to temporary ADCP compass bias was developed and assessed (see Chapter 4). Instead of substituting the compass data as a whole, the method integrates the compass with a low-cost external sensor providing relative heading information. Potential sensors for this task are Inertial Measurement Units (IMUs) consisting of Micro Electro-Mechanical Systems (MEMS) gyroscopes and accelerometers or on-board cameras providing orientation information based on visual odometry (see Chapter 5). Low-cost IMUs are available off-the-shelf and provide high-frequency orientation measurements relative to the direction of gravity. These are constrained neither in motion nor to any specific environment or location (Madgwick et al., 2011). Prior to publications arising from the PhD research (Kriechbaumer et al., 2016), the potential of low-cost IMUs to correct for ADCP compass errors had been unexplored in the scientific literature.

3.4.3 Spatial data localisation in GNSS-denied areas

The quantification of spatially referenced hydrodynamic metrics in relation to a fish pass entrance relies on the availability of an accurate ADCP positioning

system. Moreover, accurate positioning is required to estimate the boat velocity for ensembles with invalid BT signals, a problem particularly pronounced near engineered flow obstacles (see Section 3.4.2). Accurate ADCP positioning can, however, be a major challenge in areas precluding the conventional use of global positioning via line of sight GNSS. This problem is particularly pronounced in smaller rivers, where bankside vegetation or urban settlement can limit the sky view to navigation satellites over a large proportion of the water surface. For example, Jamieson et al. (2013) found spatial ADCP data referencing based on the Global Positioning System (GPS) to be insufficiently reliable when monitoring the hydraulics induced by stream barbs on a river in a heavily wooded and deep valley.

Fish passes are frequently installed close to river banks, where, in addition to potentially limited line of sight to satellites, GNSS position accuracies may be reduced by so called signal multipathing effects (Rennie & Rainville, 2006). This problem occurs when the satellite signals bounce off trees or buildings on the shore before arriving at the GNSS antenna. Thereby, the signal travel time increases and the calculated satellite distance gets biased (see also Section 5.2.2).

On large rivers, Real-Time Kinematic (RTK) GNSS devices conveniently provide positioning at cm-level accuracy within most parts of the survey area (e.g. Jamieson et al., 2011; Parsons et al., 2005; Rennie & Church, 2010). The effects of the accuracies of satellite-based positioning systems on ADCP measurements of discharge (Wagner & Mueller, 2011), boat velocity (Rennie & Rainville, 2006) and apparent bedload velocity (Rennie & Rainville, 2008; Rennie et al., 2007) had been studied previously, particularly on large rivers. However, the performance of GNSS to localise ADCP data on small sites and near in-channel structures required further research, as did the identification of alternative sensor localisation systems. In GNSS-denied areas, the problem of localising data collected from moving vessels was yet to be solved. These gaps in research have been addressed here (see Chapter 5) through:

(i) a detailed assessment of various GNSS strategies for ADCP positioning near fish passes, and

(ii) by integrating ADCPs with other localisation strategies, identified to be potentially suitable for sensor positioning in GNSS-denied locales.

3.4.4 Limited suitability of available ADCP platforms

As outlined in Section 3.2.8, the ARC-Boat platform was used to evaluate the methodology proposed in this research. This platform offered suitable mechanical characteristics, such as large robustness and buoyancy as well as sufficient forward thrust for most fish pass study sites (see the methodology evaluation in Chapter 7). However, this and other ADCP platforms available on the market lacked the on-board electronics required to implement several of the techniques suggested here to make ADCPs more robust against common errors associated with in-channel structures. Some of these techniques involve the integration of external sensors (see Sections 3.4.2 and 3.4.3 as well as Chapters 4 and 5), which relies on the availability of an on-board data logging system capable of recording data from multiple sensors (including equipment not supplied by ADCP manufacturers) in a time-synchronised manner. Where possible, an on-board system with wired connections to the sensors was preferred to wireless data transmission to a computer on shore, in order to increase the system reliability and to prevent transmission delays resulting in erroneous data synchronisation. For ADCP measurements on RC platforms such a system was not available prior to the PhD research.

None of the available ADCP platforms allowed for autonomous or semi-autonomous deployment. Autonomous features (e.g. active heading hold, position hold or automatic navigation along a user-defined track) would facilitate the accurate implementation of pre-defined sampling strategies. In repeated transect sampling, they may also decrease the boat path variability between transects and thus improve the overall data quality (see Section 3.3.1.2). Autonomous platform control relies on the integration of a reliable platform

positioning system with the platform propulsion system, e.g. through a micro-controller.

Finally, the relatively large size of the marketed RC platforms meant that their deployment relied on at least two personnel for platform transport, launching and recovery. While larger platforms might be required to achieve sufficient stability and forward thrust at fish pass sites in fast flowing rivers or under conditions of high discharge, the relatively inconvenient handling limits their suitability in smaller, slow flowing rivers, where a smaller and lighter platform would be more practicable.

The limited suitability of the available RC platforms was addressed in the PhD research by developing the prototype for a small-sized ADCP platform with integrated control and data logging system (see Chapter 6).

3.5 Towards a methodology for the ADCP-based quantification of near-pass hydrodynamics

Based on findings of previous studies (see Sections 3.3 and 3.4) and under consideration of the operational principles and specifications of ADCPs (see Section 3.2), a methodology for the ADCP-based near-pass hydrodynamics quantification has been proposed (see Figure 3-7). The methodology covers the stages from the selection of survey equipment to the interpretation of the results in relation to fish pass attractiveness. It involves the quantification of the 3D distribution of $\{\bar{u}, \bar{v}, \bar{w}\}$, from which more sophisticated hydrodynamic indicators can be derived. This approach has been common in the context of eco-hydraulic research related to fish passage (Andersson et al., 2012; Enders et al., 2009; Nestler et al., 2008; Piper et al., 2015; Russon & Kemp, 2011; Vowles & Kemp, 2012). Moreover, the proposed methodology is based on the finding from previous studies that moving-vessel ADCP measurements along repeatedly sampled sections are a suitable strategy for quantifying $\{\bar{u}, \bar{v}, \bar{w}\}$ (see Sections 3.3.1.2 and 3.3.1.3). The quantification of metrics derived from the temporal velocity fluctuation around the mean $\{u', v', w'\}$, on the other hand, has

not been included, because of the overwhelming evidence on the inadequacy of ADCPs for such measurements (see Section 3.3.2).

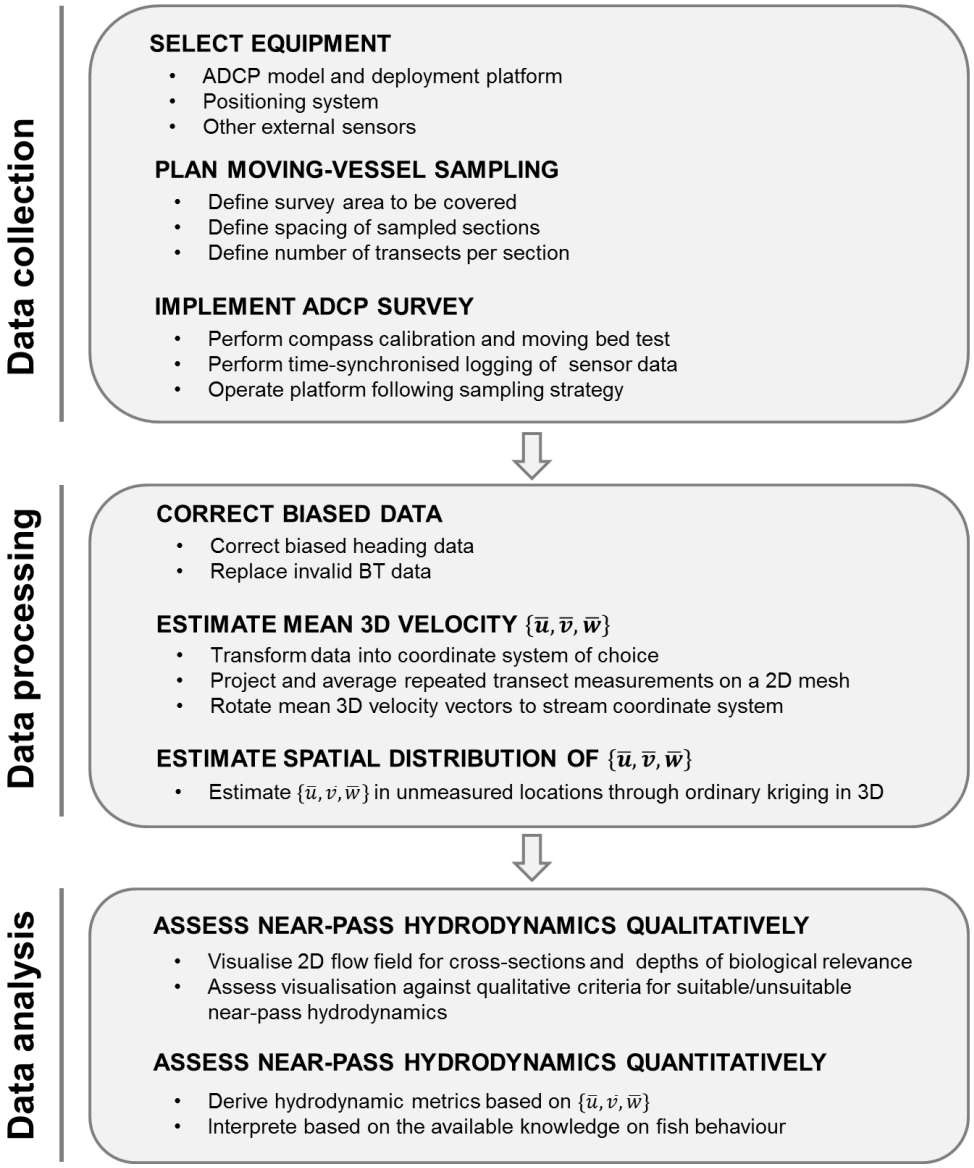

Figure 3-7. Proposed methodology for the ADCP-based quantification of near-pass hydrodynamics

The methodology has been formulated to result in:

(i) flow maps visualising the spatial distribution of temporally averaged velocities $\{\overline{u}, \overline{v}, \overline{w}\}$and enabling an initial assessment

of the near-pass hydrodynamics in relation to established qualitative criteria (see Section 2.3), and

(ii) quantitative hydrodynamic indicators of fish pass attractiveness, based on those used previously in fish behavioural studies (see Section 2.6.1), in order to enable an objective assessment of hydrodynamic fish pass attractiveness that is comparable across sites and hydraulic conditions, and can be quantitatively related to measures of fish pass success (as indicated in Figure 2-1).

The implementation of the methodology conceptualised in Figure 3-7 relied on the technical enhancement of ADCP deployment equipment and data processing, to make ADCP data more robust against errors particularly pronounced near engineered in-channel structures. The methodology uptake in practice relied on its time- and cost-effective implementation. Therefore, the minimum number of transects per section required to capture the mean velocities, as well as the effect of the section spacing on the resulting flow maps had to be explored. Finally, the effectiveness of the methodology in terms of its adequacy to capture hydrodynamic features relevant to fish passage as well as its transferability across sites had to be evaluated at a variety of fish pass sites and environmental measurement conditions. These aspects correspond to objectives 3 to 5 of the PhD research (see Section 1.2). The methodological approach to the accomplishment of these objectives has been outlined in the following sections, whereas detailed methodologies have been described at the beginning of the respective thesis chapters (Chapters 4-7).

3.5.1 Developing techniques for improved ADCP data quality and practicable ADCP deployment near in-channel structures

Figure 3-8 summarises the major limitations of ADCPs when taking measurements near fish passes, as reviewed in the preceding sections of this chapter.

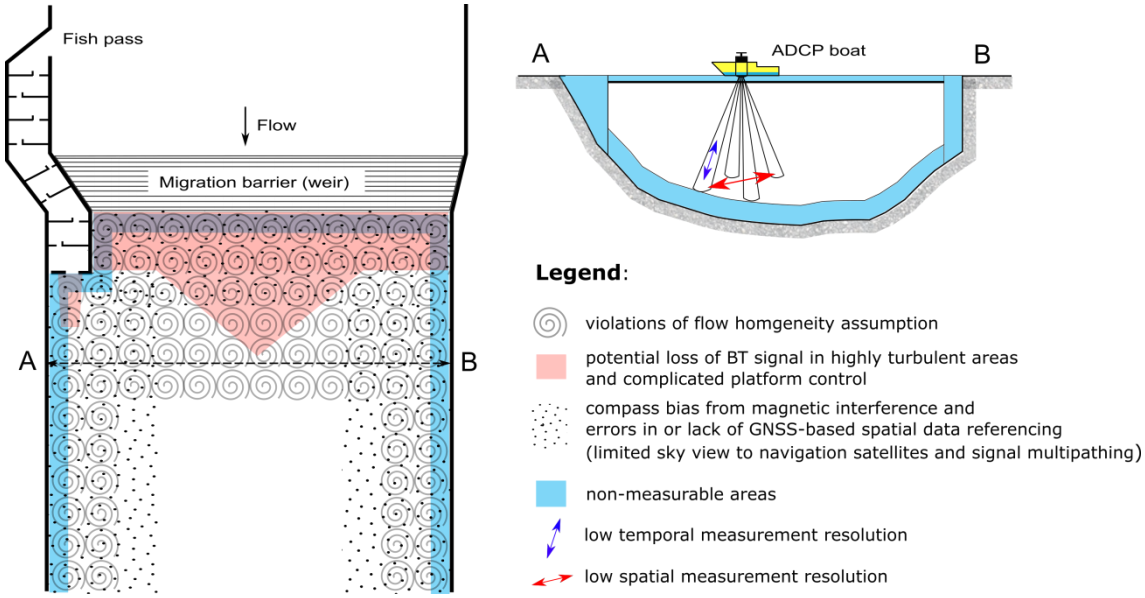

Figure 3-8. Exemplary illustration of major limitations and error sources during ADCP measurements downstream of fish passes (drawing not to scale).

While some of these limitations are grounded in the fundamental principles of ADCPs, others are primarily due to the environmental conditions at the measurement site. The latter category of limitations were addressed in the PhD research, which, based on the findings from previous studies (see Section 3.4), was assumed to be necessary to accomplish accurate ADCP-based quantification of near-pass hydrodynamics. Moreover, the equipment developed in the PhD research facilitated the practical implementation of the ADCP-based methodology in terms of cost and time effort and increased the number of sites with conditions suitable for the methodology implementation.

3.5.1.1 Increasing robustness against spatial flow heterogeneity, compass bias and BT loss

To address errors from spatial flow heterogeneity, temporary bias of the ADCP compass and BT signal loss, the processing method by Vermeulen et al. (2014; see Section 3.4.1.1), a novel ADCP-IMU integration algorithm (see Section 3.4.2), and a TS-based platform tracking technique have been evaluated (see Chapter 4). The methods were integrated on an ARC-Boat platform carrying a 1,200 kHz RioGrande ADCP (see Sections 3.2.7 and 3.2.8). The technical

feasibility of these methods, as well as their effectiveness were initially assessed downstream of a vertical slot fish pass on the River Severn at Shrewsbury, UK (see the survey denoted SHREW1 in Figure 3-9, Section 3.5.2). The study site was one of several involved in the PhD research. The rationale for their selection has been outlined in Section 3.5.2.

The effectiveness of the processing method by Vermeulen et al. (2014), the ADCP-IMU integration and the TS-based estimation of boat velocities, were evaluated based on a comparison of selected near-pass hydrodynamic metrics quantified with and without application of these respective techniques. Moreover, the necessity of the ADCP-IMU integration and the correction of biased BT-based boat velocities were assessed based on the number of ADCP ensembles affected by biased compass readings and BT loss, respectively. The analysis was extended to a further study site as part of the methodology evaluation (see Section 3.5.2).

3.5.1.2 Assessing systems for ADCP positioning in GNSS-denied locales

To assess the reliability and availability of GNSS-based ADCP positioning, four widely used GNSS devices implementing different GNSS correction strategies were evaluated during a total of five ADCP surveys, covering three different fish pass sites (see Section 3.5.2 for an overview of study sites). The main purpose of the evaluation was (i) to inform the requirement for alternative solutions to ADCP positioning in conditions, where sky view to GNSS satellites was partly blocked by bankside vegetation or buildings, and (ii) to assess the performance of a low-cost GNSS positioning approach based on the open-source GNSS processing software RTKLIB (Takasu & Yasuda, 2008; Takasu, 2013). The evaluation was based on the positioning errors quantified by comparison against reference measurements from a tracking TS providing 3D position accuracies at cm-level.

In a review of positioning systems independent from line of sight to satellites, ADCP positioning via an on-board stereo camera rig was found to offer a promising performance in terms of accuracy and equipment cost. The technique

is referred to as stereo visual odometry and has been well researched in the domain of mobile robotics (see Section 5.2.3). Therefore, here the main questions were how well the technique performed when applied in the context of vessel-based river monitoring and which measures would have to be taken to effectively and efficiently improve stereo visual odometry for this specific application. To answer these questions, two widely used, but fundamentally different, techniques of stereo visual odometry were implemented on an ARC-Boat platform and tested in a GPS-denied river environment covering a variety of scenery types. The position error from visual odometry was quantified against reference measurements from a tracking TS and a statistical model was formulated to explain the error contributions of variables related to platform kinematics and environment scenery.

The effect of positioning errors on the resulting near-pass hydrodynamics depends on the spatial heterogeneity of the water velocities, and thus on the site and the hydraulic conditions on the measurement day. In the absence of protocols defined specifically for hydrodynamic mapping applications, common hydrographic surveying standards were used as a benchmark in this research. The EA national standard for bathymetric surveying of river channels and lakes (Environment Agency, 2013) prescribes the use of RTK GNSS to determine the position of the survey vessel and an Inertial Navigation System (INS; see Section 5.2.4.3) as a substitute whenever RTK GNSS positioning is not available. The standard further specifies that the positioning system used should provide an accuracy (defined as 3 times the S.D.) better than 1 m. The standard is similar to hydrographic surveying protocols by other national agencies (e.g. Queensland Government, 2009) and has been used as a benchmark for the positioning systems evaluation in the PhD research. The full evaluation has been presented in Chapter 5.

3.5.1.3 Developing a small-sized ADCP platform with data logging system and integrated control

As outlined in Section 3.4.4, the lack of ADCP platforms with on-board data logging system and integrated control was addressed by developing a platform prototype, which informed the production of a product platform suitable for use in practice. The design of the prototype comprised of three stages:

(i) the selection of hull form, propulsion system and electronic components based on basic design formulae, criteria to support ADCP data quality and the specific requirements of ADCP-based near-pass hydrodynamics quantification as outlined in Section 3.4.4,

(ii) the physical development of the platform including initial laboratory-based tests to inform the need for modifications of the components selected in (i) and

(iii) the field-based platform prototype assessment in terms of platform operability, stability, speed and other features.

A particular focus was put on the development of the data logging and integrated control systems, which were designed using low-cost hardware to support their integration on ADCP platforms in practice. Field-based platform assessments were conducted downstream of a weir to assess the platform behaviour in conditions similar to those found near fish passes. The platform development and assessment have been presented in Chapter 6.

3.5.2 Methodology evaluation

The ADCP-based methodology was evaluated at numerous fish pass sites in order to assess the methodology limitations in relation to site conditions and thus its transferability. In total, the evaluation involved three study sites in the UK:

(i) a vertical slot fish pass at Shrewsbury Weir on the River Severn in Shrewsbury, Shropshire,

(ii) a super-active baffle (Larinier) pass near a small-scale HEP on the River Stour at Flatford Mill, Suffolk, and

(iii) a nature-like bypass channel next to the turbine of a planned HEP on the River Kennet near Theale, Berkshire.

In Shrewsbury, three separate data collection campaigns were conducted during conditions of low, medium and high discharge (see Table 3-4).

Table 3-4. Discharge conditions and fish passes at the study sites; the reported discharge during the survey time is based on readings from the closest gauging station, i.e. Montford station for SHREW1-3; the sum of Langham and Higham for FLATF and Theale for THEAL; the percentile of daily $\boldsymbol{Q}$ records is based on EA recordings of daily discharge from 1953-2015 for SHREW1-3 and FLATF and from 1961-2015 for THEAL.

	SHREW1	**SHREW2**	**SHREW3**	**FLATF**	**THEAL**
Survey date	20/08/2014	25/02/2015	21/05/2015	04/03/2015	12/08/2015
Q (m^3s^{-1})	7.1	113.9	33.8	4.4	4.1
percentile of daily Q records (%)	8.2	90.4	60.5	82.6	8.0
Obstruction type	Concrete slope weir			Vertical drop weir, HEP & sluice	Vertical drop weir & sluice
Pass type	Vertical slot pass			Super-active baffle pass	Nature-like bypass channel
Pass length (m)	~55.3			9.3	330
Mean pass slope (%)	~3.5			14.9	~0.6

Figure 3-9 shows the geographic locations of the study sites and the environmental conditions at the time of the data collection. It also introduces the abbreviations used throughout the thesis to refer to the respective ADCP surveys.

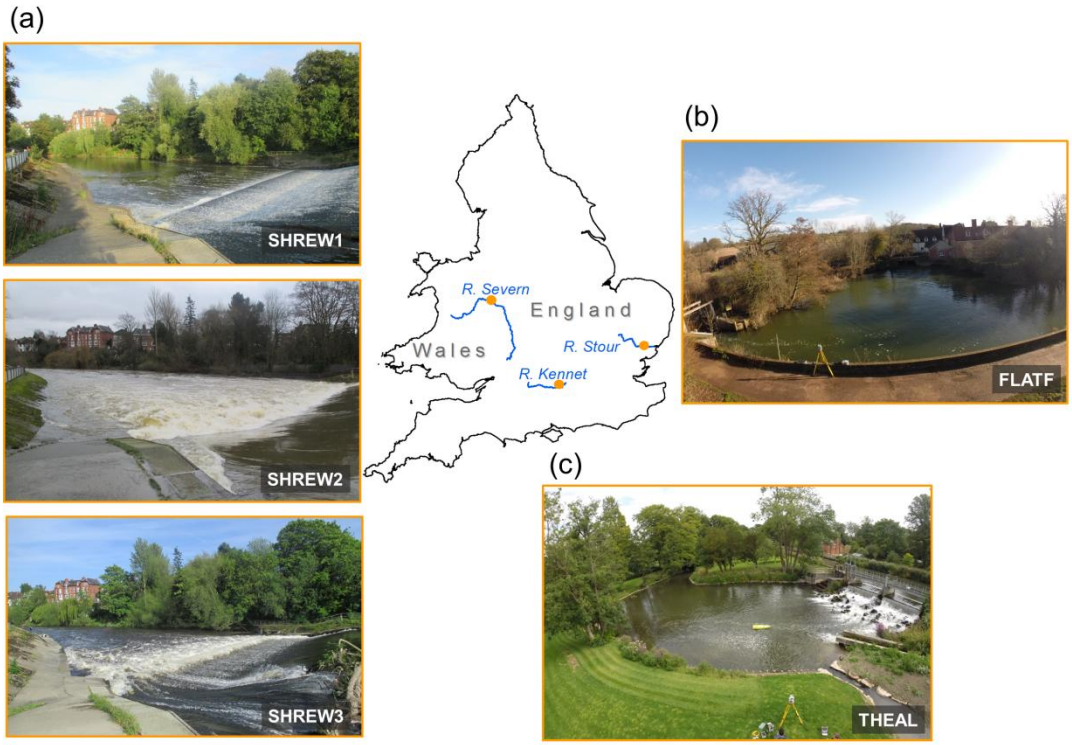

Figure 3-9. Overview of study sites for the methodology evaluation; the photographs show the environmental conditions on the day of the data collection; (a) River Severn at Shrewsbury Weir on 20/08/2014 (SHREW1), 25/02/2015 (SHREW2) and 21/05/2015 (SHREW3); (b) River Stour at Flatford Mill on 04/03/2015 (FLATF); (c) River Kennet near Theale on 12/08/2015 (THEAL); (photographs in (b) and (c) provided by Nick Everard, EA)

The study sites and survey times were selected to cover a wide range of hydraulic conditions (in terms of water velocity and depth), that were thought to determine the suitability of the ADCP-based methodology and would thus inform its limitations in relation to these site characteristics. This was achieved by selecting a set of sites including both fast-flowing conditions closer to the river source (SHREW1-3) and slow-flowing conditions in typical lowland rivers (FLATF and THEAL) as well as survey times during conditions of low, medium and high discharge as outlined above. Moreover, the sites were selected to cover a variety of fish pass structures in terms of pass type, slope and length, as some of these characteristics had previously been found to affect the fish pass attractiveness (see Section 2.5.1). It should be noted that a national fish pass database in the UK was not available at the time of the study, which

complicated a more systematic site selection. Such a database is currently (2015) under development at the EA and might facilitate the site selection for future studies.

The methodology evaluation was focused on upstream passage and thus covered the conditions downstream of fish pass entrances, because:

(i) these conditions were considered more challenging for ADCP deployment than those upstream of fish passes and thus allowed for a more rigorous methodology evaluation and identification of methodology limitations, and

(ii) the literature review in Chapter 2 revealed that the quantification of spatially continuous near-pass hydrodynamics had been particularly rare in the context of upstream passage, despite wide acknowledgement of their relevance to upstream migration delays.

The methodology can, in principle, be applied in the context of both up- and downstream fish passage. Evaluation of the latter is recommended for future research.

The full methodology evaluation has been presented in Chapter 7.

Chapter 4

ADCP MEASUREMENTS NEAR A WEIR WITH FISH PASS: ASSESSING SOLUTIONS TO COMPASS ERRORS, SPATIAL FLOW HETEROGENEITY AND DATA LOCALISATION

A modified version of this chapter has been published in *Hydrology Research*:

Kriechbaumer, T., Blackburn, K., Everard, N. & Rivas Casado, M. (2016). Acoustic Doppler Current Profiler measurements near a weir with fish pass: assessing solutions to compass errors, spatial data referencing and spatial flow heterogeneity. *Hydrology Research*, 47 (3), pp. 591-605.

4.1 Introduction

The literature review in Part I of the thesis showed that ADCP data collected in the vicinity of engineered in-channel structures are particularly prone to

(i) errors from magnetic interference biasing the ADCP-internal compass readings (see Section 3.4.2),
(ii) errors from violations of the spatial flow homogeneity assumption inherent to conventional ADCP data processing (see Section 3.4.1), and
(iii) frequent unavailability of BT signals and limited GNSS availability to substitute for BT-based boat velocity measurements (see Section 3.4.3).

Potential solutions to make ADCP data more robust against these issues and thus to increase the accuracy and transferability of ADCP-based near-pass hydrodynamics mapping have been reviewed in Section 3.4. Those solutions found to be most promising have been assessed in the research presented in this chapter. For their evaluation, the techniques have been integrated on an ADCP platform and used to quantify the reach-wide temporally averaged 3D flow field downstream of a fish pass.

Thereby, this chapter contributed to the fulfilment of **objective 3** of this PhD research (see Section 1.2):

to enhance ADCP measurements near engineered in-channel structures in terms of accuracy, availability and practicability of sensor deployment

This involved the following **research tasks**:

(i) to develop an IMU-based heading sensor integration algorithm that corrects ADCP compass data biased by magnetic interference,
(ii) to evaluate the derivation of 3D water velocities as suggested in Vermeulen et al. (2014) to address the ADCP data bias caused by spatial flow heterogeneity,

(iii) to test a TS-based technique that provides spatially referenced ADCP data in areas of limited sky view and determines boat velocities in areas of BT loss, and

(iv) to quantify the effect of the proposed data quality enhancement techniques on selected metrics describing near-pass hydrodynamics.

4.2 Methods

4.2.1 Case study site

The case study site was a 55 m reach immediately downstream of Shrewsbury Weir on the River Severn (see Figure 4-1). The River Severn is the longest river in the UK and one of its main salmon rivers (NASCO, 2009). It flows from Plynlimon, Ceredigion, in the Welsh mountains to Gloucestershire, where it discharges into the Bristol Channel. A total of 41 obstructions, with nine of them being considered significant barriers to upstream fish migration, can be identified along the course of the river. Shrewsbury Weir is the last major migration barrier to Atlantic salmon before spawning grounds in the upper catchments. This study presented here focused on the fish pass installed on the right river bank, constructed in 1976 as a pool and weir pass and then refurbished in 2006 as a deep vertical slot pass.

4.2.2 Data collection

4.2.2.1 ADCP setup

Velocity and depth data were collected using a 1,200 kHz RioGrande ADCP (Teledyne RDI, 2007) deployed from an ARC-Boat platform (HR Wallingford, 2014; see Sections 3.2.7 and 3.2.8). The data were collected along 13 cross-sectional and eight longitudinal profiles spaced approximately four meters apart (see Figure 4-2). The first cross-sectional measurements were taken at a distance of 4 m to the weir foot. Each profile was repeatedly sampled to capture the mean 3D velocity patterns.

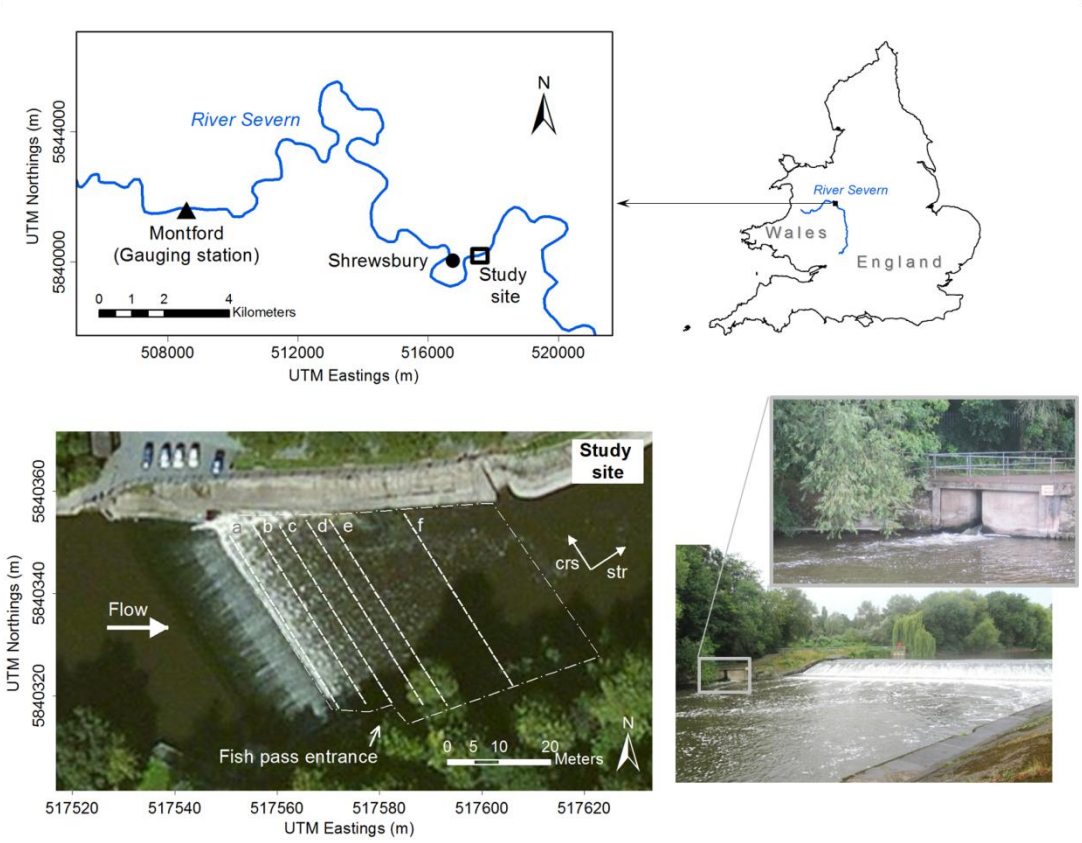

Figure 4-1. Study location; the white dash-point line depicts the extent of the study area and the white dashed lines show cross sections referred to throughout the main text; the arrow pointing to the location of the fish pass entrance is orientated perpendicular to the front wall of the fish pass; the streamwise direction (***str***) was defined to be orthogonal to the weir crest; the images on the bottom right show the study site on the day of the data collection looking in the upstream direction (20/08/2014).

Cross sections within 28 m from the weir foot as well as longitudinal profiles were sampled six times to account for larger turbulence. Cross sections further than 28 m were sampled four times. The ADCP recorded velocity and depth data at an average frequency of 1.5 Hz and with a mean boat speed of 0.42 ms^{-1}. The instrument was configured to Water Mode 12 with seven sub-pings per ensemble and a bin height of 0.12 m. Based on the software PlanADCP (Teledyne RDI, 2009a), this setting resulted in a measurement precision (S.D.) of 0.1081 ms^{-1} for the velocity components V_x, V_y and V_z of the 3D velocity vector. Assuming the conventional relationship between these

components and the radial velocities (see Equation (3-2)), this corresponds to an S.D. for the radial velocities of 0.0523 ms^{-1}. The discharge was assumed to be constant and equal to 7.1 m^3s^{-1} based on records from the nearest gauging station (see Figure 4-1).

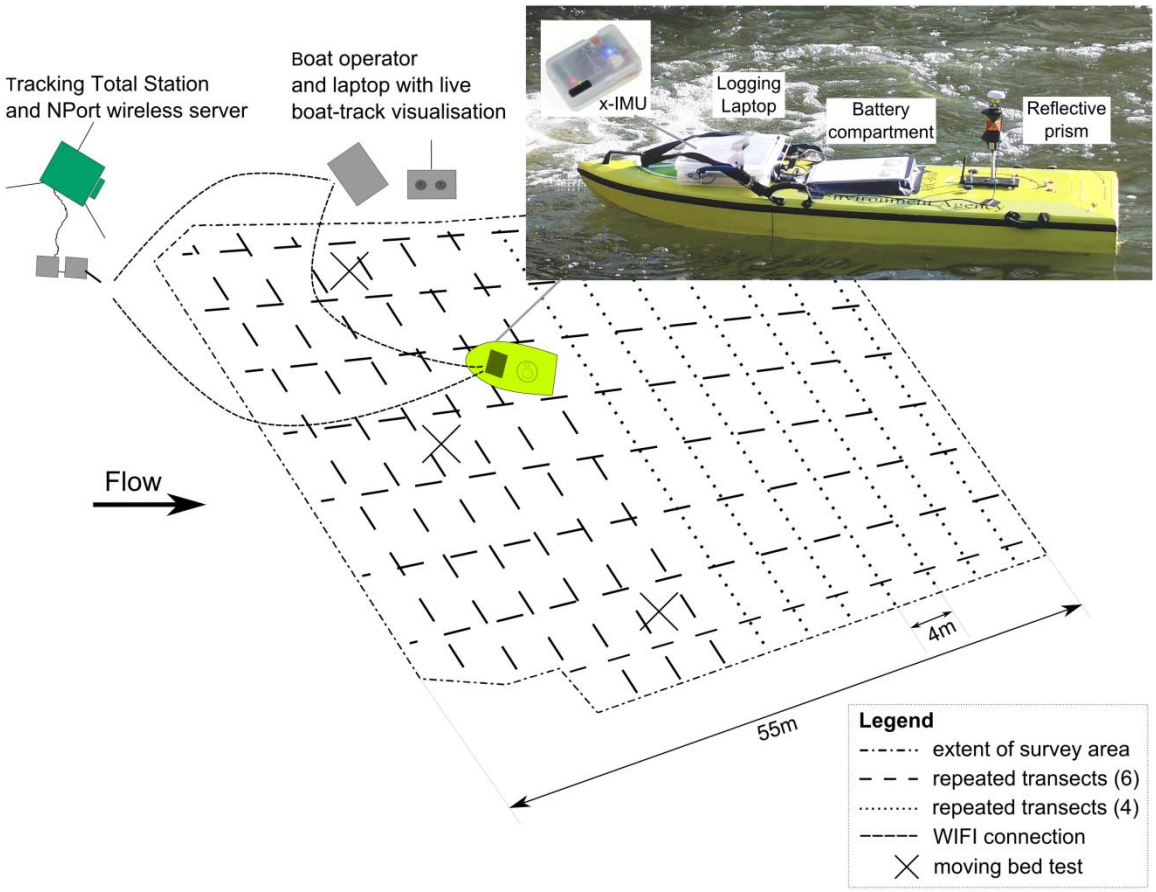

Figure 4-2. Sampling strategy and technical survey setup (not to scale); the left boarder of the survey area corresponds to the weir foot.

4.2.2.2 Data localisation

ADCP data localisation was achieved with a Leica Nova MS50 (Leica Geosystems, 2015a) placed at a fixed location on the river bank and tracking a reflective 360 deg prism installed directly above the centre of the ADCP (see Figure 4-2). The MS50 computes 3D target locations by integrating the distance measurements from an Electronic Distance Meter (EDM; emitting a modulated laser beam and implementing a hybrid phase shift and time of flight method;

Bayoud, 2006) with horizontal and vertical angular measurements from an electronic theodolite. The manufacturer-stated errors (S.D.) are 0.001 m + 1.5 µm m^{-1} for distance measurements to a prism with a maximum tracking distance of 600 m, and 1 arcsecond for angular measurements (Leica Geosystems, 2015a). Kirschner & Stempfhuber (2008) verified the ability of tracking TS devices to measure target kinematics of a few millimetres on a calibration track line up to distances of about 50 m. During data post-processing, the ADCP positions were transformed to global positions in the Universal Transverse Mercator (UTM) coordinate system based on reference measurements with a differentially corrected GPS (Trimble GeoExplorer 6000 GeoXH).

To support the accurate implementation of the sampling strategy, a software application was developed in MATLAB (R2014a, Mathworks, Natick, MA, USA) to display the real-time platform positions against the planned cross-sectional path. This ensured that the spatial variation of the individual transects of a measurement section and the resulting loss in spatially dependent flow features were minimised (see Section 3.3.1.2). On average, 81.0% of all ensembles were at distances below 1 m to a straight line fitted through the ensemble locations of the respective measurement section.

4.2.2.3 Data recording

All data were recorded on a laptop with an Intel Core2Duo 2 GHz processor mounted on the ARC-Boat and controlled on shore from another laptop via Windows Remote Desktop Connection (see Figure 4-2). The TS data were transmitted wirelessly to the on-board laptop using a MOXA NPort W2150 wireless device server connected to a TP-LINK 150Mbps Wireless Local Area Network (WLAN) access point. Bespoke software was developed in C++ to record the data from the MS50 and an x-IMU inertial measurement unit (x-io Technologies, 2012). The ADCP data were recorded using the ADCP software WinRiver II (v. 2.8, Teledyne RD Instruments Inc., San Diego, CA, USA).

To enable temporal synchronisation of the sensors, their data were time stamped with the Windows PC time of the logging computer (for TS and IMU) and the ADCP-internal Real-Time Clock (RTC; for the ADCP). To keep the accumulated drift of the RTC within a maximum of 0.05 s, the absolute time of the clock was set by the Windows PC time of the logging computer at least every 30 minutes in WinRiver II.[4] The error of the time synchronisation depends on the recording frequencies of the sensors, which were 1.5, 5.4 and 64 Hz on average for the ADCP, TS and IMU, respectively. In total, 0.56% of all ensembles had a temporal offset to the nearest TS sample above 0.15 s. These were excluded from the analysis to limit the error in spatial data referencing.

4.2.3 Compass correction

4.2.3.1 ADCP-IMU integration

Temporary compass errors were corrected by integrating the absolute heading data from the ADCP-internal fluxgate compass with relative heading data from the ADCP-external x-IMU. The x-IMU fuses tri-axis MEMS gyroscopes, accelerometers and magnetometers to record pitch, roll and yaw around the axes of the platform frame in Euler angles with a dynamic error <1.7 deg root mean square (Madgwick et al., 2011; x-io Technologies, 2012). For the ADCP-IMU integration, the use of the magnetometers was de-activated (x-io Technologies, 2013), so that the x-IMU provided (relative) heading information based solely on the data of the gyroscopes and accelerometers and thus unaffected by changes in the local magnetic field.

The proposed ADCP-IMU integration algorithm detects biased ADCP compass data through cross-correlation analysis of the time synchronised compass and IMU data within a shifting window of width ω and for lags of -1, 0 and 1 (see Figure 4-3). The data within a window were considered biased if none of the three cross-correlation coefficients was positive and significant ($\alpha=0.05$). The

[4] The RTC of the 1,200 kHz RioGrande ADCP has a drift of -10 to 30 µs s^{-1} (pers. comm., Teledyne RDI, Dan Murphy).

window was shifted by $\omega/2$ until the end of the data series was reached. Data detected as biased were then replaced by corrected heading values (H_{CORR}), which were computed as:

$$H_{CORR}(i) = H_{COMP}(i\text{-}d) + H_{IMU}(i) - H_{IMU}(i\text{-}d) \quad \textbf{(4-1)}$$

where H_{COMP} are the ADCP compass heading data, H_{IMU} are the IMU heading data, i is the ADCP ensemble index and d is the distance in the data series from i to the centre position of the closest previous window with unbiased ADCP compass data. If the beginning of the compass data series was biased, H_{CORR} was computed as:

$$H_{CORR}(i) = H_{COMP}(i\text{+}d) + H_{IMU}(i) - H_{IMU}(i\text{+}d) \quad \textbf{(4-2)}$$

with d becoming the distance from i to the centre position of the closest subsequent window with unbiased compass data. Figure 4-3 illustrates the implementation of the algorithm using data collected at a river cross section with a steel hulled narrowboat moored on one of the river banks and affecting the local magnetic field.

The algorithm accounts for the limitations of both the ADCP compass and the IMU as well as those arising from their integration. Specifically,

(i) it uses differenced heading data in order to eliminate the effects of drift in the x-IMU heading data, and

(ii) it includes the lags of -1 and 1 to account for imperfect time synchronisation of the sensors and different response times to changes in true instrument heading.

Moreover, the statistical significance of the cross-correlation coefficient provides a criterion for detecting biased compass data which is objective and comparable across sites.

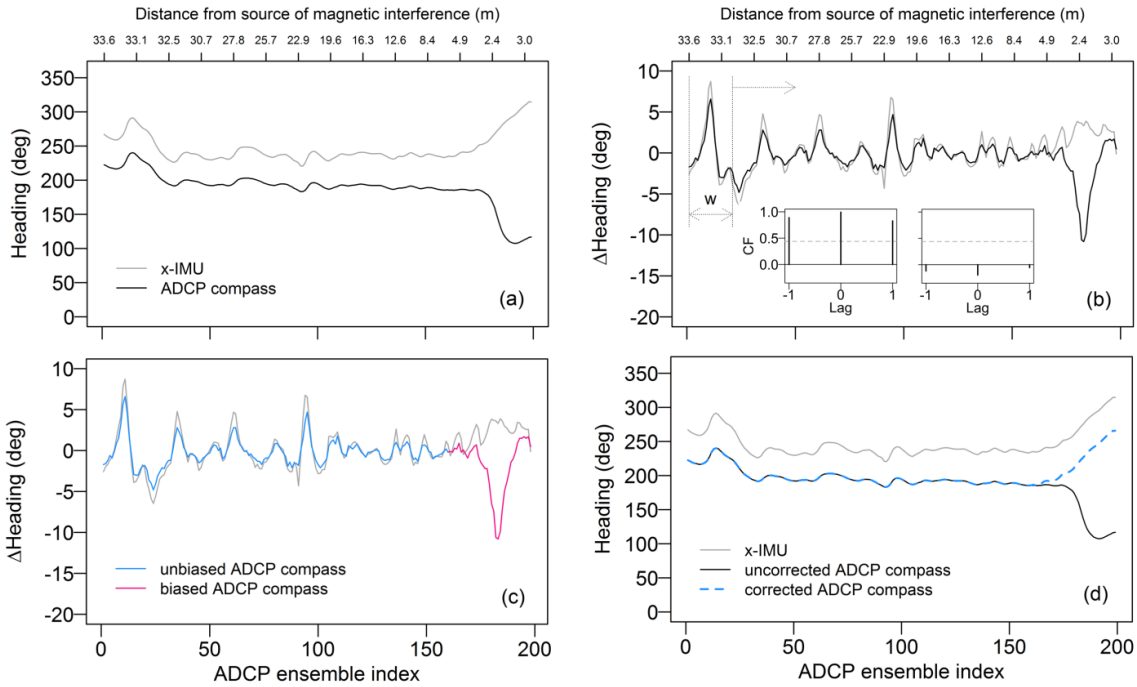

Figure 4-3. ADCP-IMU integration illustrated using data collected on a cross section of the River Thames at Eynsham, Oxfordshire (UK), with a moored steel hulled vessel acting as source of magnetic interference; (a) Time synchronised data of ADCP compass and x-IMU; (b) Detection of biased ADCP compass data; the two inlay plots show the results of the cross-correlation analysis for unbiased (left plot) and biased (right plot) compass data, where *CF* stands for cross-correlation function; (c) Results of the compass error detection; (d) Results of the compass error correction

4.2.3.2 Field-based assessment

The algorithm was tested at the case study site and the statistical and spatial distribution of the error detected in compass heading (ε_H) were quantified, whereby:

$$\varepsilon_H = H_{COMP} - H_{CORR} \quad \textbf{(4-3)}$$

The effects of the circular nature of degrees were accounted for (e.g. if H_{COMP}=3 and H_{CORR}=359, $|\varepsilon_H|$=4).

The statistical significance of the proposed compass correction technique on the estimated reach-wide 3D distribution of water velocities and selected

hydrodynamic metrics derived from it, was analysed as outlined in Section 4.2.6.

4.2.3.3 Sensitivity to shifting window width

The integration algorithm requires the user to select the width of the sliding window for which to compute the correlation coefficients. Small widths lead to smaller samples in the tests for significant cross-correlations, so that even relatively subtle discrepancies between the compass and IMU data might be sufficient for cross-correlations to be insignificant and interpreted as compass bias. Hence, lower windows might be prone to over-correction, if discrepancies caused by imprecision of the compass or IMU are detected as bias (rather than actual compass errors from magnetic interference or platform dynamics). Large widths, on the other hand, might be prone to missing small, but actual, compass errors persisting over short periods of time. To assess the sensitivity of the proposed compass correction to the window widths, the algorithm was implemented at the study site with window widths ranging from 15 to 27 ensembles.

4.2.4 3D velocity derivation by Vermeulen et al. (2014)

The 3D water velocities were estimated from the radial velocities using the MATLAB application ADCPtools implementing the method by Vermeulen et al. (2014; see Section 3.4.1.1 for an outline of the technique). The longitudinal (Δl), lateral (Δn) and vertical (Δz) mesh cell dimensions were chosen to be 2.00 m, 0.40 m, and 0.15 m, respectively (see Figure 4-4a). The cell size selection determines the volume for which spatially homogeneous flow is assumed, which is in contrast to conventional repeated transect ADCP data processing, where the minimum size of this volume is fixed and determined by the ADCP beam spread and measurement depth (see Figure 4-4b). The sensitivity of the 3D velocity estimates to the mesh cell size was quantified by comparing the average number of radial velocity samples per cell ($\bar{x}$) and the average of the resultant water velocities of the mesh cells of a cross section ($\overline{V_{T,Vermeulen}}$) for

36 different mesh cell sizes. The effect of the number of transects taken along a cross section on $\overline{V_{T,Vermeulen}}$ was quantified by calculating the mean change in $\overline{V_{T,Vermeulen}}$ caused by including another transect (see Chapter 7 for an extension of this analysis).

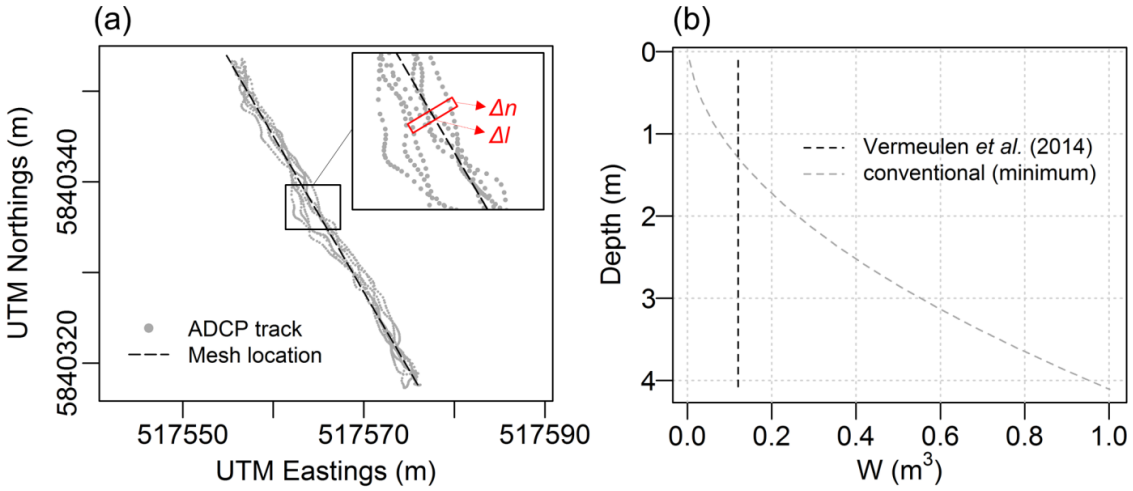

Figure 4-4. (a) Plane view of the 3D velocity projection mesh on the ADCP track (shown for section b in Figure 4-1; (b) Volume ($\boldsymbol{W}$) for which spatially homogeneous flow is assumed in the processing method by Vermeulen et al. (2014) with the cell dimensions used in this study and the minimum $\boldsymbol{W}$ in conventional processing of data from a 1,200 kHz RioGrande ADCP with a vertical measurement resolution of 0.12 m; an instrument draft of 0.12 m was assumed for both methods.

4.2.5 Assessment of data localisation through TS

The tracking TS was used to localise the ADCP data and to estimate the boat velocity for ensembles affected by BT signal loss or with unrealistically high BT-based total boat speed (>1.4 ms^{-1}).

4.2.5.1 Time synchronisation

The positioning error (ε_P) caused by the temporal offset (Δt) between ADCP and TS data was estimated as:

$$\varepsilon_P = \Delta t * B_{T,BT} \quad \textbf{(4-4)}$$

where $B_{T,BT}$ is the resultant BT-based boat velocity for ensembles with a valid BT signal. This provided an indicator of the positioning error introduced through imperfect time synchronisation.

4.2.5.2 Boat velocity estimation

The valid BT signals provided reference boat velocity measurements against which the boat velocity estimates from the TS were assessed (Rennie & Rainville, 2006). Hence, the error (ε_B) in the resultant TS-based boat velocity ($B_{T,\,TS}$) was estimated as:

$$\varepsilon_B = B_{T,\,TS} - B_{T,\,BT} \quad \textbf{(4-5)}$$

To assess whether $B_{T,BT}$ was directionally biased by a non-stationary channel bed, moving bed tests were performed in three locations of the study area (see Figure 4-2) for durations of at least 400 s each.

4.2.6 Effect of data corrections on 3D hydrodynamic mapping

To assess the effects of (i) the IMU-based compass correction, (ii) the water velocity estimation by Vermeulen et al. (2014) and (iii) the TS-based recovery of ensembles with BT loss, the 3D distribution of water velocities in the case study reach was quantified with and without the application of each of these techniques. As counterpart to the 3D water velocity estimation by Vermeulen et al. (2014), a more conventional approach to processing repeated transect measurements was implemented using the MATLAB application VMT (Parsons et al., 2012). This involved the averaging of conventionally derived 3D water velocities (see Equation (3-2)) projected onto a straight line fitted to the boat trajectory.

To obtain a spatially continuous map of bathymetry and 3D flow, depths and water velocities in unmeasured locations of the study area were estimated through ordinary kriging interpolation (see Section 3.3.1.3), using a 0.25 x 0.25 m^2 grid for depths and a 0.50 x 0.50 x 0.15 m^3 grid for velocities. For

an assessment of the interpolation technique, covering a cross-validation analysis of the predicted velocities, the reader is referred to Chapter 7.

The near-pass hydrodynamics quantified with and without the proposed data quality enhancement techniques were compared based on the resultant water velocities (V_T) and the absolute area-weighted vorticity measure ($\frac{\Gamma_{ABS}}{A_{TOT}}$) (see Table 3-3). These two hydrodynamic measures were chosen because they compactly describe the distribution of temporally averaged velocity magnitudes and the strength and abundance of spatial velocity gradients, and thus represent the group of hydrodynamic metrics to be quantified by the methodology defined in this PhD research (see Table 2-3). The metrics were computed from the 3D flow distribution obtained after kriging interpolation. The statistical significance of differences in V_T was assessed through Wilcoxon signed-rank tests. To explore spatial variations in the effects, the analysis was carried out for the cross sections b, d and f shown in Figure 4-1 and for the horizontal planes at depths of 0.35 m and 1.10 m.

4.3 Results and Discussion

4.3.1 Performance of ADCP-IMU integration

Using a window width of 21, the ADCP-IMU integration algorithm corrected 836 ensembles (4.8% of the total number of ensembles) potentially affected by compass errors. Table 4-1 and Figure 4-5 show the statistical and spatial distribution of the detected errors. The largest errors (up to 35 deg) occurred close to the left river bank and near the right bank immediately downstream of the fish pass. It is not straightforward to attribute the detected compass errors to distinct error sources. The presence of steel sheet pilings along the entire left bank suggests that the errors there were caused by magnetic interference. Compass errors detected further away from the banks were considerably smaller in magnitude and errors >3 deg typically persisted over only a few

ensembles. These errors might have been caused by instrument dynamics (see Section 3.4.2).

Table 4-1. Errors in ADCP compass heading (ε_H) as well as TS-based positioning (ε_P) and boat velocity estimation (ε_B)

		Mean	Median	S.D.	Sample size
Compass correction					
$\lvert\varepsilon_H\rvert$	(deg)	2.59	1.68	3.47	836
Data localisation					
ε_P	(m)	0.021	0.016	0.018	13,543
Boat velocity measurement					
ε_B	(ms^{-1})	-0.001	-0.001	0.075	13,543
$\lvert\varepsilon_B\rvert$	(ms^{-1})	0.047	0.028	0.058	

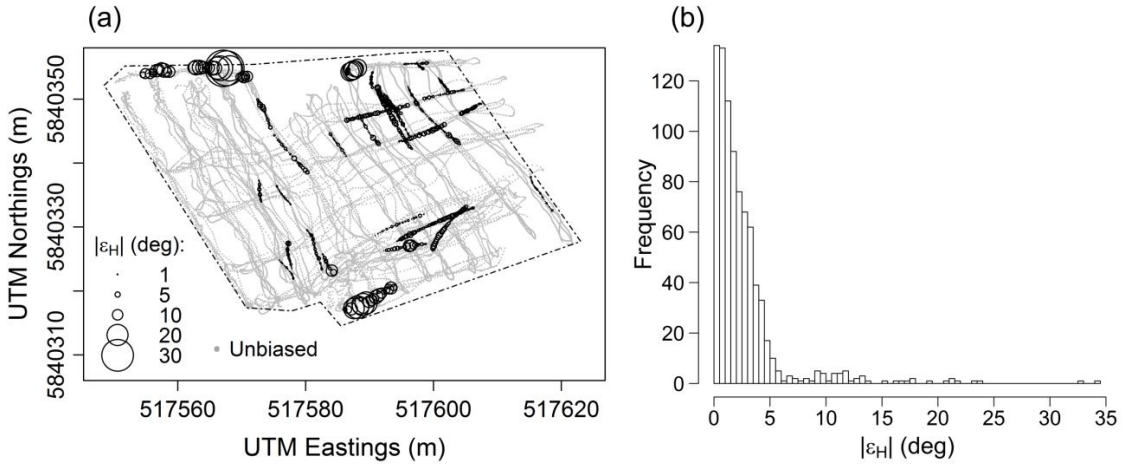

Figure 4-5. (a) Spatial distribution and magnitude of the detected absolute ADCP compass error ($\lvert\varepsilon_H\rvert$); the dash-point line denotes the extent of the study area; (b) Statistical distribution of $\lvert\varepsilon_H\rvert$ (n=836).

4.3.1.1 Effects of ADCP-IMU integration on near-pass hydrodynamics

The differences in V_T obtained with and without compass correction (all other processing steps held constant) were significant in statistical terms (α=*0.05*), but subtle in physical terms for all cross sections and horizontal planes analysed (see Table 4-2).

Table 4-2. Effects of the suggested ADCP data correction techniques on the water velocity magnitude V_T and the area-weighted vorticity Γ_{ABS}/A_{TOT}; * marks the statistically significant effects of the respective techniques on V_T.at $\boldsymbol{\alpha = 0.05}$

		V_T (ms^{-1})						$\frac{\Gamma_{ABS}}{A_{TOT}}$ (s^{-1})
Section / Plane		**Min**	**Max**	**Mean**	**S.D.**	**Sample size**	**p-value**	
All corrections applied								
Cross	b	0.012	0.917	0.130	0.116	1,133	-	0.061
	d	0.019	0.487	0.285	0.107	526	-	0.052
	f	0.006	0.543	0.203	0.159	433	-	0.034
Horizontal at depth (m)	0.35	0.003	0.938	0.217	0.149	8,104	-	0.066
	1.10	0.003	0.598	0.195	0.129	6,030	-	0.073
No compass correction (all other corrections applied)								
Cross	b	0.012	0.870	0.130	0.114	1,133	<0.01*	0.061
	d	0.020	0.488	0.287	0.107	526	<0.01*	0.051
	f	0.006	0.543	0.200	0.160	433	<0.01*	0.034
Horizontal at depth (m)	0.35	0.002	0.904	0.217	0.150	8,104	<0.01*	0.066
	1.10	0.003	0.611	0.195	0.129	6,030	<0.01*	0.073
No BT replacement (all other corrections applied)								
Cross	b	0.013	0.799	0.131	0.111	1,133	0.43	0.061
	d	0.018	0.523	0.291	0.113	526	0.01*	0.068
	f	0.004	0.499	0.198	0.156	433	<0.01*	0.032
Horizontal depth (m)	0.35	0.002	0.881	0.211	0.144	8,104	<0.01*	0.066
	1.10	0.007	0.592	0.193	0.126	6,030	0.24	0.073
Conventional 3D velocity estimation instead of Vermeulen et al. (2014; all other corrections applied)								
Cross	b	0.003	0.607	0.119	0.093	1,133	<0.01*	0.057
	d	0.065	0.574	0.289	0.112	526	0.05	0.057
	f	0.008	0.444	0.203	0.156	433	0.81	0.027
Horizontal at depth (m)	0.35	0.003	0.864	0.219	0.146	8,104	<0.01*	0.061
	1.10	0.003	0.825	0.200	0.135	6,030	<0.01*	0.067
No corrections applied								
Cross	b	0.009	0.716	0.122	0.097	1,133	0.01*	0.061
	d	0.027	0.584	0.301	0.109	526	<0.01*	0.079
	f	0.010	0.466	0.204	0.159	433	<0.01*	0.029
Horizontal at depth (m)	0.35	0.003	0.868	0.219	0.148	8,104	0.02*	0.067
	1.10	0.002	0.735	0.199	0.137	6,030	<0.01*	0.072

4.3.1.2 Effect of shifting window width

The analysis showed that the number of compass biases detected by the ADCP-IMU integration was sensitive to the selected width of the shifting window, whereby smaller windows led to more data marked as biased (see Figure 4-6). The window size had, however, little effect on the statistical distribution of the detected compass errors; the mean (and S.D.) of $|\varepsilon_H|$ computed with window widths of 15 to 27 ensembles ranged from 2.59 deg (3.47 deg) to 3.68 deg (4.53 deg). A comparison of the spatial error distribution showed that the largest and most consistent errors (close to the left river bank) were detected and corrected with all window widths tested, whereas the spatial distribution of smaller errors showed considerable differences. This indicates that the proposed algorithm is a robust method to correct for relatively large compass errors, such as those caused by magnetic interference, but requires further refinement to reliably and consistently detect smaller errors such as those caused by instrument dynamics. The latter are difficult to isolate from differences between the two sensors caused purely from differing response times to changes in heading or imperfect time synchronisation.

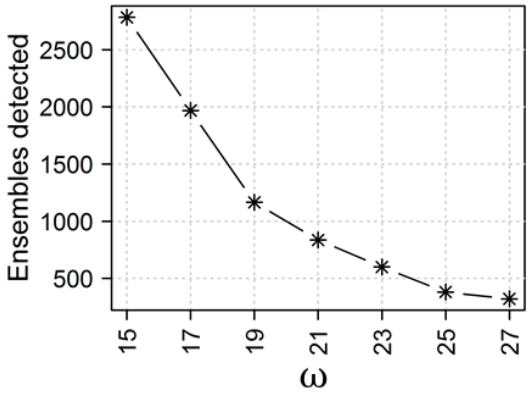

Figure 4-6. Sensitivity of the width of the shifting window (***ω***) to the number of ADCP ensembles detected as potentially affected by compass errors

4.3.1.3 Remaining uncertainty in instrument heading

The uncertainty in the instrument heading after application of the ADCP-IMU integration depends on the precision of the ADCP compass (an S.D. of ≈1 deg

has been assumed in previous studies, e.g. Rennie & Rainville, 2006) and, for the corrected compass data, also that of the IMU (<1.7 deg for the x-IMU; Madgwick et al., 2011). Applying conventional error propagation (e.g. Taylor, 1996) to Equation (4-1), yields the uncertainty in the corrected heading data, $\sigma_{H_{CORR}}$:

$$\sigma_{H_{CORR}} = \sqrt{{\sigma_{H_{COMP}}}^2 + 2 * {\sigma_{H_{IMU}}}^2} \quad \textbf{(4-6)}$$

where $\sigma_{H_{COMP}}$ and $\sigma_{H_{IMU}}$ are the S.D. of the ADCP compass and the IMU heading data, respectively. Assuming the precisions stated above, this results in an S.D. of the corrected heading data of <2.6 deg. In addition to this random error component, the data can contain systematic errors from persistent misalignment between true geographic north and compass north (misalignments after compass correction are often below ±0.5 deg; Gaeuman & Jacobson, 2005).

4.3.2 Performance of 3D velocity derivation by Vermeulen et al. (2014)

Figure 4-7 shows the results of the sensitivity analysis for the water velocity estimation method by Vermeulen et al. (2014). The total number of cells for which 3D velocities could be estimated and the average number of radial velocity samples per cell were highly sensitive to changes in the mesh cell size dimensions (see Figure 4-7a and b). $\overline{V_{T,Vermeulen}}$ showed little sensitivity to the lateral and vertical cell dimensions, but strongly decreased with an increase in the longitudinal dimension up to around 1.5 m (see Figure 4-7c). The change in $\overline{V_{T,Vermeulen}}$ caused by including more transects approached zero as the total number of transects increased (see Figure 4-7d). For the tested section (section b in Figure 4-1) the effect of including the 6th and 7th transect were below 0.03 ms^{-1}, respectively. Similar sensitivities were found for the other measurement sections (see also Section 7.2.4.1).

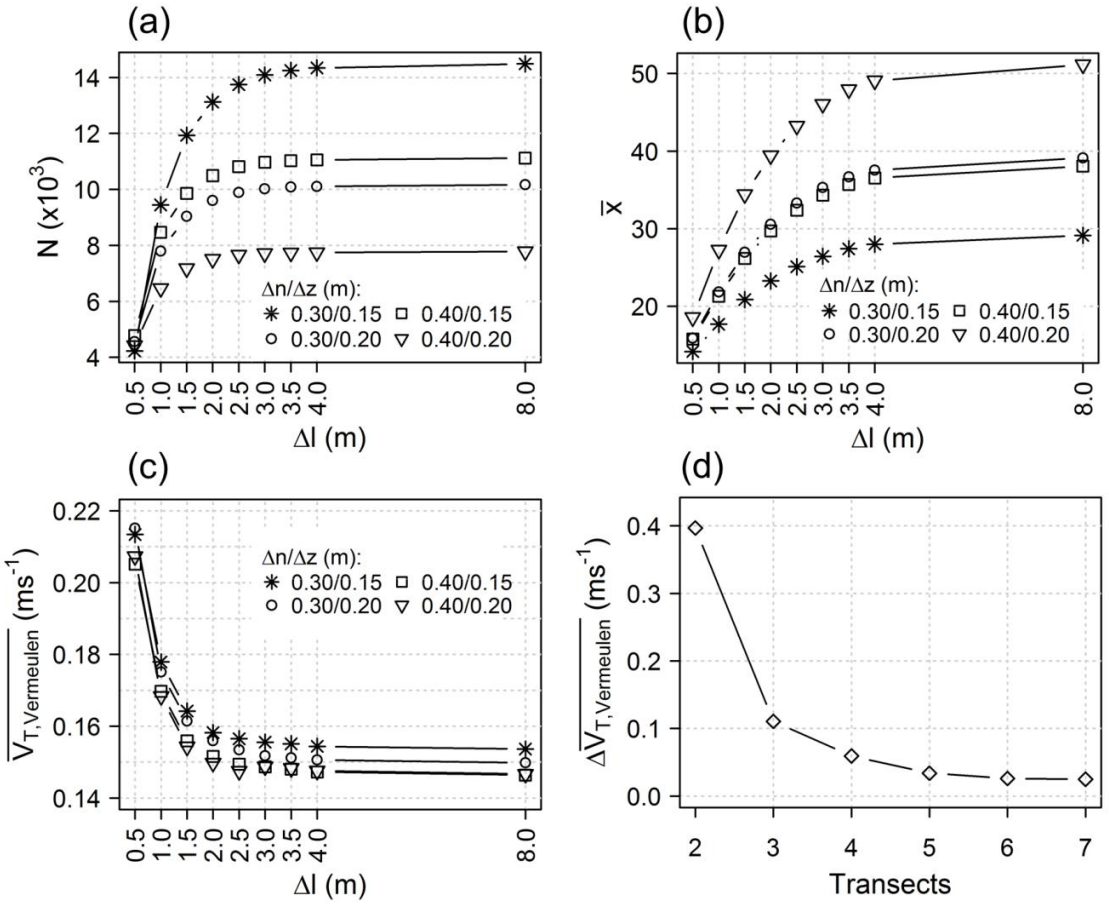

Figure 4-7. Sensitivity analysis for the 3D velocity estimation by Vermeulen et al. (2014); (a, b) Sensitivity of the total number of cells with 3D velocity estimates (*N*) and the average number of radial velocity samples per cell ($\bar{x}$) to the mesh cell dimensions (shown for the data of all sections processed); (c) Sensitivity of the estimated average water velocity magnitude in the mesh cells of a section ($\overline{\boldsymbol{V}_{\boldsymbol{T,Vermeulen}}}$) to the mesh cell dimensions (shown for the data of section b in Figure 4-1); (d) Change in the estimated average water velocity magnitude ($\Delta\overline{\boldsymbol{V}_{\boldsymbol{T,Vermeulen}}}$) caused by including another transect, calculated for mesh cell dimensions of Δl=2.00m, Δn=0.40m and Δz=0.15m (shown for the data of section b in Figure 4-1).

In the complex flow conditions near fish passes, small cell sizes are desirable because: (i) they increase the accuracy of ADCP measurements by decreasing the volume for which spatially homogeneous flow is assumed and (ii) they provide velocities at resolutions closer to the spatial scales thought to be most relevant for fish behaviour (see Section 2.6.2). The sensitivity analysis showed that a further decrease in the cell size relies on a sufficiently large number of

radial velocity samples per cell. This might be achieved by further decreasing the boat track variability, which, in this study, could have potentially led to an increase in the number of radial velocity samples per mesh cell of approximately one third (see Figure 4-7b). The distinct surface flow patterns near the weir made it difficult to follow straight transect lines with the RC platform, but relatively easy to follow previous (curved) boat tracks. The current implementation of the 3D velocity derivation by Vermeulen et al. (2014) supports the estimation of a straight mesh. The modification of the technique to allow for the estimation of a non-linear mesh would enable a further increase in the spatial resolution of the estimated 3D velocities. A larger number of radial velocity samples per cell could also be achieved by increasing the number of repeated transects per section or the measurement duration per transect. Under time constraints, this comes at the cost of a decreased spatial density of sampled sections or a reduction of the surveyed area (see also Chapter 7).

The use of the 3D velocity estimation by Vermeulen et al. (2014) instead of the conventional repeated transect processing method led to statistically significant (α=0.05) changes in V_T for three of the five sections analysed (see Table 4-2). Moreover, using the method by Vermeulen et al. (2014) highlighted a decrease in the area-weighted absolute vorticity from cross sections (b) to (d) by 15%, whereas the conventional procedure resulted in the same area-weighted vorticity estimates for both cross sections.

4.3.3 Performance of data localisation with tracking Total Station

The temporal offset between the ADCP and the TS data translated to an average positioning error of 0.021 m (see Table 4-1 and Figure 4-8). Given the high precision of tracking TS devices and the relatively low measurement distances to the prism (maximum of 95.37 m), it can be assumed that errors in time synchronisation contributed by far the most to the total error in spatial ADCP data referencing. ADCPs commonly used in river research are limited in their capabilities of low-latency external triggering, so that the integration of the TS relies on the temporal alignment of the ADCP and TS data during post-

processing, which is not an optimal solution. While not quantified here, the time required to transmit the position data from the TS to the wireless device server and subsequently to the on-board laptop will have introduced additional synchronisation errors.

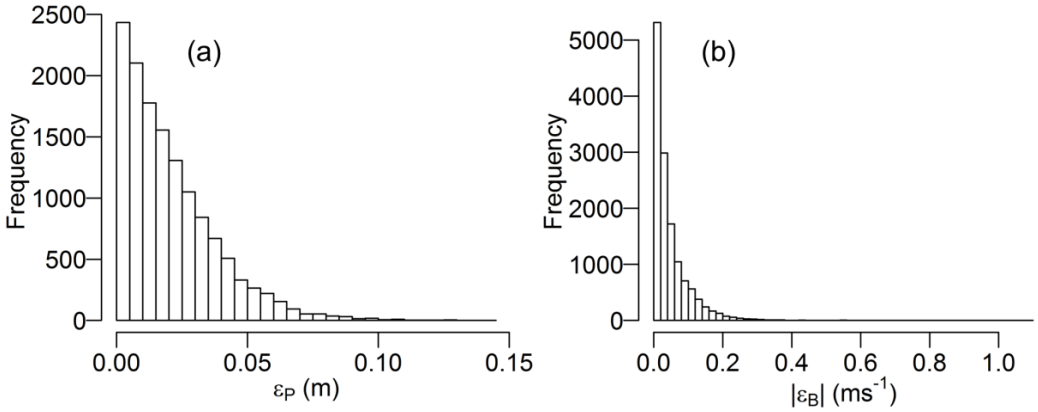

Figure 4-8. (a) Error (ε_P) in spatial data referencing caused by the temporal offset between ADCP and TS data (n=13,543); (b) Absolute error ($|\varepsilon_B|$) in the TS-based boat velocity estimates (n=13,543).

The TS-based and valid BT-based boat velocities showed a mean difference of 0.047 ms^{-1} (see Table 4-1 and Figure 4-8b). This discrepancy might be largely explained by errors introduced through imperfect time synchronisation as outlined above. For comparison, the mean difference was larger than the 0.031 ms^{-1} reported by Rennie & Rainville (2006) for RTK GPS with 10 Hz recording frequency. None of the three moving bed tests suggested a non-stationary channel bed based on the criterion provided in Mueller and Wagner (2009) for stationary moving bed tests with external boat position reference.

4.3.3.1 Effect of recovering ensembles with invalid BT signals

In total, 22.3% of the ensembles (3,880) had invalid BT signals. Ensembles collected in very shallow areas near the edges of the study area as well as those located closer to the weir were more prone to loss of BT (see Figure 4-9). The TS-based recovery of ensembles with BT loss led to statistically significant ($\alpha=0.05$) changes in V_T only for three of the five studied sections (see Table

4-2). For cross section (d), the uncorrected loss of BT led to an increase in the area-weighted vorticity by more than 30%.

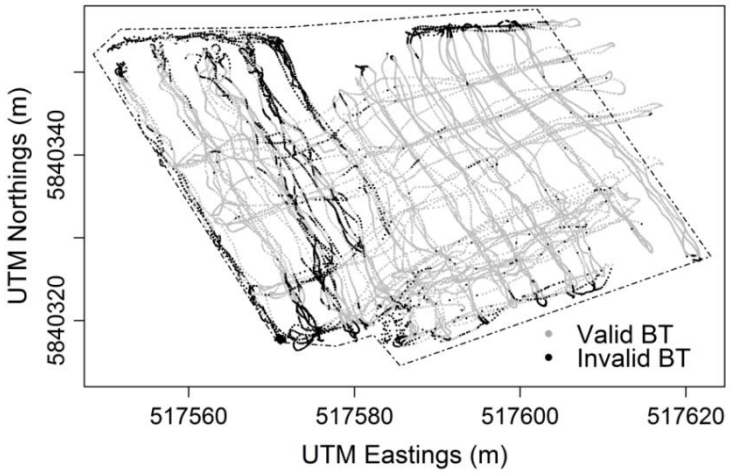

Figure 4-9. Spatial distribution of ensembles with invalid BT signals – the dash-point line denotes the extent of the study area.

4.3.3.2 Practical limitations of TS-based platform positioning

The instant wireless transmission and on-board recording of the TS data requires the ADCP platform to constantly remain within WIFI transmission range and thus limits the extent of the survey area. Some of the TS data recorded at further distances were affected by temporary WIFI signal losses. This problem led to occasional gaps in the TS data recordings of a few seconds, followed by a block of several TS positions recorded with the same time stamp. This pattern might be explained by the wireless device server buffering the data received via the serial link to the TS until the wireless data transmission was possible. The affected data were identified and their time stamps were re-defined during post-processing by comparing the duration between subsequent TS data samples determined based on the time stamps from the on-board laptop and those from the Windows operating system of the MS50. The latter were recorded as part of the TS data, but were restricted to a resolution of 0.1 s. If the difference of the durations was above a threshold of 0.15 s, the data time stamp was re-calculated based on the time from the MS50. In total, 8.85% of the TS data samples were affected by this procedure. To prevent this problem in the future,

alternative approaches to time synchronising the ADCP and TS data have been investigated and tested in further studies presented in this thesis (see Section 7.2.2.4).

Apart from time synchronisation, the major limitation of tracking TS in ADCP applications is the requirement of line of sight to the tracked reflector. Permanent loss of line of sight requires the operator to regain lock to the prism. In this study, this was complicated by permanent boat motion and increased the overall time for data collection. Given the typically rough hydraulic conditions near fish pass entrances, this limitation is likely to affect the ADCP-based quantification of near-pass hydrodynamics at many sites (see Chapter 5 for alternative ADCP positioning technologies).

4.3.4 3D flow and bathymetry at the study site

Figure 4-10 to Figure 4-12 show the bathymetry and 3D flow distribution downstream of Shrewsbury Weir obtained using all of the ADCP data correction techniques suggested. The bathymetric map shows a large scour hole (≈4 m deep) near the weir foot towards the left river bank, coinciding with the area of the fastest water flow from the weir (V_T up to 0.9 ms^{-1}). This jet may act as a competing flow that guides fish away from the pass entrance, potentially leading to delays in upstream migration, a phenomenon observed previously in tailraces of HEPs (e.g. Scruton et al., 2007; see Section 2.5.3.1). On the measurement day, the discharge was sufficiently low for this main jet to be diverted towards the centre of the channel as it approached an area of increased material accumulation and bed elevation approximately 20 m downstream of the scour hole centre. Figure 4-11 shows the magnitude and orientation of the fish pass attraction flow on the right river bank. Figure 4-12d reveals a large vortex close to the fish pass, presumably induced by the plunging flow issued from the fish pass entrance. The jet from the pass entrance developed to a more uniformly directed attraction flow further downstream (Figure 4-12f), where it joined the water jet from the left bank to form a 15 m wide field of water velocity with similar magnitudes and directions.

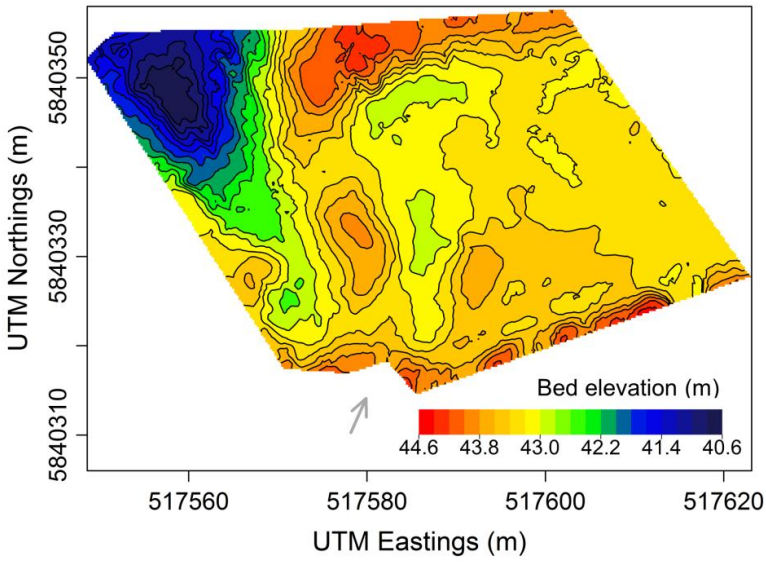

Figure 4-10. Bed elevation downstream of Shrewsbury Weir; the elevation is referenced to the mean sea level as obtained from GPS; the grey arrow points to the location of the fish pass entrance and is orientated perpendicular to the front wall of the fish pass.

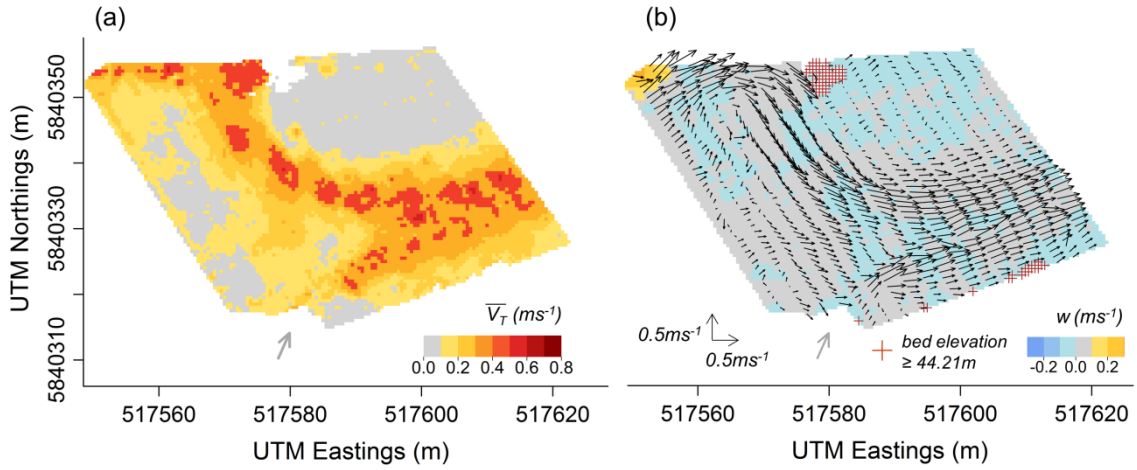

Figure 4-11. Spatial water velocity distribution downstream of Shrewsbury Weir; (a) Magnitude of depth-averaged velocities ($\overline{V_T}$); (b) Streamwise and cross-stream velocities (depicted as arrows) and vertical velocities (w) at an elevation of 44.21 m above the sea level, corresponding to a distance of 0.35 m below the mean water surface elevation of the study area; the grey arrow in both plots (a) and (b) points to the location of the fish pass entrance and is orientated perpendicular to the front wall of the fish pass.

Chapter 7 discusses the potential implications of the quantified flow distribution and near-pass hydrodynamic metrics derived from it to fish pass attractiveness

in more detail. Moreover, it compares these near-pass hydrodynamics with those measured during conditions of medium and high discharge and evaluates the transferability of the suggested methodology for near-pass hydrodynamics quantification to other fish pass sites.

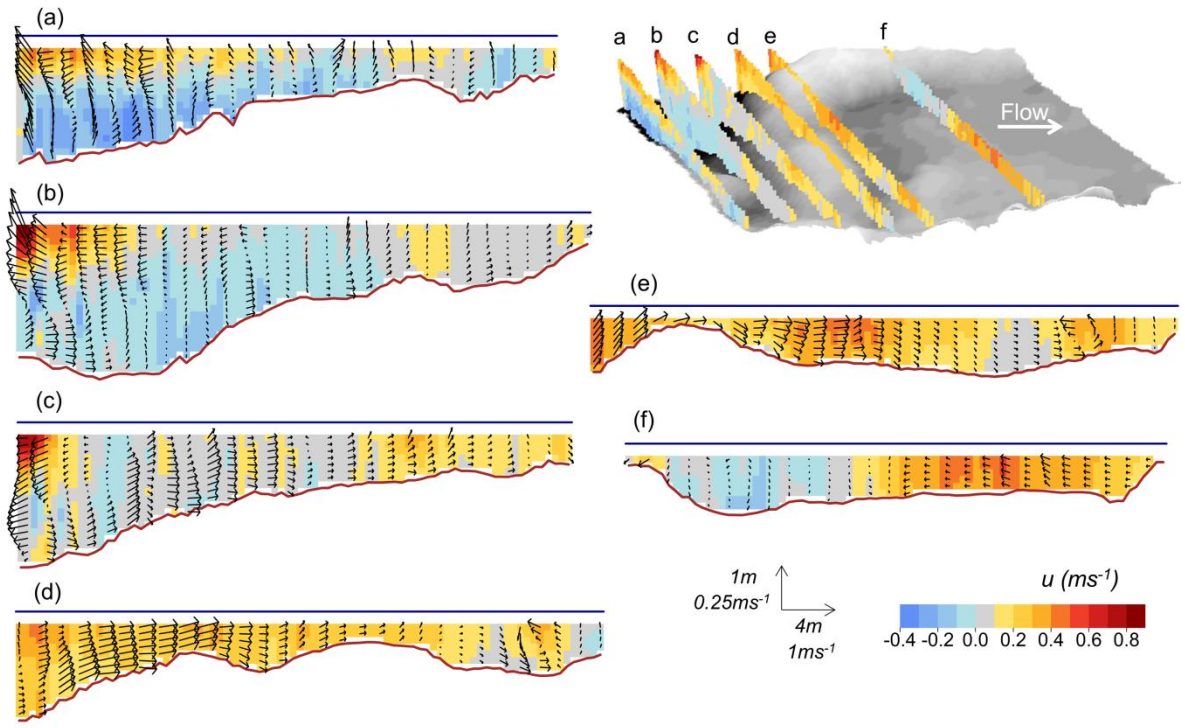

Figure 4-12. Spatial water velocity distribution at selected cross sections downstream of Shrewsbury Weir; the top right plot shows the location of the cross sections on a 3D bathymetric display (see also Figure 4-10) and plots (a) to (f) show the streamwise velocities (u) as well as the cross-stream and vertical velocities (depicted as arrows) of these sections in detail.

4.4 Conclusions

In this chapter, three of the main limitations to the ADCP-based quantification of hydrodynamics near engineered in-channel structures have been addressed. A simple algorithm based on a low-cost IMU was shown to be a suitable solution to correct for ADCP compass errors from magnetic interference and enabled what, to the author's knowledge, is the first study to quantify the magnitude of ADCP compass errors in the field. The unconventional data processing method by Vermeulen et al. (2014) considerably reduced the volume for which spatially

homogeneous flow had to be assumed and was shown to be a viable method for estimating 3D velocities near engineered structures. Finally, the tracking TS was illustrated to provide a suitable solution for localising ADCP data at cm-level 3D accuracy independent from navigation satellites, and for estimating ADCP boat velocities for the recovery of ensembles affected by BT loss.

The suggested techniques were shown to have statistically significant effects on the estimated resultant water velocities and to strongly affect area-weighted measures of vorticity. Moreover, the high relevance of accurate data localisation and compass correction in ADCP measurements near fish passes was underlined by the relatively large number of ensembles affected by BT loss. For these ensembles, the accurate data localisation is required to reliably estimate the boat velocities and the correction of compass errors is essential to avoid potentially large error propagation to the estimated 3D water velocities (see Section 3.4.2).

The integration of the proposed data quality enhancement techniques on an RC ADCP platform enabled the estimation of the 3D distribution of temporally averaged water velocities immediately downstream of a weir with a fish pass. The obtained 3D flow maps were suitable to describe the magnitude and orientation of the fish pass attraction flow in relation to competing flows and to highlight areas of increased vorticity. The derivation of further near-pass hydrodynamic metrics from the estimated velocity distribution and a discussion of their relevance to the attractiveness of the fish pass on site have been provided in Chapter 7.

This study also highlighted further research requirements, some of which have been addressed in the PhD research and presented in the following chapters of this thesis. Alternative approaches to time synchronising the ADCP and TS data are required to prevent restrictions associated with instant wireless data transmission (see Section 7.2.2.4). While the TS is a convenient solution because it is available off-the-shelf and easy to use, the relatively high cost of the device may restrict its wide-spread use in ADCP applications. From this

arises the requirement of assessing alternative, low-cost solutions to ADCP localisation in GNSS-denied areas (see Chapter 5). While in this study the sensitivity of the estimated mean resultant velocities to the inclusion of further repeated transects was relatively low after six transects had been included, the effect may differ depending on the actual turbulence conditions on site. Therefore, this sensitivity analysis has been extended to further sites and the results have been presented in Chapter 7. Moreover, the insensitivity to including further transects does not necessarily mean that the temporally averaged velocity has been quantified accurately so that, ultimately, there is a need to validate the estimated 3D velocities through reference measurements (see also Section 8.5.3). Further research is also required to study the trade-off between the number of transects per section and the density of section spacing as well as their effect on the estimated 3D water velocity distribution (see Chapter 7).

Chapter 5

ADCP POSITIONING NEAR ENGINEERED IN-CHANNEL STRUCTURES: QUANTITATIVE ASSESSMENTS OF SATELLITE-BASED NAVIGATION AND STEREO VISUAL ODOMETRY

Parts of this chapter have been published in *Sensors*:

Kriechbaumer, T., Blackburn, K., Breckon, T.P., Hamilton, O. & Rivas Casado, M. (2015). Quantitative evaluation of stereo visual odometry for autonomous vessel localisation in inland waterway sensing applications. *Sensors*, 15, pp. 31869-31887.

5.1 Introduction

The accurate and continuous ADCP positioning within the river environment is a crucial part of near-pass hydrodynamics quantification. It is required to:

(i) allow for spatial referencing and analysis of the ADCP data and the derived hydrodynamic metrics,

(ii) correct the ADCP measurements for boat velocity in areas of BT loss, and

(iii) enable ADCP platform navigation, i.e. to follow a pre-defined route under guided RC operation or autonomously.

The literature review (Chapter 3) showed that global line of sight positioning through navigation satellites (i.e. GNSS) has been a widely used technique for ADCP positioning in hydrodynamic mapping applications, but is confined by the natural occurrence of bankside vegetation and urban settlement. Given that this problem can be particularly pronounced near fish passes (see Section 3.4.3), it is questionable whether GNSS-based ADCP positioning is sufficiently accurate for near-pass hydrodynamics quantification. The tracking TS was illustrated to be an effective and highly accurate solution to ADCP positioning in GNSS-denied locales (see Chapter 4). However, it is associated with relatively high equipment cost and constrained by the requirement of additional personnel on site for its operation as well as permanent line of sight from the TS to the on-board reflecting target. The identification or development of more practicable (i.e. lower equipment and deployment cost), but yet reliable and accurate systems for ADCP positioning in GNSS-denied locales has been a key challenge, limiting the practicability and transferability of ADCP-based near-pass hydrodynamics mapping.

In this context, the research presented in this chapter contributed to the fulfilment of **objective 3** of this PhD thesis (see Section 1.2):

to enhance ADCP measurements near engineered in-channel structures in terms of accuracy, availability and practicability of sensor deployment

This involved the following **research tasks**:

(i) to review modern technologies potentially suitable for ADCP positioning in hydrodynamic mapping applications near engineered in-channel structures,

(ii) to assess differentially corrected GNSS positioning against the sub-meter accuracy criterion (see Section 3.5.1.2) at a diverse set of fish pass sites on UK rivers,

(iii) to assess the position accuracy of feature-based and appearance-based stereo visual odometry algorithms implemented on an ADCP platform in a typical riverine environment, and

(iv) to identify effective strategies for the enhancement of stereo visual odometry on ADCP vessels by quantifying the error contribution of covariates related to river environment scenery and ADCP platform kinematics.

5.2 Review of positioning technologies

A state-of-the-art review of modern positioning technologies was undertaken to identify systems potentially suitable for ADCP positioning. The technologies have been reviewed in terms of accuracy, practicability of deployment in the context of ADCP application as well as equipment cost (see Table 5-1).

The technologies listed in Table 5-1have been described in more detail in the remainder of this section. Particular emphasis was put on GNSS as the most widely used technique for ADCP positioning as well as camera-based localisation (in the form of visual odometry), as the technique found to be most promising to achieve high accuracy ADCP positioning at low cost in GNSS-denied locales. The positioning performance of tracking TS devices was not covered in this chapter, as it has been evaluated in detail in Chapter 4.

Table 5-1. Overview of selected modern technologies potentially suitable for ADCP positioning

Position fixing technologies	
GNSS	*Pro*: Cm-level accuracy (horizontal) if used in RTK or Post Processed Kinematic (PPK) mode; easy to use and quick setup; modern ADCPs provide GNSS interface for simple integration; *Con*: High cost for geodetic grade RTK GNSS equipment (from ~ £10,000; as of 2015); requirement of line of sight to satellites; prone to errors from signal multipathing near river banks
Tracking TS (see Chapter 4)	*Pro*: Cm-level accuracy (3D); potentially mm-level accuracy at close distances *Con*: High cost (from ~£15,000; as of 2015); line of sight requirement to tracked object; limited recording frequency (up to ~7Hz depending on object distance)
Radio frequency networks	*Pro*: Systems are becoming available off the shelf (Omnisense, 2013) *Con*: 3D position accuracy (Circular Error Probable; CEP) currently limited to 1m for Time Of Arrival (TOA) systems (Omnisense, 2013) and ~3m for systems based on radio signal strength (Peneda et al., 2011); time-consuming setup of fixed beacons distributed evenly around the survey area; line of sight requirement to beacons; limited testing in riverine environment
Dead reckoning technologies	
Camera-based positioning (visual odometry)	*Pro*: Relatively low equipment cost as consumer grade mono or stereo cameras can be used; self-contained on-board system; drift over time can be constrained through "loop-closure" technique, potentially improving accuracy to cm-level; imagery and simultaneously built environment map as a potentially useful by-product for river monitoring purposes *Con*: limited testing in (potentially challenging) riverine environment
ADCP Bottom Tracking	*Pro*: No additional cost as inherent part of ADCP capability; no additional equipment integration *Con*: Occasional loss of BT, particularly near river engineering structures (see Section 4.3.3, Figure 4-9); bias of BT in conditions of non-stationary channel bed
INS	*Pro: C*ontinuous operation without constraints to motion or environment; very high recording rates (>100Hz possible); self-contained on-board system *Con:* fast degradation in accuracy with time; high cost unless (insufficiently accurate) MEMS sensors are used
Integrated navigation systems	
GNSS/INS	*Pro:* Cm-level accuracy possible (if RTK or PPK GNSS used); very high (>100Hz) position recording rates possible; bridges short periods of GNSS loss; *Con*: high equipment cost; dependent on at least regular GNSS availability

5.2.1 Basic categories of positioning technologies

Positioning concerns the basic problem of determining the position of an object (e.g. a sensor or vehicle) relative to a reference coordinate frame, whereby two fundamental methods can be distinguished (Groves, 2008):

(i) position fixing, and
(ii) dead reckoning

In position fixing, the position of an object is determined from range (i.e. distance), bearing (i.e. angle) or range and bearing measurements, relative to one or more reference points with known positions. The position accuracy depends on the errors in the range and bearing measurements and, in most cases, on the distance of the object to the reference points, but is independent from the accuracy of previously determined object positions. Range measurements can be made using electromagnetic waves (e.g. radio signals, lasers or radars). Bearing measurements can be accomplished through compasses, theodolites or inertial sensors. An example for a position fixing device is the TS evaluated in Chapter 4, which determines the 3D position of a tracked object relative to itself (the reference point) based on one range and two bearing measurements about the vertical and one of the horizontal instrument axes.

In dead reckoning, the position of an object at any time is determined as the sum of a series of position changes, after starting from a known position or position fix. Each of the position change measurements is subject to an error, which accumulates over time. The position changes can, for example, be determined based on measurements of the object velocity and orientation. For example, INS systems are 3D dead reckoning systems providing positions by integrating object velocities derived from accelerometer measurements and attitudes derived from gyroscope measurements (see also Section 5.2.4.3). The combined use of position fixing and dead reckoning is referred to as integrated navigation (Groves, 2008).

For meaningful spatial data analyses and vehicle navigation, the measured positions are to be expressed relative to a known coordinate frame, whereby two main frames are distinguished:

(i) the object or vehicle frame, whose position (and sometimes attitude) is described, and
(ii) the reference frame.

The latter is often an Earth-centred frame, describing a coordinate system with defined origin and axes, e.g. the World Geodetic System 1984 (WGS84), so that the object can be uniquely positioned on the surface of the Earth. Unless global positioning devices are used (e.g. GNSS), additional measurements are required to transform the positions (e.g. recorded from a TS or INS) to a coordinate system with an Earth-referenced frame (see for example Section 4.2.2.2)

5.2.2 GNSS

“Global Navigation Satellite Systems“ is a collective term for navigation systems that provide a 3D positioning solution by one-way (passive) ranging using radio signals transmitted by satellites orbiting the Earth (Groves, 2008). The 3D positions are obtained by measuring the range from a ground-based GNSS receiver and antenna to the satellites based on the signal Time Of Arrival (TOA), determined from the receiver clock. Range measurements to at least four satellites are needed to resolve the 3D position; three would theoretically be sufficient to determine the position via trilateration, where the position is at the intersection of three spheres with radii of the respective antenna to satellite distances and the respective satellites located in the sphere centres. A fourth satellite is required to account for the receiver clock offset (El-Rabbany, 2006).

There are currently two GNSS systems with full global coverage, i.e. at least four satellites are visible from any location on the globe:

(i) the GPS (maintained by the US Air Force and globally available since 1994) and

(ii) the system called GLONASS (maintained by the Russian Aerospace Defence Forces and available since 2011).

The following descriptions are focused on the GPS, because it is the most widely used GNSS.

Each GPS satellite continuously transmits at least two microwave radio-signals, termed L1 and L2 with carrier frequencies of 1,575.42 MHz and 1,227.60 MHz, respectively, carrying digital codes (known as Pseudo Random Noise, PRN, codes) and a navigation message (El-Rabbany, 2006). GPS receivers can be categorised into single-frequency (L1) and dual-frequency (L1/L2) devices based on the signals they receive and process. The latter achieve higher accuracies by eliminating most of the range measurement error component stemming from ionospheric signal propagation delays, which depend on the temporary composition of the ionosphere and vary with frequency (see also Table 5-2). Moreover, the receivers differ depending on whether they perform the range computation based on the PRN code(s) or the carrier frequency (sometimes referred to as “carrier phase tracking”). The latter achieves considerably more precise range measurements because the carrier frequency changes phase at a much higher frequency than the PRN codes that are modulated on it, allowing phase shift measurement at finer resolution. The navigation message is modulated on both the L1 and L2 signals and contains, amongst others, information to determine the satellite position as a function of time (termed “broadcast ephemeris”), satellite clock correction model parameters and atmospheric correction model parameters required to account for the atmospheric conditions affecting the signal transmission time and thus the range computation (El-Rabbany, 2006).

5.2.2.1 Range measurement and position errors

The error in the range measurement is the sum of (Groves, 2008):

(i) temporally and/or spatially correlated errors (see Table 5-2),

(ii) signal tracking noise from receiver thermal noise, Radio Frequency (RF) interference, and other sources, as well as

(iii) multipathing errors, where the satellite signal is reflected from the ground, buildings, trees or other objects before reaching the GNSS antenna.

Table 5-2. Typical variation of correlated GNSS error sources over time and space (Groves, 2008; modified)

Error source	Variation over 100 s	Variation over 100 km horizontal separation	Variation over 1 km vertical separation
Ionosphere (uncorrected, i.e. single frequency receiver)	0.1-0.4 m	0.2-0.5 m	negligible
Troposphere (uncorrected, i.e. single frequency receiver)	0.1-1.5 m	0.1-1.5 m	1-2 m
Residual satellite clock	~0.1 m	none	none
Ephemeris	~0.02 m	~0.01 m	negligible

In addition to the errors in the range measurements, the GNSS position accuracy depends on the number of satellites tracked and the signal geometry. Some newer GNSS receivers are capable of tracking both GPS and GLONASS satellites to increase the number of tracked satellites. For optimised horizontal position accuracy, signals from low-elevation satellites and line of sight vectors evenly distributed in azimuth are required. The effect of the signal geometry on the position solution is quantified using the Dilution Of Precision (DOP) concept (Groves, 2008). For example, the effect of the signal geometry expressed as horizontal dilution of precision ($HDOP$) and the uncertainty in the range measurements (σ_r) on the resulting uncertainty in the horizontal position (σ_H) is described as (Groves, 2008):

$$\sigma_H = HDOP * \sigma_r \quad \textbf{(5-1)}$$

Thus, $HDOP$ values ≤1 indicate ideal satellite geometry.

5.2.2.2 Differential GNSS correction

The temporally and/or spatially correlated range measurement errors shown in Table 5-2 can be reduced through differential correction using data from reference or base stations at known locations, whereby the resulting accuracy depends on the age of the differential correction signal and the distance between the base station and the mobile receiver. In the context of this study, two types of differential correction systems have been relevant:

(i) the European Geostationary Navigation Overlay Service (EGNOS), a Space Based Augmentation System (SBAS) providing wide area differential correction data based on a ground-based network of more than 40 sparsely distributed reference stations located mainly in Europe, and four geostationary satellites transmitting the correction data to the GNSS user devices (ESA, 2009); and

(ii) local area differential correction based on correction data from a single nearby base station that is either set up and operated by the user at the study site, or operated by public bodies (e.g. the Ordnance Survey, OS, in the UK) or private commercial suppliers.

GNSS equipment performing carrier phase tracking and differential correction from a local base station are typically referred to as RTK or Post-Processed Kinematic (PPK) GNSS, depending on whether the correction is performed in real-time or during post-processing. The terms DGNSS or DGPS, on the other hand, are sometimes used to refer to equipment using differential correction (from any source), but computing the ranges based on PRN codes.

The GNSS equipment available on the market ranges from single frequency receivers with patch antennas and without any differential correction with position errors of several meters to dual frequency receivers with geodetic grade antennas and RTK reaching cm-level positioning accuracy.

5.2.2.3 GNSS for ADCP positioning

The wide-spread use of GNSS in ADCP positioning has been discussed in Section 3.4.3. The major limitations of this technology are the requirement of line of sight and the relatively high cost for equipment reaching positioning accuracy at cm-level. The results of a detailed field-based assessment of GNSS equipment for ADCP positioning near fish passes have been presented in Section 5.4.1 of this chapter.

5.2.3 Visual odometry

Visual odometry describes the process of estimating the ego-motion of a robot or vehicle using the input of a single or multiple cameras attached to it (Nistér et al., 2004). The incremental pose estimate between camera frames is obtained based on the change in the recorded images induced by motion, and the technique relies on sufficient illumination in the environment, a static, textured scene and sufficient scene overlap between consecutive frames (Scaramuzza & Fraundorfer, 2011). Based on the sensor used, monocular and stereo visual odometry can be distinguished. Here, only the latter was considered because techniques based on a single camera rely on additional measurements, further on-board sensors or motion constraints in order to recover the absolute scale of the camera motion; this is referred to as scale ambiguity problem (Nistér et al., 2004; Scaramuzza & Fraundorfer, 2011). In contrast, stereo vision using calibrated cameras with known baseline (i.e. the distance between the two camera lenses) allows for the extraction of depth information with every recorded frame through triangulation. The existing visual odometry algorithms can be categorised into feature-based (also referred to as “sparse”) and appearance-based (also called “dense”) techniques (Koletschka et al., 2014; Konolige et al., 2007; Scaramuzza & Fraundorfer, 2011).

5.2.3.1 Sparse visual odometry

Sparse visual odometry algorithms estimate camera poses based on the displacement of a sparse set of salient features that are detected and matched

across subsequent images using well established techniques from the domain of computer vision (Li & Allinson, 2008). Sparse visual odometry involves the projection of feature points from the (2D) image domain to the (3D) real world domain. The pose increment between frames is then commonly computed by minimising the differences between corresponding 3D feature locations from subsequent frames (absolute orientation methods), or by minimising the error in the re-projection of the transformed 3D features into the image domain (perspective in *n*-point methods). For robustness against outliers, these optimisation procedures are frequently wrapped into a Random Sample Consensus (RANSAC) scheme (Fischler & Bolles, 1981). Using stereo cameras, sparse visual odometry has been demonstrated on aerial and ground vehicles in a range of settings including outdoor urban environments (Geiger et al., 2011; Kitt et al., 2010; Lemaire et al., 2007; Magnabosco & Breckon, 2013; Warren et al., 2010) and rough terrain (Grimes & LeCun, 2009; Konolige et al., 2007, 2010). For example, on a 9 km long trajectory with a motorcar in rough terrain Konolige et al. (2007) achieved a root mean square error ($RMSE$) in 3D position of 45.74 m (0.49% of the trajectory), which was reduced to 4.09 m (0.04% of the trajectory) by integrating the visual odometry with angular motion estimated from a low-cost IMU.

5.2.3.2 Dense visual odometry

Dense visual odometry avoids the potentially error-prone feature extraction and matching, but instead estimates the camera motion based on a direct model that involves the dense set of pixels for which depth information is available. The underpinning idea of this technique is that after the camera motion from a reference to a target frame, the re-projection of the dense cloud of previously extracted and transformed 3D points to the image plane will yield a deformed or warped intensity image of the target frame. The solution is to find the camera pose increment that minimises a cost function based on the differences between the pixel intensities of the warped target frame and the reference frame. This optimisation has also been described as photoconsistency

maximisation (Steinbrucker et al., 2011). Audras et al. (2011) argued that minimising a cost function that is directly based on the image measurement (pixel intensities) avoids the systematic propagation of feature extraction and matching errors, reducing the resulting drift in the camera pose estimate. Dense visual odometry has found increased application with consumer depth cameras offering co-registered colour and depth imagery (RGB-D) in indoor environments (Audras et al., 2011; Kerl et al., 2013; Steinbrucker et al., 2011), but has also been applied with monocular (Engel et al., 2013) and stereo cameras in urban settings (Comport et al., 2007, 2010). For a 220 m long loop trajectory with a motorcar in a city, Comport et al. (2010) reported an $RMSE$ of 1.37 m (0.6% of the trajectory).

5.2.3.3 Visual odometry in river environments

Previous studies assessing visual odometry in the river environment have been rare and focused exclusively on feature-based techniques with a dominance of aerial vehicles navigating a few metres above the water surface (Chambers et al., 2011; Scherer et al., 2012; Yang et al., 2011). Chambers et al. (2011) and Scherer et al. (2012) proposed the fusion of a classic feature-based technique with inertial measurements from gyroscope and accelerometers and intermittent readings from a GPS device through a graph-based optimisation to correct for unbounded position drift. Although the system was designed with focus on aerial vehicles, tests were conducted on a manned floating platform. They reported a consistent under-estimation of the platform translation (by 10% on average) due to a lack of features at close range; this being a problem that is specific to certain river environments where structure is limited to the river banks. After correcting for this bias, the system (visual odometry, IMU, sparse GPS) was shown to achieve a mean position error of 5 m over a 2 km traverse (Rehder et al., 2012).

Fang & Zhang (2015) emphasised the need for an increased understanding of the effect of covariates related to vehicle kinematics and scenery on the performance of existing visual odometry algorithms, in order to guide the

development of more robust techniques. The challenges to robust visual odometry in the river environment arise from:

(i) a landscape structure that is different to that in indoor settings and urban environments, so that a specific structure of the scenery such as orthogonality constraints and the presence of distinct corner features cannot be assumed *a priori* (Yang et al., 2011), and

(ii) from the platform kinematics, which are specific to the respective survey application and sampling strategy.

The kinematics of ADCP vessels differ from those covered in visual odometry assessment datasets in the automotive context (e.g. Geiger et al., 2012) by the very low speed and large changes in yaw (often with no translational motion) at the beginning and ending of river crossings, e.g. in repeated transect ADCP measurements (see for example Chapter 4). The latter has been shown to be potentially detrimental to the accuracy of feature-based visual odometry due to motion blur and degeneration of the linear system to calculate the fundamental matrix (Fang & Zhang, 2015). Also dense visual odometry has been shown to be susceptible to errors from large camera orientation changes (Comport et al., 2010). Moreover, the sceneries encountered in ADCP surveys can be dominated by feature-rich, but repetitive, vegetated river banks, far-distant features (e.g. with the cameras pointing directly up- or downstream on a wide river), reflections from the water surface, or feature-poor engineered river structures such as piers (see also Figure 5-2).

5.2.3.4 Extension to visual Simultaneous Localisation and Mapping

Visual odometry can be used as the front-end to the visual Simultaneous Localisation and Mapping (SLAM) problem, which involves further refinements of the position estimates (Scaramuzza & Fraundorfer, 2011). SLAM describes the classic problem in the domain of mobile robotics, where a robot builds a consistent map of a previously unknown environment while at the same time determining its own location within this map (Durrant-Whyte & Bailey, 2006). The map consists of landmarks detected from one or more sensors attached to

the robot and the landmark and robot positions relative to each other are estimated incrementally as the robot moves along. Most commonly, active range sensing devices such as laser, LIDAR or millimetre wave radar are used to extract the landmark information (Magnabosco & Breckon, 2013). However, the rapid developments of digital camera technology for the mass consumer market and the associated low hardware cost have triggered much research into *visual* SLAM, where the SLAM landmark information is extracted from optical imagery of one or more cameras, similar to the feature extraction in sparse visual odometry (see Section 5.2.3.1).

The map and trajectory estimation problem is solved either through probabilistic filtering (typically Extended Kalman Filters; EKF) or bundle adjustment approaches (see Durrant-Whyte & Bailey, 2006, and Strasdat et al., 2012, for more details). These techniques can, in some cases, improve the positioning accuracy beyond that achieved through visual odometry alone, but are also more complex, computationally expensive and in some cases less robust (Scaramuzza & Fraundorfer, 2011). Moreover, in visual SLAM, the major drawback of dead reckoning positioning, i.e. the error accumulation over time, can be overcome, through the so called loop-closure technique, where a previously seen scenery is revisited and the drift in position is minimised by integrating this constraint into the environment map and robot trajectory (Cummins & Newman, 2010; Zhang et al., 2015).

Visual SLAM with stereo cameras has been demonstrated to achieve positioning errors of only a few meters over long trajectories (>1 km in some cases), which can be reduced to a few centimetres if the loop-closure technique is implemented (Lemaire et al., 2007; Mei et al., 2009). These results, combined with the low-cost availability of cameras, triggered the detailed assessment of camera-based ADCP positioning presented in this chapter (Sections 5.3.2 and 5.4.2). Visual odometry was implemented in this study, rather than a full SLAM algorithm with loop-closure, because it provided sufficient information to assess the suitability of camera-based positioning in river monitoring, given the potential challenges outlined in Section 5.2.3.3. Moreover, the initial

implementation was intended to inform effective and efficient strategies for further enhancements of camera-based positioning for the specific application of ADCP positioning.

5.2.4 Other positioning technologies

This section covers further modern positioning technologies, whose wide-spread use in ADCP surveys was found to be currently limited by insufficient positioning accuracy, high equipment cost and/or impracticalities of deployment in the river environment.

5.2.4.1 Networks of radio frequency or acoustic beacons

Local networks of RF signal transmitting beacons (or nodes) with known locations can be used to position a mobile node within the network. The position estimates are typically based on distance measurements from the mobile node to the beacons, whereby, broadly, two types of systems can be distinguished:

(i) those that measure the distances based on the TOA of a coded signal, with all nodes in the network having time synchronised clocks (e.g. Omnisense, 2013), and

(ii) those that measure the distances based on the Radio Signal Strength (RSS; i.e. the power present in the received radio signal) of the signal transmitted from each beacon. This technique has been implemented with wireless hardware such as Radio Frequency Identification (RFID) technology (Bekkali et al., 2007; Retscher & Fu, 2010; Ting et al., 2011) and ZigBee (Azenha et al., 2010).

For two main reasons, such RF-based positioning systems have been considered unsuitable for ADCP positioning:

(i) They do not (yet) achieve position accuracies below 1 m (Peneda et al., 2011), not even if integrated with low-cost (MEMS) INS (e.g. (Retscher & Fu, 2010).

(ii) They involve the setup of a relatively large number of fixed nodes, evenly distributed around the survey area, which is time-consuming and not possible at some sites, where access to the river banks is limited. Although, in theory, 3D positions can be obtained from only three distance measurements through trilateration (e.g. Borenstein et al., 1996), a larger number of nodes is required to account for uncertainties in the distance measurements affecting the positioning accuracy.

Similar to RF localisation, networks of acoustic beacons installed on the seabed or on ships are sometimes used to position underwater vessels based on the TOA of the acoustic signals (Paull et al., 2014). The principle is also used to position fish with acoustic tags during fish tracking as part of fish passage research (Piper et al., 2015). The high equipment cost and installation effort make the technique impractical for ADCP positioning, although future research into the simultaneous positioning of sensor platforms and fish using acoustic beacons may be worthwhile, as it would facilitate the simultaneous ADCP-based hydrodynamic mapping and fish tracking (see Section 8.5.3).

5.2.4.2 Bottom tracking

An apparent approach to ADCP positioning is the integration of the boat velocity vectors determined from BT over time (e.g. Jamieson et al., 2013). However, this is not a viable solution in complex hydraulic conditions near river engineering structures, where a large number of ADCP ensembles can be affected by BT loss (e.g. 22.3% of the ensembles in the study presented in Chapter 4).

5.2.4.3 Inertial navigation

The positioning error of INS depends primarily on the accuracy and precision of the inertial sensors used (i.e. three gyroscopes and three accelerometers for a 3D INS; Salychev, 2012). This is explained by the large error propagation from the inertial sensor data to the derived positions, resulting from the requirement

of integrating the gyroscope and double-integrating the accelerometer measurements (Woodman, 2007). Specifically, the gyroscope measurements (angular velocity about the three axes) are integrated once to obtain the object orientation, which is required to project the accelerometer measurements (specific force) onto the global axes of a reference coordinate system. In turn, the accelerometer measurements are integrated twice to obtain velocities and subsequently 3D positions.

Inertial navigation with low (but still unbounded) drift thus relies on higher-grade inertial sensors, such as fibre optic or ring laser gyroscopes, and mechanical or solid-state accelerometers (see Kelly, 1994, or Woodman, 2007, for an overview). These systems are too expensive to be a realistic option in most ADCP river applications (optical gyroscopes cost up to hundreds of thousands of dollars; Paull et al., 2014). Low-cost MEMS inertial sensors (such as those used on the x-IMU introduced in Chapter 4) were found to be insufficiently accurate to keep the drift in position below 1 m during operations for longer than 1 minute (Hasan et al., 2009; Woodman, 2007). Thus, they are not suitable for ADCP positioning, based on the sub-meter accuracy criterion outlined in Section 3.5.1.2.

5.2.4.4 Integrated GNSS/INS

INS are suitable to complement GNSS based positioning or to bridge short periods of GNSS loss, because of their high recording rates (>100 Hz), continuous operation without motion or environmental constraints and relatively low short term noise (Chiang et al., 2013; Groves, 2008). Depending on the accuracy of the inertial sensors, the strategy used to correct for GNSS positioning errors and the integration algorithm, integrated GNSS/INS can achieve positioning accuracies at cm-level, but rely on regular line of sight to a sufficient number of navigation satellites with suitable geometric distribution (see Section 5.2.2). Moreover, commercially available systems (e.g. OXTS, 2015) are associated with relatively high cost.

5.3 Methods

This section outlines the methods of the field-based assessment of GNSS (Section 5.3.1) and stereo visual odometry (Section 5.3.2). The former has been evaluated at a variety of fish pass sites using different GNSS devices and correction strategies to capture a range of possible performances of GNSS in the context of ADCP-based near-pass hydrodynamics quantification. In contrast, stereo visual odometry was assessed in detail at a single site, including a statistical error analysis and explanation, in order to assess the general suitability of this novel approach to ADCP positioning and to guide further enhancements of the technique for this specific application.

Further, the error analyses implemented for the evaluation of GNSS and stereo visual odometry were different. This was due to the fact that the former is a position fixing technique, where each position can be regarded as an independent sample, and the latter is a dead reckoning technique, where the position errors of subsequent samples are strongly related, so that the extent of the error accumulation over time is of particular interest (see Section 5.2.1). Moreover, stereo visual odometry estimates both the 3D position and the camera attitude in 3D space. Although this study was concerned primarily with positioning, the errors in the attitude estimates have been analysed too, as this can inform strategies for the overall error reduction (as outlined in Section 5.4.2.3).

5.3.1 Evaluation of GNSS

5.3.1.1 Study sites

GNSS data have been collected as part of all five ADCP surveys introduced in Section 3.5.2. The GNSS performance depends on the number and distribution of GNSS satellites, which differs depending on the sampling site location on the globe as well as the sampling time. The approach of collecting data at various sites in different locations and at different times was chosen to obtain a comprehensive overview of the GNSS error distributions potentially

encountered near fish pass structures in latitudes similar to England and on small to medium rivers.

The environmental conditions at the study sites during data collection have been shown in Figure 3-9. Throughout this chapter, the ADCP surveys have been referred to by the abbreviations given in Figure 3-9.All study sites had trees or urban settlement on at least one river bank surrounding the survey area. For each study location and data collection time, the number of GPS satellites that could theoretically be tracked (assuming perfect sky view) and their geometric arrangement (expressed as $HDOP$) were computed using the GNSS planning tool by Trimble Navigation (2015, see Table 5-3). During all data campaigns, at least 6 satellites were, in theory, trackable at all times and the median number of satellites was 7 for THEAL and 8 for all other sites. The mean $HDOP$ was close to 1, with deviations from an ideal satellite geometry occurring particularly at SHREW2 ($HDOP$ up to 3.00) and FLATF ($HDOP$ up to 3.50). This information supports the transferability of the findings of this study to other locations on the globe.

Table 5-3. Number and distribution of trackable GPS satellites during data collection campaigns assuming perfect sky view and using an elevation mask of 10 deg (based on Trimble Navigation, 2015)

	Sampling time		**Satellites**			**HDOP**	
	Day	Time (UTC) (hh:mm)	Min	Median	Max	Mean	S.D.
SHREW1	20/08/2014	09:50-16:00	6	8	12	1.04	0.23
SHREW2	25/02/2015	11:20-14:50	6	8	11	1.30	0.61
SHREW3	21/05/2015	12:50-15:00	6	8	8	1.17	0.32
FLATF	04/03/2015	10:30–17:20	6	8	10	1.22	0.55
THEAL	11/08/2015	11:00-14:20	6	7	8	1.08	0.22

5.3.1.2 GNSS devices and correction strategies

The GNSS data were collected from four different GNSS devices in total, covering a variety of GNSS correction strategies (see Table 5-4).

Table 5-4. Overview of GNSS equipment and correction strategies evaluated

	GNSS device	Signals tracked	Correction strategy	Market Price[1]
SHREW1	u-blox NEO 6P with patch antenna	GPS L1	RTKLIB using OS base station data	£150
SHREW2	u-blox NEO 6P with patch antenna	GPS L1	RTKLIB using OS base station data	£150
	Leica Viva GS14	GPS L1/L2, GLONASS	PPK in Leica Geo Office using OS base station data	> £10,000
SHREW3	Novatel OEM615 with Forsberg ReACT antenna	GPS L1, GLONASS L1	SBAS	£1,200
FLATF	u-blox NEO 6P with patch antenna	GPS L1	RTKLIB using OS base station data	£150
THEAL	SonTek RTK GPS with Hemisphere A20 antenna	GPS L1/L2	On-site RTK base station	£8,000

[1] Approximate market prices at the time of this study (2015); actual prices will vary

The u-blox NEO 6P GNSS receiver was chosen because it allowed the recording of raw satellite data that could be post-processed using the open-source software RTKLIB v.2.4.2 (Takasu, 2013). Some studies demonstrated that low-cost L1 GPS receivers can achieve dm-level position accuracies if post-processed in RTKLIB using GNSS correction data provided from own base stations (Takasu & Yasuda, 2008) or public base station networks (Wisniewski et al., 2013). In the UK, a dense network of base stations is provided by the OS with correction data available online. Thus, the use of RTKLIB with OS GNSS correction data has the potential to substantially lower the cost of high-accuracy GNSS-based ADCP positioning (on condition of good sky view to GNSS satellites) and thus overcome one of the main limitations of commercial RTK GNSS solutions (see Table 5-1). The u-blox NEO 6P data were recorded on an on-board laptop with bespoke software written by the author in C++. The raw u-blox NEO 6P data from SHREW1 and SHREW2 were post-processed in

RTKLIB set to kinematic mode (implementing carrier phase tracking), using 1 Hz GNSS correction data from the nearest OS base station, i.e. Shrewsbury (horizontal separation of 1.7 km to the study site). The data from FLATF were post-processed with the same setting, but correction data was obtained from the OS base station in Ardleigh (horizontal separation of 6.3 km).

At the time of the PhD research project, the Novatel OEM615 integrated with a ReACT antenna (Forsberg, 2015) was under evaluation by the EA for the wide-spread use during measurements with the 1,200 kHz RioGrande ADCP, so that this study provided additional information for this purpose. The system applies SBAS differential correction and tracks both GPS and GLONASS satellites, so that it represents an alternative, lower-cost option to the RTK and PPK systems assessed. The GNSS data were collected using the software WinRiver II v. 2.8 (Teledyne RD Instruments, San Diego, CA, USA).

The SonTek RTK GPS (SonTek, 2014a) was selected for evaluation because it was offered specifically for ADCP surveys by one of the main ADCP manufacturers, and thus is used potentially often within the community of ADCP researchers and practitioners. This device included a base station receiver and antenna to provide correction data in real-time. The base station was installed at a fixed location on the shore as recommended by the manufacturer (SonTek, 2014a). The GNSS data were collected using the software RiverSurveyor Live v.3.8 (SonTek/YSI, San Diego, CA, USA).

Finally, the Leica Viva GS14 was used as a high-cost geodetic-grade receiver and antenna reference system, representing the category of most accurate GNSS devices available on the market at the time of this study. The GS14 data were recorded in the proprietary Leica format on a device-internal SD card for PPK correction using the software Leica Geo Office v.8.4 (Leica Geosystems, Heerbrugg, Switzerland) with 1 Hz GNSS correction data from the nearest OS station (Shrewsbury).

5.3.1.3 Data collection

The respective GNSS devices were mounted on an ARC-Boat ADCP platform and their data recorded on an on-board laptop for SHREW1, SHREW2 and FLATF and a laptop on shore with the data being transmitted wirelessly via Bluetooth for SHREW3 and THEAL, respectively. The mean boat speeds were 0.42 ms^{-1} (SHREW1), 0.83 ms^{-1} (SHREW2), 0.75 ms^{-1} (SHREW3), 0.39 ms^{-1} (FLATF) and 0.41 ms^{-1} (THEAL). In all surveys, a Leica NOVA MS50 with tracking TS capability was used to provide “ground-truth” reference positions (see also Section 4.2.2.2). When possible, the GNSS antenna was mounted directly on top of the reflective 360 deg prism tracked by the MS50, and otherwise as close as possible to it, while ensuring that the prism did not block line of sight from the GNSS antenna to navigation satellites (see Figure 5-1).

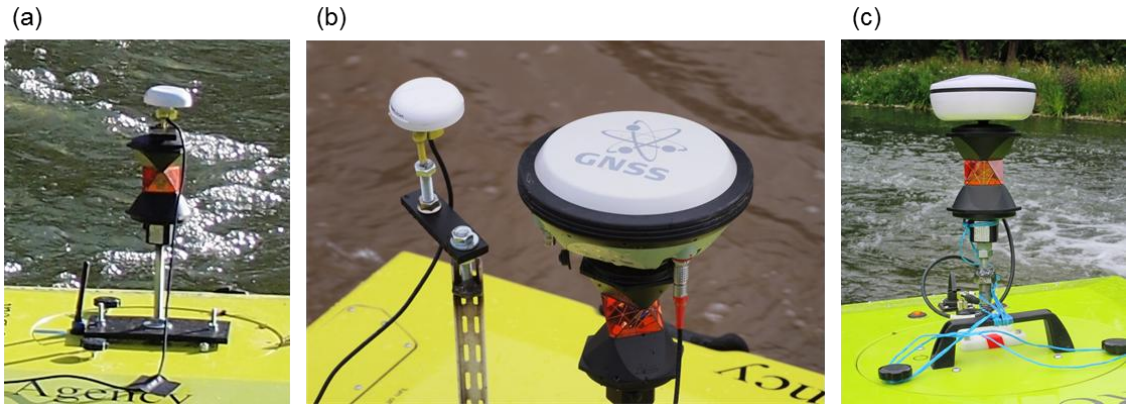

Figure 5-1. Setup of GNSS and TS reference data collection; (a) u-blox NEO 6P as used for SHREW1 and FLATF; (b) u-blox NEO 6P and Leica Viva GS14 as used for SHREW2; (c) SonTek RTK as used for THEAL

The u-blox NEO 6P and SonTek RTK GPS recorded position data at 1 Hz and the Leica GS14 and Novatel OEM 615 at 5Hz. The MS50 data were recorded at an average frequency of 5.4 Hz (SHREW1), 7.5 Hz (SHREW2), 5.6 Hz (SHREW3), 5.4 Hz (FLAT), and 6.4 Hz (THEAL). The GNSS and TS data were time synchronised by logging and time stamping the data from both sensors on the same on-board laptop (for SHREW1; see Section 4.2.2.3) or on two different computers with clocks synchronised to a local GPS-based Network Time Protocol (NTP) server (for SHREW2, SHREW3, FLAT and THEAL; see

Section 7.2.2.4 for more details on this time synchronisation strategy). Based on the time stamps, the GNSS and TS data were temporally aligned during post-processing. Data with a temporal offset above 0.1 s between the GNSS and the TS recorded positions were discarded to limit the error introduced from imperfect time synchronisation. Moreover, only GNSS data that were recorded during the time of actual ADCP data collection (i.e. during ADCP transects measurements) were used in the analysis. To enable comparison between the GNSS and TS position data, they were both transformed into the UTM coordinate system during post-processing. Global reference measurements for the transformation of the TS data were obtained from a PPK GPS device (Trimble GeoExplorer 6000 GeoXH).

5.3.1.4 Validation

The performances of the GNSS devices with the respective correction strategies were quantitatively evaluated based on their position errors along the axes of the UTM coordinate system (ε_m^{GNSS}) computed as:

$$\varepsilon_m^{GNSS} = m_{TS} - m_{GNSS} \qquad \forall m = \{east, north, up\} \tag{5-2}$$

where m_{TS} and m_{GNSS} are the translation parameters measured by the TS and the respective GNSS device, and $\{east, north, up\}$ are the UTM coordinate system axes. The resulting total position error (ε_p^{GNSS}) was quantified as:

$$\varepsilon_p^{GNSS} = \sqrt{\varepsilon_{east}^{GNSS\,2} + \varepsilon_{north}^{GNSS\,2} + \varepsilon_{up}^{GNSS\,2}} \tag{5-3}$$

This error was computed both in 3D and 2D space (denoted $\varepsilon_{p,3D}^{GNSS}$ and $\varepsilon_{p,2D}^{GNSS}$), whereby for the latter, the translation error in the vertical direction was omitted.

In addition to general descriptive statistics (min, max, mean, median and S.D.), the $RMSE$ was computed for $\varepsilon_{p,3D}^{GNSS}$ and $\varepsilon_{p,2D}^{GNSS}$ as a commonly used measure to describe positioning errors:

$$RMSE = \sqrt{\frac{1}{N}\sum_{j=1}^{N} \varepsilon_{p,j}^{GNSS^2}} \quad \textbf{(5-4)}$$

5.3.2 Evaluation of stereo visual odometry

5.3.2.1 Study site

The visual odometry evaluation was based on stereo images collected along a 663 m long trajectory (>15,000 image frames) on a 50 m long reach of the River Great Ouse near Bedford, UK (see Figure 5-2). This site was particularly suitable for the evaluation because it incorporated both engineered river structures (bridges, piers) and more natural, vegetated river banks. Intentionally, a site without a fish pass was selected in order to minimise the complexity of the stereo image frame collection during this first feasibility study. The data collection was undertaken on the 30th of May 2013 at approximately 16:00 UTC, during cloudy weather conditions, a gentle breeze of wind (wind speeds of 3.4-5.4 ms^{-1}) and a visibility of 9 km according to data from the nearest UK Met Office weather station (Bedford). The flow conditions within the survey area were calm with resultant water velocities ranging from <0.01 to 0.24 ms^{-1} and water depths up to 3.72 m based on readings from a 1,200 kHz Rio Grande ADCP.

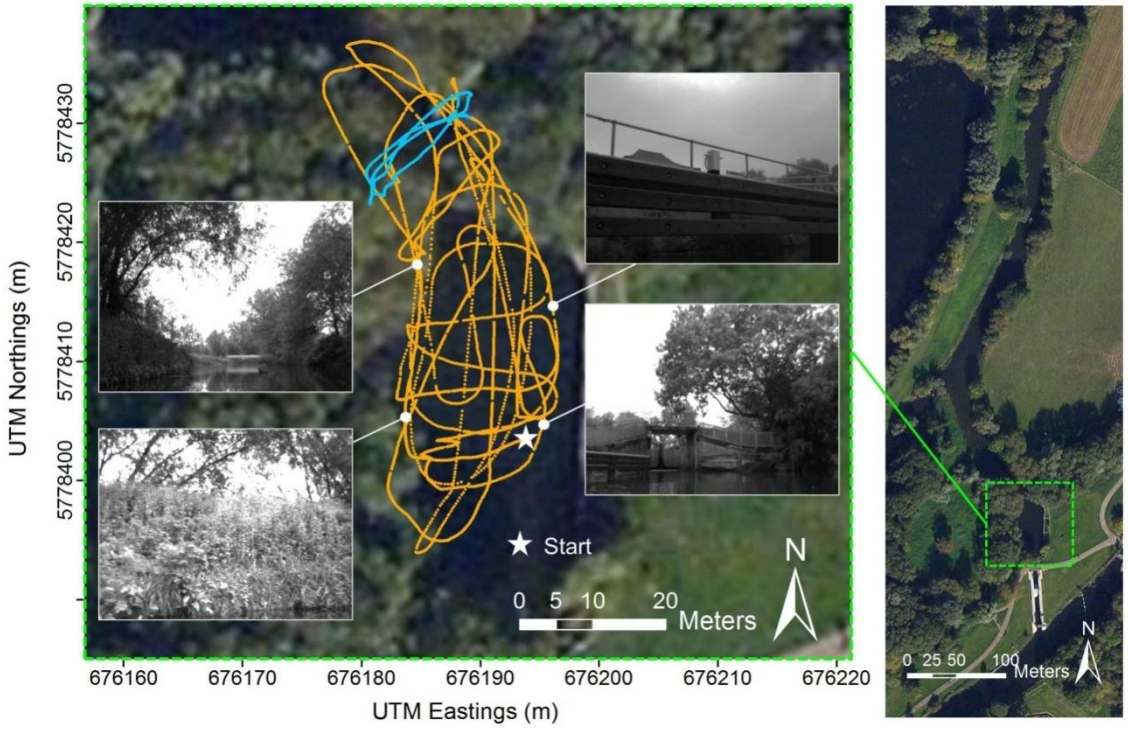

Figure 5-2. Full (orange) and cross-sectional repeated transect measurement trajectory (blue) with exemplary left intensity image samples

5.3.2.2 Data collection

Greyscale stereo image frames were collected with a Bumblebee2 stereo camera (Point Grey Research, 2015) mounted on an ARC-Boat platform. The platform was operated through RC with a mean boat speed of 0.57 ms^{-1} and following a random sampling pattern (see Figure 5-2). The sampling strategy was similar to that implemented by others in single transect ADCP surveys of bathymetry and hydrodynamics (e.g. Tsubaki et al., 2012) and was chosen to cover a variety of scenarios regarding scenery and platform kinematics. Moreover, the trajectory contained a sequence of four consecutive river section crossings (total length of 54 m with a mean boat speed of 0.17 ms^{-1}), representative for a repeated transect ADCP measurement (see, for example, the sampling strategy presented in Chapter 4).

The Bumblebee2 had an image resolution of $1024x768$ pixels and a stereo baseline of 0.12 m. Additionally, the platform was equipped with an x-IMU

inertial measurement unit (see Section 4.2.3.1) to record pitch, roll and yaw around the sensor frame axes in Euler angles, a GPS device to capture GPS performance indicators along the test trajectory, namely $HDOP$ and the number of satellites in view; and a 360 deg prism tracked by a Leica Viva TS15 Total Station (Leica Geosystems, 2015b) placed at a fixed location on the river bank (see Figure 5-3). The manufacturer stated errors (S.D.) of the TS15 were 0.003 m + 1.5 µm m^{-1} for continuous distance measurements to a prism with a maximum tracking distance of 800 m, and 1 arcsecond for angular measurements (Leica Geosystems, 2015b). The data from all sensors were logged and time stamped on the same on-board laptop using software written in C++ and temporally aligned during post-processing. The recording frequencies for the stereo camera, IMU, GPS and TS samples were 8.2 Hz (average), 128 Hz (constant), 1 Hz (constant) and 4.0 Hz (average), respectively, resulting in a total of 7,491 stereo image frames with registered reference positions over the duration of the test sequence. On average, the TS and camera data had a temporal offset of 0.03 s, translating to a mean error in the TS based reference positions of 0.02 m. The temporal offset of the IMU data was negligible due to its high recording frequency. To allow for error analysis, the TS and stereo camera coordinate systems were aligned using the absolute orientation algorithm of Horn (1987).

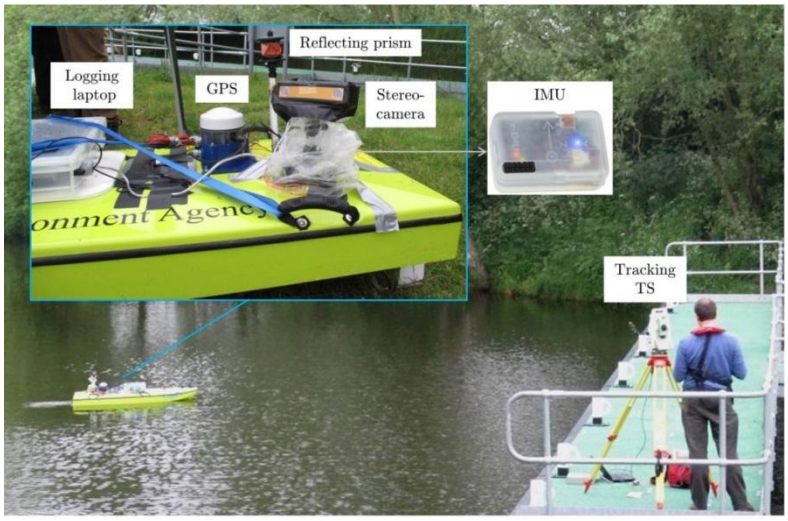

Figure 5-3. Technical setup for the collection of a dataset of stereo image frames; 30/05/2013 at Cardington Sluice on the River Great Ouse near Bedford

5.3.2.3 Visual odometry algorithms

The visual odometry algorithms implemented in this study made use solely of visual data from the stereo rig mounted on the back part of the ARC-Boat and tilted sideward from the platform centre line (line from bow to stern; see Figure 5-3). Two fundamentally different visual odometry approaches were implemented and assessed separately:

(i) a classic algorithm based on the matching of sparse features in left, right and consecutive stereo image frames, that had been shown to achieve high accuracies in urban automotive applications (Geiger et al., 2011) and indoor environments (Fang & Zhang, 2015), and

(ii) an appearance-based algorithm similar to that presented in Steinbrucker et al. (2011) and Audras et al. (2011) for RGB-D cameras.

The inputs to the first algorithm were rectified greyscale image frames from a calibrated stereo camera. Conversely, the input to the second algorithm was stereo depth information, for co-registered greyscale pixel intensity for the scene, recovered over the same rectified image pairs via the Semi-Global Block Matching (SGBM) stereo approach of Hirschmuller (2008). Rectified images were captured directly from the stereo sensor unit based on camera pre-calibration by the manufacturer.

5.3.2.3.1 Using sparse features

The sparse feature-based algorithm used in this study was first introduced in Geiger et al. (2011). Given a pair of stereo image frames with colour brightness (intensity) functions $\left[I^{(l)}\left(p^{(l)}, t_0\right),\ I^{(r)}\left(p^{(r)}, t_0\right)\right]$ and $\left[I^{(l)}\left(p^{(l)}, t_1\right),\ I^{(r)}\left(p^{(r)}, t_1\right)\right]$, where $p^{(l)}$ and $p^{(r)}$ are the pixels in the left and right images acquired at time t, the algorithm estimates the incremental camera motion from t_0 to t_1 in the following consecutive steps:

(i) detection of minimum/maximum blob and corner features in all four intensity images through image filtering with blob and corner masks of

$5x5$ pixels size (see Figure 3 in Geiger et al., 2011), followed by non-maximum and non-minimum-suppression (Neubeck & Van Gool, 2006; see Figure 5-4);

(ii) matching of feature pairs between the intensity images (see Figure 5-4) by comparing the sum of absolute differences of their $11x11$ block windows of horizontal and vertical Sobel filter responses (i.e. the feature descriptor; see Figure 3 in Geiger et al., 2011);

(iii) extraction of the 3D real world position P of feature points in $\left[I^{(l)}, I^{(r)}\right]$ as:

$$P(p) = \left(X(p) = \frac{Z(p).(p_x - c_x)}{f}; \quad Y(p) = \frac{Z(p).(p_y - c_y)}{f}; \quad Z(p) = \frac{fB}{D}\right)^T \qquad \textbf{(5-5)}$$

where X, Y and Z are the real word coordinates relative to the camera reference frame in meters, p_x and p_y are the coordinates of the feature points in the image domain, c_x and c_y are the coordinates of the image centre along the optical axis, f is the focal length of the camera in pixels, B is the stereo baseline in meters and D is the pixel disparity of feature pairs matched between $I^{(l)}$ and $I^{(r)}$; and

(iv) estimation of the rotation R and translation T, describing the incremental camera motion by iteratively minimising the re-projection error e of the extracted 3D feature points into the 2D space of $\left[I^{(l)}, I^{(r)}\right]$ using Gauss-Newton optimisation, with:

$$e = \sum_{i=1}^{N} \left\| p_i^{(l)} + \pi^{(l)}(P_i; R, T) \right\|^2 + \left\| p_i^{(r)} + \pi^{(r)}(P_i; R, T) \right\|^2 \qquad \textbf{(5-6)}$$

(v) whereby here, $p_i^{(l)}$ and $p_i^{(r)}$ are the feature locations in the left and right current images, respectively, and $\pi^{(l)}(P_i; R, T)$ and $\pi^{(r)}(P_i; R, T)$ denote the projection from 3D to 2D space.

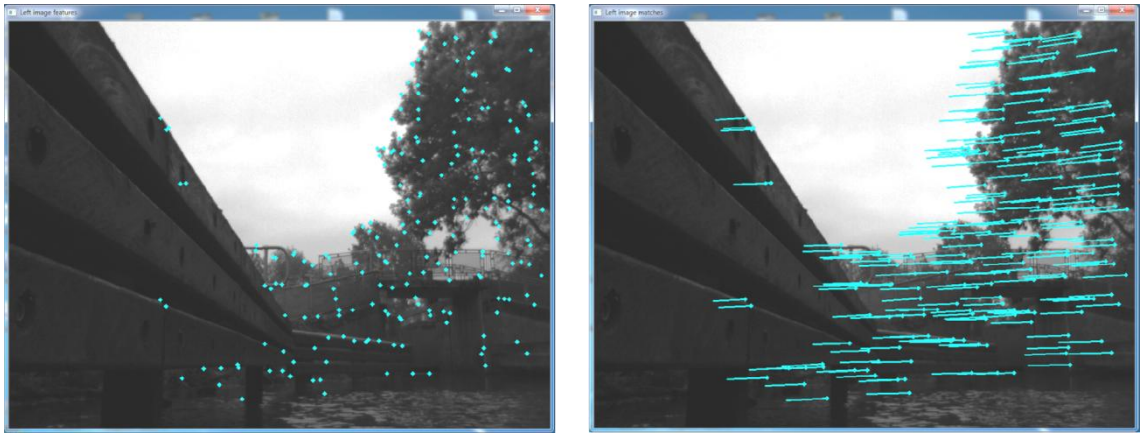

Figure 5-4. Detection (left) and matching (right) of sparse image features after feature reduction through bucketing

Prior to the incremental pose estimation, the number of feature matches per $50x50$ pixel window was reduced to two (bucketing), in order to increase the speed for real-time applications. For robustness against outliers, the minimisation procedure of the re-projection error was wrapped into a RANSAC scheme (Fischler & Bolles, 1981), where the re-projection error was independently estimated 50 times using 3 randomly selected matches, and the matches of the iteration with the most inliers were used in a final optimisation to refine the estimates of R and T.

R and T were expressed as a $3x3$ rotation matrix and a $3x1$ translation vector, respectively, so that the incremental pose estimate became a $4x4$ homogeneous transformation matrix H of the form $H = \begin{pmatrix} R & T \\ 0 & 0 \end{pmatrix}$ and the global camera pose $\widehat{H}$ was updated after each frame (apart from the very first) as:

$$\widehat{H} \leftarrow \widehat{H}H \tag{5-7}$$

Finally, a standard Kalman filter (assuming constant acceleration) was used to smooth the estimated trajectory (Thrun et al., 2005). The state equation was formulated as:

$$\begin{pmatrix} v \\ a \end{pmatrix}^{(t)} = \begin{pmatrix} I & \Delta_t I \\ 0 & I \end{pmatrix}^t \begin{pmatrix} v \\ a \end{pmatrix}^{(t-1)} + \varepsilon \tag{5-8}$$

and the output equation as:

$$\frac{1}{\Delta_t}\begin{pmatrix}R\\T\end{pmatrix}^{(t)} = (I \quad 0)\begin{pmatrix}v\\a\end{pmatrix}^{(t)} + \nu \tag{5-9}$$

where v is the velocity vector $v = (R \quad T)^T/\Delta_t$, Δ_t is the time between frames, a is the acceleration, I is the $6x6$ identity matrix, ε is the process noise and ν is the measurement noise.

5.3.2.3.2 Using dense features

The dense visual odometry technique implemented in this study was based on the work on RGB-D sensors by Audras et al. (2011) and Steinbrucker et al. (2011), and was adapted for the use with optical stereo image frames. As in Section 5.3.2.3.1, the algorithm starts with a pair of stereo image frames with colour brightness (intensity) functions $\left[I^{(l)}\left(p^{(l)}, t_0\right),\ I^{(r)}\left(p^{(r)}, t_0\right)\right]$ and $\left[I^{(l)}\left(p^{(l)}, t_1\right),\ I^{(r)}\left(p^{(r)}, t_1\right)\right]$ and estimates the camera pose increment from t_0 to t_1. A disparity map could be readily obtained from inter-pixel matching of $I^{(l)}$ and $I^{(r)}$. In this study, SGBM (Hirschmuller, 2008) was used due to its superior performance demonstrated in Mroz & Breckon (2012). From this, a dense cloud of 3D Points P was computed as shown in Equation (5-5). Consider the camera motion from the reference frame $I^{(l)}\left(p^{(l)}, t_0\right)$ with corresponding 3D points $P(p, t_0)$ to the target frame $I^{(l)}\left(p^{(l)}, t_1\right)$, expressed as a $4x4$ homogeneous transformation matrix H of the form $H = \begin{pmatrix}R & T\\0 & 0\end{pmatrix}$, where R is a $3x3$ rotation matrix and T is a $3x1$ translation vector. The transformation $G(H, P)$ of the 3D points $P(p, t_0)$ corresponding to the camera motion is:

$$G(H, P) = RP + T \tag{5-10}$$

The transformed 3D points were re-projected to the image domain of the target frame using the projection π:

$$\pi(G) = \left(\frac{G_1 + f}{G_3} - c_x, \frac{G_2 + f}{G_3} - c_y\right)^T \tag{5-11}$$

This yielded a warped intensity image of the target frame, which could generally be described through the so called warping function (Audras et al., 2011) or image warp (Steinbrucker et al., 2011) as:

$$\varpi(p,t) = \pi\left(G\left(H, P(p)\right)\right) \quad \textbf{(5-12)}$$

Using the Levenberg Marquardt (LM) method, the algorithm finds the camera pose transformation H that minimises the non-linear least-squares cost function $E(H)$:

$$E(H) = \sum_{p} [I(\varpi(p,t_1),t_1) - I(p,t_0)]^2 \quad \textbf{(5-13)}$$

A conceptual flow diagram of the dense visual odometry algorithm is given in Figure 5-5.

The optimisation was implemented using a multi-resolution approach as suggested in Comport et al. (2010), where the camera pose transformation was iteratively estimated on the levels of an image pyramid encompassing four image resolutions. The algorithm started with the lowest resolution to obtain a first estimate of H, which was then used to initialise the subsequent minimisation applied to the next highest resolution, and so on, until the resolution of the original images was reached. This approach increased the computational efficiency, because smaller images were used to perform the minimisation for larger frame to frame motion, whereas the minimisation with the larger images served to refine the transformation estimate (Comport et al., 2010). The maximum number of iterations was set to 40, 20, 3, and 1, for the four scales from coarsest to finest. The decimated images were generated using a simple bi-linear interpolation method with scaling factors of 0.125, 0.25, 0.5, and 1, for the four pyramid levels. To eliminate aliasing induced by image re-sampling, the downscaled intensity images were blurred using a Gaussian filter with a kernel S.D. of 3 in the x and y directions.

From the estimated pose increments the global pose trajectory was obtained as in Equation (5-7).

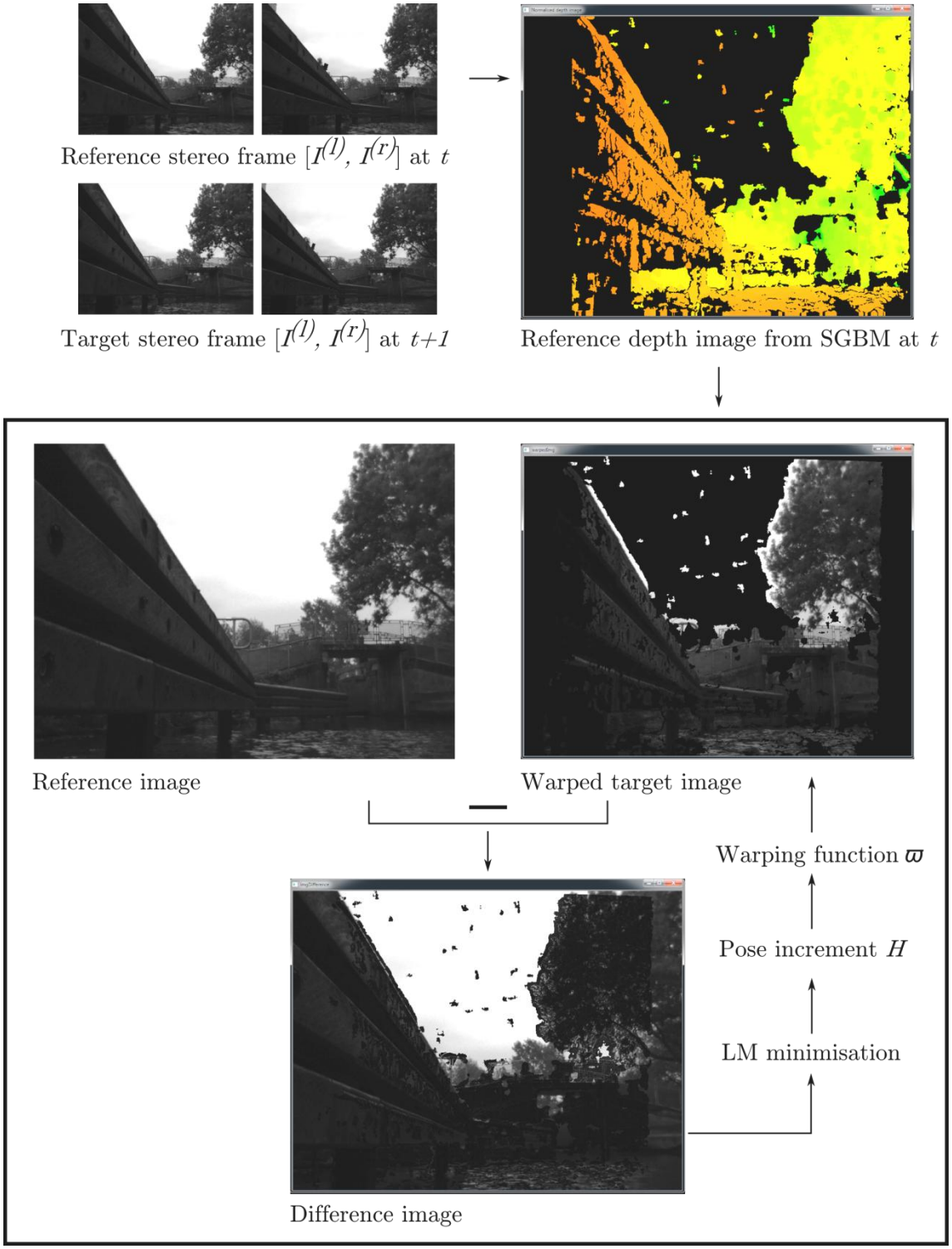

Figure 5-5. Illustration of the dense visual odometry algorithm for the final image pyramid level

5.3.2.4 Validation

Both visual odometry algorithms were quantitatively evaluated regarding their pose estimation accuracy and their robustness for a variety of sceneries and vehicle kinematics. The evaluation approach was based on that in Konolige et al. (2007), who presented a valid framework to separately quantify the random and systematic error components of the 6D pose estimation from visual odometry. The analysis followed an odometry model consisting of translation and angular errors over displacement. The translation errors (ε_m^{VO}) and the angular errors (ε_n^{VO}) were computed as:

$$\varepsilon_m^{VO} = m_{TS} - m_{VO} \qquad \forall m = \{x, y, z\} \tag{5-14}$$

and

$$\varepsilon_n^{VO} = n_{IMU} - n_{VO} \qquad \forall n = \{\phi, \theta, \psi\} \tag{5-15}$$

where m_{TS}, and m_{VO} are the camera translation parameters measured by the TS and estimated through visual odometry, n_{IMU}, and n_{VO} are the rotation parameters measured by the IMU and estimated through visual odometry, $\{x, y, z\}$ are the sensor frame axes (y pointed along the camera optical axis and a right hand coordinate system was followed) and $\{\phi, \theta, \psi\}$ are the pitch, roll, yaw rotations about these axes in Euler angles. The total position error in 3D space (ε_p^{VO}) was computed as

$$\varepsilon_p^{VO} = \sqrt{\varepsilon_x^{VO^2} + \varepsilon_y^{VO^2} + \varepsilon_z^{VO^2}} \tag{5-16}$$

Following Konolige et al. (2007), the test trajectory was divided into 100 consecutive sections of approximately 6.5 m length each. The length of 6.5 m was meaningful given the very low platform speeds and the context of surveying small rivers. For each section, the position drifts in the x, y and z direction and the angular drifts about each of these axes (in Euler angles) were integrated. The errors over displacement (denoted $\varepsilon_m^{VO'}$, $\varepsilon_n^{VO'}$ and $\varepsilon_p^{VO'}$) were computed by

dividing the respective error (ε_m^{VO}, ε_n^{VO}, ε_p^{VO}) at the end of the section by the section length.

A multiple linear regression model was formulated to explain the position error over displacement ($\varepsilon_p^{VO\prime}$) for the sample of 6.5 m long sections indexed by i, using covariates related to scenery and platform kinematics:

$$\varepsilon_{p,i}^{VO\prime} = \beta_0 + \beta_1 v_i + \beta_2 h_i + \beta_3 f_i + \beta_4 d_i + u_i \quad \textbf{(5-17)}$$

where the covariates are:

- v: the section mean of resultant vessel velocity (in ms^{-1}), quantified as distance travelled over time based on the TS measurements;
- h: the section variability in platform yaw (in deg), quantified as the S.D. of the platform yaw measured by the IMU;
- f: the section mean number of inlier feature matches (for sparse visual odometry) or the number of pixels with valid depth information (for dense visual odometry); and
- d: the section mean depth (in m) of matched inlier features (for sparse visual odometry) or the mean depth of pixels with valid depth information (for dense visual odometry).

The partial regression coefficients β_1, β_2, β_3 and β_4 describe the marginal contribution of the associated covariates to variations in $\varepsilon_p^{VO\prime}$ provided that all other covariates are held constant. u is the model error capturing differences in the predicted and observed values (also referred to as residuals) of $\varepsilon_p^{VO\prime}$. The partial regression coefficients were estimated using Ordinary Least Squares (OLS) and the assumptions for linear regression with OLS (i.e. normally distributed residuals $u \sim N(0, \sigma^2)$, uncorrelated and homocedastic residuals and lack of multicollinearity between the covariates) were assessed via residual and correlation analysis. The statistical significance of the coefficients was tested through t-tests ($\alpha = 0.05$) and the overall model validity was assessed through

F-tests ($\alpha = 0.05$). For a detailed outline of multiple linear regression analysis, the reader is referred to Sokal (1994).

Moreover, to evaluate the visual odometry algorithms over longer trajectories, the maximum and $RMSE$ of ε_p^{VO} from all registered position estimates N of the 663 m long trajectory as well as for the sub-trajectory of the cross-sectional repeated transect measurement were computed. The $RMSE$ was computed as in Equation (5-4).

5.4 Results and Discussion

5.4.1 Performance of GNSS

Table 5-5 shows the statistical distribution of the positioning errors for all GNSS devices evaluated and all study sites.

Table 5-5. Positioning errors (in m) of GNSS devices evaluated; *N* stands for the number of registered GNSS and TS samples

		Min	Mean	Median	S.D.	Max	RMSE	N
SHREW1, u-blox + RTKLIB	$\varepsilon_{p,3D}^{GNSS}$	0.10	8.36	5.07	17.11	672.10	19.04	11,159
	$\varepsilon_{p,2D}^{GNSS}$	0.02	6.26	3.37	14.79	650.20	16.06	
	$\varepsilon_{east}^{GNSS}$	-29.99	1.18	0.99	2.97	91.10		
	$\varepsilon_{north}^{GNSS}$	-650.20	-0.32	-0.33	15.74	193.40		
	ε_{up}^{GNSS}	-263.90	-2.59	-1.52	9.90	170.20		
SHREW2, u-blox + RTKLIB	$\varepsilon_{p,3D}^{GNSS}$	0.11	3.27	2.40	2.77	21.32	4.28	1,830
	$\varepsilon_{p,2D}^{GNSS}$	0.02	2.05	1.31	2.14	17.57	2.97	
	$\varepsilon_{east}^{GNSS}$	-8.76	-0.24	-0.19	0.86	3.17		
	$\varepsilon_{north}^{GNSS}$	-17.24	-1.24	-0.73	2.54	15.23		
	ε_{up}^{GNSS}	-18.70	-1.36	-1.03	2.76	18.94		
SHREW2, Leica GS14	$\varepsilon_{p,3D}^{GNSS}$	0.05	0.34	0.32	0.15	1.51	0.37	2,438
	$\varepsilon_{p,2D}^{GNSS}$	0.01	0.33	0.31	0.15	1.04	0.36	
	$\varepsilon_{east}^{GNSS}$	-0.35	0.01	0.02	0.08	0.61		
	$\varepsilon_{north}^{GNSS}$	-1.03	-0.31	-0.30	0.16	0.34		
	ε_{up}^{GNSS}	-1.17	0.05	0.06	0.09	0.51		
SHREW3, Novatel OEM615	$\varepsilon_{p,3D}^{GNSS}$	0.05	2.25	2.25	0.90	11.73	2.43	21,643
	$\varepsilon_{p,2D}^{GNSS}$	0.01	1.68	1.71	0.74	9.29	1.84	
	$\varepsilon_{east}^{GNSS}$	-3.25	-0.85	-0.90	0.48	1.23		
	$\varepsilon_{north}^{GNSS}$	-9.29	-0.58	-1.09	1.44	3.91		
	ε_{up}^{GNSS}	-7.85	-1.20	-1.07	1.04	2.97		
FLATF, u-blox 6P + RTKLIB	$\varepsilon_{p,3D}^{GNSS}$	0.04	3.49	2.23	4.48	82.20	5.68	7,904
	$\varepsilon_{p,2D}^{GNSS}$	0.01	1.96	1.34	2.54	58.56	3.21	
	$\varepsilon_{east}^{GNSS}$	-22.14	0.10	0.03	1.64	19.64		
	$\varepsilon_{north}^{GNSS}$	-58.12	0.61	0.64	2.68	31.12		
	ε_{up}^{GNSS}	-57.69	-1.72	-0.80	4.36	23.12		
THEAL, SonTek RTK	$\varepsilon_{p,3D}^{GNSS}$	1.43	2.40	2.28	0.77	11.07	2.52	7,540
	$\varepsilon_{p,2D}^{GNSS}$	0.89	2.21	2.10	0.76	10.97	2.34	
	$\varepsilon_{east}^{GNSS}$	-4.90	0.38	0.30	0.80	7.51		
	$\varepsilon_{north}^{GNSS}$	-8.27	-2.07	-2.03	0.63	3.18		
	ε_{up}^{GNSS}	-1.46	0.82	0.81	0.44	2.64		

The RTKLIB evaluation did not result in the high accuracies found in previous studies (see Section 5.3.1.2). At all three occasions (SHREW1, SHREW2 and FLATF), the mean and median 3D and 2D position errors of the GNSS strategy involving the u-blox NEO 6P and RTKLIB post-processing were clearly above 1 m. Indeed, the post-processing with RTKLIB did not result in improvements of the unprocessed position data from the u-blox NEO 6P (which recorded SBAS-corrected position data from satellite range computations based on the PRN code). Further position corrections in RTKLIB with data available from the International GNSS Service (IGS), specifically precise satellite clock data, ephemeris, ionospheric model parameters and tropospheric model parameters, did not lead to accuracies better than those prior to post-processing either.

The large errors in the positions obtained with RTKLIB might be explained by a low performance of the cheap patch antenna regarding the filtering of errors from signal multipathing and/or its susceptibility to ambiguity errors in the phase shift resolution of the carrier signal (Takasu & Yasuda, 2008). Further trials with this open-source software are required to assess the position accuracies achieved with GNSS antennas capable of more sophisticated strategies against signal multipathing and other error sources. The relatively low number of satellites used in the RTKLIB position solutions (median of 6, 8, and 7 satellites for SHREW1, SHREW2 and FLATF, respectively) might have been a further reason. The increase in satellites from SHREW1 to SHREW2 indicated an improved sky view, presumably caused by the higher water level (increase by 2.44 m from SHREW1 to SHREW2) and the time of the SHREW2 survey in the winter season when the bankside trees were leafless (see Figure 3-9). This change in the number of satellites was also reflected in the position error, which was considerably lower for SHREW2 than for SHREW1 (see Table 5-5). The problem of a low number of satellites commonly tracked by the base and mobile GNSS device and thus used in the kinematic position solution might be reduced by setting up a base station at the survey site (instead of using the fixed OS base station network)

The Novatel OEM615 achieved a 2D position error with mean (and S.D.) of 1.68 m (0.74 m). The device tracked both GPS and GLONASS satellites and the number of satellites tracked reached from 0 to 16, with a median of 11. In 0.2% of the samples, no position fix could be achieved as the number of satellites tracked was below 4.

The SonTek RTK device showed a 2D position error with a mean (and S.D.) of 2.21 m (0.76 m). The position error had a large systematic component along the north direction (mean of -2.07 m; see below for a discussion of this issue). The relatively large error for an RTK system might, in part, be explained by a generally low number of satellites tracked (ranging from 0 to 9, with a median of 7), a relatively high $HDOP$ with mean (and S.D.) of 1.49 (0.73), and the fact that only 59.9% of the samples were corrected with data from the RTK base station, according to the GPS quality indicators provided in the software RiverSurveyor Live. The remaining 40.1% were differentially corrected based on data provided through EGNOS. For these samples, the number of satellites commonly tracked by the mobile GNSS receiver and the base station might have been too low to provide RTK quality.

The highest accuracies were achieved with the Leica GS14, which showed a mean (and S.D.) 2D position error of 0.33 (0.15 m). However, also for this system, maximum errors (in 2D and 3D) above 1.00 m were found. Those samples with 3D position errors larger than 0.75 m (20 samples in total, corresponding to 0.8%) exclusively occurred very close to the right river bank, where the sky view was constrained by bankside trees (see SHREW2 in Figure 3-9). This was reflected in the relatively high $HDOP$ values for these samples (up to 2.5) indicating a sub-optimal satellite signal geometry, as well as the fact that 17 of these position estimates were based on L1/L2 PRN codes rather than carrier-phase tracking. In total, ambiguity resolutions for carrier-phase tracking failed for 31 samples. These samples were highlighted by the post-processing software and, thus, could easily be removed prior to further data processing to avoid large error in spatial data referencing. After their removal, the maximum

measured 3D and 2D position errors decreased to 0.78 m and 0.78 m, respectively.

All devices evaluated showed systematic errors, i.e. the mean translation errors along the East, North and/or vertical directions were different from zero. This might have been due to a sub-optimal signal geometry caused by the line of sight to satellites being systematically blocked in one direction or by an uneven distribution of GNSS satellites theoretically in view from the survey site at the time of data collection. Another possible source for systematic errors is the transformation of the GNSS- and TS-based positions into the same coordinate system. Table 5-6 shows the 2D and 3D position errors after correcting for the systematic error component and the percentage of samples with position errors below 1 m.

Table 5-6. 3D and 2D positioning errors (in m) of GNSS devices evaluated after correcting for systematic error components

		Min	Mean	Median	S.D.	Max	RMSE	<1m (%)
SHREW1, u-blox + RTKLIB	$\varepsilon_{p,3D}^{GNSS}$	0.22	8.09	4.43	17.00	672.50	18.83	1.1
	$\varepsilon_{p,2D}^{GNSS}$	0.02	6.09	3.19	14.81	649.90	16.01	9.4
SHREW2, u-blox + RTKLIB	$\varepsilon_{p,3D}^{GNSS}$	0.12	2.93	2.26	2.51	21.28	3.86	10.8
	$\varepsilon_{p,2D}^{GNSS}$	0.02	1.89	1.35	1.91	18.55	2.68	35.4
SHREW2, Leica GS14	$\varepsilon_{p,3D}^{GNSS}$	0.01	0.16	0.13	0.12	1.40	0.20	99.7
	$\varepsilon_{p,2D}^{GNSS}$	0.00	0.15	0.13	0.09	0.74	0.18	100
SHREW3, Novatel OEM615	$\varepsilon_{p,3D}^{GNSS}$	0.09	1.63	1.47	0.85	10.60	1.84	19.7
	$\varepsilon_{p,2D}^{GNSS}$	0.02	1.29	.1.11	0.81	8.76	1.52	49.2
FLATF, u-blox 6P + RTKLIB	$\varepsilon_{p,3D}^{GNSS}$	0.07	3.34	2.25	4.21	81.46	5.38	13.0
	$\varepsilon_{p,2D}^{GNSS}$	0.01	1.83	1.23	2.56	59.18	3.15	40.7
THEAL, SonTek RTK	$\varepsilon_{p,3D}^{GNSS}$	0.01	0.66	0.39	0.89	9.28	1.11	84.5
	$\varepsilon_{p,2D}^{GNSS}$	0.01	0.55	0.36	0.86	9.27	1.02	92.5

Standards for the hydrographic surveying of river channels specify a positioning error lower than 1 m, whereby the error is defined as 3 times the S.D. (see Section 3.5.1.2). Assuming an error following the standard normal distribution

(S.D. of 1), this would mean that 99.73% of the measured positions would have to be within a distance of 1 m to the true position. This was achieved by the Leica GS14, but none of the other systems evaluated, also not after correcting for the systematic error component.

Each of the three GNSS evaluation sites had bankside tree cover, blocking the line of sight to GNSS satellites, but allowing for sufficient sky view to obtain GNSS position fixes during all (100% of the GNSS data for SHREW1[5], SHREW2[5], FLATF[5] and THEAL) or nearly all times (99.8% for SHREW3). In contrast, the study site for the stereo visual odometry assessment had a denser vegetation cover on the shore. Based on the GPS performance indicators collected along with the stereo image frames, the number of GPS satellites in view was below 4 during 46.4% of the data collection time, the median number of satellites in view was 4 and for those samples with a position fix, the mean $HDOP$ was 2.8, indicating a suboptimal satellite signal geometry.

5.4.2 Performance of stereo visual odometry

5.4.2.1 Error statistics

Table 5-7 shows the statistical distributions of the 3D position, translation and angular errors over displacement for both visual odometry techniques assessed.

With a magnitude of 0.067 m m^{-1}, the mean position error per metre displacement of the sparse visual odometry technique was almost three times lower than that of the dense technique. The translation errors of both techniques showed a mean very close to zero, suggesting that the error was not systematic over the trajectory distance evaluated. The errors in the estimated pitch and roll were considerable with magnitudes up to nearly 4 deg m^{-1} (for sparse) and more than 8 deg m^{-1} (for dense). Figure 5-6 illustrates the error accumulation over the course of the 6.5 m long sub-trajectories.

[5] based on the GPS data prior to correction with RTKLIB

Table 5-7. 3D position and translation error over displacement (in m m^{-1}) and angular errors over displacement (deg m^{-1}) for sparse and dense visual odometry, computed from $\boldsymbol{n}$ sections of approximately 6.5 m length each

		Min	Mean	Median	S.D.	Max	n
	$\varepsilon_p^{vo'}$	0.004	0.067	0.048	0.060	0.345	
	$\varepsilon_x^{vo'}$	-0.197	0.001	-0.003	0.064	0.229	
	$\varepsilon_y^{vo'}$	-0.180	-0.002	-0.005	0.054	0.209	
sparse	$\varepsilon_z^{vo'}$	-0.117	0.002	0.002	0.033	0.263	
	$\varepsilon_\phi^{vo'}$	-4.16	-0.01	0.07	1.39	3.87	
	$\varepsilon_\theta^{vo'}$	-3.95	0.00	0.03	1.25	3.13	
	$\varepsilon_x^{vo'}$	-3.44	0.03	0.13	0.70	2.24	96
	$\varepsilon_p^{vo'}$	0.007	0.177	0.139	0.149	0.757	
	$\varepsilon_x^{vo'}$	-0.563	0.002	-0.002	0.151	0.564	
	$\varepsilon_y^{vo'}$	-0.755	-0.010	-0.002	0.152	0.505	
dense	$\varepsilon_z^{vo'}$	-0.366	0.005	-0.000	0.089	0.278	
	$\varepsilon_\phi^{vo'}$	-7.10	-0.14	-0.14	2.84	6.54	
	$\varepsilon_\theta^{vo'}$	-8.48	0.10	0.05	2.94	8.46	
	$\varepsilon_\psi^{vo'}$	-5.27	0.23	0.40	1.51	4.20	92

Figure 5-7 and Figure 5-8 illustrate the performance of visual odometry over the 54 m long repeated transect trajectory involving four consecutive river crossings. The trajectory started with a large rotation about the vertical axis to bring the platform into position for the first river crossing. This rapid change in yaw might explain the large error accumulation in both visual odometry techniques at the beginning of the trajectory. At the end of the four crossings, the 3D position estimates of the sparse and dense techniques had drifted by 1.20 m and 4.56 m, respectively, from the TS based ground truth platform position. Given the flat water surface across the measurement section, it is reasonable to take into account only the positions in 2D, in which case the sparse technique achieved an error of 0.81 m at the end of the trajectory and an $RMSE$ of 0.83 m for the full repeated transect measurement track (see Table 5-8).

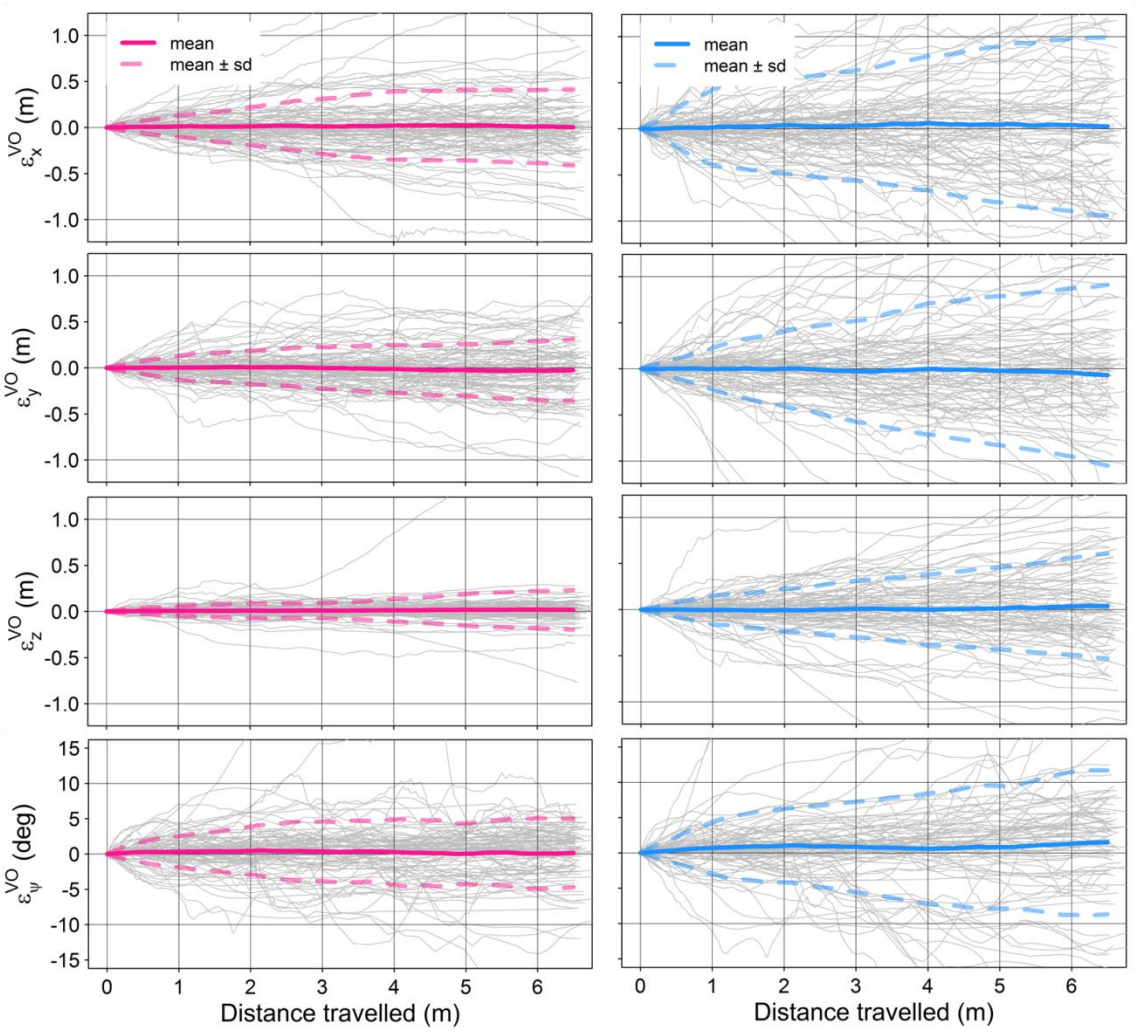

Figure 5-6. Translation and angular errors (shown for yaw only) over a sample of approximately one hundred 6.5 m long trajectories for sparse (left column) and dense (right column) visual odometry

As illustrated in Figure 5-8, both visual odometry techniques kept track of the frequently changing platform yaw, but estimated pitch and roll magnitudes and patterns without apparent relation to the true platform pitch and roll with amplitudes typically $\ll$1 deg (see inlay plot in Figure 5-8). This led to a maximum error in the pitch and roll estimates of 17.78 deg and 13.88 deg for the sparse as well as 45.48 deg and 40.56 deg for the dense technique, over the course of the repeated transect measurement trajectory (see Figure 5-8).

The error statistics for the repeated transect measurement and the full test trajectory are shown in Table 5-8. While the sparse visual odometry technique overestimated the total trajectory length slightly by 14.06 m (2.1% of the true trajectory length), the dense technique resulted in an under-estimation of the trajectory length by 40.70 m (6.1%).

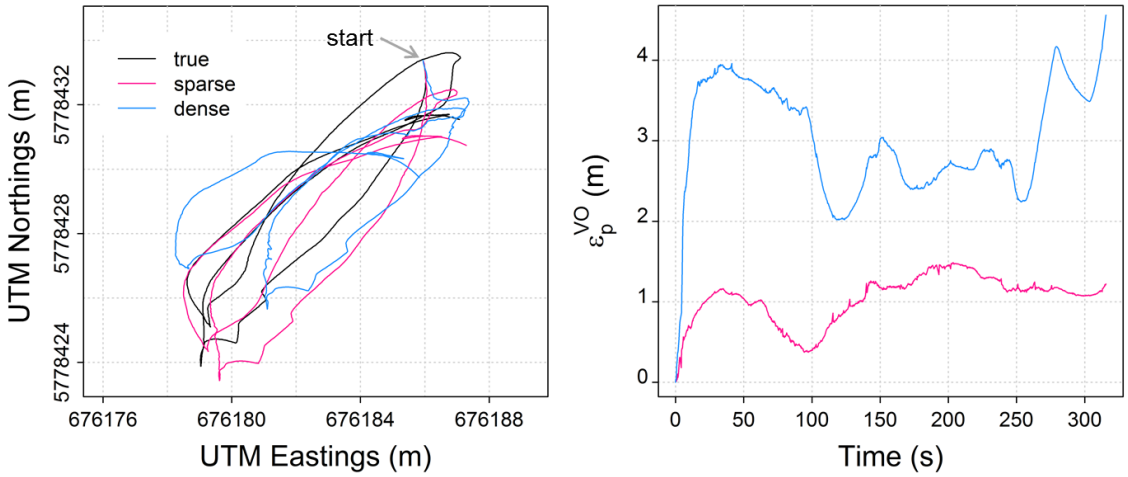

Figure 5-7. Position estimates (left) and accumulation of 3D position error $\boldsymbol{\varepsilon_p^{VO}}$ (right) for a measurement track of four consecutive river crossings

Table 5-8. Distribution of the 3D and 2D visual odometry position error for a measurement track of four consecutive river crossings and the full test trajectory; errors are given in m and % of track length (in brackets); *N* stands for the sample size of registered stereo image frames.

			Mean	Median	S.D.	Max	RMSE	<1m (%)	N
Repeated transects	**sparse**	$\varepsilon_{p,3D}^{VO}$	1.04 (1.9)	1.12 (2.1)	0.30 (0.5)	1.49 (2.8)	1.08 (2.0)	31.6	
		$\varepsilon_{p,2D}^{VO}$	0.78 (1.5)	0.77 (1.4)	0.30 (0.6)	1.22 (2.3)	0.83 (1.5)	68.1	
	dense	$\varepsilon_{p,3D}^{VO}$	3.02 (5.6)	2.88 (5.3)	0.69 (1.3)	4.56 (8.4)	3.10 (5.7)	1.3	
		$\varepsilon_{p,2D}^{VO}$	1.78 (3.3)	1.73 (3.2)	0.76 (1.4)	3.08 (5.7)	1.94 (3.6)	13.2	1,265
Full trajectory	**sparse**	$\varepsilon_{p,3D}^{VO}$	12.25 (1.8)	13.84 (2.1)	5.31 (0.8)	25.01 (3.8)	13.36 (2.0)	2.8	
		$\varepsilon_{p,2D}^{VO}$	8.83 (1.3)	9.43 (1.4)	3.67 (0.6)	18.03 (2.7)	9.56 (1.4)	2.8	
	dense	$\varepsilon_{p,3D}^{VO}$	28.14 (4.2)	28.51 (4.3)	14.12 (2.1)	65.43 (9.9)	31.49 (4.8)	5.2	
		$\varepsilon_{p,2D}^{VO}$	17.14 (2.6)	13.29 (2.0)	13.03 (2.0)	56.83 (8.6)	21.53 (3.3)	6.5	7,491

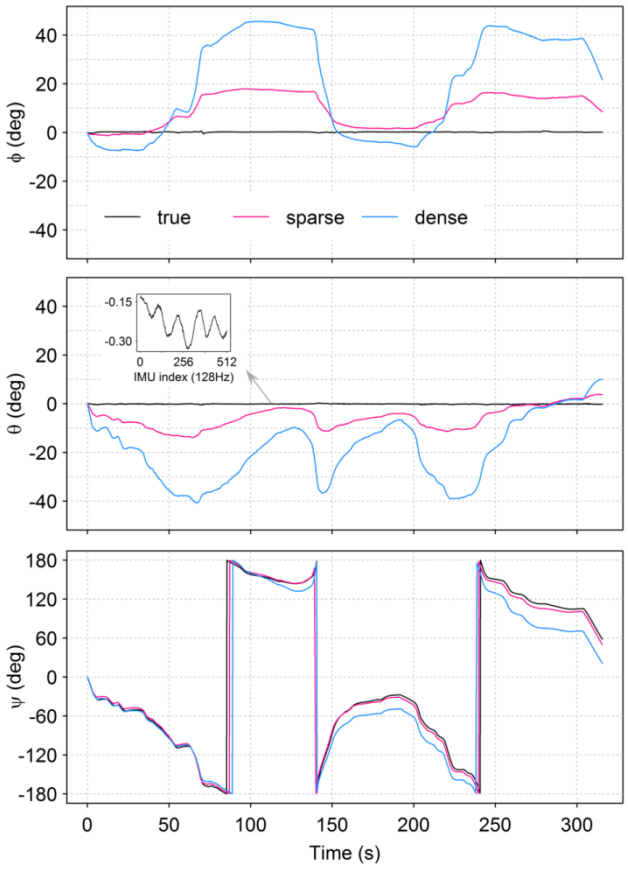

Figure 5-8. Camera orientation estimates in Euler angles for a measurement track of four consecutive river crossings; $\boldsymbol{\phi}$, $\boldsymbol{\theta}$ and $\boldsymbol{\psi}$ stand for pitch, roll and yaw, respectively.

5.4.2.2 Effects of platform kinematics and scenery

The multiple linear regression models explained 56% and 25% of the variability in the 3D position error over displacement for the sparse and the dense visual odometry technique, respectively (see the values of the respective measures of determination, R^2, in Table 5-9). In the case of sparse visual odometry, statistically significant effects on $\varepsilon_p^{VO'}$ were found only for the section variability in platform yaw (h) and the section mean depth of matched inlier features (d) (see Table 5-9). In contrast, the linear model of the dense visual odometry error showed a statistically significant effect of the mean vessel speed (v), but no effect of the platform yaw variability. Here, the effect of d was also significant. The distributions of the covariates are presented in Table 5-10, illustrating the

spectrum of platform kinematics as well as abundance and depths of feature/depth points covered.

The residual analysis revealed evidence for heteroscedastic residuals (all other model assumptions were fulfilled). While this did not affect the unbiasedness of the coefficient estimators, it meant that the t- and F-statistics could not assumed to be exact. This limited the predictive use of the model, but did not compromise the explanatory purpose of the analysis, i.e. to explain the visual odometry errors in order to inform further improvements of the technique.

Table 5-9. Multiple linear regression model coefficients and predictive power for both sparse and dense visual odometry; * marks the statistical significance at $\boldsymbol{\alpha = 0.05}$

		β	t	p-value (t)	F	p-value (F)	R^2
sparse	*Intercept*	$-2.23e^{-02}$	0.82	0.42			
	v	$5.22e^{-04}$	0.04	0.97			
	h	$2.33e^{-04}$	9.53	<0.01*			
	f	$6.84e^{-05}$	1.12	0.27			
	d	$1.46e^{-03}$	2.73	0.01*	28.70	<0.01*	0.56
dense	*Intercept*	$-3.51e^{-02}$	-0.20	0.85			
	v	$1.24e^{-01}$	2.06	0.04*			
	h	$1.39e^{-03}$	1.24	0.22			
	f	$-1.08e^{-07}$	-0.43	0.67			
	d	$9.84e^{-03}$	3.52	<0.01*	7.10	<0.01*	0.25

Table 5-10. Statistical distribution of multiple linear regression model covariates for both sparse and dense visual odometry

		Min	Mean	Median	S.D.	Max	n
sparse	*v* (ms^{-1})	0.10	0.57	0.53	0.37	1.49	
	h (deg)	0.33	17.42	10.45	18.37	75.08	
	f	40	233	238	90	422	
	d (m)	4.13	21.60	20.53	9.30	39.38	96
dense	*v* (ms^{-1})	0.10	0.56	0.53	0.35	1.42	
	h (deg)	0.33	17.79	11.13	18.48	75.08	
	f	306,400	540,700	568,000	88,598	656,400	
	d (m)	6.13	20.75	20.03	7.90	36.85	92

The proportion of variability in the positioning error that remained unexplained by the regression models could be due to model misspecifications (e.g. omitted explanatory variables) or inherent stochasticity in the data generation process of $\varepsilon_p{}'$ (Sokal, 1994). The latter is grounded in the uncertainty of the positions of image points or features, which propagates to the stages of stereo matching and point/feature extraction to 3D, incremental pose estimation and finally the absolute camera pose estimate (Lemaire et al., 2007). Further potential error sources were the absolute orientation algorithm to align the TS and camera coordinate systems (Warren et al., 2010) and the time synchronisation of these two sensors.

5.4.2.3 Enhancing visual odometry for ADCP positioning

The statistical error analysis and the multiple linear regression model informed the effective and efficient enhancement of visual odometry for ADCP positioning. The large errors found in the vessel pitch and roll estimates indicate that techniques such as the integration of on-board inertial sensors would be essential to constrain the estimated platform pitch and roll. Konolige et al. (2007) showed that even low-cost IMUs can improve the position accuracy of visual odometry by more than an order of magnitude.

For sparse visual odometry, the error was shown to increase with the variability of vessel yaw. The 50% of the sub-trajectory samples with the lowest yaw variability showed a mean 3D position error over displacement of 0.032 m m^{-1}, whereas the 50% with the largest variability had a mean error of 0.100 m m^{-1}. This sensitivity was not found for dense visual odometry, where the mean error of samples with large yaw variability (0.194 m m^{-1}) was similar to that for samples with low variability (0.215 m m^{-1}). Those sub-trajectory samples for which the dense algorithm had a lower 3D position error over displacement than the sparse technique (22 in total), were mainly such with a relatively large yaw variability, with 10 of them belonging to the quarter of samples with the largest yaw variability (>25.97 deg). While the dense technique requires further improvement to reduce its position error overall, this contrast in the sensitivity to

yaw variability could be exploited in a hybrid visual odometry technique that switches between sparse and dense algorithm based on platform kinematics. A general improvement of the dense algorithm might be achieved by implementing a quadrifocal geometry model (Comport et al., 2010) rather than assuming that pixel locations in the depth image correspond to pixel locations in the left intensity image of the stereo pair ($p_L \approx p$). Moreover, in contrast to the sparse technique, the dense algorithm did not include a trajectory smoothing Kalman filter, which limited the direct comparison of the two techniques in this study.

The increase of the position error with the distance of objects in view relative to the camera can be explained by the uncertainty in the 3D positions of these objects derived from stereo matching. This uncertainty increases quadratically with the distance and is inversely proportional to the stereo baseline (Hamilton et al., 2013; Lemaire et al., 2007). A larger baseline can reduce this effect, e.g. for a distance of 20 m a baseline increase from 0.12 to 0.50 m reduces the S.D. of the object's displacement error from 0.23 m to 0.06 m, assuming the disparity estimation error empirically found in Hamilton et al. (2013). The under-estimation of the trajectory length as reported in Scherer et al. (2012) was not confirmed in this study, which might be explained by the small scale of the case study site ensuring a sufficient number of features at close range during most times. No statistically significant effect on the error over displacement was found for the number of RANSAC inlier features. The lowest feature number (40; see Table 5-10) occurred when moving along a relatively unstructured pier on site (see the corresponding sample intensity image in Figure 5-2). Even there, the position error was not found to be increased relative to the mean position error. Moreover, there was no evidence of large errors caused by violations of the static scene assumption (e.g. moving animals or vegetation).For the specific conditions during the test data collection, the RANSAC-based detection of outlier feature matches and the simple Kalman filter were sufficient to overcome these potential error sources. Further studies are required to assess the effect of windier conditions causing a more dynamic

scenery and larger turbulence causing higher vessel pitch and roll amplitudes on the visual odometry performance.

Further attempts to improve visual odometry for ADCP positioning should focus on the integration of a low-cost IMU (such as the x-IMU used in Chapter 4) to constrain drift in pitch and roll. Moreover, the sensitivity difference of sparse and dense visual odometry to variability in yaw revealed in this study can be exploited to reduce the effect of this significant error source in camera-based ADCP positioning. Based on the literature review, the position error could be reduced further by implementing the loop-closure technique (see Section 5.2.3.4), which might prove particularly useful in repeated transect measurements, where the same scenery is encountered with each transect repetition. Other potential error sources, such as dynamic scenes and feature-poor river structures, were shown to be less problematic when using the outlier detection (RANSAC) and incremental pose estimation techniques of the sparse visual odometry algorithm implemented in this study.

5.4.3 Implications on vessel-based river monitoring

This study showed that GNSS-based ADCP-positioning on sites with constrained line of sight to navigation satellites relies on high-cost geodetic grade receivers and antennas if positioning accuracies within the sub-meter criterion are to be achieved. However, also dedicated RTK GPS devices were shown to suffer from large errors if conditions differ from ideal. At the study site near Theale with continuous tree vegetation on one bank, degradations in the precision of RTK GPS by more than an order magnitude below the manufacturer-stated performance were measured (SonTek, 2014a states a precision of ±0.03 m under ideal conditions for the SonTek RTK GPS device evaluated). More detailed evaluations are required to relate the site characteristics (in terms of theoretically trackable satellites, their distribution at the measurement time and signal masking by bankside objects) to the performance of PPK / RTK GNSS devices. This would facilitate the prediction of

the GNSS performance at a particular site and thus inform the need for alternative positioning systems.

The results of the stereo visual odometry assessment indicate that camera-based positioning can become a useful technique for localising ADCP platforms and other river monitoring vessels in GNSS-denied areas. Over short trajectories, such as repeated cross-sectional transects in relatively small rivers, a classic feature-based algorithm using an off-the-shelf stereo camera was shown to achieve an $RMSE$ 2D position error below 1 m (see Table 5-8). The visual odometry techniques assessed require further improvements to limit the accumulation of the position error in surveys involving longer trajectories.

5.5 Conclusions

This chapter covered the assessment of various GNSS devices and correction strategies at a range of fish pass sites in the UK and, what to the author's knowledge is, the first implementation of camera-based positioning on a typical river survey vessel and in the context of ADCP measurements. Despite its wide-spread use in ADCP-based hydrodynamic mapping, the position accuracy of GNSS was shown to degrade below manufacturer-stated accuracies at typical fish pass sites on small to medium rivers with bankside tree cover confining the line of sight to satellites. Only one of the two systems marketed as PPK / RTK devices met the sub-meter accuracy criterion defined in hydrographic surveying standards. Positioning with on-board cameras in the form of visual odometry or visual SLAM was identified to be a promising technique to achieve sufficient positioning accuracy at low equipment cost in GNSS-denied locales. Its application on ADCP platforms was demonstrated to involve particular challenges, with the position error being driven by variation in platform yaw and the depth of features in the scenery relative to the camera. Moreover, large errors were encountered in the platform pitch and roll estimates. These findings enable the design of effective strategies to enhance stereo visual odometry algorithms for the specific application of vessel-based river monitoring. In

particular, the integration of a low-cost IMU to constrain drift in pitch and roll, and the hybrid application of sparse and dense visual odometry algorithms to reduce the susceptibility to platform yaw are promising solutions and subjects for further research. In the short term, more expensive solutions, such as the tracking TS (see Chapter 4) are necessary to achieve cm-level ADCP positioning in near-pass hydrodynamic mapping applications at sites without optimal conditions for GNSS.

Chapter 6

DEVELOPMENT OF A SMALL-SIZED ADCP PLATFORM WITH INTEGRATED PROPULSION CONTROL AND DATA LOGGING SYSTEM

6.1 Introduction

Mobile ADCP measurements for hydrodynamic mapping applications rely on the availability of an ADCP vessel that allows for high operator safety, the effective and efficient implementation of pre-defined sampling strategies and the minimisation of vessel-induced data errors. The literature review (Chapter 3) identified a lack of ADCP platforms incorporating on-board systems for the time-synchronised data logging from multiple sensors and integrated propulsion control. As outlined in Section 3.4.4, these platform capabilities are required to implement some of the techniques proposed for increased robustness against ADCP data errors and to facilitate the accurate implementation of sampling strategies via autonomous platform control features. Furthermore, there has been a lack of small-sized RC platforms, which would enable single-person deployment and thus make ADCP-based near-pass hydrodynamics quantification considerably more practicable to implement, particularly at fish passes on small rivers.

The research presented in this chapter contributed to the fulfilment of **objective 3** of this PhD research (see Section 1.2):

to enhance ADCP measurements near engineered in-channel structures in terms of accuracy, availability and practicability of sensor deployment

This involved the development of a small-sized ADCP platform with integrated control and data logging system, covering the following **research tasks**:

(i) to identify a platform hull and propulsion system that reduce vessel-induced errors in ADCP data and ensure high operator safety,

(ii) to identify a low-cost system enabling the logging of multiple on-board sensor data and the autonomous platform operation via integrated propulsion control,

(iii) to design and build platform hardware and software based on (i) and (ii), and

(iv) to test the developed platform at various sites and assess its in-field performance in terms of stability and manoeuvrability on the water.

All platform engineering tasks ranging from hull crafting to electronic wiring and microcontroller programming were conducted by the author. A platform size allowing for single-person deployment and a maximum speed of at least ≈3 ms^{-1} were the only design restrictions provided by the project sponsor.

6.2 Methods

6.2.1 Hull form assessment and design

The hull form selection was based on an evaluation of fundamental platform layouts in terms of resistance to forward motion in the water and stability. The resistance was chosen as a design criterion because it affects the maximum platform velocity and the platform efficiency in terms of battery usage. If used for near-pass hydrodynamics quantification, these features determine the platform applicability at sites with high water velocities near the fish pass entrance or migration barrier and the survey area that can be covered with limited power resources (see also Chapter 7). Large platform stability, on the other hand, is important to reduce pitch and roll of the ADCP. These can cause position errors in the radial velocity measurements as well as errors in the measured river depths, particularly if fast pinging measurement configurations are employed (Mueller et al., 2013; Woodgate & Holroyd, 2011).

The following basic layouts were considered (see Figure 6-1 and Table 6-1): trimaran, triangular-shaped mono-hull, rectangular mono-hull, square-shaped mono-hull and circular mono-hull. The first three of these alternatives were included based on the hull forms of the ADCP platforms marketed at the time of this study (see Figure 6-2). The latter two were included because of their presumably large stability against platform roll and minimal alignment with the direction of water flow in the river, potentially supporting platform control in complex hydraulic conditions.

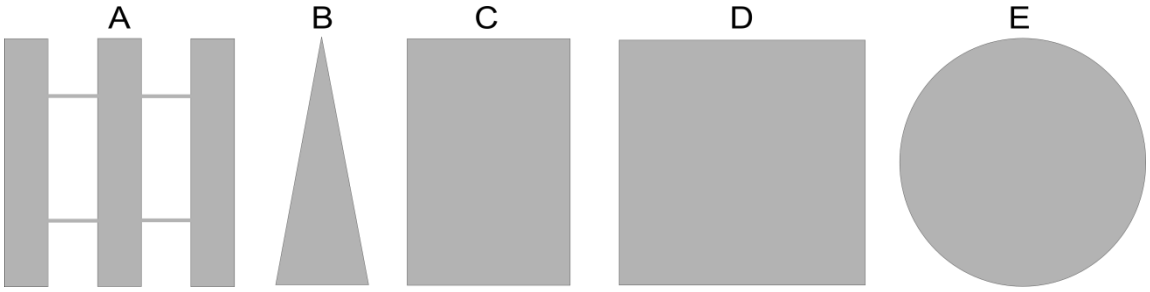

Figure 6-1. Basic platform hull form alternatives; the capital letters have been used throughout this chapter to refer to the respective platform hull forms.

In the absence of a towing tank facility, basic design formulae and appropriate simplifying assumptions were used in the resistance and stability evaluation. Table 6-1 shows the hull form dimensions assumed in this evaluation, whereby the hull lengths were based on that of a benchmark tethered ADCP platform (i.e. the TorrentBoard by YSI/Sontek; see Figure 6-2).

Table 6-1: Dimensions of hull form alternatives considered in the assessment; the capital letters denominating the hull form alternatives refer to those shown in Figure 6-1.

	Hull form alternatives				
Dimensions	A	B	C	D	E
Length on water line (m)	1.05	1.05	1.05	1.05	1.05
Total beam (m)	1.05[a]	0.39	0.65	1.05	1.05
Height (m)	0.18	0.18	0.18	0.18	0.18
Total weight including ADCP (kg)	15	15	15	15	15

[a] For each of the three hull components of alternative A, a width of 0.18m was assumed.

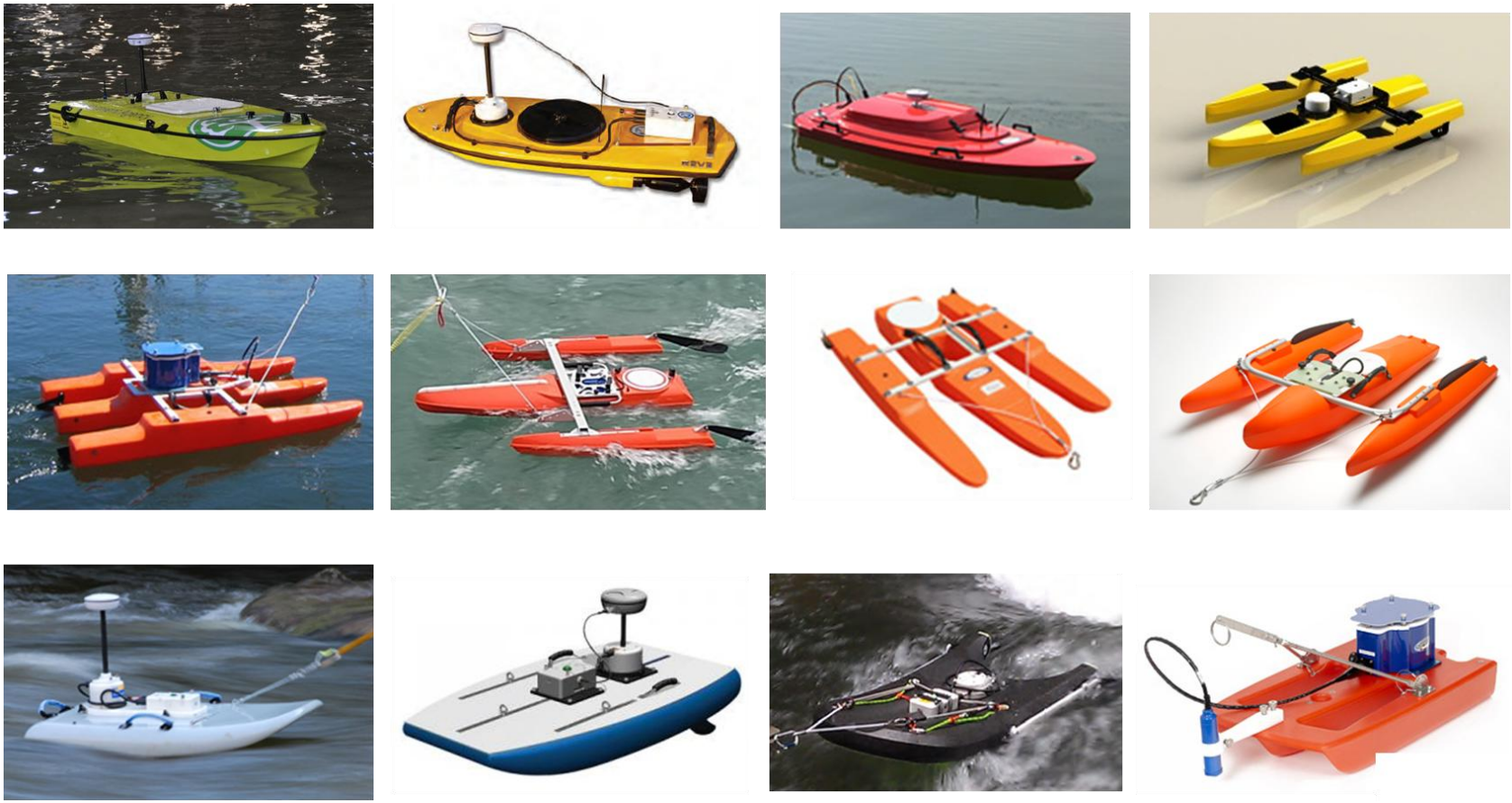

Figure 6-2. Examples of RC and tethered ADCP deployment platforms available on the market as of January 2013; top row from left to right: ARC-Boat (HR Wallingford, 2015), R2V2 (Xylem Analytics UK, n.d.), Q-Boat 1800(P) (Oceanscience, 2011b), Q-Boat 1550T (Oceanscience, 2011a); middle row from left to right: Riverboat SP (Oceanscience, 2011c), High-Speed Riverboat (Oceanscience, 2011d), Riverboat (Oceanscience, 2011e), RiverRay Trimaran (Teledyne RDI, 2009b); bottom row from left to right: TorrentBoard (YSI/Sontek), HydroBoard (SonTek, 2014a), HydroBoard II (SonTek, 2014a), StreamPro Boat

6.2.1.1 Platform resistance

The resistance of the ADCP platform determines the required capacity of its propulsion system, whether used to produce motion in calm water or to counteract flowing water to maintain a static position. Based on the concept of resistance decomposition, the total resistance (R_T) of the platform in calm water can be decomposed into frictional resistance (R_F), viscous pressure resistance (R_{PV}), and wave resistance (R_W) (Larsson & Baba, 1996; Schneekluth & Bertram, 1998):

$$R_T = R_F + R_{PV} + R_W \quad \textbf{(6-1)}$$

Note that the resistance against the air was considered to be negligible due to the low height of ADCP platforms above the water.

6.2.1.1.1 Frictional resistance

The interaction between the wetted platform hull surface and the water causes the formation of water layers with different water velocities. This results in shear stresses, which, in sum, constitute the frictional resistance of a hull. Thus, for a given platform speed, the frictional resistance depends largely on the wetted surface area of the hull. In this study, the frictional resistance was computed as (Bertram, 2000):

$$R_T = C_F * {}^{1}/_{2}\,\rho {B_T}^2 S \quad \textbf{(6-2)}$$

$$C_F = \frac{0.075}{(log_{10}R_n - 2)^2} \quad \textbf{(6-3)}$$

$$R_n = \frac{B_T L}{\vartheta} \quad \textbf{(6-4)}$$

where C_F is the frictional resistance coefficient, ρ is the water density, B_T is the platform speed relative to the water, S is the wetted platform surface in calm water, R_n is the Reynolds number, L is the platform length and ϑ is the kinematic viscosity of water.

6.2.1.1.2 Viscous pressure resistance

The flow field induced by the water-platform interaction causes a reduction in the pressure supporting forward motion in the aft part of the hull, referred to as viscous pressure resistance (Bertram, 2000). To estimate the viscous pressure resistance, the form factor approach suggested by Alte and Baur (1986, cited by Schneekluth & Bertram, 1998) was chosen. It considers the viscous pressure resistance to be a function of R_F:

$$R_{PV} = kR_F \tag{6-5}$$

$$k = 14\left({\nabla}/{L^3}\right)\left({B}/{T}\right) \tag{6-6}$$

where k is a form factor, ∇ is the displacement volume of the hull, L is the hull length, B is the hull beam and T is the draught.

6.2.1.1.3 Wave resistance

The resistance from the wave systems created by the hull-water interaction is usually determined from model tests in a towing tank, and is too complex to be estimated based on simple design formulae (Bertram, 2000). Therefore, this resistance component could not be taken into account in the hull form comparison.

6.2.1.2 Platform stability

The stability against roll of all hull forms considered was assessed through righting moment curves. These describe the tendency of the platform to restore its original attitude after it has been tilted by an external force in flat water and are a typical stability indicator used in ship hull design (Moore, 2010). The stability against pitch was not considered to be a distinguishing criterion because the hull form alternatives had the same length and weight distribution.

In the so called equilibrium position, the platform centres of gravity and buoyancy are located along the same vertical line and the platform will not rotate unless an external force is imposed on it (see Figure 6-3). A slight

clockwise rotation from this position will cause the platform centre of buoyancy to move to the right resulting in a righting moment RM that tends to move the platform back into its original position (Moore, 2010):

$$RM = \overline{GZ}\Delta \tag{6-7}$$

where the distance $\overline{GZ}$ is the righting arm (see Figure 6-3) and Δ is the weight of the displaced water, which is approximately equal to the platform weight. A larger righting moment means that the platform has a stronger tendency to restore its equilibrium position after it has been tilted.

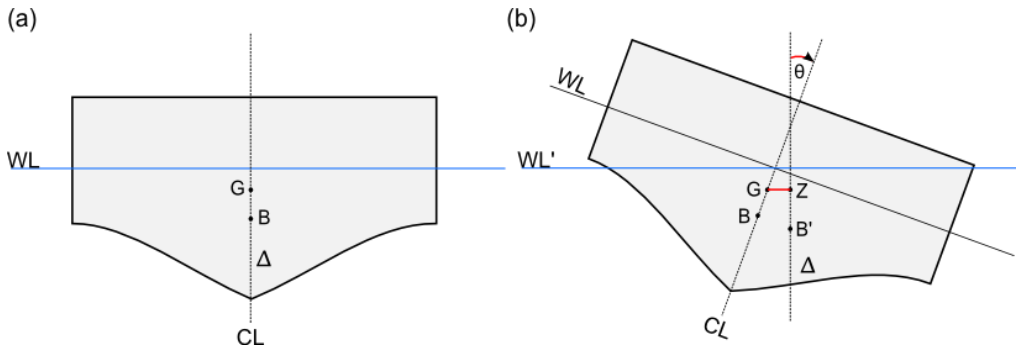

Figure 6-3. Righting arm resulting from platform tilt (based on Moore, 2010); (a) Platform in equilibrium position; (b) Slightly tilted platform; WL, G, B, Δ, CL, θ, and B' stand for water line, centre of gravity, centre of buoyancy, weight of displaced water, hull centre line, roll angle, and centre of buoyancy after platform tilt, respectively. The distance $\overline{\mathbf{GZ}}$ denotes the righting arm.

The righting arm curve shows the relationship between RM and the inclination angle (Moore, 2010). Righting arm curves were computed for the hull form alternatives B to E (see Figure 6-1) for roll angles up to 10 deg using the software tool by Lovett (2004). A uniform gravitational field (i.e. the centre of gravity equals the centre of mass) and a uniform platform density (i.e. the centre of mass is located at the centroid of the hull) were assumed in the computations to avoid the requirement for more sophisticated specialist software. Such software would have been required also to compute a righting moment curve for hull form A (trimaran), but was beyond the scope of this study.

6.2.1.3 Hull materials and design details

To support platform modifications in response to findings from field tests, the hull was built from low-cost, easily workable materials; specifically a polyethylene board reinforced with aluminium sheets and angles, and carved blocks of polyurethane for additional buoyancy. For increased robustness against damage, the polyurethane blocks were coated with body filler, and for improved visibility on the water, the hull was coated with yellow aerosol cellulose paint.

To prevent the platform alignment with the direction of the flow, a flat hull design was initially chosen. During platform field tests (see Section 6.2.4), the low platform yaw stability associated with the flat hull was found to complicate operation during cross-sectional measurements in straight channels. In this ADCP application, a certain degree of alignment with the flow is desirable as it facilitates heading holding during so called “ferry gliding” operation, where the platform bow is pointed upstream and slightly rotated towards the targeted river bank, causing the platform to smoothly travel side-wards and across the river using the force of the water flow. Consequently, optionally attachable and height-adjustable fins from polyethylene were added to the platform prototype. These enable the user to adjust the platform yaw stability depending on the site conditions and ADCP application.

The propulsion system components and the propulsion control and data logging system were mounted on the hull within separate aluminium and ABS plastic enclosures with an Ingress Protection (IP) rating of at least IP67 for water proofing. This modular platform design was chosen to facilitate prototype modifications as well as relatively inexpensive component replacement in case of damage. A hole with a diameter of 0.24 m was carved into the hull and reinforced with a polyethylene pipe, allowing for the platform to carry the most dominant ADCPs for river measurements on the UK and US market (see Section 3.2.7).

6.2.2 Propulsion system selection and design

The main parts of the platform propulsion system were two forward thrusters and a stern thruster, electric motors with a water-cooled Electronic Speed Controller (ESC) each as well as a total of three batteries. Two horizontally separated and independently controlled waterjets were used to achieve the required forward thrust (see Section 6.2.2.2) and to increase platform manoeuvrability by means of differential thrust. Given the small platform size, most propulsion system components were available from the model making market.

6.2.2.1 Waterjets versus propellers

At the time of the PhD research, all marketed RC ADCP platforms identified in the review (see Section3.2.8) were propeller-driven. Propellers bear safety risks to platform operators and increase the platform draught, which complicates launching and operation in areas of very shallow water. In an attempt to overcome these limitations, waterjets were selected for the platform prototype, specifically two Graupner jet drives 2340 with an impeller diameter of 0.04 m. The sufficiency of their forward thrust in relation to the estimated platform hull resistance was tested in a laboratory-based experiment as described in Section 6.2.2.2. For increased platform manoeuvrability, the jet thrusters were equipped with steering nozzles and reversing buckets, controlled from electric servo motors via push-rod links.

6.2.2.2 Motor selection

Brushless outrunner Direct Current (DC) motors were selected due to their longevity, low maintenance and relatively high efficiency, compared to their brushed counterparts (Chapman, 2005). The required motor power was computed from the effective towing power (P) necessary to achieve the desired maximum platform speed (B_T) of 3 ms^{-1} in still water, assuming an efficiency of 50% for the waterjet and a motor efficiency of 80% (actual efficiency data were

not available from the component manufacturers). P was calculated as (MAN, 2011):

$$P = R_T * B_T \quad \textbf{(6-8)}$$

where R_T is the total towing resistance, estimated as described in Section 6.2.1.1. Moreover, the actual performance of the selected motors and waterjets in terms of forward thrust was assessed empirically in a laboratory-based experiment conducted at an early stage of the platform building process. In the experiment, the maximum achievable thrust of a single propulsion unit comprising of the Graupner jet thruster directly driven by the selected motor was measured with a calibrated load cell and related to the estimated total resistance of the selected hull form (see Figure 6-4). This allowed for estimating the maximum platform speed in relation to the design criterion of 3 ms^{-1}.

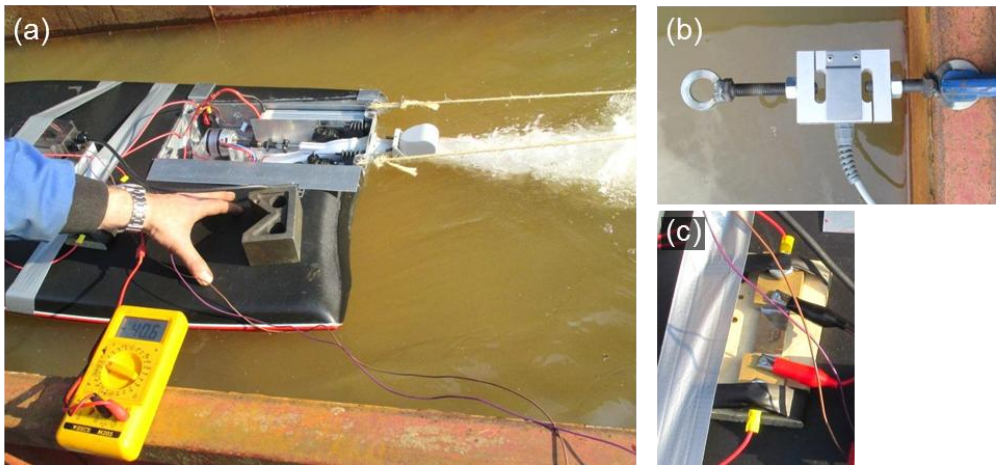

Figure 6-4. Measurement of thrust and motor current draw of a single propulsion unit prototype; (a) Single propulsion unit attached to a load cell in a water tank; (b) Load cell mounted on the tank edge; (c) Calibrated shunt resistor used to measure the motor current draw

6.2.2.3 Battery selection

The battery selection involved the choice of battery chemistry type, voltage, capacity and maximum current discharge. In terms of battery chemistry, Lithium Polymer (LiPo), Nickel Metal Hydrate (NiMH) and Lead Acid (PbAc) were considered. The latter two types dominated the marketed RC ADCP platforms, but had considerably larger weight per unit of battery capacity than Lithium-type

batteries. For example, the weight to capacity ratio of a 16 cell (19.2 V) NiMH battery pack was twice as large as that of a 5 series (18.5 V) soft-pack LiPo battery (0.28 kg(Ah)$^{-1}$ versus 0.14 kg(Ah)$^{-1}$; based on Powerizer C-5000mAh NiMH cells and Gens ace 5500 mAh 25C LiPo series marketed as of January 2013). Given the importance of a low platform weight for single-person deployment, LiPo batteries were preferred in this study. The battery voltage was based on the requirement of the selected motor. The capacity was selected to allow for platform operation of at least 3h based on practical experience from operation with other ADCP platforms. To inform the required discharge capability of the battery (as well as the choice of an appropriate fuse and safe wiring), the current draw at full throttle of the selected motor was measured in a laboratory-based experiment by means of a calibrated shunt resistor (see Figure 6-4).

6.2.2.4 Stern thruster

The capability to turn the platform on the spot can be helpful particularly at the start and end of ADCP transects during repeated cross-sectional measurements and during ADCP compass calibration on the water. Therefore, the platform prototype was equipped with a stern thruster. It was favoured to a bow thruster to prevent magnetic interference on the ADCP-internal compass from power cables running from the thruster motor in the platform front to the battery in the back.

The selected thruster was driven by a brushed DC motor with 7.2 V requirement, which differed from the voltage of the batteries selected to power the main forward thrusters and the propulsion control and data logging system (18.5 V each). To enable the powering of the stern thruster motor from one of these higher voltage batteries without motor overheating, the motor control was calibrated for a maximum current draw of 3 A. In the absence of detailed manufacturer-stated motor specifications, this limit was determined in platform field trials based on the apparent motor temperature and sufficiency of platform turning moment gained from the stern thruster. The calibration was based on

the relationship between the motor current draw and the Pulse-Width Modulation (PWM) signal controlling the motor via the ESC. This relationship was determined in a laboratory-based experiment, where a controlled PWM signal was generated with an Arduino Uno Rev. 3 electronic prototyping platform (Arduino, 2015) and the associated motor current draw was measured with a calibrated shunt resistor.

6.2.3 Integrated control and data logging system

Following a modular platform design, the propulsion control and data logging system was designed to be housed within a single enclosure with IP68 rated sockets to connect the signal wires of ESCs and servos of the propulsion system. This design facilitates the integration of the system on other RC ADCP platforms as part of future research.

6.2.3.1 Propulsion control

Propulsion control concerns the translation of the platform user inputs via the radio transmitter into the electric signals controlling the motors and servos and thus the platform behaviour on the water. In an ordinary RC setup, the RF signals transmitted on multiple channels from the radio transmitter would be directly distributed from the on-board radio receiver to the ESCs and servos, controlling the motors, jet nozzles and reversing buckets. For increased propulsion control, an ATmega328P microcontroller (Atmel, 2009) embedded on an Arduino Uno Rev. 3 board (Arduino, 2015) was used to process the signals from the radio receiver before sending them to the ESCs and servos (see Figure 6-5). This hardware was used because of its relatively low cost and the availability of a wide range of open-source libraries to program the microcontroller; the ATmega328P was programmed in C via the Arduino Integrated Development Environment (IDE), v. 1.0.1.

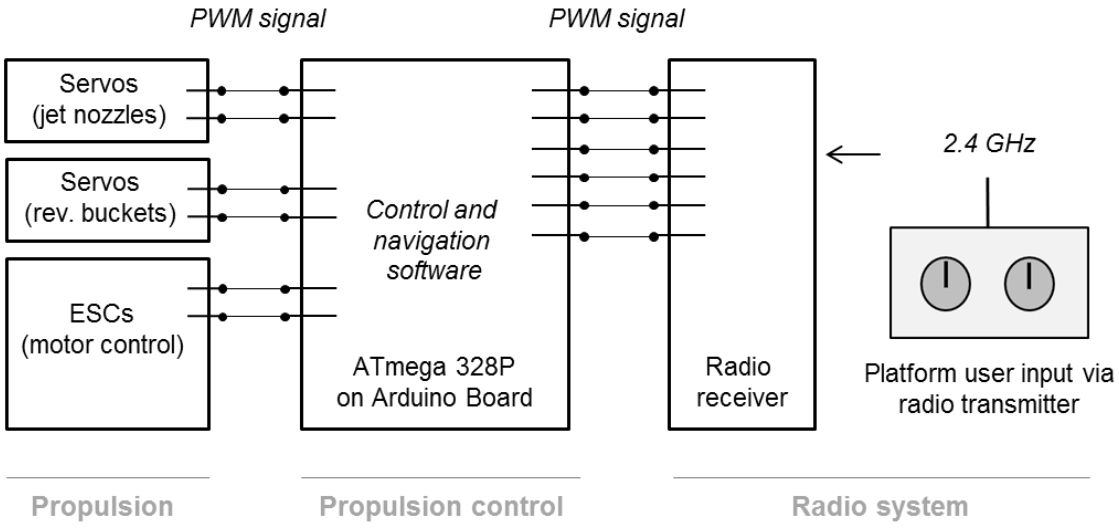

Figure 6-5. Block diagram illustrating the propulsion control via an integrated microcontroller (ATmega 328P)

The accurate input and permanent updating of the PWM signals from the receiver channels into the microcontroller was achieved through so called interrupts, where an external event triggers an interrupt to the normal flow of the microcontroller program and causes a function referred to as Interrupt Service Routine (ISR) to be called (Gridling & Weiss, 2007). Here, the external events were the changes in the PWM signal voltage between 0 V and 5 V at the respective microcontroller digital input pins, and the ISRs served as timing functions measuring the time (in µs) between these changes, and thus the pulse widths containing the information of the incoming signals. The duration of the main loop of the microcontroller program (and thus the frequency at which the PWM signals were output to the propulsion system components) was fixed to 50 Hz, which corresponded to the update rate of the control signal of the ESC and servos used (50 pulses per second).

The input PWM signals were manipulated prior to signal output in order to implement special control features, including differential thrust, adjustments of the sensitivity of thrust and steering to transmitter stick handling, or the protection of the stern thruster motor as described in Section 6.2.2.4. Moreover, this setup allowed the implementation of two separate RC control modes: a

simple mode, where the platform was fully operated with two transmitter channels only, and a more sophisticated mode with separate control over several of the propulsion system components. This allowed the platform operator to switch between RC control modes based on user experience and site-specific flow conditions.

6.2.3.2 Multiple sensor data logging

A Single Board Computer (SBC) with Linux-based operating system in the form of a Raspberry Pi 1 Model B+ (Raspberry Pi Foundation, 2015a) was embedded on the ADCP platform for simple data logging from multiple on-board sensors. A Raspberry Pi was used because of its low cost compared to other SBCs. For the purpose of this study, it was programmed in Perl to log and timestamp data from the x-IMU (see also Section 4.2.3.1) and a GPS device via Universal Serial Bus (USB) interface, along with the input and output PWM control signals sent from the Arduino Uno via the serial communication pins of the microcontroller and SBC, respectively. The serial link between the microcontroller and the SBC would also enable features of platform autonomy, where the control signals would be generated based on data from a platform positioning system (see Chapter 5) and user inputs, such as pre-defined coordinates or a command to automatically hold the position.

6.2.3.3 System health monitoring

The integrated microcontroller and SBC allowed for various system parameters to be monitored remotely. On the platform prototype, monitoring of the voltage and remaining capacity of each on-board battery and the automatic detection of water ingress in the propulsion system enclosures were implemented. The battery voltage was measured through the analogue pins of the microcontroller, whereby the input voltage was reduced through voltage dividers to prevent microcontroller damage (Horowitz & Hill, 1989). The remaining battery capacity was estimated based on the functional relationship of the motor current draw and the pulse width of the PWM motor control signal, measured in a laboratory-

based experiment applying the same procedure as described in Section 6.2.2.4 for the stern thruster calibration.

The status of the monitored parameters gets signalled to the platform operator acoustically and visually via an on-board Light Emitting Diode (LED) and a buzzer as well as through a simple Visual Basic software application with graphical user interface to be executed on a laptop on shore. This software application included a network socket for wireless communication with the on-board SBC acting as a WLAN access point to establish a local network. Figure 6-6 shows the basic system layout of the ADCP platform prototype, covering user interfaces, propulsion system and control, data logging and system monitoring.

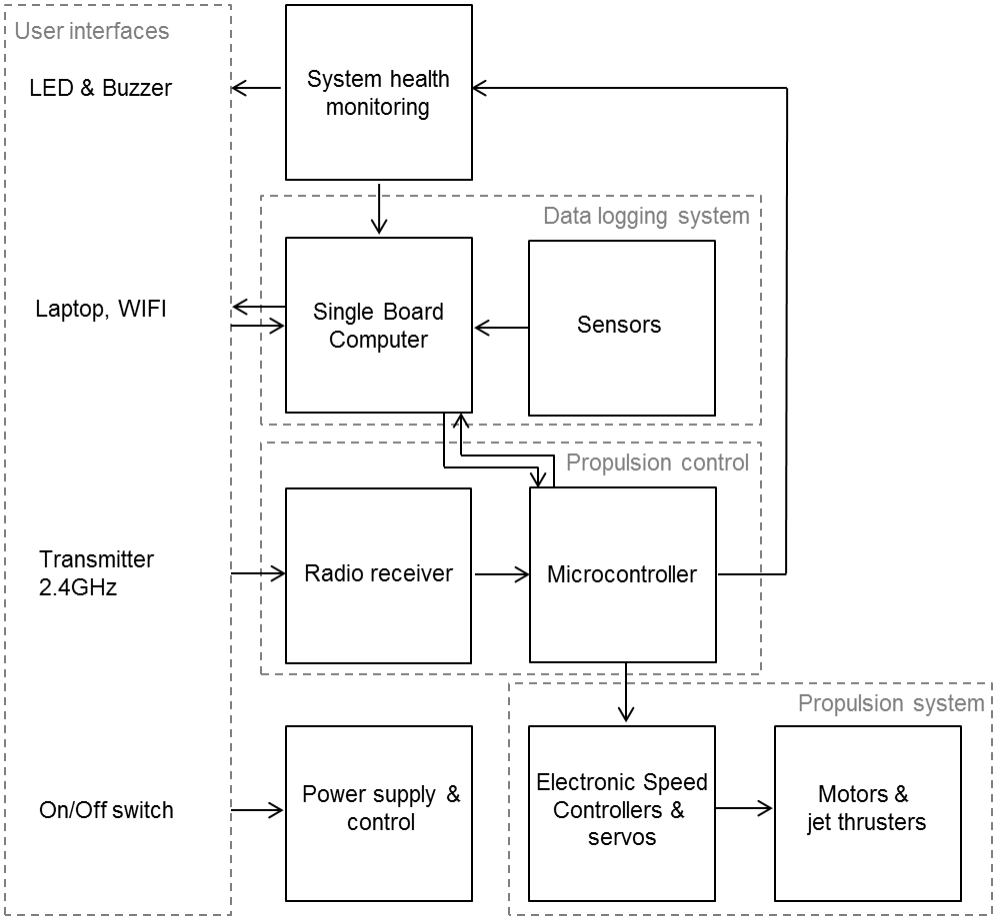

Figure 6-6. Basic system layout of the ADCP deployment platform prototype

6.2.4 In-field platform assessment

The platform stability and operation were assessed on the River Thames at Eynsham Lock, Oxfordshire, UK, during conditions of medium discharge (daily average Q of 15.74 m^3s^{-1}, corresponding to the 69th percentile of daily discharges from 1951-2014 based on data from the gauging station at Eynsham) and high discharge (daily average Q of 70.00 m^3s^{-1}, corresponding to the 99th percentile of discharges from 1951-2014). Figure 6-7 and Figure 6-8 show the site conditions during the respective platform assessments.

The platform stability was assessed by recording platform pitch and roll with an on-board x-IMU at 64 Hz (see also Section 4.2.3.1) during cross-sectional measurements with distances of approximately 35 m, 55 m and 75 m to a weir (see Figure 6-7). To assess the effect of platform pitch and roll on the ADCP data, the position error in the radial velocities potentially induced by the maximum recorded platform pitch and roll was quantified. This error has a horizontal and a vertical component and can be expressed as a linear function of the vertical measurement distance from the ADCP face (d) and the platform tilt angle, e.g. roll (θ). For a 1,200 kHz RioGrande ADCP on the platform prototype, the error was:

$$\varepsilon_{p,h} = 0.0167 d\theta + 0.0025\theta \quad \textbf{(6-9)}$$

$$\varepsilon_{p,v} = 0.0081 d\theta + 0.0016\theta \quad \textbf{(6-10)}$$

where $\varepsilon_{p,h}$ and $\varepsilon_{p,v}$ are the horizontal and vertical bin position errors at the ADCP beam pointing towards the direction of roll. The numerical parameters are specific to the ADCP instrument dimensions, beam tilt angle and the metacentre position of the ADCP platform. They were derived using basic trigonometric formulae.

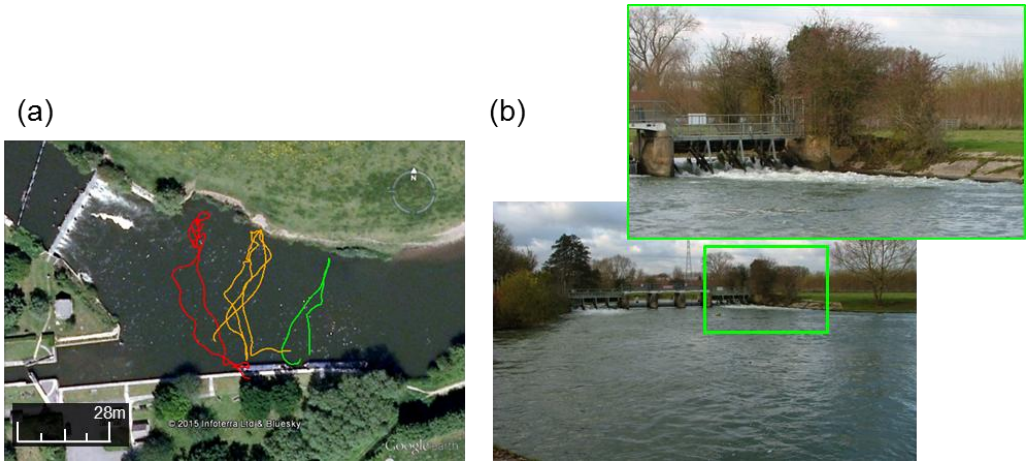

Figure 6-7. In-field platform stability assessment on the River Thames downstream of Eynsham Lock; (a) Platform trajectories for pitch and roll measurement overlaid on a Google Earth image; the distances of the cross-sectional trajectories to the weir foot are approximately 35 m 55 m and 75 m, for the red, orange and green trajectory, respectively; (b) Site conditions on the day of data collection (22/11/2013)

The platform performance in conditions of high discharge and relatively fast flowing water was assessed through cross-sectional measurements (involving four transects) with a RiverSurveyor M9 ADCP. The discharge derived from these measurements was compared to that measured at the same site and within the same hour with the ADCP deployed from an ARC-Boat (Figure 6-8). Both measurements were conducted following standard guidelines in terms of measurement duration and data processing (Mueller & Wagner, 2009). This test served not only to assess the general usability of the platform in fast flowing water, but also to identify apparent ADCP data biases induced by the new platform.

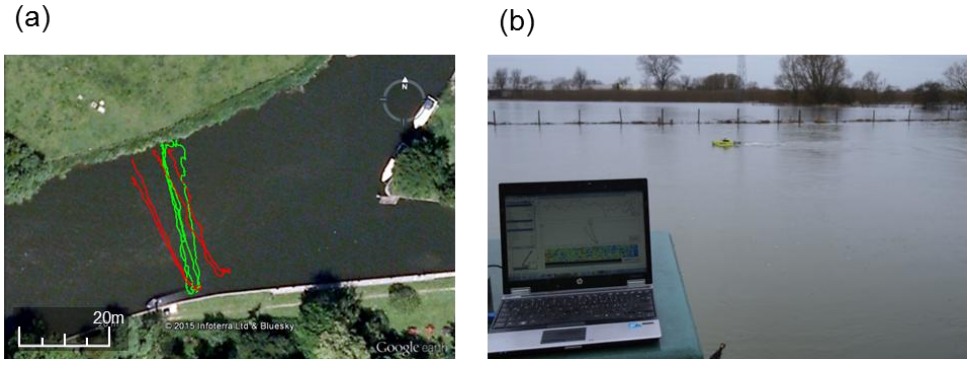

Figure 6-8. Cross-sectional measurements in fast flowing water on the River Thames upstream of Eynsham Lock; (a): Trajectories of platform prototype (red) and ARC-Boat (green) overlaid on a Google Earth image; (b): Site conditions on the day of data collection (06/02/2014)

The maximum forward speed of the fully loaded platform (equipped with a RiverSurveyor M9 ADCP) was measured through BT in conditions of nearly standing water on the River Great Ouse near Stony Stratford, Buckinghamshire, UK, on 18/09/2013.

Additionally to the assessments outlined above, numerous in-field tests were conducted to assess practical aspects of platform handling, such as ease of transport, launching, recovery and operation on the water, and to inform platform modifications during the design process.

6.3 Results and Discussion

6.3.1 Platform hull

Figure 6-9 shows the results of the platform hull comparison regarding total resistance against forward motion on the water and roll stability.

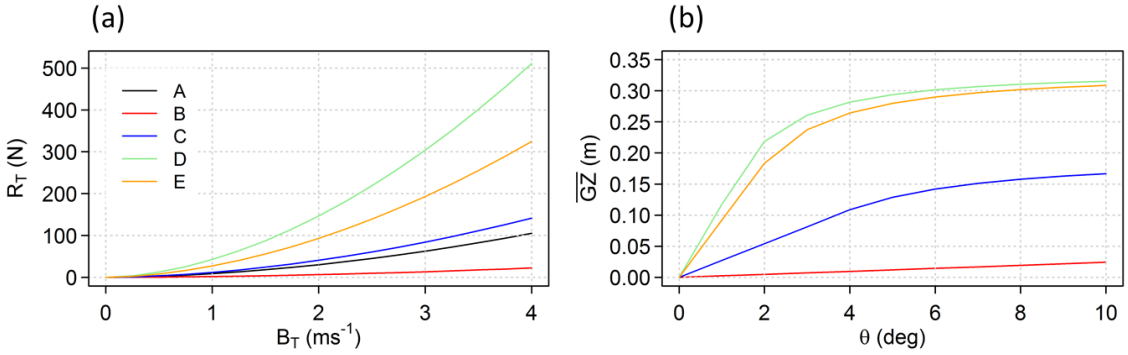

Figure 6-9. Comparison of basic hull forms; (a) Total resistance ($\boldsymbol{R_T}$) of hull forms in relation to platform speed ($\boldsymbol{B_T}$); A, B, C, D and E denominate trimaran, triangular-shaped mono-hull, rectangular mono-hull, square-shaped mono-hull and circular mono-hull, respectively; (b) Righting arm curves; $\overline{\boldsymbol{GZ}}$ and $\boldsymbol{\theta}$ stand for righting arm and platform roll angle, respectively.

Hull alternative B (narrow triangular mono-hull) had the smallest and the wide square-shaped and circular hulls (alternatives D and E) had the largest total resistance. Despite of its relatively large wetted surface area and the associated large frictional resistance, the trimaran (alternative A) had the second lowest total resistance among the hull form alternatives. In terms of stability, on the other hand, alternatives D and E showed the best performance, while

alternative B was the least stable. The large difference in stability between the hull alternatives was remarkable; for example, the increase in beam from 0.39 m (alternative B) to 0.65 m (alternative C) resulted in an 11 times larger righting arm for inclination angles up to 4 deg.

Based on these results, alternatives B, D and E were excluded from the hull selection because of their low stability and high total resistance, respectively. The rectangular mono-hull (alternative B) was found to offer a good compromise between resistance and stability and was eventually preferred over the trimaran design. The latter was excluded because of its potentially strong alignment with the flow direction and the resulting lowered manoeuvrability in complex flow conditions, such as near in-channel structures. Moreover, a trimaran design would be more prone to entanglement in bankside vegetation and more costly to build.

Table 6-2 lists the hull dimensions and Figure 6-10 shows the platform prototype. The ultimate length and weight were larger than those of the hull alternatives assumed in the hull form evaluation. The platform length was increased by adding a slightly V-shaped bow to prevent the platform from immersing into the water at high speeds as discovered in initial field-based platform tests. The larger weight could be explained largely by the aluminium used for hull reinforcement and propulsion system protection; these were features exclusive to the prototype and could be substituted by lighter, but robust, material (e.g. fibre-glass) in a platform product based on the prototype (see Section 6.3.4).

Table 6-2: Specifications of the platform prototype

ADCPs supported	any instrument with diameter up to 0.23 m
Length (m)	1.29
Width (m)	0.56
Total weight excl. ADCP (kg)	18.0
Hull materials	polyethylene, polyurethane and aluminium
ADCP draught (m)	0.05
Top speed (ms^{-1})	2.8
Forward Propulsion	2 brushless DC motors waterjets with steering nozzle and reversing buckets
Side-wards propulsion	stern thruster with brushed DC motor
Battery	3 LiPo batteries (18.5V, 5.5Ah each)

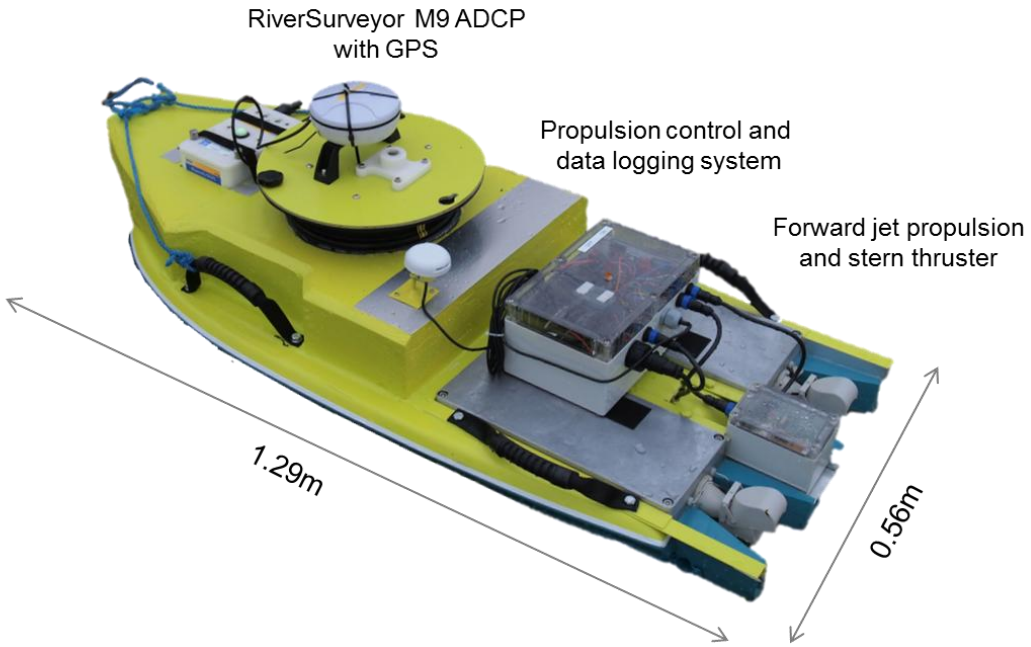

Figure 6-10. ADCP platform prototype with dimensions and main components

6.3.2 Propulsion system

The calculations for the motor selection resulted in an effective towing power of P = 252.5 W required to achieve a speed of 3 ms^{-1}, given the total resistance

estimated for the selected hull form. Under the assumptions for jet and motor efficiencies stated in Section 6.2.2.2, the resulting minimum required motor power amounted to 631.3 W. Based on this, two JP Energ C50-20 motors were selected (see Appendix A.2 for the motor specifications). The maximum thrust measurements for a single propulsion unit comprising of the selected jet thruster and motor resulted in 34 N. This indicated a maximum speed of 2.66 ms^{-1} for the selected hull form and anticipated platform weight (see Figure 6-11), which was close to the design guideline of 3 ms^{-1} and thus confirmed the selected propulsion system components.

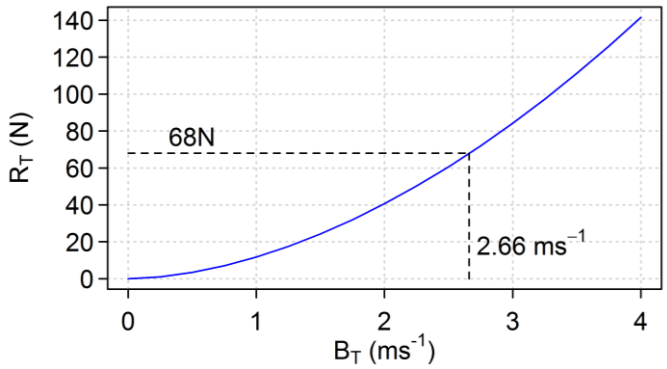

Figure 6-11. Estimated maximum speed ($\boldsymbol{B_T}$) of the selected hull form (rectangular shaped mono-hull) based on the estimated hull resistance ($\boldsymbol{R_T}$) and the measured forward thrust of the selected propulsion system

Figure 6-12 shows the setup of a single propulsion unit; the component specifications are provided in Appendix A.2.

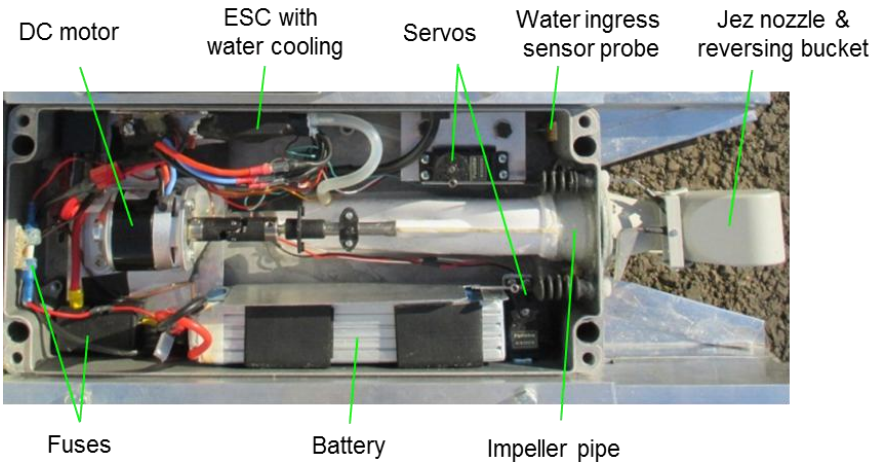

Figure 6-12. Left-hand side platform propulsion unit

Figure 6-13 shows the measured relationship of the current draw and pulse width of the PWM motor control signal for the motors driving the main waterjets; based on this relationship, the algorithm to estimate the remaining battery capacities during platform operation was implemented.

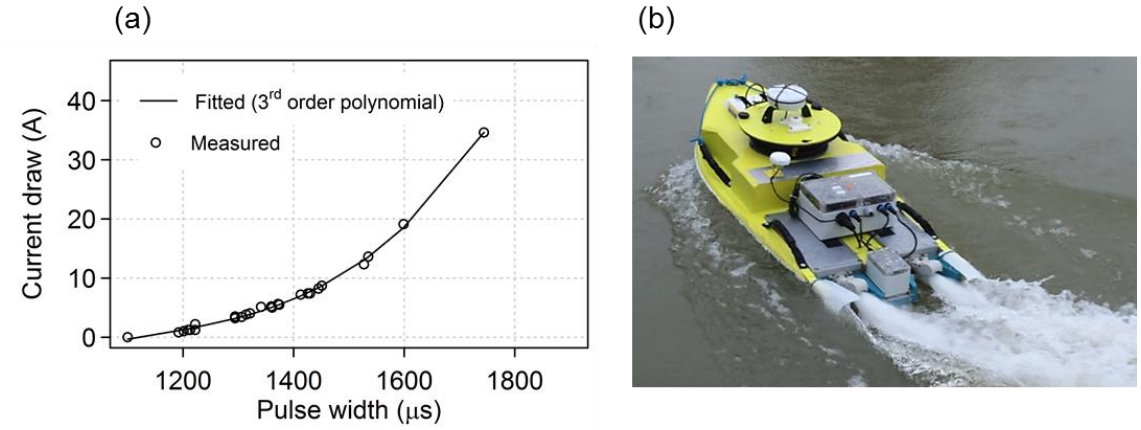

Figure 6-13. (a) Current draw of the main propulsion motors versus pulse width of PWM motor control signal (a pulse width of around 1,900 μs corresponds to full forward throttle); (b) Full throttle in-field test

The result of the current draw and pulse width measurements for the stern thruster motor is shown in Figure 6-14. Based on the fitted relationship, the pulse width of the transmitted PWM signal was limited to 1,555 μs and 1,455 μs for forward and reverse thrust, respectively, in order to constrain the current draw to 3 A for motor protection.

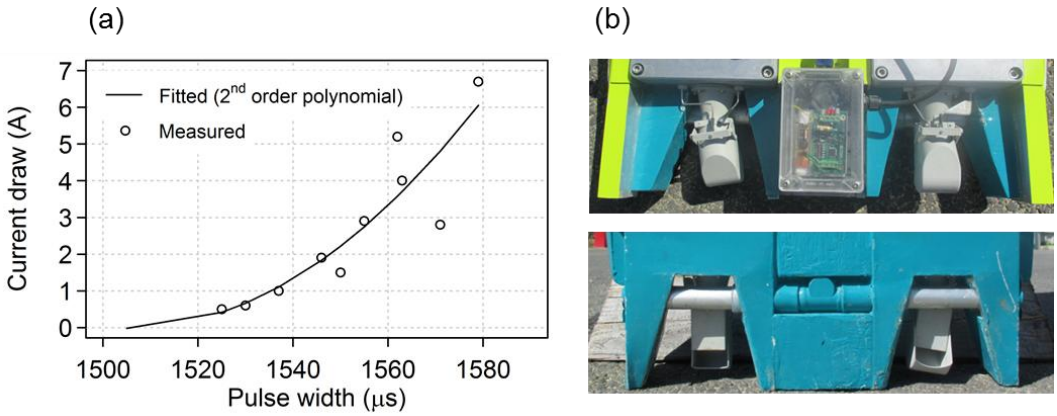

Figure 6-14. (a) Current draw of the stern thruster motor when powered by a 18.5 V battery versus pulse width of PWM motor control signal; (b) Stern thruster enclosure viewed from above and the lateral aluminium water outlet pipe viewed from below

6.3.3 In-field platform performance

Figure 6-15 shows the platform pitch and roll time series recorded during the first 125 s of each of the three test trajectories. The statistical distributions of platform pitch and roll during the full trajectories are shown in Table 6-3. The measured amplitudes decreased gradually with the distance to the weir (e.g. the maximum absolute roll angle was 12.06 deg for the trajectory closest to the weir and 3.55 deg for that furthest away). While platform roll was distributed around a mean close to zero, the test revealed a systematic platform pitch of around 4 deg. The random component (expressed as S.D.) of platform roll was larger than that of pitch for all trajectories (see Table 6-3).

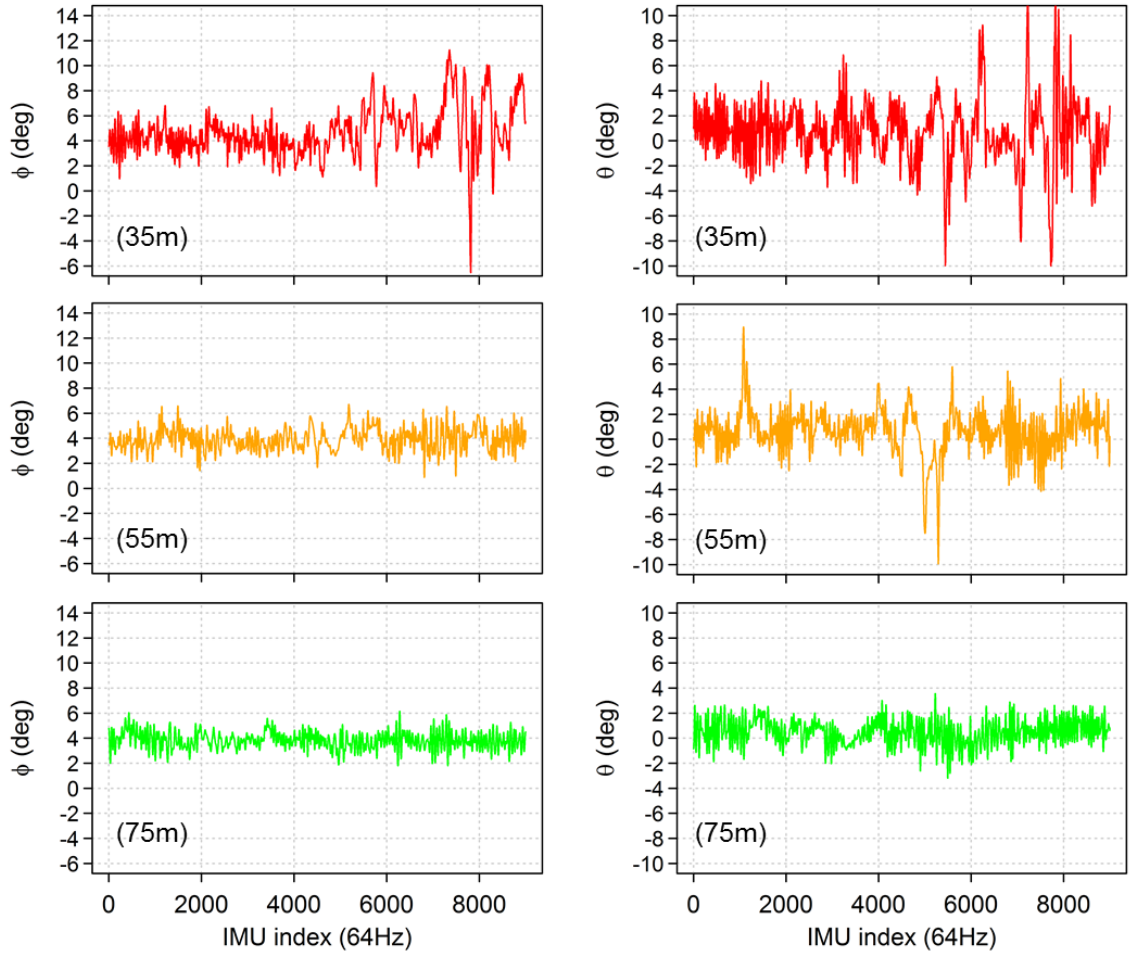

Figure 6-15. In-field platform assessments against stability to pitch (ϕ) and roll (θ) for cross-sectional trajectories downstream of a weir; the numbers in brackets denote the approximate cross section distances to the weir foot (see the corresponding trajectories in Figure 6-7).

Table 6-3. Statistical distribution of platform pitch and roll (in deg) during cross-sectional measurements at three distances to a weir; d stands for the approximate distance of the respective cross-sectional trajectories to the weir foot.

	d (m)	Min	Mean	Median	S.D.	Max	N
pitch	35	-6.53	4.42	4.20	1.81	11.26	12,975
	55	0.47	4.06	3.92	1.22	10.48	16,827
	75	1.80	3.83	3.84	0.67	6.14	9,118
roll	35	-9.99	0.68	0.73	2.40	12.06	12,975
	55	-9.93	0.62	0.71	1.57	8.98	16,827
	75	-3.19	0.50	0.52	1.00	3.55	9,118

The error in the ADCP bin positions associated with the maximum absolute roll reached up to 0.83 m at a measurement distance of 4 m to the ADCP for the trajectory closest to the weir, but was below 0.3 m for that furthest away (see Figure 6-16). These position errors represent extreme cases experienced during the test trajectories, presumably caused by large waves or rapid platform acceleration or turning. During most of the time, the roll angles were of considerably smaller magnitudes, e.g. 95% of the absolute roll angles recorded were below or equal to 4.77 deg, 3.15 deg and 2.11 deg, for the trajectories at 35 m, 55 m and 75 m distance to the weir, respectively. These amplitudes correspond to horizontal bin position errors of maximal 0.34 m, 0.23 m, and 0.15 m, respectively, at 4 m distance to the ADCP face.

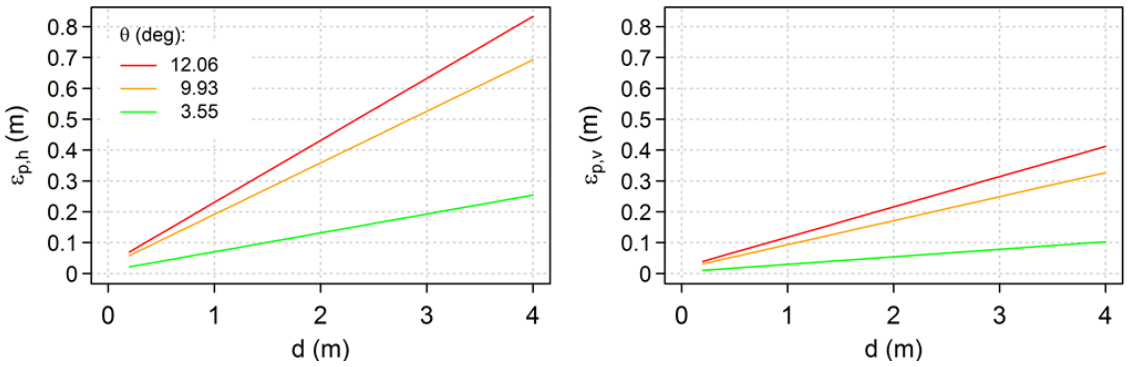

Figure 6-16. ADCP bin position error in horizontal ($\boldsymbol{\varepsilon_{p,h}}$) and vertical ($\boldsymbol{\varepsilon_{p,v}}$) direction potentially resulting from maximum absolute platform roll measured during the in-field platform assessment; $\boldsymbol{d}$ stands for the vertical measurement distance from the ADCP face.

The maximum platform speed in standing water was measured to be 2.8 ms^{-1}. The ADCP transducer faces constantly remained under water during the speed tests, enabling continuous data recording (despite an apparent platform bow lift at a speed of around 2.0 ms^{-1}).

The discharge measured using the platform prototype in conditions of fast flowing water on the River Thames was within 0.3% of the reference measurement using the ARC-Boat. The total Q (and S.D) of the four transect measurements were 69.44 m^3s^{-1} (1.69 m^3s^{-1}) for the prototype and 69.63 m^3s^{-1} (1.49 m^3s^{-1}) for the ARC-Boat. These measurements also agreed with data of daily discharge obtained from the fixed gauging station at Eynsham (see Section 6.2.4). Despite resultant water velocities up to a maximum of 1.7 ms^{-1} within a distance of 0.5 m below the water surface (based on the ADCP data), the platform prototype provided sufficient thrust and manoeuvrability throughout the measurement period.

6.3.4 Lessons learned for platform product development

The platform prototype design and assessment informed the anticipated development of a platform product by an established ADCP platform manufacturer. The most important inputs to the product development have been discussed in this section.

6.3.4.1 Platform hull

The prototype was shorter and lighter than the RC ADCP platforms marketed at the study time (e.g. 0.66 m shorter and 19.2 kg lighter than the ARC-Boat; see Table 6-2 as well as Table 3-2 in Chapter 3). The jet propulsion and the flat platform hull facilitated the platform operation in very shallow water (the platform draught in the water is 0.04 m) and ensured a low ADCP instrument draught, enabling measurements closer to the water surface. During field trials, the low-draught design facilitated platform launching in very shallow areas without the need for the user to enter the water.

The relatively low platform beam of 0.56 m was required to achieve the maximum platform speed of nearly 3 ms^{-1}, but was associated with a decrease in platform roll stability. In rough flow conditions such as near weirs, platform roll was shown to reach more than 10 deg. A measure to limit the bias in the ADCP data potentially induced by roll could be to discard data recorded in periods where the pitch or roll amplitudes are above a user-defined threshold. This could be implemented with the suggested on-board data logging system, facilitating the integration of the ADCP data with an external IMU. In this study, the platform stability was treated primarily as a function of the platform beam, draught and length as well as the height of the centre of gravity. More sophisticated hull design features to decrease the platform tendency to roll, such as bilge keels (Moore, 2010), would have compromised the low-draught platform design and thus were not implemented.

Care should be taken in the distribution of components on the platform. The prototype was shown to have a systematic pitch of 4 deg, which can be addressed either by changes in the platform weight distribution or by adjusting the ADCP mount to prevent a systematic instrument tilt. The placement of components on the platform should ensure sufficient distance of batteries and other magnetic material to the ADCP to avoid constant interference with the ADCP-internal compass. In-field prototype testing revealed that also a power cable running past the ADCP can cause apparent compass bias (e.g. when powering a bow thruster from a battery in the platform back).

The total platform weight could be further reduced by replacing the two heavy aluminium enclosures (2.3 kg each) that house the propulsion system with plastic enclosures. For robustness against damage, a fibre-glass hull would be preferable for a platform product to the materials used for the prototype hull. To simplify the replacement of damaged components, the modular platform design implemented in the prototype development would be beneficial for a platform product too.

6.3.4.2 Platform propulsion

The use of jet thrusters eliminated the operator safety risk associated with propellers. This facilitated safe platform transport, launching and recovery. However, this study revealed numerous disadvantages of jet thrusters that are to be considered in the development of a platform product. The availability of jet thrusters on the market is very limited (only three different models, all from the same manufacturer, were identified during the platform development), and they are more complex to install on the platform than propellers. The potential problem of weed entanglement in the impellers would require a design that enables the simple removal of the water outlet pipe to gain access to the impellers for cleaning. Only little reverse thrust was achieved with the reversing buckets. At full throttle, the buckets became ineffective as they provided insufficient resistance for the water jet to be diverted by more than 90 deg. The lack of reverse thrust might be problematic particularly for inexperienced RC platform operators, who might otherwise use this feature as a platform break. Additionally, waterjets might cause physical disturbance of the flow measured near the water intakes. Visual examination of the ADCP data collected during the platform prototype testing did not reveal apparent data bias and the discharge measured with the prototype was conform with that measured with the ARC-Boat. However, additional discharge comparison studies and quantitative flow disturbance analyses based on flume experiments or hydrodynamic modelling are recommended for further research.

The stern thruster was shown to be a useful platform feature, as it provides the operator with the ability to turn the platform on the spot without causing apparent bias in the ADCP data. This is an advantage to propeller-driven platforms, where this kind of manoeuvrability can be achieved through differential thrust, but involves the problem of physical disturbance of the sampled water volume through the propeller providing reverse thrust, resulting in ADCP data bias.

6.3.4.3 Integrated propulsion control and data logging

The integration of a microcontroller between the radio receiver and the propulsion system components forms an important step towards the development of autonomous platform features. The only deficiency encountered with the Arduino Uno microcontroller board was the limited precision of the function used to time the pulse width of the PWM signal (precision of 4 µs, for a pulse width ranging from 1100 to 1900 µs; see Section 6.2.3.1). This led to a minor, but noticeable, jitter of the motors and servos. Further research is required for the development of navigation software that integrates platform positions (recorded by the SBC) and propulsion control for autonomous features.

A low-cost SBC was illustrated to enable time synchronised data logging from multiple sensors on the platform. On the platform prototype, the data from the ADCP was recorded separately via Bluetooth connection to a laptop on shore, because the common software applications for ADCP data recording (WinRiver II and RiverSurveyor Live) were limited to Windows operating systems and thus could not be executed on the Linux-based operating system of the SBC. The simplest solution to this issue would be the use of an on-board SBC running a Windows operating system that allows the recording of data from the ADCP and the other on-board sensors on the same device.

6.3.5 Implications on ADCP-based near-pass hydrodynamics mapping

The research and development presented in this chapter contributes to a simpler and cheaper implementation of ADCP-based near-pass hydrodynamics mapping and supports the uptake of the methodology developed in this thesis in practice. The developed small-sized RC platform can be particularly useful for ADCP applications on smaller river sites, where it facilitates platform transport, launching and recovery, operation in very shallow water and ADCP data recording close to the water surface due to the low platform draft. The platform was shown to be suitable for transect measurements in straight river channels

with water velocity magnitudes up to 1.7 ms^{-1}. In spatially complex hydraulic conditions downstream of fish passes, the maximum water velocities suitable for deployment of the platform prototype may be lower (see also Section 8.3.3). Further in-field assessments are required to determine the threshold.

In particularly complex hydraulic conditions, such as downstream of weirs, larger (and most importantly, wider) platforms with associated higher roll stability are preferable. For example, the roll amplitudes recorded for the platform prototype at 35 m distance from a weir on the River Thames (95% of the samples had roll ≤4.77 deg; see Section 6.3.3) were larger than those encountered with the ARC-Boat during the ADCP survey presented in Chapter 4 at distances from 2 m to 32 m from the weir foot (95% of the samples had roll ≤2.62 deg). The potential bias in ADCP data caused by platform pitch and roll should be considered in the ADCP-based near-pass hydrodynamics quantification, e.g. through an on-board IMU and filtering for potentially biased ADCP data during post-processing. In this study it was shown that the horizontal bin position error induced by platform instability can, in extreme cases, reach magnitudes that are comparable to those induced by the platform positioning system (see Chapter 5).

The implemented communication between a position logging on-board SBC and a microcontroller for propulsion control constitutes the hardware basis for autonomous platform control features. The full exploitation of the benefits of such a system in ADCP-based hydrodynamics mapping relies on further research on a reliable platform positioning system (see Chapter 5). The integration of a low-cost SBC as demonstrated in this study supports the data logging from multiple on-board sensors without the need to install on-board laptops (see Chapter 4) and thus avoids having to risk expensive equipment in field studies.

6.4 Conclusions

This chapter covered the development of an RC platform prototype to address the need for a small-sized ADCP deployment platform and systems enabling multiple on-board sensor data logging and autonomous platform operation through integrated control. To the author's knowledge, the developed prototype is the first ADCP platform with integrated control and on-board data logging system. Moreover, the platform is shorter, lighter and has a considerably lower draught than RC ADCP platforms marketed at the time of the PhD project.

Based on basic design formulae, a rectangular shaped mono hull was found to offer a good compromise between platform resistance against forward motion on the water and platform stability to pitch and roll. Jet thrusters were shown to offer a viable and safe alternative to propeller drives, but to have the disadvantages of limited market availability, relatively high complexity of installation and poor reverse thrust. The installation of a stern thruster increased the platform manoeuvrability considerably, enabling platform turning on the spot without apparent ADCP data bias. Integrated propulsion control and multiple data logging were shown to be achievable through a low-cost microcontroller platform and SBC, respectively, providing the hardware basis for autonomous platform features. The field-based assessment revealed the platform limitations in terms of stability and maximum speed. Assessment of the former illustrated the need for measures to reduce ADCP data bias from platform pitch and roll motion when using smaller platforms in hydrodynamic mapping applications.

The findings presented in this chapter informed the design of an ADCP platform product based on the prototype, contribute to the collection of ADCP data at lower cost, and support the uptake of ADCP-based hydrodynamic mapping near fish passes in practice.

Chapter 7

EVALUATION OF ADCP-BASED NEAR-PASS HYDRODYNAMICS QUANTIFICATION

7.1 Introduction

In Chapter 4, it was shown that the robustness of ADCPs against major error sources can be increased through the integration of external sensors and unconventional data processing. These techniques form an integral part of the ADCP-based methodology for near-pass hydrodynamics quantification developed in the PhD research. While Chapter 4 presented first results of the methodology application at a fish pass, the evaluation of the effectiveness and transferability of the methodology relied on its implementation at a broad range of sites and environmental conditions. This chapter presents the evaluation of the methodology covering three different fish pass types and conditions of low, medium and high discharge. The implementation of the ADCP-based methodology at various sites also enabled addressing of a further gap in knowledge related to ADCP-based hydrodynamic mapping: the lack of protocols for ADCP sampling (see Sections 3.3.1.2 and 3.3.1.3). Specifically, it was unclear how many transects were required to capture the temporally averaged water velocities within a river cross section (particularly if the relatively new post-processing technique by Vermeulen et al. (2014) was used; see Section 3.4.1.1) and how the spatial density of the sampled sections affected the estimated flow field.

The research presented in this chapter contributed to the fulfilment of both **objective 4 and 5** of the PhD thesis (see Section 1.2):

to assess the effect of the spatio-temporal ADCP data sampling strategy on the flow field quantification near fish passes, and

to evaluate the suitability of the improved ADCP-based flow maps to derive near-pass hydrodynamic descriptors based on those identified in objective (1) at a range of sites with different fish pass types and discharge conditions.

This has been accomplished through the following **research tasks**:

(i) to quantify the 3D spatial distribution of the temporally averaged water velocities as well as the riverbed morphology at a range of sites covering different discharge conditions and fish pass types,

(ii) to assess the sensitivity of the quantified flow field to the spatio-temporal ADCP sampling strategy in relation to the site-specific hydraulic conditions,

(iii) to assess the attractiveness of the quantified near-pass hydrodynamics in relation to the qualitative descriptions of suitable attraction flows and competing flow features provided in established fish pass design manuals and review texts (e.g. Armstrong et al., 2010; FAO, 2002; Larinier, 2002; Williams et al., 2012; see Section 2.3), and

(iv) to assess the suitability of the 3D velocity distributions to derive selected quantitative indicators of hydrodynamic fish pass attractiveness based on those identified and proposed in Section 2.6.

7.2 Methods

7.2.1 Study sites

The study presented here was based on a total of five ADCP surveys covering the three sites introduced in Chapter 3 (see Section 3.5.2). Figure 3-9 in Chapter 3 shows the site conditions on the respective days of ADCP data collection and introduces the acronyms by which the surveys have been referred to throughout this chapter. The surveys involved conditions of low to high discharge and three different fish pass types (see Table 3-4 in Chapter 3).

The surveys referred to as SHREW1-3 were conducted downstream of a vertical slot fish pass at Shrewsbury Weir on the River Severn (see Figure 7-1a). The high relevance of the site to upstream spawning Atlantic salmon has been introduced in Chapter 4 (Section 4.2.1), where, for conditions of very low discharge, the fish pass attraction flow was found to be well discernible and potentially enforced by the main water jet flowing over the weir. Here, the

findings of Chapter 4 have been compared against those during conditions of medium (SHREW3) and high discharge (SHREW2). Figure 7-2a illustrates the areas covered during the three surveys in relation to the migration barrier and fish pass entrance.

Figure 7-1. Fish passes at the study sites; (a) Vertical slot pass at Shrewsbury Weir; (b) Super-active baffle pass at Flatford Mill; (c) Nature-like bypass channel and super-active baffle pass near Theale (photographs provided by Oliver Roden, EA)

The ADCP survey referred to as FLATF was conducted on the River Stour at Flatford Mill downstream of a relatively short and steep super-active baffle (Larinier) pass (see Table 3-4). The pass was built in 2012 and installed on the right river bank next to the Archimedes screw of a small-scale HEP (see Figure 7-1b). In addition to the HEP, the upstream migration at the site was obstructed by a weir on the right bank channelling the flow towards the HEP as well as a sluice (see Figure 7-2b). During the data collection, the discharge was too low for the HEP to be in operation, so that the flow into the downstream area was limited to the flow through the fish pass and over the lowered sluice gate. The fish pass targets potamodromous fish migrating upstream to spawning grounds

during spring and up- and downstream to preferred feeding and dwelling habitats throughout the year.

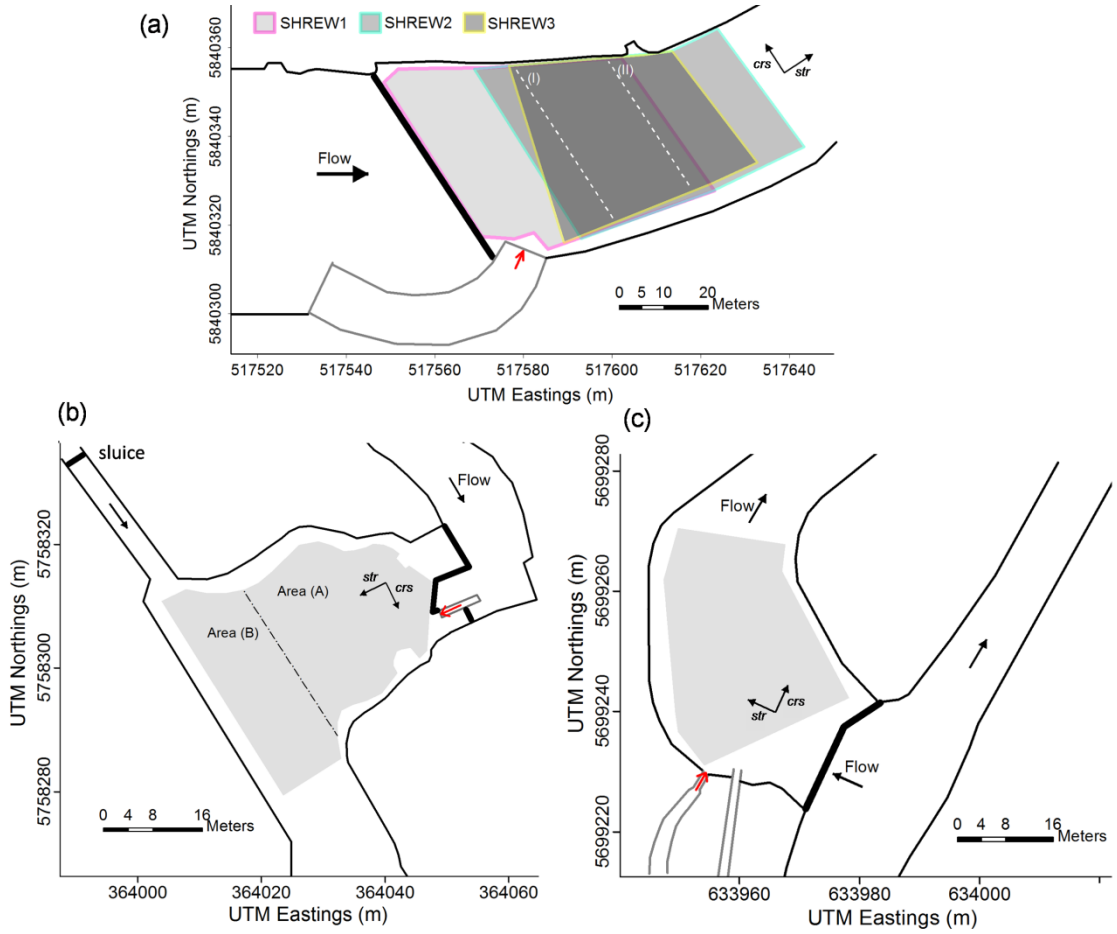

Figure 7-2. Fish pass entrance in relation to migration barriers and survey areas at the study sites; (a) SHREW1-3; (b) FLATF; (c) THEAL; the black lines illustrate the river boundaries and the thick black lines denote the fish migration barriers; the grey lines denote the fish pass and the red arrows point to the respective fish pass entrances; the surveyed areas are shown in grey; $\boldsymbol{str}$ and $\boldsymbol{crs}$ denote the streamwise and cross-stream direction, respectively.

Finally, the survey on the River Kennet (a tributary to the River Thames) near Theale (THEAL) covered the area downstream of a vertical drop weir and a 330 m long nature-like bypass channel, the construction of which had been finished approximately three months prior to the ADCP survey (see Figure 7-1c and Figure 7-2c). The River Kennet provides important breeding and nursery habitats for Atlantic salmon within the Thames catchment (Griffiths et al., 2011). In addition to salmonid species, the bypass channel targets potamodromous

fish and was meant to create habitats including gravel substrate and several backwater pools serving as fish refuges. Approximately 6 m upstream of the entrance to the bypass channel and on the same river bank was a super-active baffle (Larinier) pass built in 1999. This fish pass was to be removed for the installation of a small-scale HEP with its only turbine positioned at the location of the super-active baffle pass. The ADCP survey informed the prediction of the effect of the water jet issued from the turbine on the hydrodynamic attractiveness of the bypass channel, whereby the flow from the super-active baffle pass acted as a proxy for the turbine flow.

7.2.2 Data collection

7.2.2.1 ADCP setup

Velocity and depth data were collected using a 1,200 kHz RioGrande ADCP deployed from an ARC-Boat for the surveys SHREW1-3 and FLATF. The ADCP was configured to Water Mode 12 with 7 sub-pings per ensemble and a bin height of 0.12 m. As outlined in Section 3.2.7, the RioGrande ADCP was the preferred ADCP model because it was the only instrument offering the user access and data recording capabilities required to integrate the set of ADCP data quality enhancement techniques proposed in the PhD research (see Chapter 4). The survey THEAL, however, was coined by shallow areas around the bypass channel entrance(depth $\ll$1 m), so that a RiverSurveyor M9 ADCP was used instead of the RioGrande ADCP because of its capability to measure closer to the water surface. The associated adaptions of the ADCP data processing have been described in Section 7.2.3. The M9 ADCP was used with auto-adaptive configuration (see Section 3.2.7) with bin heights ranging from 0.02 m to 0.20 m.

7.2.2.2 ADCP sampling strategy

Table 7-1 provides an overview of the sampling strategies implemented during the five ADCP surveys. For SHREW1, cross sections with a spacing of 4 m were sampled 6 or 4 times to cover the reach immediately downstream of the

fish pass entrance (see also Section 4.2.2.1). For all subsequent surveys (SHREW2-3, FLATF, THEAL) the number of transects per section was increased to a minimum of 8 for a more accurate quantification of the temporally averaged water velocities and to support the calibration of the sampling strategy presented in this chapter (see Section 7.2.4.1). A uniform section spacing of 4 m was implemented for SHREW1-3, where the accurate implementation of a denser sampling was complicated by the rough surface flow conditions limiting the control over the survey platform. For THEAL and FLATF the spacing was reduced to 2 m for sections within 15 m distance from the fish pass entrance to capture spatial velocity variations at a finer scale in this relevant area, and a spacing of 4 m was applied at larger distances.

During all surveys the accurate implementation of the sampling strategies was supported by the real-time platform track visualisation software developed by the author as described in Chapter 4 (Section 4.2.2.2).

Table 7-1. Details of the sampling strategies implemented during the ADCP surveys; the survey duration refers to the time between recording of the first and the last ADCP sample.

	SHREW1	SHREW2	SHREW3	FLATF	THEAL
Sampling strategy					
Approx. length of reach surveyed (m)	55	45	40	40	40
Number of cross sections sampled	13	10	8	12	13
Section spacing (m)	4	4	4	2 up to 15m from pass, then 4	2 up to 15m from pass, then 4
Min. transects per section	6 up to 28m from weir foot, then 4	8	8	8	8
Mean B_T (ms^{-1})	0.42	0.83	0.75	0.39	0.41
Survey duration (h)	5.9	4.5	2.2	3.9	2.8
Mean sampling frequency (Hz)					
ADCP	1.5	1.1	1.4	1.3	1
TS	5.4	7.1	5.6	5.4	6.4
IMU	64	64	64	64	-

The survey areas were defined to start as close as possible to the respective fish pass entrances for the ARC-Boat to remain sufficiently controllable for repeated cross-sectional sampling (see Figure 7-1). The spatial extent of the surveyed reach in the downstream direction was determined based on physical site characteristics (i.e. up to the end of the weir pool for FLATF and up to the first river bend downstream of the migration barrier for THEAL) and constrained by the limited capacities of the available batteries to power the ADCP platform (for SHREW1-3). The variability in discharge during data collection was below 5% for all surveys apart from THEAL, where the variability ranged up to 11%, based on data at 15 minute intervals from the nearest gauging stations (Montford for SHREWS1-3, Langham and Higham for FLATF, and Theale for THEAL).

7.2.2.3 Complementary velocity measurements

The ADCP data were complemented with 1D point-velocities measured at the respective fish pass entrances in order to relate this traditionally used indicator of fish pass attractiveness (see Section 2.3.1) to the ADCP-based near-pass hydrodynamics quantification. The point-velocities were measured at the centres of the respective fish pass entrances at a depth of approximately 0.3 m below the water surface, using a Valeport propeller current meter oriented towards the main direction of the flow through the pass entrance. The average of three subsequent measurements lasting 50 seconds each was reported. The measurements could not be taken for SHREW2 because during the survey the fish pass was not accessible due to flooding.

7.2.2.4 Data localisation and recording

A Leica Nova MS50 was used as a tracking TS to spatially reference the ADCP data as demonstrated in Chapter 4. For SHREW2-3, FLATF and THEAL, a modified strategy to log the MS50 data was implemented to prevent time synchronisation errors from signal losses when continuously transmitting these data wirelessly to the on-board laptop, as experienced for SHREW1 (see

Section 4.3.3.2). During these surveys, the ADCP and TS data were logged on an on-board laptop and an on-shore SBC (Raspberry Pi 2 Model B; Raspberry Pi Foundation, 2015), respectively, with time synchronised system clocks. The SBC obtained its absolute system time from the information provided in the NMEA 0183 GPS sentences and the relative time between seconds based on the Pulse-Per-Second (PPS) signal output from a GPS device integrated with the SBC. Following Taylor (2015), the SBC was set up as a Stratum-1 NTP server with clock precision at µs-level. A TP-LINK 150 Mbps WLAN access point was used to connect the on-shore SBC and the on-board laptop. The latter was running NTP client software configured to automatically set the laptop system time to that of the SBC in regular intervals.

The ADCP data were recorded with the software WinRiver II (v. 2.8, Teledyne RD Instruments Inc., San Diego, CA, USA) for SHREW1-3 and FLATF, and RiverSurveyor Live (v. 3.8, SonTek/YSI Inc., San Diego, CA, USA) for THEAL. The data from an on-board x-IMU (x-io Technologies, 2012; see Section 4.2.3) and those from the MS50 were recorded using bespoke software developed by the author (see Table 7-1 for the sensor sampling frequencies). The on-board laptop and the SBC were controlled from another laptop on the shore through Windows Remote Desktop Connection and Secure Shell (SSH) connection, respectively. Based on their PC time stamps, the data from the ADCP, TS and IMU were temporally aligned during post-processing. TS data with a temporal offset from the ADCP data of more than 0.15 s were discarded to limit the error in spatial data referencing (see also Section 4.3.3).

7.2.3 Data post-processing

7.2.3.1 Compass corrections and boat velocity estimation

Temporary errors in ADCP compass data were corrected through the ADCP-IMU integration as outlined in Chapter 4 for all surveys, where a 1,200 kHz RioGrande ADCP was used. For ensembles with invalid BT signals, the boat velocity was estimated based on the TS position. For the data from THEAL the

compass correction and TS-based boat-velocity estimation could not be applied because of the limited capability to re-process data from the RiverSurveyor M9 ADCP (see also Section 3.2.7).

7.2.3.2 Estimation of temporally averaged 3D velocities

For SHREW1-3 and FLATF, the 3D water velocities along the sampled sections were estimated using the technique by Vermeulen et al. (2014) as described in Section 4.2.4. The technique was implemented only for data from Teledyne RDI ADCPs. Therefore, a conventional repeated transect averaging procedure was developed to process the data collected at THEAL.

This conventional procedure involved:

(i) resolving the 3D velocities from the radial velocities measured at the same time along the four ADCP beams,

(ii) fitting a straightened uniform 2D grid through the ensembles measured along a cross section and orthogonally projecting the 3D velocities onto the grid cells, and

(iii) averaging the velocities within the same cell.

The grid fitting was achieved through an OLS procedure and the lateral and vertical grid cell dimensions were defined to be 0.40×0.15 m². Velocity samples with a distance above 2 m from the nearest grid node were discarded to limit the loss of spatially varying hydrodynamic features (Jamieson et al., 2011). Also, samples greater than 6 or smaller than 1/6 times the median of all velocities within a mesh cell were discarded as outliers. The velocity averaging was achieved by computing the arithmetic mean for each of the 3D velocity components. This type of repeated transect processing is similar to that proposed by others (e.g. Kim & Muste, 2012; Parsons et al., 2012). However, relative to the method by Vermeulen et al. (2014), it can suffer from larger errors due to violations of the flow homogeneity assumption, and it results in a coarser representation and potential loss of spatially varying flow features due to the combination of velocity samples from a larger volume of water (see Chapter 3).

After repeated transect averaging, the estimated mean east, north and vertical velocity components were rotated from the Earth-referenced to the stream coordinate system to obtain the temporally averaged 3D velocities $\{\bar{u}, \bar{v}, \bar{w}\}$. For all sites, the stream coordinate system was defined such that the streamwise direction was perpendicular to the crest of the weir representing the migration barrier closest to the fish pass (see Figure 7-2).

7.2.3.3 Estimation of the spatial distribution of $\{\bar{u}, \bar{v}, \bar{w}\}$

Depths and 3D velocities in unmeasured locations within the surveyed reaches were estimated through ordinary kriging interpolation using a 0.25 x 0.25 m^2 grid for depths and a 0.50 x 0.50 x 0.15 m^3 grid for velocities. Separate geostatistical analyses (variogram modelling) and kriging interpolation were implemented for the velocity components $\bar{u}$, $\bar{v}$ and $\bar{w}$, following the procedure suggested in Webster & Oliver (2007). For FLATF, graphical analysis (histogram and spatial data plotting) revealed two distinct statistical distributions within the velocity dataset. These corresponded to an area of very low velocities around the fish pass entrance and an area of faster velocities caused by the flow over the sluice in the area opposite to the fish pass. Accordingly, the survey area was divided into two areas (A) and (B), for each of which ordinary kriging interpolation was implemented separately (see Figure 7-2).

7.2.4 Data analysis

7.2.4.1 Methodology calibration – number of transects per section

To identify the number of transects per section required to capture the temporal average of the velocity components, a sensitivity analysis was performed on the velocity data obtained prior to kriging interpolation. The analysis was based on the assumption that the temporally averaged velocity was captured when the average absolute change in the 3D velocities over all mesh cells of a cross section caused by including the data from another transect approached zero. The change $\{\delta_u, \delta_v, \delta_w\}$ caused by including the j^{th} transect was computed as:

$$\delta_m(i,j) = m_{i,j} - m_{i,j-1} \qquad \forall\, m = \{u, v, w\} \tag{7-1}$$

where i is an index of the mesh cells. The repeated transect measurements were processed progressively (each time including the samples from one more transect), so that $\{\delta_u, \delta_v, \delta_w\}$ could be quantified for $j = \{2, 3, \dots N\}$, where N is the total number of transects sampled per section. The analysis was conducted for the absolute velocity changes $\{|\delta_u|, |\delta_v|, |\delta_w|\}$ and the normalised velocity changes $\left\{\frac{|\delta_u|}{U}, \frac{|\delta_v|}{V}, \frac{|\delta_w|}{W}\right\}$. The area mean streamwise, cross-stream and vertical velocities $\{U, V, W\}$ used to perform the normalisation were computed from all velocity estimates of the respective cross section obtained through the method by Vermeulen et al. (2014; see Section 7.2.3.2) and prior to kriging interpolation. The sensitivity analysis was carried out for all five ADCP surveys and multiple cross sections at each site, in order to assess the variability of the required transects with the proximity of the sampled cross section to the fish pass and the hydraulic conditions at the study site.

7.2.4.2 Methodology calibration – section spacing

To assess the effect of a sparser sampling density, every other sampled cross section was omitted, resulting in a reduced spacing of 8 m (and 4 m for the first 15 m near the passes for FLATF and THEAL). The remaining data were used to predict the 3D mean velocity distributions, following the procedure described in Section 7.2.3.3. The velocity measurements along the omitted sections served as reference data to validate the predicted velocities. The errors $\{\varepsilon_u, \varepsilon_v, \varepsilon_w\}$ in the flow field estimated from the sparse section data were quantified as:

$$\varepsilon_m = m_{measured} - m_{predicted} \qquad \forall m = \{u, v, w\} \tag{7-2}$$

where $m_{measured}$ are the temporally averaged water velocities measured along the omitted sections and $m_{predicted}$ are the velocities predicted through kriging interpolation (using the sparse section data) in the same locations. In addition to common measures of descriptive statistics (mean, median, S.D.), the median of the absolute percentage error ($MedAPE$) of $\{\varepsilon_u, \varepsilon_v, \varepsilon_w\}$ was computed to put the

errors in relation to the magnitude of the velocity samples. The absolute percentage error (APE) was defined as follows:

$$APE = \left| \frac{(m_{measured} - m_{predicted})}{m_{measured}} \right| * 100 \qquad \forall m = \{u, v, w\} \qquad \textbf{(7-3)}$$

This measure was preferred to the *mean* absolute percentage error because it is less affected by large outliers in the percentage differences due to division by near-zero values for samples of very low velocities (this problem was reported by Jamieson et al., 2011).

The error $\{\varepsilon_u, \varepsilon_v, \varepsilon_w\}$ contains both the error (i) introduced by decreasing the density of sampled cross sections and (ii) due to the smoothing and overall effect of the kriging interpolation on the velocity measurements. To separate these two error contributions, the latter was quantified using a common procedure known as cross-validation (e.g. Jamieson et al., 2011; Tsubaki et al., 2012). This involved the comparison of a velocity measurement with that predicted through ordinary kriging interpolation in the same location, whereby the kriging interpolation was performed without the respective measurement, but with the variogram model estimated for all data (Webster & Oliver, 2007). This comparison was performed for the full (densely spaced) velocity dataset, and the resulting statistical distribution of the differences $\{\varepsilon_{CV,u}, \varepsilon_{CV,v}, \varepsilon_{CV,w}\}$ and their $MedAPE$ were computed for all five ADCP surveys.

7.2.4.3 Identification of qualitative descriptors of near-pass hydrodynamics

For all five surveys, the spatial distributions of $\{\bar{u}, \bar{v}, \bar{w}\}$ were assessed against the qualitative guidelines for fish pass attractiveness suggested by Larinier (2002). These guidelines concern the extent and orientation of the fish pass attraction flow in relation to competing water jets and other hydrodynamic features potentially guiding upstream migrants away from the fish pass entrance (see Section 2.3). To identify such features at the surveyed sites, the spatial water velocity distributions were visualised for the horizontal plane at a depth of 0.5 m below the water surface. While, in principle, the methodology developed

in the PhD research allows the extraction of velocities at any location within the interpolation grid, this depth was selected to target surface-oriented fish and because it approximately corresponded to the lowest possible depth of velocities measurable with the RioGrande ADCP, and thus unaffected by velocity extrapolation to the water surface (see Section 3.2.6). Furthermore, velocity distributions were visualised for a set of cross sections with varying distances to the fish pass entrance. This provided an indication of the flow field encountered by fish as they move upstream towards the migration barrier.

7.2.4.4 Derivation of quantitative descriptors of near-pass hydrodynamics

The ADCP-based flow maps were evaluated in terms of their suitability to derive quantitative metrics potentially indicating hydrodynamic fish pass attractiveness. This covered the quantitative description of large-scale eddies forming near the pass entrance, the derivation of a novel attraction flow descriptor S_{eff}, and the spatial distribution of the total acceleration measure a. The latter served as a proxy for similar metrics based on velocity gradients along different directions of the flow field (e.g. SVG and THS) that had been used previously in fish behavioural studies within the context of fish passage (see Section 2.6.1).

7.2.4.4.1 Recirculation cells

Recirculation cells within the survey areas were quantified in terms of location, orientation, spatial extent and intensity. The analysis outlined here was based on the fact that turbulent components are correlated with each other in time *and* space, so that it is possible to analyse large-scale vortical regions based on the spatial distribution of mean velocities (Jamieson et al., 2011). The suggested analysis of recirculation cells was conducted for 2D flow fields at a depth of 0.5 m below the water surface, but can be applied to any depth within the interpolation grid and readily extended to 3D space. Cell centre locations were identified as local minima and maxima of the normalised vorticity ($\widehat{\omega}_z$):

$$\widehat{\omega}_z = \frac{\Delta \widehat{V}_y}{\Delta x} - \frac{\Delta \widehat{V}_x}{\Delta y} \quad \textbf{(7-4)}$$

where $\widehat{V_y}$ and $\widehat{V_x}$ are the velocity components of the normalised water velocity vector (positive $\widehat{\omega_z}$ indicates counter-clockwise flow rotation). A temporally averaged flow field can only capture translational fluid motion, whereas pure rotation of a fluid would be shown as zero velocity. Consequently, the vorticity at the centre of a recirculation cell would be very small, despite the directional change of the flow vectors (i.e. the quantity captured in $\widehat{\omega_z}$) being at a maximum. Therefore, and in contrast to eddy analyses based on temporal velocity fluctuation (e.g. Tritico & Cotel, 2010), the velocity vectors were normalised to capture the flow direction only. The diameter of the recirculation cell (d_c) was quantified following Tritico & Cotel (2010) and Drucker & Lauder (1999), by computing the normalised circulation ($\widehat{\Gamma_c}$) about the cell centre in concentric circles until a maximum circulation was reached:

$$\widehat{\Gamma_c} = \overline{\widehat{\omega_z}} * A_c \qquad \textbf{(7-5)}$$

where A_c is the circular area defined by $\left({d_c}^2\pi/4\right)$ and $\overline{\widehat{\omega_z}}$ is the spatially averaged normalised vorticity within the circle. The diameter of the area with the maximum circulation was defined to be d_c. The diameter increments used in the analysis were $\sqrt{2}$ m (corresponding to twice the diameter of the interpolation grid cells; see Section 7.2.3.3). After A_c had been found, the circulation Γ_c was computed as a measure of the intensity of a recirculation cell, where:

$$\Gamma_c = \overline{\omega_z} * A_c \qquad \textbf{(7-6)}$$

7.2.4.4.2 Effective surface of attraction

In response to the lack of quantitative descriptors of near-pass hydrodynamics associated with upstream passage (see Section 2.6) the concept for a new metric called the “biologically effective surface of attraction” S_{eff} has been proposed as part of the PhD research. The concept is based on the assumption that the flow field distortion induced by the water jet issued from the fish pass can be isolated and described as a coherent body of water near the pass entrance. The metric S_{eff} was designed to provide a measure for the

effectiveness of the attraction flow, capturing its traceability by fish as well as its spatial extent and orientation, which have been considered particularly important for fish to locate the pass entrance (see Section 2.3.1). S_{eff} was calculated from the spatial distribution of temporally averaged water velocities as obtained through kriging interpolation (see Section 7.2.3.3). The first step of the analysis was to extract those interpolation cells that were located within a maximum 3D Euclidean distance of 20 m from the fish pass entrance. This resulted in a subset C consisting of N cells:

$$C = \{ c_1, \dots, c_N \} \quad \textbf{(7-7)}$$

The THS as defined by Nestler et al. (2008; see Equation 2-8 in Section 2.4.4), was used to quantify the flow field distortion for the interpolation cells of set C. The calculation was performed from interpolation point to interpolation point, i.e. the values used for Δx, Δy and Δz in Equation 2-8 were 0.50 m, 0.50 m and 0.15 m, respectively.

This was followed by the calculation of a threshold k, describing a minimum magnitude of flow field distortion for upstream migrants to be detectable. In the absence of quantitative biological knowledge regarding the behavioural response of upstream migrants towards THS, in this analysis the threshold k was arbitrarily defined as the 90th percentile of the statistical distribution of THS of cells within set C. Subsequently, all interpolation cells with a THS below the threshold k were excluded, resulting in a subset of cells D:

$$D = \{ c \in C \mid THS\,(c) \geq k \} \quad \textbf{(7-8)}$$

From set D, those cells, which were not part of the largest coherent cluster of cells, were also excluded, resulting in a subset of cells E representing a coherent body of water.

The metric S_{eff} describes the full surface area of the boundary of this water body, whereby, in the calculation of S_{eff}, the parts of this surface area can be weighted based on the likelihood of targeted species to visit their respective

locations and thus to detect the flow distortion when approaching a migration barrier. This allows taking into account that some species are oriented towards the water surface (e.g. upstream migrating European eel; see Section 2.5.2.1), while others prefer the areas close to the bed (e.g. upstream migrating European river lamprey, *Lampetra fluviatilis*; Kemp et al., 2011; and Pacific lamprey, *Lampetra tridentata;* Keefer et al., 2011; Moser et al., 2002). Moreover, it allows to consider previous suggestions that the attraction flow should reach zones, where fish are likely to aggregate (Andersson et al., 2012; Lindberg et al., 2013). In this first assessment of the proposed metric S_{eff}, all surface locations were weighted equally:

$$S_{eff} = \sum c_s \qquad \forall\, c \in E \tag{7-9}$$

where c_s represents the side areas of the interpolation cells within set E, which have no neighbouring cell side within set E and thus form a part of the full surface area of the water body made up by the cells of set E.

7.2.4.4.3 Total 2D flow acceleration

Finally, to illustrate the estimation of a hydrodynamic indicator similar to those used in previous fish behavioural studies (see Chapter 2, Table 2-3), the spatial distribution of the 2D total flow acceleration measure a was derived from the quantified flow fields (Piper et al., 2015):

$$a(x,y) = \sqrt{a_x^2 + a_y^2} \tag{7-10}$$

where $a_x = V_x(\Delta V_x/\Delta x) + V_y(\Delta V_x/\Delta y)$ and $a_y = V_x(\Delta V_y/\Delta x) + V_y(\Delta V_y/\Delta y)$ are the components of acceleration in the x and y directions of a 2D plane.

7.3 Results and Discussion

7.3.1 Effect of the number of transects

For all sites and cross sections assessed, the effect of adding another transect tended to decrease as the overall number of transects already included increased (see Figure 7-3 and Figure 7-4). Where the transect averaging procedure by Vermeulen et al. (2014) was applied (SHREW1-3 and FLATF), this decrease approximated an exponential curve.

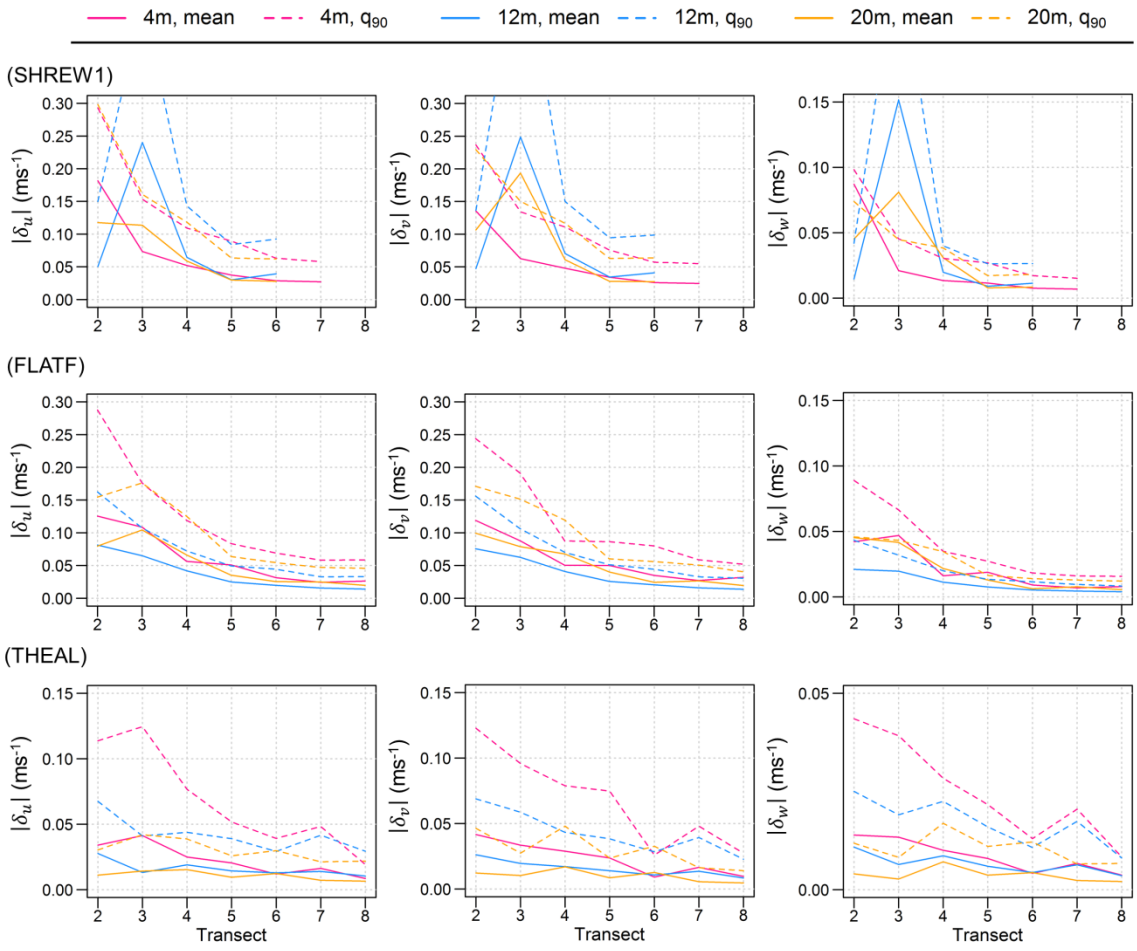

Figure 7-3. Effect of the number of transects per sampled cross section on the estimated temporally averaged velocity components, shown for three sites and cross sections at distances of approximately 4, 12 and 20 m to the respective pass entrance; $\boldsymbol{q_{90}}$ stands for the 90th percentile.

For FLATF and THEAL, the analysis revealed a tendency of the cross section located closest to the fish pass requiring a larger number of transects to capture the temporally averaged velocities (see Figure 7-3). This may be explained by the fish pass and associated in-channel structure inducing a larger temporal flow variation in their immediate surroundings. This tendency was not observed for SHREW1. Generally, beyond inclusion of the 4th transect, $|\delta_u|$, $|\delta_v|$ and $|\delta_w|$ showed little sensitivity to the distance of the sampled cross section from the fish pass entrance.

Figure 7-4 shows the effect of the number of transects for approximately the same cross section downstream of Shrewsbury Weir, but during different discharge conditions. For all three velocity components, the absolute change in the estimated velocities caused by adding another transect (top row of the plots in Figure 7-4) decreased fastest for the data collected in the lowest flow conditions (SHREW1). While for SHREW1, six transects were sufficient for $|\delta_u|$, and $|\delta_v|$ to reach values below 0.05 ms^{-1}, seven or eight transects were required for SHREW2 and SHREW3. The larger number of transects required for these surveys may also have been due to the faster boat speeds (see Table 7-1), and thus lower number of radial velocity samples collected with each transect. Interestingly, for SHREW3 (where 12 repeated transects were sampled at the section analysed) including more than eight transects did not lead to a further decrease in $\{|\delta_u|, |\delta_v|, |\delta_w|\}$. The bottom row of the plots in Figure 7-4 shows the absolute velocity changes normalised for the area mean velocity. For the streamwise velocity component, the normalised velocity changes were considerably larger for SHREW1 than for SHREW2 and SHREW3. The normalised absolute change in the streamwise velocity caused by including the 6th transect was 0.27 for SHREW1, whereas only 0.07 and 0.11 for SHREW2 and SHREW3, respectively. The differences between the three surveys were less pronounced for the cross-stream and vertical velocity components.

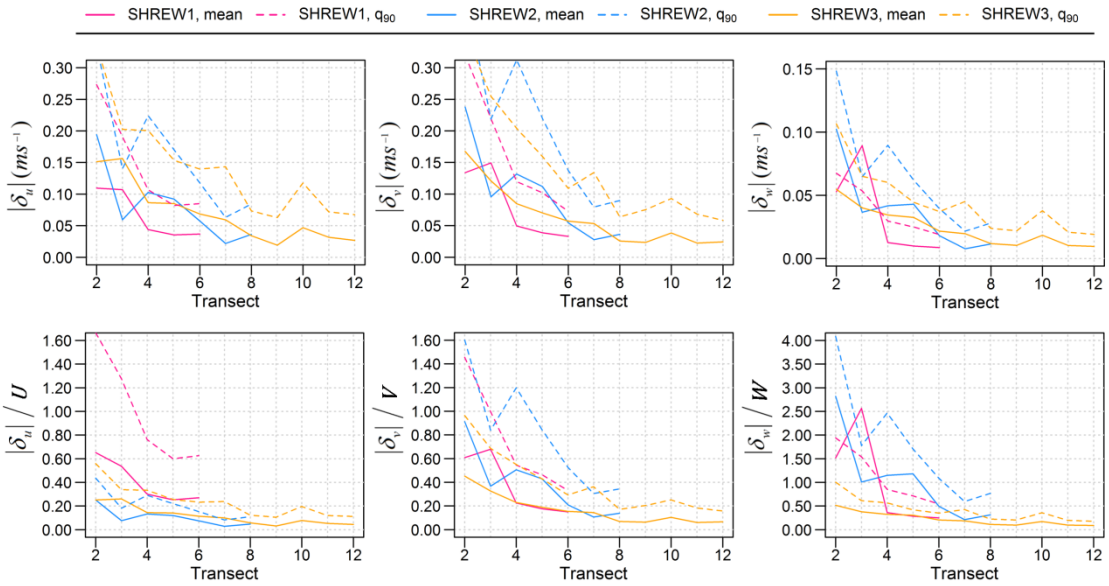

Figure 7-4. Effect of the number of transects per sampled cross section on the estimated absolute velocities and normalised absolute velocities, shown for approximately the same cross section located ≈28 m downstream of the foot of Shrewsbury Weir during conditions of low (SHREW1; $\boldsymbol{Q}$ = 7.1 m³s^{-1}), medium (SHREW3; $\boldsymbol{Q}$ = 33.8 m³s^{-1}) and high discharge (SHREW2; $\boldsymbol{Q}$ = 113.9 m³s^{-1}); $\boldsymbol{q_{90}}$ stands for the 90th percentile; normalisation was performed using the area mean streamwise, cross-stream and vertical velocities $\{\boldsymbol{U}, \boldsymbol{V}, \boldsymbol{W}\}$.

Figure 7-5 (top row of the plots) shows the mean, minimum and maximum $\{|\delta_u|, |\delta_v|, |\delta_w|\}$ over all cross sections analysed for SHREW1-3 and FLATF. This illustrates that the effect of including the first four to five transects varied strongly for the different cross sections, but this variation decreased as further transects were added (see the decreasing height of the grey area in Figure 7-5). For all cross sections, irrespective of site, discharge or distance to the fish pass, the mean change in the velocity components caused by including the 8th transect was found to be close to 0.03 ms^{-1} (for $|\delta_u|$ and $|\delta_v|$) and 0.01 ms^{-1} (for $|\delta_w|$). Also for the normalised velocities (bottom row of the plots in Figure 7-5) the variation between the sections analysed was strongest for the first four to five transects included. However, in contrast to the changes in absolute velocities this variation between cross sections tended to remain stable as transects 6 to 8 were included. The largest normalised velocity changes were found for those cross sections with the lowest area mean velocities.

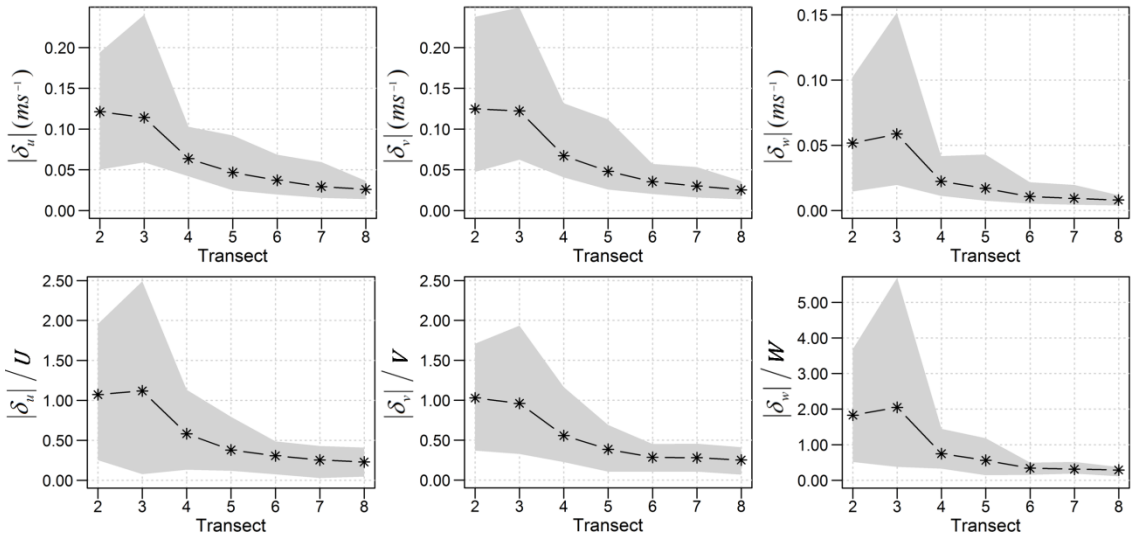

Figure 7-5. Changes in absolute velocities and normalised velocities caused by including another transect, shown as the mean and range (grey area) of all cross sections analysed (9 cross sections in total) for SHREW1-3 and FLATF; normalisation was performed using the area mean streamwise, cross-stream and vertical velocities $\{\boldsymbol{U},\boldsymbol{V},\boldsymbol{W}\}$.

These findings can have far reaching implications for the informed definition of sampling protocols for ADCP-based hydrodynamic mapping applications at sites similar to those studied in the PhD research. If the effect, in non-normalised terms, of including more than seven transects is known to be similar across sites, it means that, in normalised terms, the gain in adding another transect is smaller for faster flowing and larger for slower flowing sites. For example, including the 8th transect resulted in a mean absolute change of the streamwise velocities of 0.020 ms^{-1} for the section at 20 m distance to the pass for FLATF (extremely slow flowing conditions) and 0.036 ms^{-1} for the section at similar distance for SHREW2 (fast flowing conditions). However, relative to the area mean streamwise velocity magnitudes of the respective cross sections, the changes were 33.7 % (FLATF) and 4.3 % (SHREW2).

For those data processed with the conventional repeated transect averaging method (THEAL), the magnitudes of $\{|\delta_u|,|\delta_v|,|\delta_w|\}$ were lower than for the other surveys and their decrease with increasing transect number was less pronounced. This was particularly the case for those cross sections that were not in the immediate vicinity of the fish pass entrance (see Figure 7-3). The

difference to the results obtained for the other surveys can be explained by the ADCP model and processing approach used at THEAL, leading to a larger number of velocity samples collected per transect and thus a lower number of transects required overall. Specifically, for 43.2% and 46.0% of the ensembles collected at THEAL, the ADCP auto-configured the bin heights to 0.02 m and 0.06 m, respectively. These low bin heights particularly dominated the slow flowing areas not in the immediate vicinity of the fish pass entrance and weir, where the effects of adding further transects were lowest. The large vertical measurement resolutions meant that a single transect could already result in a relatively large number of 3D velocity samples per projection grid cell (i.e. up to seven 3D velocity samples per cell, for a bin height of 0.02 m, assuming the mean B_T given in Table 7-1 and the projection grid cell dimensions stated in Section 7.2.3.2). In contrast, the ADCP instrument used for the other surveys was configured to a constant bin height of 0.12 m. Furthermore, the conventional processing method included radial velocities from a considerably larger sampling volume. The maximum distance of the 3D velocity samples from the nearest grid node was 2 m, but many of the radial velocities used to resolve these 3D velocity samples will have been measured in locations further away because of the ADCP beam spread. The method by Vermeulen et al. (2014), on the other hand, excluded radial velocities located outside of the grid cells and thus relied on at least two transects to obtain sufficient radial velocity samples for initial 3D velocity estimates in most cells. This was reflected in the large changes in the estimated mean velocities caused by including the first few transects (see Figure 7-3).

7.3.2 Effect of section spacing

For most surveys, the error in the velocities caused by decreasing the density of the sampled sections was largest for the vertical velocity component ($MedAPE$ close to 100% across all sites) and smallest for the streamwise component (ranging from 18% to 92%; see Table 7-2). The comparison between the cross-validation error (Table 7-3 in Section 7.3.3) and the errors in Table 7-2 showed

that a doubling of the section spacing roughly led to a doubling of the overall error (expressed as S.D. or $MedAPE$) introduced by kriging interpolation. Only for FLATF and the vertical velocity component at THEAL the error increase was less pronounced or not present at all.

Figure 7-6 shows the error caused by decreasing the sampling density in relation to the distance of the validation measurements to the respective in-channel structure. The error in the streamwise velocity (Figure 7-6a) tended to slightly decrease with the distance to the structure, suggesting that, closer to the fish pass, a denser sampling strategy has the largest effect to reduce the error in the prediction of this velocity component. In contrast, no apparent trend was observed for the cross-stream and vertical velocity components.

Table 7-2. Error in the predicted velocity components when using a doubled spacing of sampled cross sections; FLATF includes data of survey area (A) only.

		Min	Mean	Median	S.D.	Max	MedAPE	N
	ε_u	-0.557	0.002	0.002	0.135	0.597	69.37	
SHREW1	ε_v	-0.603	0.001	0.000	0.108	0.690	74.41	3,425
	ε_w	-0.174	0.000	0.000	0.028	0.178	102.80	
	ε_u	-1.000	0.035	0.008	0.237	1.432	18.10	
SHREW2	ε_v	-1.334	-0.026	-0.029	0.259	1.889	51.59	2,348
	ε_w	-0.356	-0.037	-0.022	0.106	0.311	99.40	
	ε_u	-0.679	0.014	0.003	0.153	0.591	18.22	
SHREW3	ε_v	-0.618	0.030	0.028	0.144	0.525	25.46	1,258
	ε_w	-0.175	0.002	0.004	0.043	0.167	86.44	
	ε_u	-0.539	0.009	0.011	0.067	0.403	92.20	
FLATF (A)	ε_v	-0.337	0.020	0.007	0.091	0.663	95.11	3,797
	ε_w	-0.114	0.001	0.001	0.019	0.120	88.04	
	ε_u	-0.563	-0.002	0.001	0.084	0.499	43.29	
THEAL	ε_v	-0.689	0.008	0.003	0.068	0.550	46.60	2,783
	ε_w	-0.231	0.001	-0.000	0.021	0.121	96.00	

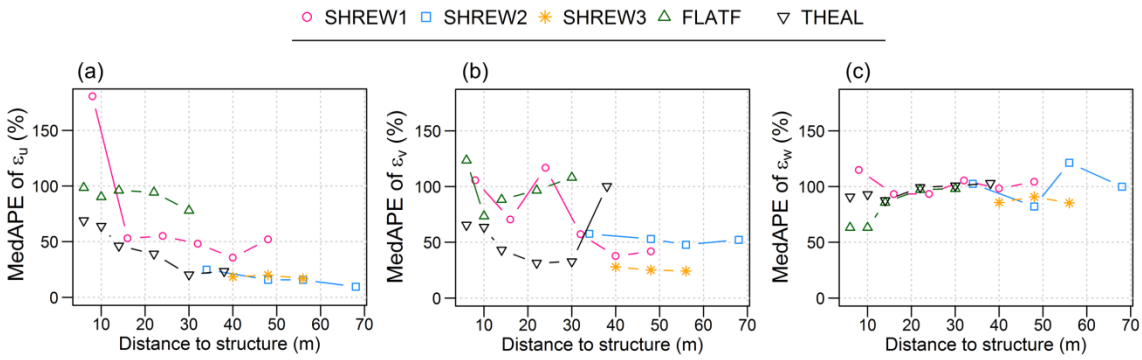

Figure 7-6. $\boldsymbol{MedAPE}$ of $\{\boldsymbol{\varepsilon_u}, \boldsymbol{\varepsilon_v}, \boldsymbol{\varepsilon_w}\}$ computed for the validation samples of each omitted cross section versus the section distance to the weir foot (for SHREW1-3) and fish pass (for THEAL and FLATF)

7.3.3 Effect of kriging interpolation

The results of the kriging cross-validation showed that the smoothing and overall effect of the interpolation on the velocity measurements varied largely between the five ADCP surveys (see Table 7-3 and Figure 7-7). In relative error terms (expressed as $MedAPE$), the sites with the fastest flow conditions (SHREW2-3) showed the lowest errors during cross-validation, whereas the data from FLATF showed by far the largest (see also Figure 7-6). The latter might be explained by a large relative uncertainty in the velocity samples collected within survey area (A) for FLATF, where a considerable proportion (29.2%) of the measured resultant velocities were smaller than the ADCP instrument noise of the radial velocity samples (0.0523 ms^{-1}; see Section 4.2.2.1). The large relative measurement errors may have reduced (or masked) the spatial correlation of the velocity data and thus the information that kriging interpolation is based on.

Table 7-3. Kriging cross-validation results; FLATF includes data of survey area (A) only.

		Min	Mean	Median	S.D.	Max	MedAPE	N
SHREW1	$\varepsilon_{CV,u}$	-0.561	0.000	0.001	0.071	0.517	31.72	6,878
	$\varepsilon_{CV,v}$	-0.529	0.000	0.000	0.072	0.650	45.03	
	$\varepsilon_{CV,w}$	-0.154	-0.000	0.000	0.019	0.164	67.40	
SHREW2	$\varepsilon_{CV,u}$	-1.196	-0.001	-0.001	0.136	1.331	8.69	6,222
	$\varepsilon_{CV,v}$	-1.184	0.000	-0.000	0.139	0.932	29.93	
	$\varepsilon_{CV,w}$	-0.276	0.000	-0.000	0.038	0.248	38.03	
SHREW3	$\varepsilon_{CV,u}$	-0.495	-0.001	-0.000	0.090	0.486	10.26	2,944
	$\varepsilon_{CV,v}$	-0.454	0.001	0.001	0.084	0.397	14.94	
	$\varepsilon_{CV,w}$	-0.128	-0.000	-0.000	0.022	0.116	47.31	
FLATF (A)	$\varepsilon_{CV,u}$	-0.241	-0.000	-0.001	0.049	0.208	77.75	6,642
	$\varepsilon_{CV,v}$	-0.325	0.000	-0.000	0.050	0.340	80.28	
	$\varepsilon_{CV,w}$	-0.067	0.000	0.000	0.013	0.060	75.04	
THEAL	$\varepsilon_{CV,u}$	-0.599	-0.000	-0.001	0.054	0.654	16.55	5,796
	$\varepsilon_{CV,v}$	-0.593	0.000	0.000	0.051	0.859	23.14	
	$\varepsilon_{CV,w}$	-0.386	0.000	-0.000	0.025	0.398	81.39	

The mean errors were very close to zero for all sites, indicating that the velocity predictions through kriging interpolation were unbiased (Webster and Oliver, 2007). The S.D. of the cross-validation errors was lower than the ADCP single ping S.D. for horizontal velocity components in conventional ADCP data processing (see Section4.2.2.1) for all sites apart from SHREW2, where it was slightly larger. Similarly, Jamieson et al. (2011) found the smoothing effect of kriging interpolation to be no greater than the uncertainty inherent in ADCP measurements and argued that the smoothing may even counter the single-ping noise effects on the hydrodynamic maps. In the context of fish passage research, however, the smoothing bears the disadvantage of underestimating the maximum water velocities near the pass entrance. This may bias the identification of hydraulic barriers where the water velocity magnitudes exceed the swimming capabilities of targeted fish species or life stages (see Section 2.3.3). This problem was observed for all five surveys covered here and is also

visible in Figure 7-7, where the maximum measured velocities are shown to exceed the maximum predicted velocities.

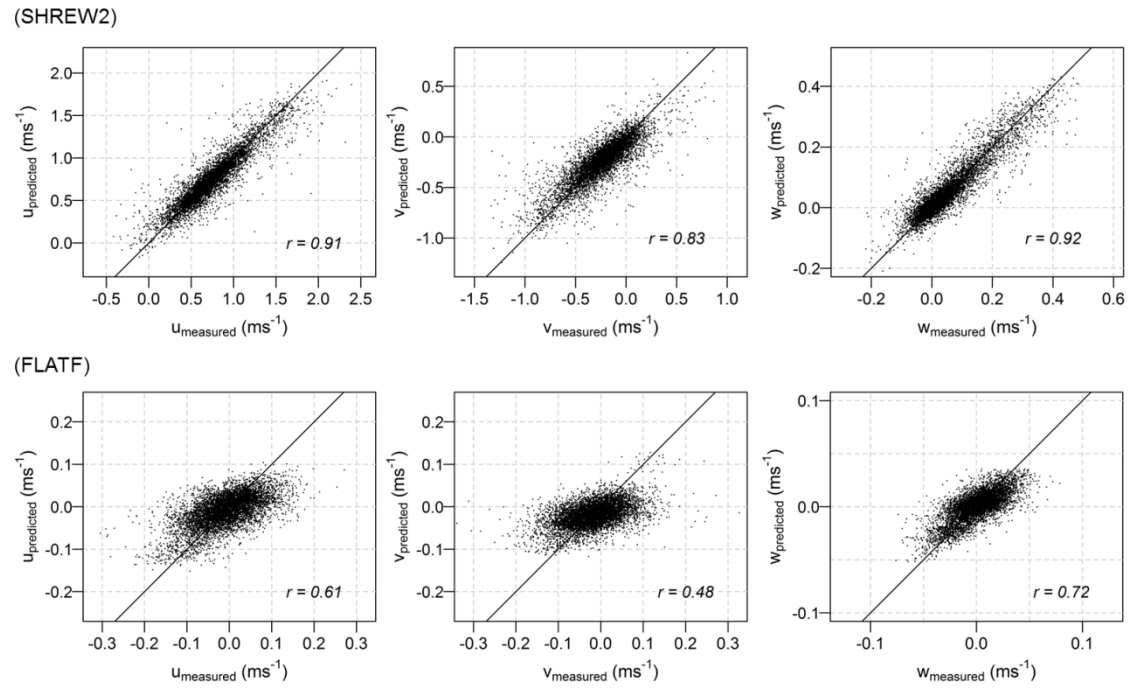

Figure 7-7. Kriging cross-validation results illustrated for the survey with the lowest (SHREW2) and largest relative errors (FLATF); r stands for the correlation coefficient.

7.3.4 Qualitative assessment of near-pass hydrodynamics

7.3.4.1 Shrewsbury vertical slot pass

Figure 7-8 shows the estimated spatial velocity distribution at a depth of 0.5 m below the water surface for SHREW1-3 and Figure 7-9 shows the velocity distribution of two cross sections at 21 m and 40 m distance from the weir foot for all three discharge conditions. The flow maps revealed that the change in discharge did not only cause large variation in the resultant water velocities, but induced three fundamentally different patterns of near-pass hydrodynamics.

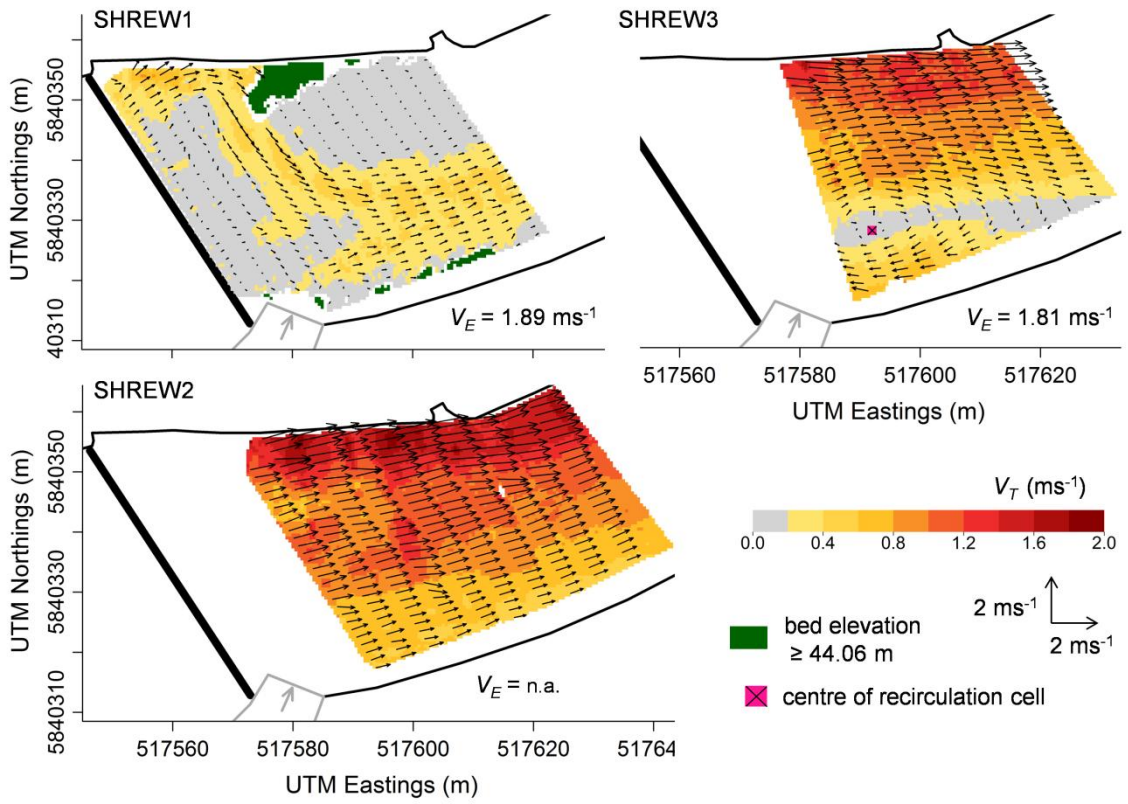

Figure 7-8. Spatial water velocity distribution downstream of Shrewsbury Weir during conditions of low (SHREW1; $\boldsymbol{Q}$ = 7.1 m^{3}s^{-1}), medium (SHREW3; $\boldsymbol{Q}$ = 33.8 m^{3}s^{-1}) and high discharge (SHREW2; $\boldsymbol{Q}$ = 113.9 m^{3}s^{-1}); the plots show the streamwise and cross-stream velocities (depicted as arrows) and the resultant velocity $\boldsymbol{V_T}$ at elevations of 44.06 m (SHREW1), 44.80 m (SHREW3) and 46.49 m (SHREW2), corresponding to 0.5 m below the mean water surface elevation of the respective survey areas; $\boldsymbol{V_E}$ stands for the velocity magnitude measured directly at the entrance of the fish pass.

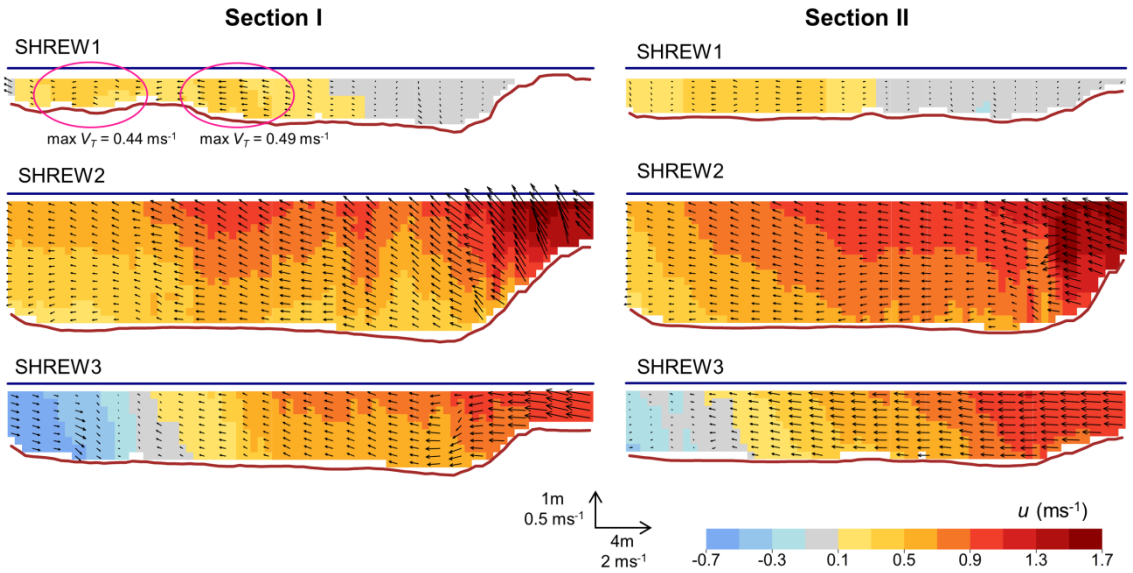

Figure 7-9. Distribution of streamwise ($\boldsymbol{u}$) as well as cross-stream and vertical velocities (depticed as arrows) for the two cross sections I and II (see Figure 7-2) downstream of the foot of Shrewsbury Weir during conditions of low (SHREW1; $\boldsymbol{Q}$ = 7.1 m^{3}s^{-1}), medium (SHREW3; $\boldsymbol{Q}$ = 33.8 m^{3}s^{-1}) and high discharge (SHREW2; $\boldsymbol{Q}$ = 113.9 m^{3}s^{-1}); the velocity plots are displayed such that the viewer is looking into the upstream direction towards the weir. The pink circles highlight areas referred to in the main text.

During conditions of low discharge (SHREW1), the fish pass attraction flow contrasted with the lower velocities in the surrounding area up to a distance of 18 m from the pass entrance into the downstream direction, where it started to merge with the strong water jet flowing over the left side of the weir (see also Figure 4-11 in Chapter 4). At a distance of 21 m from the pass entrance, these two jets of water were still differentiable (see SHREW1, Section I in Figure 7-9). This area can be interpreted as a critical zone for the fish pass attractiveness, because upstream migrating fish might be attracted towards either of these two jets. Salmonids have been shown to migrate upstream along the banks (see Section 2.3.3), so that these fish may tend to follow the jet located closer to the bank, i.e. the jet leading to the pass entrance. On the other hand, it has been suggested that upstream migrants presented with two flows tend to follow that with higher velocities (Scruton et al., 2007). The resultant velocities were slightly larger in the jet closer to the channel centre (as indicated in Figure 7-9), potentially resulting in a stronger attraction of fish and guidance towards this

flow and thus away from the pass. In contrast, the fish pass attraction flow is not discernible within the velocity visualisation for SHREW2-3, meaning that the extent of the attraction flow into the downstream direction was smaller than 12 m for SHREW2 and 9 m for SHREW3 (which are the distances of the respective survey area boundaries to the pass entrance).

During conditions of high discharge (SHREW2), the near-pass hydrodynamics were dominated by the fast velocities (max V_T of 2.15 ms^{-1}) close to the left river bank, and a nearly continuous decrease in velocity magnitudes from the left to the right bank (min V_T of 0.43 ms^{-1}). Neither of the flow visualisations for SHREW2-3 (Figure 7-8 and Figure 7-9) show any hydrodynamic cues indicating the location of the fish pass. Instead, upstream migrants might be attracted towards the left bank and thus away from the pass entrance. While this "false attraction" (Scruton et al., 2007) has not been subject to a scientific study at Shrewsbury Weir, salmon attempting to leap over the weir near the left river bank have frequently been observed at the site.

During conditions of medium discharge (SHREW3), the highest water velocities were, once again, located near the left river bank. The water jet over the left side of the weir induced a large recirculation cell along the right river bank up to a distance of around 50 m downstream from the pass entrance. The phenomenon is clearly visible both in Figure 7-8 and Figure 7-9. As outlined in Chapter 2 (Section 2.3.2), recirculation eddies near the fish pass are known to mask the pass entrance, so that upstream migrants might be drawn towards the bank opposite to the pass. The reversing flow effectively counters the jet of water issued from the pass entrance. This explains the low extent of the attraction flow relative to SHREW1, despite similar water velocity magnitudes measured directly at the pass entrance (see V_E in Figure 7-8).

7.3.4.2 Flatford Mill super-active baffle pass

At Flatford Mill, the fastest flow was issued from the sluice in the north-west direction of the study site, inducing relatively large velocities along the right river

bank (max V_T of 0.73 ms^{-1}; see Figure 7-10). Figure 7-11 shows the flow field that fish encounter when entering the survey area and indicates that fish attempting to migrate upstream may initially be attracted towards the sluice. The water jet issued from the fish pass, on the other hand, is hardly discernible in the flow field visualisation, indicating a poor hydrodynamic attraction during the flow conditions at data collection time. However, it has to be noted that the errors introduced by kriging interpolation were large for FLATF (see the cross-validation results in Section 7.3.3), and the true velocities near the pass entrance were underestimated. Within a distance of 5 m from the fish pass entrance, the maximum predicted resultant velocities were as low as 0.16 ms^{-1}, whereas the maximum measured mean resultant velocities (i.e. prior to kriging interpolation) were 0.30 ms^{-1}.

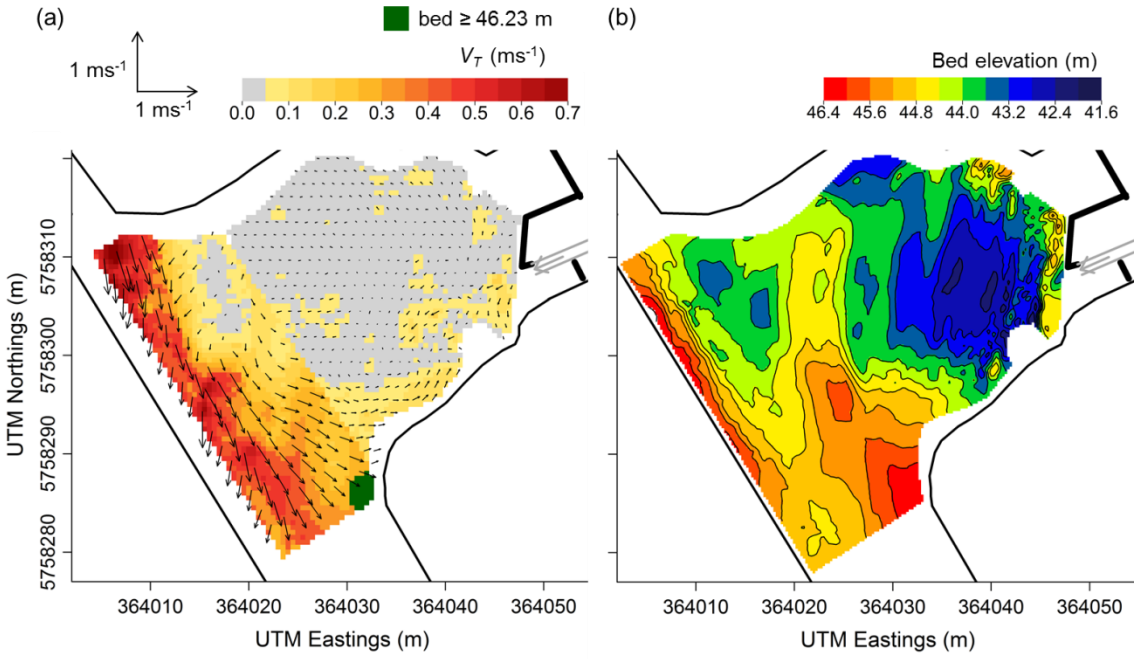

Figure 7-10. Water velocity distribution (a) and bathymetry (b) downstream of the fish pass at Flatford Mill; the water velocities are shown for an elevation of 46.23 m above sea level, corresponding to a depth of 0.5 m below the mean water surface elevation.

The majority of the predicted velocities in survey area A, i.e. the area surrounding the fish pass entrance (see Figure 7-2), had absolute magnitudes below 0.05 ms^{-1}. In the configuration used for FLATF the RioGrande ADCP was

not capable to accurately capture variation in velocities at such fine detail. Other instrument configurations enable measurements at precisions larger by one to two orders of magnitude (e.g. Water Mode 11; Teledyne RDI, 2002), but the water depths on site (max depth of 4.71 m below the water surface) were too large for these configurations to be successfully used, and they are generally not suitable for sites with large turbulence as expected near fish pass entrances (Teledyne RDI, 2002b). Apart from the generally low water velocities, the necessity to divide the survey area into two parts for separate geostatistical analysis and kriging interpolation resulted in apparent interpolation artefacts at the boundary between survey area A and B (see Figure 7-10).

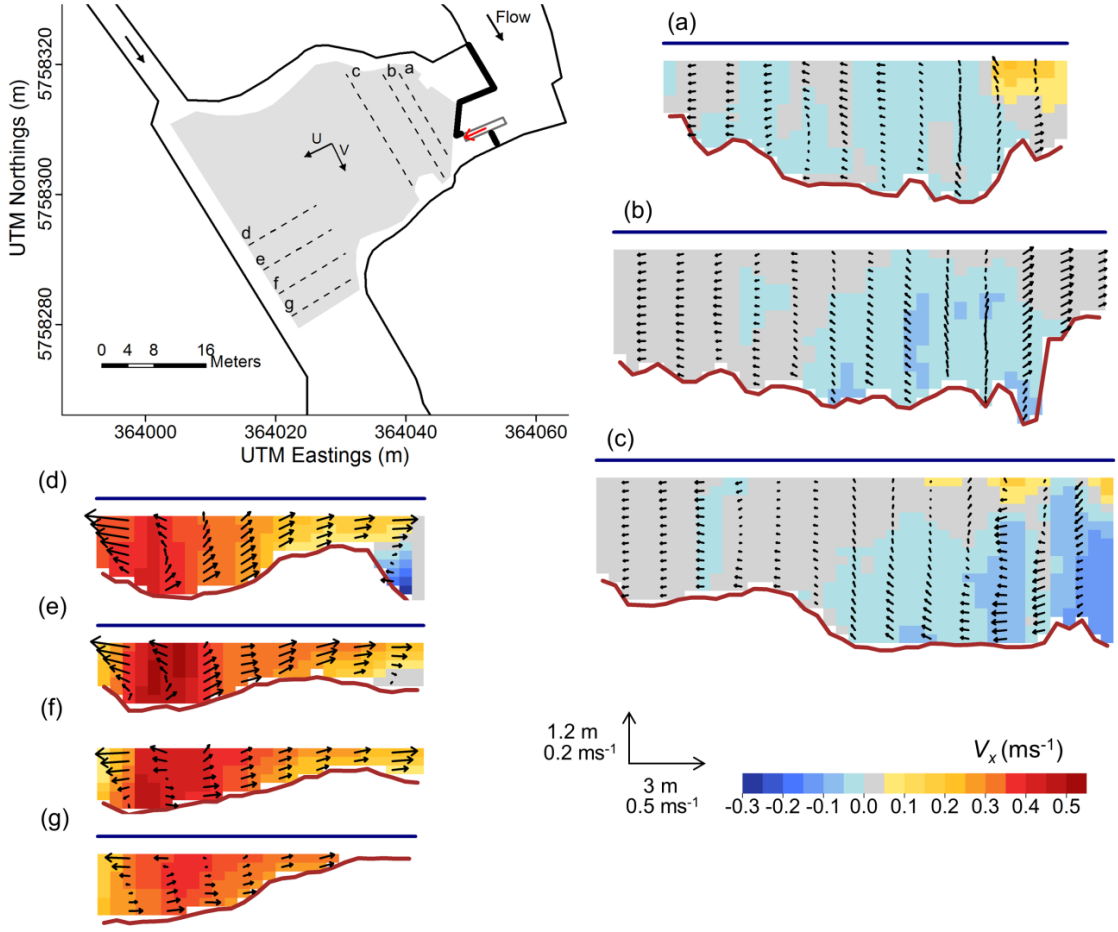

Figure 7-11. Water velocity distribution for selected cross sections downstream of the super-active baffle pass at Flatford Mill; the sections (a) to (g) are displayed such that the viewer is looking into the upstream direction, with the velocities rotated such that $\boldsymbol{V_x}$ points towards the viewer, i.e. perpendicularly out of the page, and the arrows depict the horizontal and vertical velocities perpendicular to $\boldsymbol{V_x}$.

7.3.4.3 Theale nature-like bypass channel

The velocity visualisations for THEAL (see Figure 7-12 and Figure 7-13) revealed three main jets of water into the area downstream of the migration barrier: (i) the relatively weak, but discernible jet issued from the bypass channel entrance, (ii) the strong jet issued from the super-active baffle pass, which appears to have been enforced by flow over the weir near the pass entrance (this would explain the diversion of the jet orientation towards the left bank rather than parallel to the fish pass entrance), and (iii) the flow approximately over the centre of the weir. Furthermore, the visualisation shows two large-scale eddies near the by-pass channel entrance and near the right river bank. The latter involves a reverse flow along the right river bank, reaching up to a distance of ≈23 m from the migration barrier (see also section (d) in Figure 7-13, which shows upstream flow along the right and downstream flow along the left bank). Assuming that upstream migrants tend to move against the flow direction (see Section 2.3.3), they may be repelled by the reverse flow and instead approach the migration barrier along the left river bank. Closer to the bypass channel entrance, upstream migrants are confronted with another recirculation cell along the left bank. In contrast to the recirculation cell found for SHREW3 (see Section 7.3.4.1), the location and flow direction of the cell were such that the flow issued from the by-pass channel was not countered, but potentially enforced. If fish were to avoid the reverse flow near the left bank, they would approach the by-pass channel entrance more centrally, and might initially be drawn towards the faster jet issued from the super-active baffle pass. Given the close proximity of the super-active baffle pass to the by-pass channel entrance (and in future, that of the turbine from the HEP to be installed at the site; see Section 7.2.1), the migratory delay may not be as pronounced as, for example, for SHREW1, where fish might be guided towards the side opposite to the fish pass.

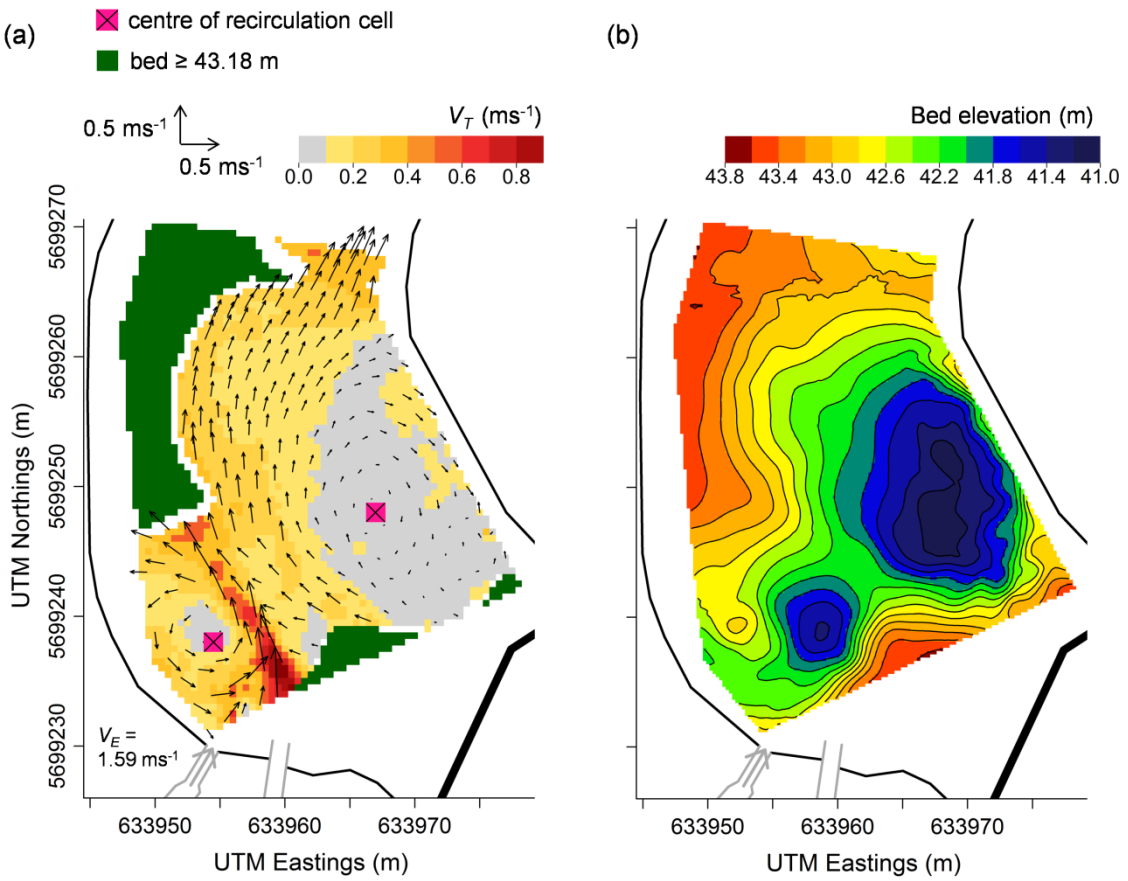

Figure 7-12. Water velocity distribution (a) and bathymetry (b) downstream of the nature-like by-pass channel near Theale on the River Kennet; the water velocities are shown for an elevation of 43.18 m above sea level, corresponding to a depth of 0.5 m below the mean water surface elevation; V_E stands for the velocity magnitude measured directly at the entrance of the fish pass.

The ADCP survey near Theale was undertaken during conditions of very low discharge (see Table 3-4). The large scour whole near the right bank (maximum depth of 2.68 m below the water surface) indicates the presence of a fast flow over the right side of the weir during conditions of higher discharge, potentially leading to the false attraction of upstream migrants towards that side.

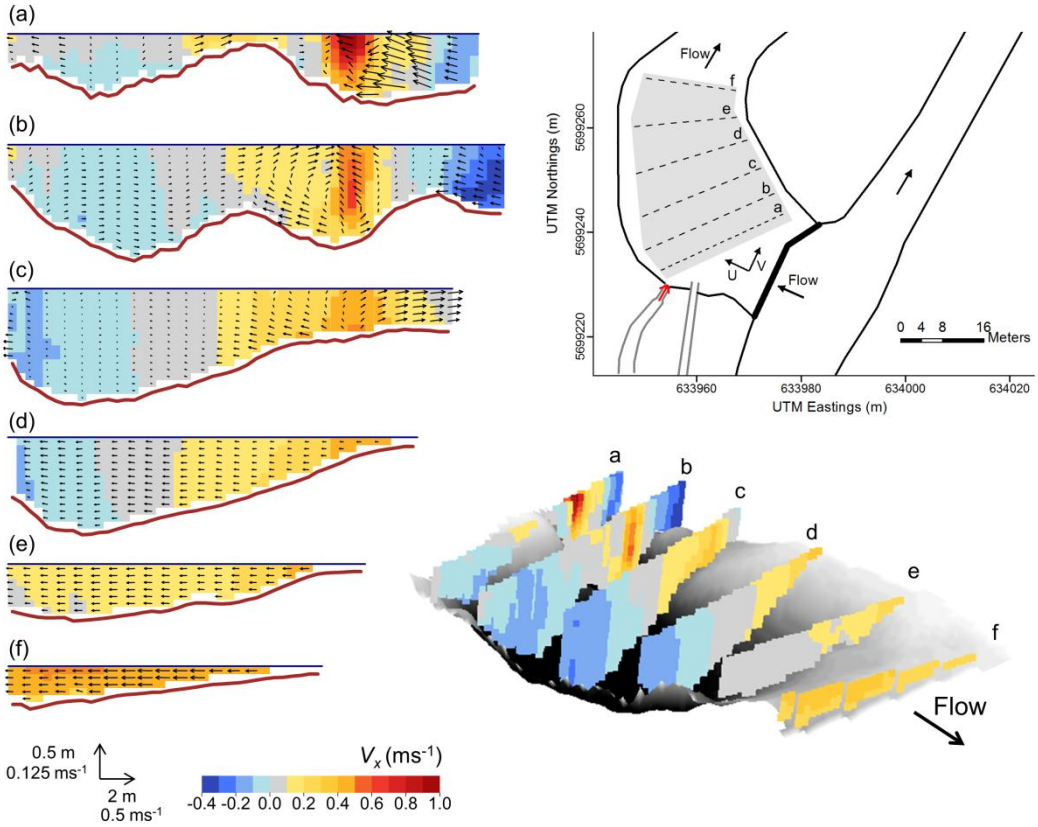

Figure 7-13. Water velocity distribution for selected cross sections downstream of the nature-like bypass cannel at Theale; the sections (a) to (f) are displayed such that the viewer is looking into the upstream direction towards the weir, with the velocities rotated such that $\boldsymbol{V_x}$ points towards the viewer, i.e. perpendicularly out of the page, and the arrows depict the horizontal and vertical velocities perpendicular to $\boldsymbol{V_x}$. The bottom right plot shows the location of the cross sections on a 3D bathymetric display.

7.3.5 Quantitative assessment of near-pass hydrodynamics

7.3.5.1 Recirculation cells

Figure 7-8 (SHREW3) and Figure 7-12a show the centre locations of the recirculation cells identified for SHREW3 and THEAL, respectively. The analysis revealed cell diameters (and circulation) of ≥21.2 m (≤ -1.74 m^2s^{-1}) for SHREW3 as well as ≥15.6 m (≥8.73 m^2s^{-1}) and 15.6 m (-2.32 m^2s^{-1}) for THEAL. Only the clock-wise rotating recirculation cell for THEAL was fully captured, whereas the other cell at THEAL and that for SHREW3 extended beyond the respective

survey areas. This might be considered in future research on a more accurate characterisation of recirculation cells near fish pass entrances.

7.3.5.2 Effective surface of attraction

The analysis resulted in S_{eff} values of 316.4 m² and 239.5 m² for SHREW1 and THEAL, respectively. The result for THEAL includes both the attraction flow from the nature-like bypass channel and the super-active baffle pass next to it. Figure 7-14 and Figure 7-15 illustrate the isolation of the distorted, coherent water body, which the metric S_{eff} is based on, for the surveys SHREW1 and THEAL and at a depth of 0.35 m below the water surface.

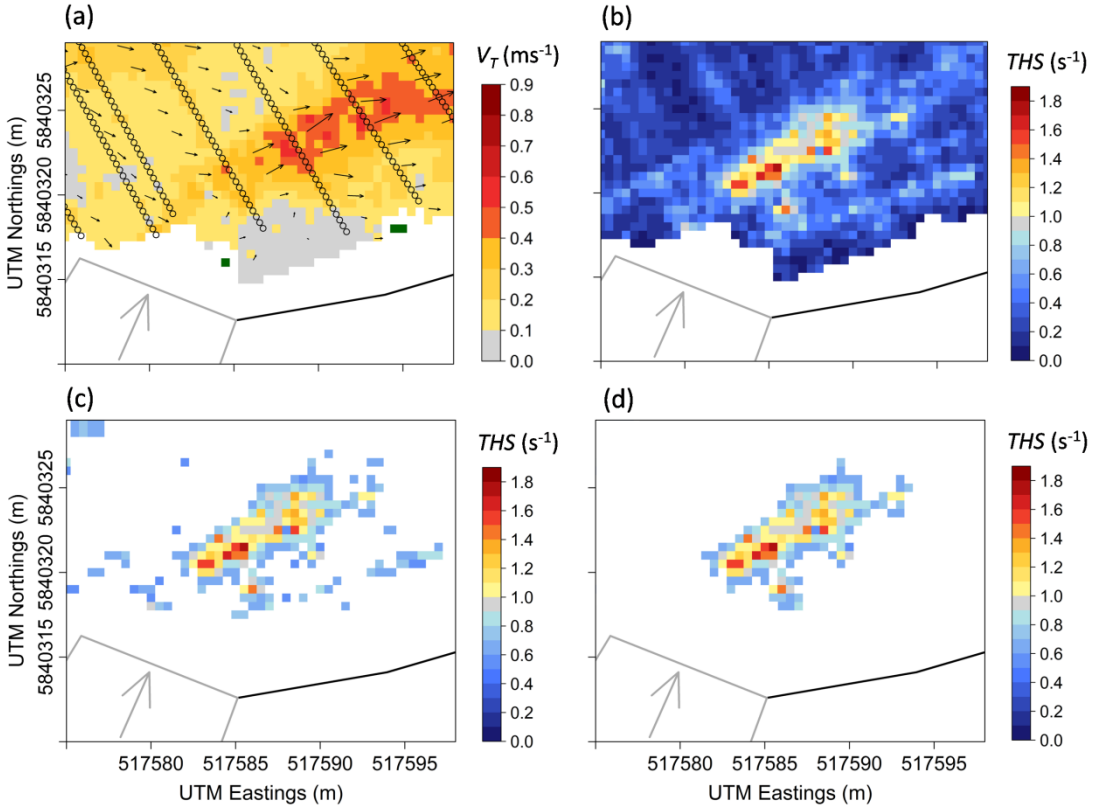

Figure 7-14. Isolation of the flow field distortion to derive the metric $\boldsymbol{S_{eff}}$, shown for the survey SHREW1 and a depth of 0.35 m below the water surface; (a) Spatial distribution of resultant velocities near the fish pass entrance; the small black circles denote the sampled cross sections; (b) Spatial distribution of $\boldsymbol{THS}$; (c) Spatial distribution of $\boldsymbol{THS}$ exceeding the threshold $\boldsymbol{k}$ (0.57 s^{-1} for SHREW1); (d) Largest coherent flow field near the fish pass entrance with $\boldsymbol{THS}$ exceeding $\boldsymbol{k}$.

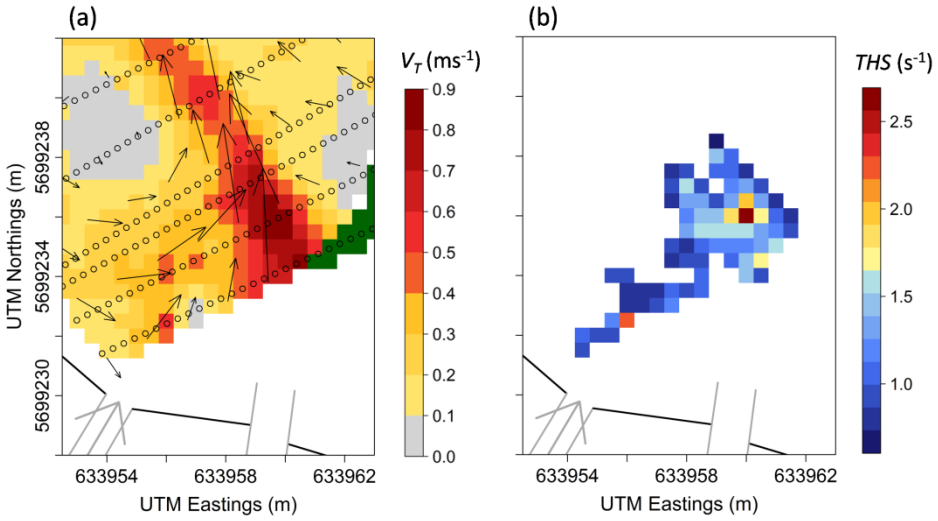

Figure 7-15. Isolation of the flow field distortion to derive the metric $\boldsymbol{S_{eff}}$, shown for the survey THEAL and a depth of 0.35 m below the water surface; (a) Spatial distribution of resultant velocities near the fish pass entrance; the small black circles denote the sampled cross sections; (b) Largest coherent flow field near the fish pass entrance with $\boldsymbol{THS}$ exceeding the threshold $\boldsymbol{k}$ (0.72 s^{-1} for THEAL).

The spatial isolation of the flow distortion near fish pass entrances can enable a more detailed quantitative description of the attraction flow. For example, Figure 7-16 shows the variation of the isolated flow distortion with depth in terms of intensity (expressed as the mean THS) and volume. It illustrates that for both SHREW1 and THEAL, the jet of water issued from the pass entrance induced the most intensive and largest flow distortions in the upper parts of the water column (down to 0.65 m below the water surface for SHREW1 and 0.95 m for THEAL), whereas those parts closer to the river bed were less intensive and considerably smaller in volume. This information indicates that the flow from these passes might be less effective in attracting bottom-oriented species to the fish pass entrance.

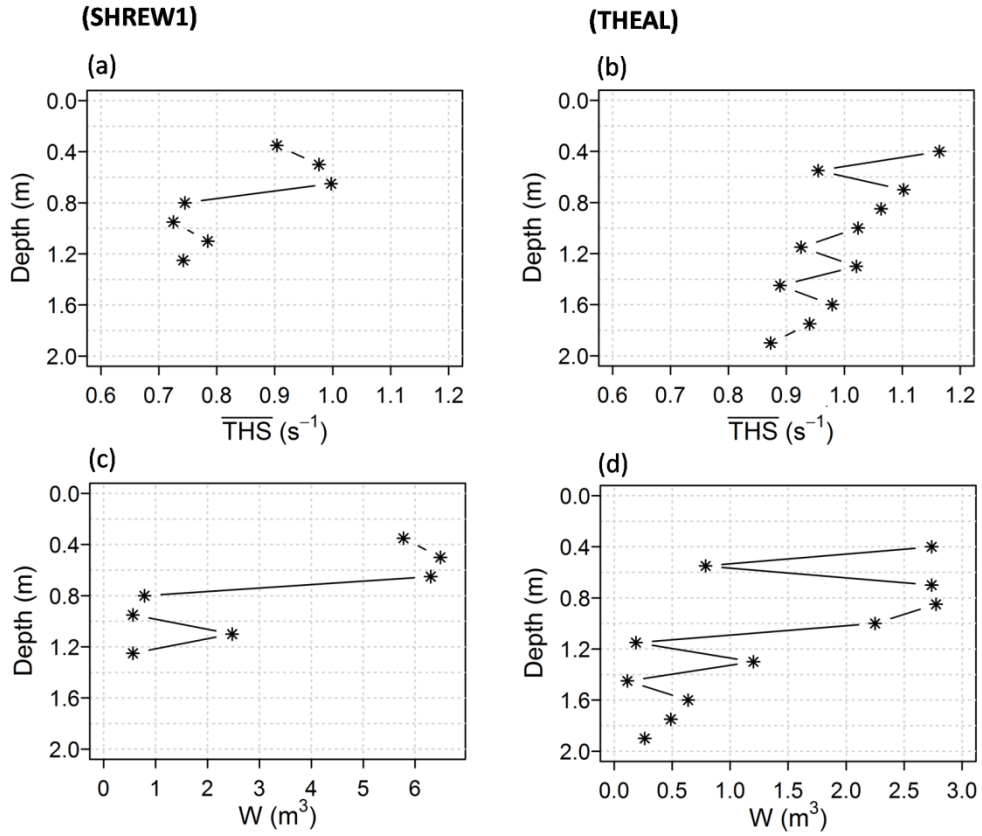

Figure 7-16. Variation of the isolated flow distortion in terms of the mean $\boldsymbol{THS}$ of all isolated interpolation cells at a given depth ($\overline{\boldsymbol{THS}}$, plots a and b) and in terms of volume ($\boldsymbol{W}$, plots c and d), shown for the ADCP surveys SHREW1 (plots a and c) and THEAL (plots b and d).

The parameter S_{eff} is used here as a concept demonstration and further refinement is needed to provide a biologically meaningful measure of fish pass attractiveness. In this study, the threshold k was defined arbitrarily based on the statistical distribution of THS in the flow field surrounding the respective fish pass (see Section 7.2.4.4.2), resulting in values of 0.57 s^{-1} (SHREW1) and 0.72 s^{-1} (THEAL). Additional biological studies are required to define a biologically meaningful threshold. Further refinement is also required to separate the flow field distortion induced by the fish pass from that induced by the channel boundaries and from spatial velocity variation introduced through interpolation artefacts (see also Section 7.3.5.3). While not investigated here, the effect of the spatial resolution used in computing THS from the interpolated flow field (i.e. the parameters Δx, Δy and Δz in Equation (2-8)) on the metric

S_{eff} and its biological meaning requires assessment in further studies. Finally, the testing of the S_{eff} for fish pass attraction efficiency relies on complementary biological data (see also Section 8.5).

The S_{eff} was not quantified for the surveys SHREW2-3 because of the inability to measure sufficiently close to the pass entrance to capture the attraction flow (see Section 7.3.4.1). For FLATF, the very low water velocities surrounding the pass entrance and associated large relative measurement errors (see Section 7.3.4.2) meant that no meaningful results could be obtained for this site.

7.3.5.3 Total acceleration

Figure 7-17 shows the spatial distribution of a for four of the ADCP surveys. For SHREW1 and THEAL, the fish pass attraction flows were found to induce total water accelerations that were distinct from their surroundings. For FLATF, on the other hand, the acceleration induced by the attraction flow is hardly discernible on the visualisation. Instead, the largest accelerations were found along the right river bank and these presumably were induced by the water jet from the sluice and the large variation in bathymetry (steep slope) along that bank (see also Figure 7-10b).

For SHREW3, the visualisation of a (erroneously) suggests that the largest total accelerations were located along the sampled cross sections. This was caused by interpolation artefacts in the predicted flow field. As shown in the cross-validation (see Table 7-3), the kriging smoothing effect was lowest for the data from SHREW3, which might explain why this problem was particularly pronounced for the data from this survey. Further smoothing of the velocity maps through statistical techniques may reduce these effects, but would distort the resulting values of a and thus complicate their interpretation in relation to fish behaviour. While not investigated here, these errors may be more effectively reduced by physical (rather than statistical) techniques, such as the velocity distribution correction based on mass conservation (continuity correction), as suggested by Tsubaki et al. (2012).

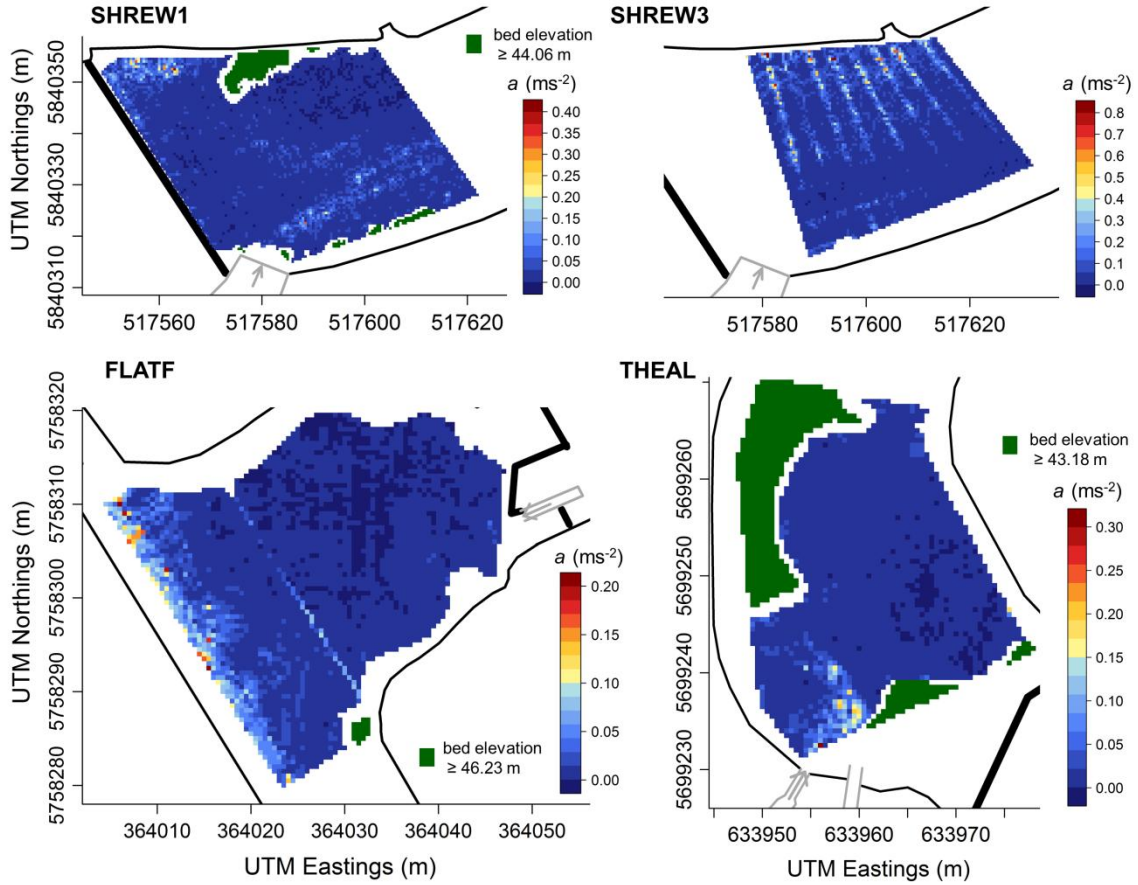

Figure 7-17. Spatial distribution of the 2D total acceleration measure $\boldsymbol{a}$, shown for an elevation of 44.06 m (SHREW1), 44.80 m (SHREW3), 46.23 m (FLATF) and 43.18 m (THEAL), corresponding to a depth of 0.5 m below the mean water surface elevation

7.3.6 Remarks on the ADCP data quality enhancement techniques

The study presented here involved the evaluation of some of the ADCP data quality enhancement methods proposed in the PhD research at a further site (Flatford Mill) and thus enabled an extension of the evaluation presented in Chapter 4. At Flatford Mill, the ADCP-IMU integration led to the correction of heading data for a total of 432 ensembles, corresponding to 5.2% of all ensembles. Half of these ensembles were found to have absolute heading errors ≤6.0 deg. Large absolute errors (ranging up to 81.3 deg) were found exclusively along the river bank opposite to the fish pass entrance, i.e. in the south-west of the survey area (see Figure 7-2b). The findings indicate the

presence of ferro-magnetic materials along that river bank and confirm the necessity of the ADCP-IMU integration to correct for ADCP compass bias.

Moreover, for 338 ensembles (4.0 % of all ensembles), the boat velocity had to be estimated based on the TS data due to invalid BT signals. Nearly all of the affected ensembles were located in the immediate vicinity of the fish pass entrance or within the fast water jet issued from the sluice. The proportion of affected ensembles was considerably smaller than that found at Shrewsbury Weir (see Section 4.3.1), which can be explained by the relatively calm hydraulic conditions and few measurements in very shallow areas at Flatford Mill.

7.3.7 Main lessons learned for fish pass monitoring and design

7.3.7.1 Large effects of variation in discharge

The findings of this chapter showed that the natural changes in discharge throughout the year can induce strongly varying near-pass hydrodynamic conditions with potentially large effects on fish pass attractiveness and potentially upstream passage success. Thus, for any particular site, the near-pass hydrodynamics require to be quantified multiple times for a comprehensive understanding of fish pass attractiveness. Clearly, the attractiveness of a fish pass is most relevant during times of increased fish migration. Figure 7-18 puts the near-pass hydrodynamics identified during three different discharge conditions at Shrewsbury Weir in relation to the main upstream migration period of Atlantic salmon at the site. The unsuitable near-pass hydrodynamics found for conditions of medium and high discharge (i.e. formation of eddies masking the pass entrance and potentially false attraction towards the bank opposite from the pass) are likely to dominate the period of the autumn salmon run at the study site (typically in the time from October to December; Cowley, 2011). The spring salmon run period is characterised by lower discharges, so that the potentially more attractive near-pass hydrodynamic conditions found for SHREW1 are more likely to occur during this period. However, Atlantic salmon

prefer peak discharges to move upstream (Cowley, 2011), so that these fish cannot be assumed to “make use” of these more favourable near-pass hydrodynamic conditions.

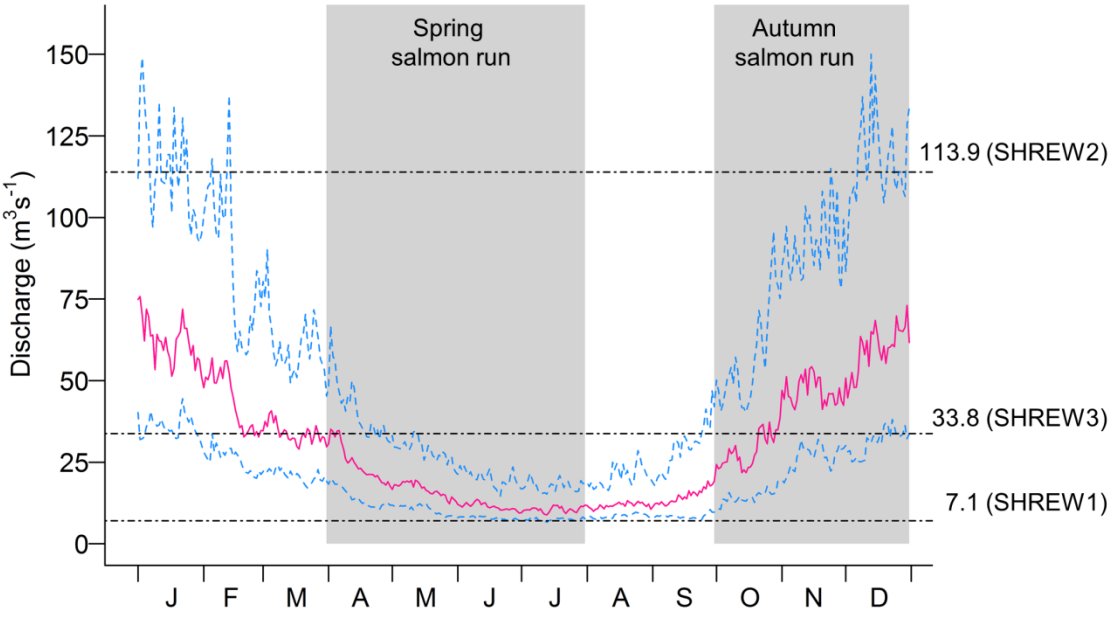

Figure 7-18. Discharge at Shrewsbury Weir throughout the year in relation to Atlantic salmon migration period; the pink line shows the median discharge of each day of the year from 1953-2015 and the dashed blue lines show the 25th and the 75th percentile; the salmon run periods for Shrewsbury are based on Cowley (2011).

7.3.7.2 Traditional indicators of fish pass attractiveness

Traditional guidelines describe the extent of the attraction flow as a function of the discharge through the pass and the velocity at the entrance (see Section 2.3.1). The methodology application at the study site in Shrewsbury illustrated that this traditional criterion falls short in capturing the effects of interactions of the flow issued from the pass with other near-pass hydrodynamic features. A change from low to medium discharge at the site led to a reduction in the extent of the attraction flow by more than 50% (see Section 7.3.4.1). This change was not reflected in the point velocity magnitude measured at the fish pass entrance (which was largely unaffected by the changes in discharge). Measurements beyond the fish pass structure were essential to identify the likely cause of the

reductions: the formation of a recirculation cell with reverse flow towards the pass entrance, presumably countering the attraction flow.

7.3.7.3 Different types of recirculation cells near fish passes

Two of the five ADCP surveys presented in this chapter revealed recirculation cells downstream of the respective fish pass entrances (SHREW3 and THEAL). These were caused by fast jets of water discharged from (or over) the studied obstructions. Such jets can occur at many migration barriers (e.g. turbine discharge from HEPs or flow from sluice gates) so that the formation of recirculation cells downstream of fish passes may be an abundant phenomenon and the effects of these cells on fish pass attractiveness pose a relevant topic for further research.

The results presented here indicate that there are at least two types of recirculation cells, which interact differently with the attraction flow issued from the pass (see Figure 7-19). One type involves recirculating flow in the direction opposed to that of the water jet issued from the pass entrance. The effects of this type of recirculation cell on fish pass attractiveness are (i) a reduction in the spatial extent of the fish pass attraction flow, and (ii) the masking of the pass entrance due to the formation of zones of very low velocities or reverse velocities, which upstream migrants tend not to prefer (see Section 2.3.3). This type corresponds to that found at Shrewsbury Weir during medium discharge conditions and described by Larinier (2002; see Section 2.3.2) as an example for unsuitable near-pass hydrodynamic conditions.

The second type of recirculation cell is located and oriented such that its downstream current aligns with the flow issued from the fish pass, so that the flow remains distinct in the downstream direction. This type involves upstream currents located besides the pass entrance, so that the preferred pathways of upstream migrants may effectively be channelized towards the pass. Such a recirculation cell was found at the nature-like bypass channel near Theale, where it was caused by the interaction of the flow issued from the (older) technical fish pass (located next to the by-pass channel) with the bathymetric

variation downstream of the pass, specifically a steep reduction in depth diverting the flow. Complementary biological studies are required to validate the described effects of recirculation currents in the field and to allow for a more differentiated view on this relevant near-pass hydrodynamic feature.

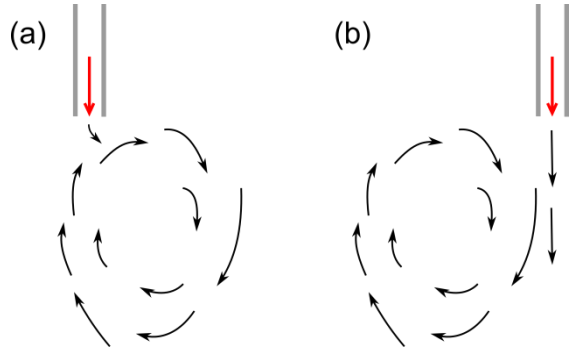

Figure 7-19. Examples of recirculation cells near fish pass entrances reducing attractiveness (a) and potentially increasing attractiveness (b); the red arrow marks the fish pass entrance location and the black arrows depict flow directions; drawings not to scale

7.3.7.4 Fish pass structural effects

Reviews of previous fish pass monitoring studies showed that the same fish pass type can have attraction efficiencies ranging from 0% to 100%, depending on other covariates affecting passage success (Bunt et al., 2012; see Section 2.5.1). This was also reflected in the findings of this chapter. The near-pass hydrodynamics at the same site (Shrewsbury Weir) varied largely with factors independent of fish pass structural characteristics and despite very similar water velocities at the pass entrance. Nonetheless, fish pass structural characteristics can provide useful information to explain near-pass hydrodynamics. For example, the low extent of the attraction flow for the super-active baffle pass at Flatford Mill may be explained by low velocities directly at the pass entrance and the relatively high fish pass slope, a characteristic that can reduce the fish pass attractiveness (Noonan et al., 2012). Where factors other than structural characteristics determine the near-pass hydrodynamic conditions (e.g. the hydraulics induced by competing flows and bathymetric patterns at a particular site), these can be effectively identified through the ADCP-based methodology proposed in the PhD research.

7.4 Conclusions

This chapter presented an evaluation of the methodology developed in the PhD research, covering multiple fish pass sites and conditions of low, medium and large discharge. The results showed that the methodology is suitable to identify hydrodynamic features, the relevance of which to fish passage success has been emphasised in fish pass design manuals and review texts. The hydrodynamic visualisations resulting from the methodology are adequate to describe the strength (velocity magnitudes), spatial extent and orientation of the fish pass attraction flow in relation to other, potentially competing flows. The methodology is particularly suitable to identify recirculation cells and to enable a detailed interpretation of their effect on the hydrodynamic fish pass attractiveness. Moreover, the spatially continuous 3D water velocity distribution obtained from the methodology enables the visualisation of the velocities within consecutive cross sections with varying distances to the pass entrance. This provides an indication of the flow field potentially encountered by fish approaching the migration barrier and forms a useful starting point for the formulation of hypotheses to explain swim path selection of upstream migrants in relation to complex hydrodynamics.

Beyond visual examination, the hydrodynamic maps are useful to derive quantitative indicators of fish pass attractiveness. An effective methodology for the quantitative characterisation of recirculation cells in terms of their centre location, spatial extent and intensity has been proposed. Moreover, the suitability of the ADCP-based near-pass hydrodynamic maps for the derivation of the effective surface of attraction, a novel attractiveness indicator proposed as part of the PhD research, has been demonstrated. It was shown that the flow distortion induced by the water jet issued from the pass entrance can be isolated from the surrounding hydrodynamics, enabling the detailed quantitative characterisation of the attraction flow in 3D. This can, for example, be useful to objectively evaluate whether a fish pass is more attractive to surface-oriented and bottom-oriented fish species. Finally, the quantification of the spatial distribution of metrics based on spatial velocity gradients (e.g. a and SVG; see

Chapter 2) was found to be affected by artefacts in the flow maps stemming from the spatial velocity interpolation.

This chapter also covered an analysis of the effect of the spatio-temporal sampling strategy on the ADCP-based flow maps. The results showed that, after the 7^{th} transect measurement along a cross sections, the effect of including further transects on the estimated temporally averaged velocity is similar across sites, conditions of discharge and distance of the sampled section from the in-channel structure. The finding is useful for the formulation of efficient sampling strategies and provides a valuable input to the development of robust sampling protocols for ADCP-based hydrodynamic mapping. The analysis of the effect of the section spacing revealed evidence to suggest that the largest gains in precision can be obtained by increasing the section density in those parts of the survey area that are closest to the migration barrier and fish pass.

The transferability of the methodology across sites was found to be constrained by the RC platform control and power consumption at sites with water velocities above approximately 2.6 ms^{-1}, as well as by the ADCP-inherent instrument noise leading to large relative errors in hydrodynamic maps at sites with very low water velocities. A detailed discussion of the methodology transferability in relation to on-site conditions has been provided in Chapter 8. Further research is required to assess methods for the reduction of interpolation artefacts and to extend the analysis presented here to a larger range of sites. This may enable a robust, quantitative definition of the methodology transferability in relation to site characteristics.

Chapter 8

SYNTHESIS

8.1 Introduction

In this final chapter, the main findings of the PhD research have been synthesised, addressing **objective 6** of the thesis (see Section 1.2):

to synthesise the findings from objectives (1) to (5) into a methodology for the ADCP-based near-pass hydrodynamics quantification and a methodology appraisal in terms of effectiveness, practicability and transferability

This chapter is structured as follows: **Section 8.2** reviews the main steps of the methodology for near-pass hydrodynamics quantification developed in the PhD research. **Section 8.3** answers the research question posed in Chapter 1 by appraising the developed methodology in terms of effectiveness, practicability and transferability. In **Section 8.4** the contributions of the PhD research beyond fish passage are discussed. Finally, **Section 8.5** highlights future research requirements.

8.2 Methodology for near-pass hydrodynamics quantification

Table 8-1 provides an overview of the methodology developed in the PhD research, synthesising the findings from both the literature reviews (Chapters 2 and 3) and the experiments (Chapters 4 to 7) presented in this thesis. The methodology involves repeated transect ADCP measurements from an RC platform to quantify the temporally averaged water velocities along densely spaced cross sections, followed by the estimation of the mean 3D flow field through spatial interpolation using geostatistics. The predicted 3D distribution of mean velocities provides an interim result, from which hydrodynamic features that indicate fish pass attractiveness can be derived. While the ADCP-based mapping of river hydrodynamics has been evaluated in previous studies (see Chapter 3), an outstanding characteristic of the developed methodology (and a major contribution of the PhD research) is the integration of techniques to increase the accuracy and availability of ADCP data as well as the practicability of ADCP deployment in the environmental conditions associated with fish passes and other engineered in-channel structures.

Table 8-1. Overview of the ADCP-based methodology for near-pass hydrodynamics quantification

	Task	Task specification based on research findings
DATA COLLECTION	**(i) SELECT EQUIPMENT**	
	ADCP selection	Consider instrument capability of raw data output and integration of external sensors as well as site conditions (depth and velocity)
	Platform selection	Consider platform speed and pitch/roll stability; fastest available RC platforms for fast-flowing sites (up to V_T≈2.6ms^{-1}); platform prototype (Chpt. 6) for sites with V_T<1.7ms^{-1}; requirement of on-board logging system
	Positioning system	Tracking TS; in future: potential for stereo visual odometry
	(ii) DEFINE MOVING-VESSEL SAMPLING STRATEGY	
	Survey area	Upstream direction: foot of fish migration barrier; Downstream direction: at least sufficiently far to capture flow distortion induced by flow from pass;
	Sampling sections	Recommendation of maximal 4m section spacing; increased (e.g. doubled) cross section density in area closest to in-channel structure
	Transects per section	Minimum of 6 to 8 transects per section at mean platform speed of 0.4ms^{-1}; including 8th transect leads to mean change of $\{\bar{u}, \bar{v}\}$ by ≈0.03ms^{-1}
	(iii) IMPLEMENT ADCP SURVEY	
	Compass calibration	Prior to all surveys, following guidelines in Mueller et al. (2013)
	Moving bed test	Multiple stationary tests with positioning system reference in locations where moving bed is likely the greatest (Mueller et al., 2013)
	Data recording	Wireless NTP network on site for synchronisation of on-board computer (logging ADCP and IMU) and on-shore computers (logging TS data); avoid wireless sensor data links; need for dedicated logging software
	Platform operation	Smooth, B_T≈0.4ms^{-1}; using real-time track visualisation software
PROCESSING	**(iv) CORRECT BIASED DATA**	
	Heading	ADCP-IMU integration algorithm with sliding window width of 21 ensembles
	Boat velocity	TS-based boat velocity estimation for ensembles with invalid or lacking BT
	(v) ESTIMATE SPATIAL DISTRIBUTION OF MEAN 3D VELOCITIES AND BATHYMETRY	
	Transect averaging	3D mean velocity estimation using method by Vermeulen et al. (2014); sensitivity of estimates to mesh cell dimensions to be considered
	Spatial interpolation	Ordinary kriging interpolation applied separately to each of $\{u, v, w\}$ as well as depth following guidelines in Webster & Oliver (2007); main source of uncertainty in near-pass quantification, requirement for further research
ANALYSIS	**(vi) DERIVE INDICATORS OF HYDRODYNAMIC FISH PASS ATTRACTIVENESS**	
	Qualitative indicators	Visualisation of 2D flow near surface (surface-oriented fish), near bed (bottom-oriented fish) and for cross sections of interest; description of: attraction flow (extent, orientation), competing flows, recirculation
	Quantitative indicators	Derivation of metrics indicating fish pass attractiveness: effective surface of attraction (S_{eff}), characterisation of recirculation cells, spatial distribution of flow acceleration (a) and THS

The methodology consists of six stages covering the tasks from equipment selection to the quantification of indicators of hydrodynamic fish pass attractiveness (see Table 8-1). In the following sections, these stages and the intended methodology outputs have been reviewed, drawing on the findings of the PhD research.

8.2.1 Intended methodology outputs

The literature review presented in Chapter 2 highlighted a lack of common metrics to assess the hydrodynamic attractiveness of fish passes in the field. This complicated the answering of the fundamental question, *what* variables the methodology should be designed to measure (see Section 2.6). In the absence of standardised quantitative indicators, the methodology was formulated to enable:

(i) the identification of near-pass hydrodynamic features, the ecological relevance of which had been emphasised in established fish pass design manuals and review texts (see Section 2.3),

(ii) the quantification of novel hydrodynamic metrics proposed as part of the PhD research and indicating fish pass attractiveness in the context of upstream passage (see Section 7.2.4.4.2), and

(iii) the quantification of selected metrics previously used in the context of downstream passage (see Section 2.6.1), based on the consideration that these may also be of relevance to upstream migrants (see Section 2.4.5).

8.2.2 Equipment selection

The literature review on ADCP-based hydrodynamic mapping (Chapter 3) and the methodology evaluation studies (Chapters 4 and 7) highlighted key criteria for the selection of ADCP models, deployment platforms and positioning systems to ensure the accurate methodology implementation. Beyond the equipment available on the market, the PhD research involved the development

of prototype equipment (Chapter 6) and assessment of emerging technologies (Chapter 5), which can support the methodology implementation in the future.

8.2.2.1 ADCP model

The suitability of an ADCP model for a specific site depends on the hydraulic site conditions (maximum depths and velocities) as outlined in Section 3.2.7. Beyond these basic selection criteria, the implementation of some parts of the methodology relies on ADCP models that offer sufficient user access and the output of minimally processed data to facilitate the integration of external sensors and the use of unconventional data processing methods. These instrument capabilities are specifically required for the correction of biased instrument heading data with the proposed ADCP-IMU integration technique, the reprocessing of water velocity data based on boat velocities estimated from TS positioning, and the processing method by Vermeulen et al. (2014) to reduce errors from flow heterogeneity (see Chapter 4). Based on this, the 1,200 kHz RioGrande ADCP was identified as the preferred instrument for the methodology evaluation in the PhD research. Using the software tools developed in the PhD research (see also Section 8.3.2.2.2), all parts of the developed methodology can be readily implemented with this instrument. Further software development and cooperation with ADCP manufacturers is required to extend the applicability of the data quality enhancement techniques to a wider range of ADCP models (see Section 8.5.4).

8.2.2.2 ADCP platform

While, in principle, the methodology can be implemented with any type of ADCP platform, RC boats were preferred in the PhD research because they increase the flexibility and operational safety of data sampling in small to medium sized rivers, relative to tethered or manned boats (see Section 3.2.8). For sites with fast flowing water, the fastest available RC platforms dedicated to ADCP measurements are preferable (see Table 3-2), because they enable measurements in high-velocity areas close to the fish pass entrance and migration barrier. In the PhD research, the methodology was implemented with

the ARC-Boat platform. It was found to provide sufficient thrust and manoeuvrability for repeated transect measurements in areas with resultant water velocities up to ≈2.6 ms^{-1}. This corresponds to the maximum temporally averaged resultant water velocity that was measurable close to the water surface during the methodology evaluation at the fastest flowing site (i.e. the survey denoted SHREW2; see Chapter 7). It is about half of the maximum ARC-Boat speed in standing water (see Table 3-2). This information provides an indication of the applicability (in terms of the water velocity threshold) of platforms other than the ARC-Boat. The exact threshold for a specific ADCP platform may vary with platform hull design features and the flow complexity induced by the in-channel structure and fish pass under study. Beyond the criterion of platform speed, the platform stability against pitch and roll is to be considered in the platform selection. In an evaluation of basic platform hull forms (see Section 6.3.1), the platform roll stability was found to increase over-proportionally with the platform width, so that the use of larger platforms limits potential errors from periodic ADCP tilt.

The methodology implementation relies on the availability of an on-board logging computer with software to record data from the ADCP and the other on-board sensors (see also Section 8.2.4.1). A laptop within a plastic enclosure mounted on board was used in the methodology evaluation (see Figure 4-2 in Chapter 4). However, this is a sub-optimal solution for the wide-spread methodology use in practice because it involves unnecessarily high power requirements, equipment cost and risk of damage. As part of the PhD research, prototype ADCP deployment equipment has been developed to enable a more practicable and accurate methodology implementation. This included:

(i) a low-cost on-board data logging system to support the time-synchronised recording from multiple on-board sensors and the real-time monitoring of platform health features, such as the remaining battery capacity, from the shore (see Sections 6.2.3 and 6.3.4.3),

(ii) a system for the platform propulsion control via an integrated microcontroller, supporting features of autonomous platform operation

to facilitate the accurate implementation of pre-defined sampling strategies (see Sections 6.2.3 and 6.3.4.3), and

(iii) a small-sized ADCP platform that integrates the systems described in (i) and (ii), and is suitable for the cost-effective methodology implementation at sites with lower water velocities (<1.7 ms^{-1}; see Section 6.3.5).

The findings from the design and assessment of this equipment can inform the development of products to be considered in the equipment selection for future methodology applications (see Section 6.3.4).

8.2.2.3 Positioning system

The tracking TS was identified as a suitable technology to achieve ADCP positioning at cm-level accuracy and precision, provided continuous line of sight between the TS and a reflecting prism installed on the ADCP platform (see Section 4.2.5). The time synchronisation of the TS and ADCP data requires particular consideration, as it was found to be the main error source in TS-based ADCP positioning (see also Section 4.3.3).

This local positioning system is preferable to GNSS-based positioning, because fish pass sites are frequently installed close to river banks, where vegetation can block the line of sight to GNSS satellites. In the PhD research, the precision of GNSS positioning was found to degrade in the environmental conditions near fish passes. Among four different GNSS systems evaluated in Chapter 5 (covering RTK, PPK and SBAS-corrected systems), only one achieved 2D position accuracies within the sub-meter criterion given in hydrographic surveying standards (see Section 5.4.1). The results showed that at sites with continuous tree cover along one of the river banks, also RTK systems with on-site base station can suffer from degradations in precision by more than an order of magnitude below manufacturer-stated instrument capabilities. Based on the findings of the PhD research, the use of GNSS for ADCP positioning can be recommended only at sites with very good sky view throughout the survey area, and when employing systems with geodetic grade antennas as well as

rigorous discarding of samples below RTK or PPK quality during post-processing (see also Section 5.4.3).

In search for positioning systems offering a good compromise between equipment cost and accuracy, stereo visual odometry from the domain of mobile robotics was identified as a promising solution (see Section 5.2). The empirical assessment of the technique on an ADCP platform (see Chapter 5) resulted in mean 3D position errors of 0.067 m per metre displacement, for a basic sparse visual odometry algorithm. At the end of four slowly driven consecutive river crossings, the 2D position error was found to be 0.81 m (see Section 5.4.2.1). The statistical error analysis presented in this thesis has informed effective strategies to improve the positioning accuracy, so that stereo visual odometry can become useful for future applications of ADCP-based hydrodynamics mapping near in-channel structures (see Section 5.4.2.3). The technique has the advantage of low equipment cost and may become particularly useful for measurements covering larger river reaches, where the prerequisite of continuous line of sight can make the TS-based solution unpractical (see Section 4.3.3).

8.2.3 Definition of sampling strategy

The methodology is based on a moving-vessel sampling strategy, because this allows for coverage of a large survey area within relatively little time and does not require the exact locations of hydrodynamic features relevant to fish pass attractiveness to be known *a priori* (see Section 3.3.1).

8.2.3.1 Survey area

The definition of the survey area to be covered at a specific fish pass site is not straightforward, because the spatial extent of the attraction stage within the process of fish passage and thus that of the relevant near-pass hydrodynamics have not been defined in previous studies. Based on the PhD research, it is recommended to define the foot of the physical migration barrier as the boundary of the survey area in the upstream direction (subject to controllability of the ADCP platform; see Section 8.3.3). The quantification and visualisation of

the flow issued from or over the migration barrier support the explanation and interpretation of near-pass hydrodynamic features forming further downstream of the barrier. Moreover, measurements close to the fish pass entrance and in-channel structure support the identification of “hydraulic barriers” (see Section 2.3.3) by comparing the typically high water velocities near the structures with the swimming capabilities of targeted fish species or life stages.

In the downstream direction, the survey area is recommended to reach at least sufficiently far to capture the spatial extent of the flow field distortion induced by the water jet issued from the fish pass. This is based on the assumption that upstream migrants may use the flow field distortion as cue guiding the fish to the pass entrance (see also Section 2.4.5). Observations of the water surface can provide an indication of the extent of the flow field distortion and thus the minimum survey area to be covered. Ideally, the survey area would reach further into the downstream direction to support the identification of migration pathways that fish may prefer when approaching the barrier. Knowledge of these pathways supports the interpretation of the near-pass hydrodynamic features in terms of their relevance to passage success.

The survey area should ideally cover the full width of the river channel in order to identify flows potentially competing with the attraction flow.

8.2.3.2 Number of transects and section spacing

There has been a lack of sampling protocols for ADCP-based hydrodynamic mapping applications (see Section 3.3.1). This complicates the *a priori* determination of the number of transects per section required to isolate the temporally averaged water velocity and the spacing of sampling sections required to capture relevant hydrodynamic features.

The near-pass hydrodynamics presented in Chapters 4 and 7 were achieved with a minimum of 4 to 8 transects per section and a maximum cross section spacing of 4 m. The effect of the number of transects on the 3D velocity estimated with the method by Vermeulen et al. (2014) was quantified based on data from two different fish pass sites and conditions covering low, medium and

high discharge. It was found that, irrespective of the site, conditions of discharge or distance from the fish pass, the mean change in the velocities of a cross section caused by including data from the 8th or further transects was close to 0.03 ms^{-1} for the streamwise and cross-stream velocities and 0.01 ms^{-1} for the vertical velocities. When considering the velocity changes normalised by the area-mean velocity, on the other hand, the effects of including another transect were several times larger for the cross sections with low velocities than for those with high velocities. This suggests that faster flowing sites require less transects per cross section to achieve a velocity estimate that is robust in relative terms. The information can be used to weigh up the gain in adding more than seven transects per section against the loss in the spatial section density or survey area that can be covered within limited time (see Section 7.3.1) and thus supports the formulation of efficient sampling strategies. Further studies at a wider range of sites are required to specify the validity of the finding with respect to the site conditions (see also Section 8.5.4).

It was found that a doubling in the section spacing approximately leads to a doubling in the uncertainty of the velocity maps introduced through spatial interpolation. For the streamwise velocity component, evidence was found to suggest that denser section spacing provides the largest gains in precision in those parts of the survey area that are closest to the in-channel structure and fish pass (see Section 7.3.2). This is to be considered in the definition of the sampling strategy, for example by doubling the section density for areas close to the in-channel structure.

The results presented in this thesis provided initial insights on the effects of the spatio-temporal sampling strategy, which provide impulses for further research towards the establishment of robust sampling guidelines for ADCP-based hydrodynamic mapping applications. Ideas for such research have been given in Sections 8.5.1 and 8.5.4.

8.2.4 Implementation of ADCP survey

This section covers the equipment setup and operation on site. A distinct characteristic of the methodology is the integration of data from multiple sensors onboard and onshore, so that a particular emphasis is to be put on the data recording and synchronisation strategy. Standard procedures prior to ADCP data collection, specifically, the on-site calibration of the ADCP-internal fluxgate compass as well as moving-bed tests (Mueller et al., 2013), are part of the methodology, but have not been a particular focus of the PhD research and thus not discussed in further detail.

8.2.4.1 Data recording

The methodology involves the time-synchronised recording of data from the ADCP, positioning system and an IMU. The proposed data recording strategy involves three computers (two logging computers and one control computer) linked via a WLAN network set up on site (see Figure 8-1). The PC times of the computers are time-synchronised via a local GPS-based NTP server (represented by one of the computers) and NTP client software (running on the other two computers). The software on the logging computers is operated through a control computer via wireless access (e.g. through SSH or Windows Remote Desktop Connection). To increase the reliability of the data transmission and minimise errors from transmission delays, the sensor data are recorded exclusively via wired connections to the respective computers. The sensor data are temporally aligned during post-processing, based on their PC time stamps.

This data recording strategy has proven successful during the methodology evaluation at various sites (see Chapter 7). Although the wireless transmission of the TS data to the on-board computer would reduce the number of required logging computers, it was found not to be an optimal solution in terms of data quality. The approach was implemented at one of the study sites and, on some occasions, resulted in data transmission delays, presumably caused by temporary WLAN signal losses (see Sections 4.2.2.3and 4.3.3.2). Low-cost

SBCs can be used as logging computers to reduce the overall equipment cost. For example, in the methodology evaluation, a Raspberry Pi 2 was used to log the TS data and as an NTP server (see Section 7.2.2.4).

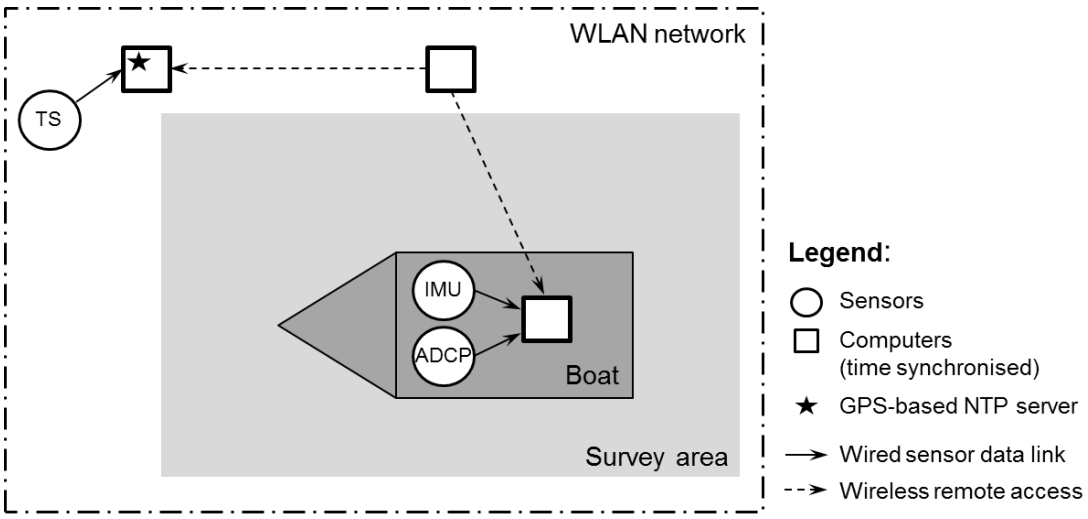

Figure 8-1. Data recording setup for methodology implementation (drawing not to scale)

8.2.4.2 Platform operation

A smooth platform operation is generally preferable to avoid dynamic compass errors of magnitudes below the detection capability of the ADCP-IMU integration algorithm (see Section 8.2.5.1). Likewise, lower platform speeds are favourable to reduce positioning errors resulting from a temporal offset between data from the ADCP and the TS (see Section 4.3.3). The near-pass hydrodynamics presented in Chapter 7 were achieved with mean platform speeds ranging from 0.4 to 0.8 ms^{-1}. Further studies are required to assess the role of the platform speed within the spatio-temporal sampling strategy and its effect on the resulting near-pass hydrodynamics.

During all ADCP surveys presented in this thesis, the accurate implementation of repeated transect sampling strategies has been facilitated through the real-time platform track visualisation software developed as part of the PhD research (see Section 4.2.2.2). The software helps to repeatedly sample the same cross section or to conduct temporally separated measurements along the same

section (e.g. when surveying the same site repeatedly) without the need for physical markers along the river banks. While not investigated here, it is likely that the use of the track visualisation software reduces the track variability between transects and thereby increases the radial velocity samples gained per transect and thus the data collection efficiency.

8.2.5 Correction of data biases

Prior to further data processing, the methodology involves the correction of the radial velocities for bias stemming from temporary errors in the ADCP compass data as well as the correction or recovery of radial velocities with invalid or lacking BT signals.

8.2.5.1 Heading data

The ADCP-IMU integration presented in Chapter 4 offers a low-cost and robust solution for the correction of ADCP compass data biased by magnetic interference and or rapid platform acceleration. The integration algorithm requires the user to define a sliding window width (see Section 4.3.1.2). At mean platform speeds of ≈0.4 ms^{-1}, a width of 21 ensembles was found to be suitable to reliably detect errors from magnetic interference and large dynamic compass errors while preventing over-correction of the data. At the two evaluation sites, the technique detected errors up to 35 deg (Shrewsbury Weir) and 81 deg (Flatford Mill) with the largest errors occurring close to the river banks (see Figure 4-5 in Chapter 4). Given the magnitude of these errors and the fact that fish passes are often installed close to river banks, these findings underline the relevance of compass errors in ADCP-based near-pass hydrodynamics quantification and the need for techniques to counter this data quality issue.

The loose integration of the ADCP compass with a low-cost MEMS IMU is favourable to previously suggested solutions involving the replacement of all compass data with those from another heading sensor (e.g. GNSS compass or gyrocompass; Marsden et al., 2002; Zhao et al., 2014), because it is unaffected by heading misalignment between the ADCP and the external heading source

and largely unrestricted in terms of environmental conditions (see Section 3.4.2). The only prerequisite for its use is that the compass errors are temporary rather than persistent throughout the survey. Unless the ADCP vessel itself causes permanent magnetic interference (e.g. steel hulled vessels), this assumption will hold for many sites, where significant magnetic interference is likely to occur only in the immediate vicinity of modified river banks or engineering structures.

8.2.5.2 Boat velocity data

BT signal losses were found to occur particularly frequently downstream of in-channel structures, presumably due to increased water turbidity and turbulence. The proportion of ensembles affected by this issue depends on the hydraulic on-site conditions and can reach up to nearly one quarter of all ensembles of an ADCP survey near a fish pass, as shown in one of the methodology evaluation studies (see Section 4.3.3.1). The methodology defined here involves the estimation of the boat velocity for the affected ensembles based on the TS position data, and the recalculation of the water velocities during post-processing. While the use of positioning systems (mostly GNSS) to estimate boat velocities has been a common procedure in ADCP measurements (e.g. Mueller et al., 2013; Rennie & Rainville, 2006), the TS-based technique is particularly suitable for near-pass hydrodynamics quantification, because:

(i) the TS continuously achieves cm-level positioning accuracy, also in the ecologically relevant areas close to river banks and in-channel structures, where GNSS positioning accuracy tends to degrade (see Section 8.2.2.3), and

(ii) the technique replaces only invalid or lacking BT signals, rather than all (as done in common manufacturer-provided ADCP software). Thus, it takes into account that (unbiased) BT is considered the most accurate method for the correction of ADCP data for instrument velocities (Rennie et al., 2002; Teledyne RDI, 2011; see Section 3.2.3).

8.2.6 Estimation of the 3D distribution of mean velocities

8.2.6.1 Transect averaging

The corrected radial velocity measurements are combined to estimate the temporally averaged 3D water velocities using the processing method suggested in Vermeulen et al. (2014; see Section 3.4.1.1). Near in-channel structures, the technique was found to be favourable to conventional methods of repeated transect processing methods because it reduces the errors introduced by spatially heterogeneous flow, a problem that had previously caused ADCP measurements near in-channel structures to be strongly biased (e.g. Johnson et al., 2009; see Section 3.4.1). In the PhD research, the technique was found to lead to significantly different 3D flow field quantifications and near-pass hydrodynamic metrics compared to conventional repeated transect processing (see Section 4.3.2).

The application of the technique requires particular consideration of the dimensions of the mesh cells for which the mean 3D velocities are estimated. Small mesh cells are desirable to reduce errors from remaining spatial flow heterogeneity and to increase the spatial resolution of the predicted velocity, but rely on a sufficiently large sample of radial velocities to isolate the temporal velocity average. The near-pass hydrodynamics presented in this thesis (see Chapters 4 and 7) were obtained with mesh cell dimensions of 2.00 x 0.40 x 0.15 m^3. The estimated mean velocities were shown to be sensitive particularly to the longitudinal cell dimension, which defines the maximum distance of the radial velocity samples from the straight mesh fitted through all samples of a cross section. In Section 4.3.2, further enhancements of the processing technique have been suggested to enable a decrease in this cell dimension while minimising the associated loss in radial velocity samples (see also Section 8.5.4).

8.2.6.2 Spatial velocity and depth interpolation

The methodology involves the prediction of water velocities in unmeasured locations within the survey through ordinary kriging interpolation (see Section

7.2.3.3), which has been a commonly used method in ADCP-based hydrodynamic mapping of river reaches (see Section 3.3.1.3). Likewise, the depths measured along each of the ADCP beams are used to predict a bathymetric map, which supports the interpretation of the near-pass hydrodynamics. The error analysis presented in this thesis (see Sections 7.3.2 and 7.3.3) revealed that the spatial interpolation of the mean velocities remains the largest source of uncertainties in the near-pass hydrodynamics quantification and a primary area for future research (see also Sections 8.3.1.2 and Section 8.5.2).

The PhD research highlighted two main issues when using ordinary kriging interpolation in ADCP-based near-pass hydrodynamics quantification:

(i) the smoothing effect of the technique leads to an underestimation of the (typically high) velocity magnitudes close to the fish pass and migration barrier, and
(ii) the method introduces interpolation artefacts, which can bias the derivation of hydrodynamic metrics based on the spatial velocity gradients in the water velocities.

The former issue requires careful consideration when relating the predicted velocity magnitudes to known fish swimming capabilities. It is recommended to perform a comparison of the maximum measured and predicted velocities to obtain an indication of the severity of the smoothing effect. Alternatively, a full cross-validation analysis can be conducted to quantify the effect (see Section 7.3.3).

8.2.7 Derivation of near-pass hydrodynamics descriptors

In the last stage of the methodology, the 3D flow field quantification is used to:

(i) visually assess the near-pass hydrodynamics against qualitative guidelines from the literature, and
(ii) to derive quantitative metrics potentially indicating fish pass attractiveness.

In a first step, the estimated 3D flow field is “sliced” to obtain 2D visualisations of the velocity distribution at depths and sections of interest. Based on the fish species and life stage targeted, the velocities near the surface or near the river bed may be studied in more detail. The visualisation of the flow distribution within several cross sections with decreasing distance from the pass entrance provides and illustration of the flow field that upstream migrants may encounter when approaching the pass entrance and can be useful to indicate preferred swim paths (see, for example, Figure 7-13). The 2D flow field visualisations are used to identify the following features affecting the fish pass attractiveness (see Section 2.3):

(i) the spatial extent and orientation of the attraction flow,
(ii) the interactions of the attraction flow with competing flows issued from or over the migration barrier (e.g. overflow of weirs or flow issued from HEP turbines), and
(iii) recirculation currents that may affect the detectability of the pass entrance.

In a second step, some of these features are described quantitatively, along with other hydrodynamic metrics previously used in eco-hydraulic fish passage research (see Section 2.6.1). Specifically, the quantitative description of the following indicators of fish pass attractiveness is proposed:

(i) the effective surface of attraction, S_{eff}, which is a novel indicator capturing the detectability of the water jet issued from a fish pass in 3D space (see Section 7.2.4.4.2),
(ii) the centre location, spatial extent and intensity of recirculation cells, which, depending on their interaction with the attraction flow, reduce the spatial extent of the attraction flow or may enforce its detectability (see Section 7.3.7.3), and
(iii) the spatial distribution of the total flow acceleration, a, or other measures based on spatial velocity gradients, which can help to

explain the swimming behaviour of migrating fish (see Sections 2.4 and 7.3.5.3).

The capabilities and limitations of the developed methodology to achieve these outputs have been discussed in the following section.

8.3 Methodology appraisal

In Chapter 1, the overarching research question of this PhD thesis has been formulated:

At the current state and availability of technology, is it possible to define an effective and practicable methodology for the measurement of hydrodynamic indicators of fish pass attractiveness in non-wadeable rivers?

This research question involves three criteria to be reflected upon in its answering: effectiveness, practicability and transferability (see Figure 8-2).

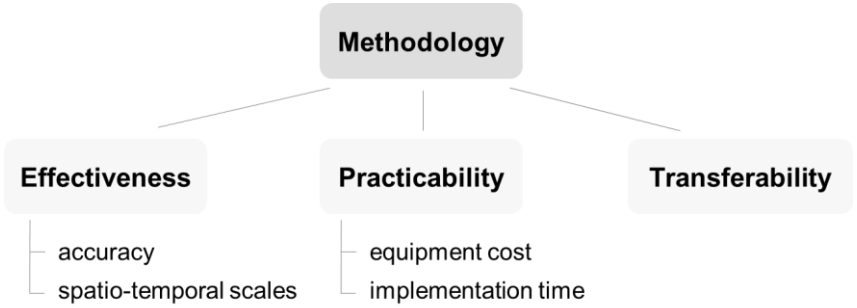

Figure 8-2. Dimensions of the PhD research question

The effectiveness relates to the adequacy of the methodology to deliver the intended methodology outputs, i.e. to measure variables that indicate hydrodynamic fish pass attractiveness (see Section 8.2.1). It implies that the measurement occurs with sufficiently high accuracy and at spatial and temporal scales relevant to migrating fish. The practicability criterion concerns the implementation of the methodology at adequate cost and time effort to support its wide-spread uptake in river management. Finally, the transferability relates to

the applicability of the methodology across fish pass sites, with a particular focus on non-wadeable rivers.

8.3.1 Methodology effectiveness

8.3.1.1 Adequacy to measure indicators of fish pass attractiveness

In an evaluation covering multiple sites and conditions of low, medium and high discharge (see Chapter 7), the proposed methodology was shown to be adequate to deliver the intended methodology outputs listed in Section 8.2.1, subject to site conditions within the transferability constraints (see Section 8.3.3).

8.3.1.1.1 Qualitative hydrodynamic descriptors

The methodology is suitable to describe the spatial extent, orientation and strength (velocity magnitudes) of the fish pass attraction flow and its spatial distinction from and interaction with other, potentially competing flows. In particular, the methodology was shown to be effective for identifying recirculation cells and to indicate their effect on the pass attractiveness as discussed in Section 7.3.7.3. Moreover, the flow maps resulting from the methodology are adequate to identify zones that are potentially critical to the rapid fish passage at barriers (see also Section 8.3.4.4).

8.3.1.1.2 Quantitative hydrodynamic descriptors

The developed methodology was shown to provide a means for extracting the flow distortion induced by the attraction flow from the surrounding flow field, providing novel opportunities for the detailed quantitative characterisation of attraction flows in 3D space (see Section 7.3.5.2). Such analysis allows for the development of novel indicators of hydrodynamic fish pass attractiveness, such as the biologically effective surface of attraction (S_{eff}) proposed in this research. The quantification of this and other indicators based on the isolation of the attraction flow is, however, constrained by the capability to measure hydrodynamics close to the fish pass entrance (see also Section 8.3.1.1.3). In

the research presented in this thesis, this was possible for only two out of five ADCP surveys. Moreover, additional biological knowledge on the swimming behaviour of upstream migrants is required to calibrate the derivation of S_{eff} in terms of the threshold k evoking a reaction in upstream migrants and to validate its explanatory power of fish pass attractiveness.

The methodology also enables the quantitative characterisation of recirculation cells near the pass entrance. The analysis of recirculation cells presented in Chapter 7 resulted in the identification of cell centre locations, which were plausible based on visual examination of the predicted flow field.

Finally, the ADCP-based flow maps are, in principle, suitable to derive metrics based on spatial velocity gradients as used in previous fish behavioural studies (e.g. SVG, THS, a; see Section 2.6.1). As highlighted in Section 8.2.6.2, these can, however, be affected by interpolation artefacts.

8.3.1.1.3 Limitations to the adequacy of the methodology

Several ADCP limitations to the measurement of fish pass attractiveness indicators have been effectively countered through techniques developed as part of the PhD research. These involve the lack of (accurate) data close to the river banks or in-channel structures due to magnetic compass interference, BT signal loss or degradation of GNSS-based positioning accuracy. Remaining limitations arise from:

(i) the inability to sample velocities at sufficiently high frequencies to accurately measure temporal velocity fluctuations (see Section 3.3.2), and

(ii) the inability to measure water velocities in the immediate vicinity to the water surface, river bed and banks (see Section 3.2.6).

The former means that the methodology is not suitable to directly quantify the intensity and periodicity of temporal velocity changes. This limits the ability to predict whether vortical flows identified within the near-pass hydrodynamics have an attracting effect to migrants (e.g. allowing them to decrease muscle

activity; Coutant, 1998; Liao, 2007; Liao et al., 2003) or a disturbing effect (e.g. reducing their stability and maximum swimming speed; Enders et al., 2003; Lupandin, 2005; Tritico & Cotel, 2010). Generally, fish do not experience mean, but instantaneous velocities, so that the methodology only gives an indication of the flow field actually encountered by upstream migrants at a specific point in time (e.g. Shields & Rigby, 2005). This limit is, however, inherent to all representations of temporally averaged velocities, irrespective of whether the flow field is quantified using steady-state hydrodynamic models (e.g. Lindberg et al., 2013; Nestler et al., 2008) or in-field water velocity measurements.

The latter limitation excludes the hydrodynamic characterisation of areas potentially preferred by some fish species and life stages (e.g. primarily surface-oriented fish species such as upstream migrating European eel, or bottom-oriented species such as river lamprey). With the instrument configuration for the studies presented in this thesis (see Section 7.2.2.1), the 1,200 kHz RioGrande ADCP recorded the first velocity at a depth of 0.44 m below the water surface. Other ADCP models provide data considerably closer to the water surface (e.g. the RiverSurveyor M9 ADCP used at the site near Theale provided data from 0.18 m below the water surface), but are constrained in the application of some of the data processing techniques found to be crucial for robustness against common errors near in-channel structures (see Sections 3.2.7 and 7.2.3). On the bottom end of the water column, reliable mean velocity estimates were obtained down to a minimum of 0.25 m above the river bed.

The ability to obtain data close to the river banks is constrained on some sites, where bankside vegetation physically limits the platform access to areas near the banks, and where the water depth near the banks is difficult to judge for the platform operator, which increases the risk of going aground and potentially loosing platform control. The minimum sampling distance to the migration barrier and fish pass structure, on the other hand, is constrained by the maximum water velocities and boat speed (see also Section 8.3.3).

8.3.1.2 Remaining measurement uncertainty

The data collection and processing techniques identified or developed in the PhD research have contributed towards a reduction of errors in ADCP data associated with the environmental conditions near in-channel structures. Therefore, the proposed methodology can be assumed to be robust against:

- large errors from violations of the flow homogeneity assumption (through application of the method by Vermeulen et al., 2014),
- temporary systematic errors from magnetic compass interference (through the ADCP-IMU integration),
- degradation or unavailability of GNSS-based positioning (through integration of a tracking TS), and
- bias or loss of BT signals (through boat velocity estimation via tracking TS).

The main sources of the remaining uncertainties in the ADCP-based near-pass hydrodynamics quantification are listed in Table 8-2, along with an estimation of their approximate magnitudes as found in this research.

The uncertainty in the radial velocities incorporates instrument noise as well as errors in instrument heading, boat velocity and ADCP positioning (see Table 8-2). In the prediction of the 3D velocity vector these errors are averaged, along with the spatio-temporal velocity variation within the volume of a mesh cell (see Section 3.4.1.1). The averaging reduces the effect of the remaining (random) errors in the radial velocities. Given the typically large number of radial velocities per mesh cell (e.g. a mean number of 30 samples for the first survey at Shrewsbury Weir; see Section 4.3.2), this uncertainty can be assumed to be a small contributor to the overall uncertainty in the resulting hydrodynamic maps.

In Chapter 7, it was found that in repeated cross-sectional measurements, the absolute change in the predicted mean velocity caused by including data from another transect tends to converge to around 0.03 ms^{-1} for streamwise and cross-stream velocities and 0.01 ms^{-1} for vertical velocities. These values were

typically reached after seven to eight transects and the results indicated that further transects would lead to only little reductions in these values. While further research is required to quantify the error in the predicted temporally averaged water velocity components (e.g. against reference measurements; see Section 8.5.3), the values provide initial estimates of the lower error boundaries.

Table 8-2. Main remaining sources of random errors in the ADCP-based 3D flow maps near fish passes

Source		Error	Error specification and further details
Errors in radial velocities			
Instrument noise		0.052 ms^{-1}	S.D. of radial velocities, for 1,200 kHz RioGrande in Mode 12 with 7 sub-pings and bin height of 0.12 m; based on Teledyne RDI (2009); see Section4.2.2.1
Instrument heading (for ensembles corrected through ADCP-IMU integration)		<2.6 deg	S.D. of the error; see Section 4.3.1
TS-based boat speed		0.075 ms^{-1}	S.D. of the error; see Section 4.3.3
TS-based 3D instrument positioning		≈0.021 m	corresponds to mean position error from temporal offset between ADCP and TS (main error source) for a mean boat speed of 0.42 ms^{-1} and ranges <100 m; see Section 4.3.3
Errors in spatial distribution of mean velocities			
Mean 3D velocity estimation	u	> 0.03 ms^{-1}	mean absolute changes in mean velocity components caused by including the 8th transect; provides a lower boundary for the remaining uncertainty; see Section 7.3.1
	v	> 0.03 ms^{-1}	
	w	> 0.01 ms^{-1}	
Spatial interpolation	u	0.049 – 0.136 ms^{-1}	range of cross-validation results (S.D. of the error) found for the study sites of Chapter 7; represents a lower error boundary; upper boundary is approx. twice as large (see main text in Section 8.3.1.2)
	v	0.050 – 0.139 ms^{-1}	
	w	0.013 – 0.038 ms^{-1}	

The error introduced by spatial velocity interpolation is one of the largest contributors to the overall uncertainty in the near-pass hydrodynamics quantification (see Table 8-2). The error was computed through cross-validation, an approach chosen in previous studies too (e.g. Jamieson et al., 2011; Tsubaki et al., 2012). However, it should be noted that the cross-validation error represents a lower boundary of the actual uncertainty introduced. Due to the ADCP-specific sampling strategy along cross sections, the cross-validation is based on measurements along sampled sections and thus in close proximity to other velocity samples. The uncertainty of velocities

predicted for unmeasured locations increases with increasing distance to the nearest velocity samples (Webster & Oliver, 2007). Therefore, the largest uncertainty can be assumed in locations *between* (rather than *along*) sampled sections. For a doubled section spacing of 8 m at maximum, the error between sampled sections was quantified in Chapter 7. These errors were approximately twice as large as the errors found in cross-validation (see Section 7.3.2). They represent an upper boundary of the error introduced through interpolation in the flow maps presented in this research (which were produced with a maximum spacing of 4 m). As shown in Chapter 7, the spatial interpolation also resulted in unrealistic spatial velocity gradients, which, for some surveys led to considerable bias in the derivation of hydrodynamic metrics based on these gradients (see Section 7.3.5.3).

The approach chosen in the PhD research was to firstly increase the accuracy and availability of raw (i.e. radial velocity) ADCP data to enable an unbiased estimation of the temporally averaged velocity. As a next step, improvements to the technique for spatial velocity interpolation should be prioritised to further reduce the uncertainty in the predicted 3D velocity distribution and to increase the accuracy in hydrodynamic metrics derived from it (see also Section 8.5.2). After that, a comprehensive uncertainty analysis (including error propagation between the various data processing stages) is recommended for future research as it will improve the interpretation of the flow field in relation to fish pass attractiveness. The error estimates from the research presented here (see Table 8-2) provide a basis for such uncertainty analyses.

8.3.1.3 Spatial and temporal scales

The scales of hydrodynamic changes determine the kinematic response of fish towards these changes, such as the adoption of specific swimming patterns or avoidance responses, as well as their displacement effects (see Section 2.4). The findings from some laboratory-based fish behavioural studies indicate that spatial scales of high relevance to fish kinematic responses are related to the fish body length (see Chapter 2). While the instruments and sampling strategies

used in laboratory-based studies (e.g. densely spaced ADV point velocity measurements or PIV; see Section 2.4) enable hydrodynamic measurements at such fine spatial scales, these can currently not be achieved with ADCPs.

Due to the convex arrangement of the ADCP transducers and the resulting beam spread, the 3D water velocity is derived from radial velocities sampled in different locations. This instrument setup causes the spatial resolution of the 3D velocities to be much coarser than that of the radial velocities (see Section 3.2.4). Using the method suggested in Vermeulen et al. (2014) led to a reduction in the water volume enclosing the radial velocities combined to estimate the 3D velocity vector, relative to conventional ADCP data processing (see Figure 4-4 in Chapter 4). Still, the grid cells within which the 3D velocities were measured in the methodology evaluation had dimensions of 2.00 x 0.40 x 0.15 m^3, which is too large for capturing velocity gradients along the body of fish found in UK rivers. Reductions in the mesh cell dimensions (particularly the longitudinal dimension) can lead to a relatively large decrease in the number of radial velocity samples per cell, with considerable effects on the mean velocity estimates (see Section 4.3.2). Smaller mesh cell dimensions, and thus measurements at scales closer to those found to be most relevant to fish behaviour, can be achieved by a decrease in the boat path variability between transects or modifications to the velocity estimation technique as discussed in Section 4.3.2. This mismatch of spatial scales between laboratory-based and field-based ADCP measurements complicates the interpretation of the biological relevance of hydrodynamic metrics derived from ADCP data, based on the existing laboratory-based insights.

The low temporal resolution of ADCP data and the resulting limitations to ADCP-based near-pass hydrodynamics quantification have been discussed in Section 8.3.1.1.3.

8.3.2 Methodology practicability

8.3.2.1 Equipment cost

The methodology relies on ADCP measurements, for which some national agencies have equipment (sensor and deployment platforms) as well as expertise available in-house (see Section 1.1.3). This facilitates the methodology uptake in river management practice.

The practical requirement for low additional equipment cost was also considered when selecting external sensors to address ADCP data quality issues. Particularly, the IMU used in this research to correct for instrument heading bias was considerably cheaper than alternative technologies for ADCP heading measurement (as of 2015, the x-IMU had a market price of £309). The hardware required for integrating the ADCP with external sensors, specifically that for the on-board multiple-sensor data logging system, is available in the form of low-cost SBCs from the mass market. For example, in Chapters 6 and 7, Raspberry Pi SBCs (cost of <£30, as of 2015) were shown to provide a low-cost solution for logging and time-synchronising the data from external sensors with the ADCP for research purposes. Industrial PCs can be used where more physically robust solutions are needed.

While tracking TS devices enable ADCP positioning at cm-level accuracy, they are relatively expensive (from ≈£15,000, as of 2015), which represents a financial barrier to the wide-spread methodology uptake in practice. To address this challenge, future research is required to enhance stereo visual odometry for ADCP vessels based on the error analysis and resulting recommendations presented in this thesis (see Chapter 5). The technique relies on relatively low-cost hardware (consumer-grade optical cameras are applicable; see Section 5.2) and thus has the potential to considerably reduce the cost of high-precision ADCP positioning in the future.

8.3.2.2 Implementation time and effort

8.3.2.2.1 Data collection

A comparison between the five ADCP surveys conducted as part of the methodology evaluation showed that the methodology involves a survey duration between 2.2 and 5.9 h (from first to last ensemble recording; see Table 7-1). The variation between surveys was due to different sites and thus river widths, partly different sampling strategies, varying boat speeds, as well as learning effects from the first to the last survey, which speeded up the equipment use. In addition, approximately 1-2 hours were required for the equipment setup (including ADCP compass calibration and moving bed tests) and dismantling. The methodology implementation relies on three personnel to operate (i) the ADCP platform, (ii) the control computer (see Section 8.2.4.1) and (iii) the TS. Even though the TS operates as an automatic tracking system, the additional personnel is needed for regaining lock to the reflecting prism on the ADCP platform after interruptions of line of sight between the TS and the prism (see Section 4.3.3).

The development of a small-sized ADCP platform as part of the PhD research (see Chapter 6) has contributed towards a more efficient methodology implementation in the future. Specifically, for sites with lower water velocities, the platform enables a single person to complete platform transport, launching and recovery (see Section 6.3.5). Moreover, the implementation and assessment of stereo visual odometry presented in Chapter 5 has contributed towards the development of an on-board positioning system for GNSS-denied locales that does not require the operation of platform-external positioning devices on the shore (such as the TS).

8.3.2.2.2 Data processing

The software for processing and analysing the data from the ADCP and external sensors has been implemented in the form of various functions in the languages R (R Core Team, 2015) and MATLAB. Future work is required to implement these functions in user-friendly software with Graphical User

Interface (GUI) to considerably decrease the time and skills required for the methodology implementation and thus support the wide-spread use of the methodology in practice.

8.3.3 Transferability across sites

In Chapter 7, the proposed ADCP-based methodology was evaluated at multiple sites and conditions of discharge. It was found that the methodology effectiveness and applicability depend on the hydraulic conditions on site. Specifically, the capability to measure sufficiently close to the migration barrier and fish pass to characterise the attraction flow is constrained by the maximum water velocities. Although the ARC-Boat is capable of speeds up to 5 ms^{-1} (faster RC ADCP platforms have not been available on the market; see Section 3.2.8), the platform control was found to be insufficient for the accurate repeated transect sampling if the water velocities near the migration barrier exceeded approximately 2.6 ms^{-1}. Endured platform operation at full throttle will also lead to rapid current drain of the platform batteries, because the current draw increases exponentially with throttle position as shown in Chapter 6 (Section 6.3.2). In practice, this limits the overall measurement time and thus the reach that can be surveyed.

The results obtained for the study site at Flatford Mill illustrated that ADCPs may be unsuitable for the accurate quantification of near-pass hydrodynamics at sites combining the characteristics of very low water velocities and large depths (>4 m; see Chapter 7). In conditions of slow flow and maximum depths less than 4 m, the 1,200 kHz RioGrande ADCP can be configured to high precision measurement modes, but these involve problems of acoustic signal de-correlation leading to inaccurate or lack of velocity data in turbulent conditions close to the pass entrance (Teledyne RDI, 2002b). The use of ADCPs with capability for auto-adaptive configuration may reduce this problem and thus increase the transferability of the methodology.

The minimum and maximum river depths for the methodology to be applicable are determined mainly by the ADCP profiling ranges. In the ADCP surveys of

this research, the minimum depth for the 1,200 kHz RioGrande ADCP to provide velocity data was found to be 0.80 m (with the centre of the first bin at 0.44 m below the water surface). Further software development is required to integrate the data quality enhancement techniques in ADCP models other than the RioGrande ADCP, specifically those with a velocity profiling range reaching closer to the water surface (see Table 3-1 in Chapter 3). This will widen the methodology transferability to shallower sites. For example, the RiverSurveyor M9 ADCP used for the survey near Theale (see Chapter 7) recorded velocity data at depths down to a minimum of 0.35 m (with the centre of the first bin at 0.18 m below the water surface). ADCP deployment from a platform with low draught, such as that developed as part the PhD research (draught of 0.05 m, i.e. 0.07 m less than the ARC-Boat, see Section 6.3.4.1), further reduces the minimum depth required. The maximum water velocity profiling range of ADCPs produced for river measurement is 75 m (Teledyne RDI, 2006a), so that the water depth will not constrain the methodology application in most rivers.

The application in shallow, narrow channels is constrained by the physical size of the deployment platform. The prototype platform developed as part of the PhD research (see Chapter 6) has a width of 0.56 m and the methodology can readily be adapted for the use of narrower, tethered platforms (available down to 0.42 m width; Teledyne RDI, 2006b). For wide rivers, the methodology can be implemented with manned boats, with the only limit being the maximum range of the tracking TS (up to 1000 m for newer instruments, e.g. Leica Geosystems, 2015b) in case of limited GNSS availability on site.

8.3.4 Final remarks on the methodology suitability and answer to the research question

In theory, a perfect methodology for near-pass hydrodynamics quantification would capture all changes that fish are able to detect and may react to. Sensitivities as high as 0.025 mm s^{-1} have been reported for the mechanosensitive lateral line system (Schwartz, 1974; cited in Bleckmann, 1986) that fish use to detect velocity variation along their body. Clearly, the

uncertainties in the proposed methodology are larger, and the spatio-temporal measurement resolution is lower than needed to capture all velocity variations that fish are able to detect (see Sections 8.3.1.2 and 8.3.1.3). However, the required capabilities and acceptable limitations of the methodology depend on the specific purpose of its application. Examples for intended applications of the methodology outputs have been given in Chapter 1 (Section 1.1.2). In the following sections, the research question has been answered based on the suitability of the methodology for these applications.

8.3.4.1 Rapid assessment of hydrodynamic fish pass attractiveness

The first methodology application outlined in Section 1.1.2 is the rapid assessment of hydrodynamic fish pass attractiveness in order to identify fish passes requiring enhancement and to prioritise passes for more detailed monitoring. The methodology is suitable for this application because it can effectively be used to identify large-scale hydrodynamic features emphasised in fish pass design guidelines (see also Section 8.3.1.1.1). This was illustrated during the methodology evaluation, where the visual assessment of the quantified velocity distributions near the pass provided sufficient information for an initial appraisal of the discernibility of the fish pass attraction flow in relation to competing flows. Thus, with regards to this first methodology application, the research question can be positively answered. Given that there are thousands of fish passes around the globe, but limited resources for detailed fish pass monitoring studies, this methodology application contributes to an informed and efficient use of resources invested in fish passage.

8.3.4.2 Incorporating near-pass hydrodynamics in fish pass monitoring

The second methodology application relates to the complementation of fish pass monitoring studies with near-pass hydrodynamics quantification. This application addresses the need to quantify the links between measures and covariates of fish pass success in order to inform effective and efficient strategies of fish passage improvement (see Section 2.2). In several previous fish pass monitoring studies, low attraction or overall passage efficiencies have

been attributed to poor hydrodynamic attractiveness, but these hydrodynamics have not been measured directly (see Sections 2.5.3). The methodology defined in the PhD research can enrich the outcomes of future monitoring studies by providing a means to describing these hydrodynamics in quantitative terms at relatively little time and potentially low cost effort. It was shown to enable the formulation of new indicators of fish pass attractiveness, such as the metric S_{eff}, which can be quantitatively related to measures of fish passage success, particularly the attraction efficiency. Thus, the research question can be positively answered also regarding the second methodology application.

8.3.4.3 Transferring fish behavioural studies from the laboratory into the field

The methodology was also intended to contribute to the transfer of studies on fish behaviour towards hydrodynamics from the laboratory into the field, the need for which had been emphasised in Lacey et al. (2012). Given the relatively coarse spatial scale of ADCP data (see Section 8.3.1.3) and the remaining measurement uncertainties in the resulting flow maps (see Section 8.3.1.2), such a transfer would involve a considerable loss in measurement accuracy and spatial resolution, relative to the measurement approaches applicable in the laboratory. The methodology certainly provides a starting point for the formulation of hypotheses attempting to explain swim path selection of upstream migrants. However, further research including biological studies is required to assess whether the accuracy and spatial resolution of the methodology output is sufficient to relate the measured hydrodynamics to swim path selection or energetic cost of fish approaching migration barriers (see also Section 8.5.3). From the experience with ADCPs it can be concluded that the transfer of laboratory-based to field-based fish behavioural studies may require the modification of metrics used to describe hydrodynamics generated in the laboratory, and the development of novel indicators that consider the capabilities of the measurement devices suitable and practicable for use in the field.

8.3.4.4 Further uses of the methodology

Beyond the applications outlined in the previous sections, the findings of the PhD research indicate a strong potential of the methodology to improve the understanding of hydrodynamic fish pass attractiveness and to refine traditional guidelines. Already, the findings during the methodology evaluation at three sites (see Chapter 7) revealed the following insights:

(i) The water velocity magnitude at the entrance of the fish pass is a weak indicator of the extent of the attraction flow because it cannot capture its interactions with other near-pass hydrodynamic flow features (see Section 7.3.7.2).

(ii) Recirculation cells forming near the pass entrance do not necessarily have a detrimental effect, but may in some cases increase the detectability of the attraction flow to fish (see Section 7.3.7.3).

(iii) There are critical zones of near-pass hydrodynamics, which may determine whether fish are attracted directly towards the pass entrance (i.e. without delay) or firstly to the foot of the migration barrier (see Section 7.3.4.1). These zones may thus be crucial for the achievement of “transparent” migration, which is the most stringent goal of fish pass facilities for diadromous fish, as described in Section 2.2.

Finally, the methodology was shown to support the definition of new quantitative indicators of fish pass attractiveness. This contribution is particularly important in the context of upstream passage, where there has been a lack of quantitative indicators (see Section 2.6). It supports the objective description and assessment of near-pass hydrodynamics and their comparability across sites. This enables the quantification of the effects of pass design modifications and changes in environmental conditions on hydrodynamic fish pass attractiveness, and thus facilitates innovations in fish pass design.

8.4 Contributions beyond fish passage

Field-based measurements are essential to observe previously understudied hydraulic phenomena and to validate results from computer-based numerical or laboratory-based physical modelling, but the research on acquiring such data has been severely underrepresented in fluvial hydraulics (Sukhodolov, 2015). The PhD research presented in this thesis has improved the in-field collection of water velocity and depth data in environmental conditions, where accurate measurements had previously been particularly challenging. As such, the equipment and methods developed in the PhD research and the findings gained during their empirical assessment are useful beyond the context of fish passage. They facilitate the quantification of the temporally averaged flow field induced by engineered in-channel structures as part of ecological and hydromorphological assessments (e.g. Jamieson et al., 2011, 2013; Radspinner et al., 2010; Remo et al., 2013). Moreover, they increase the usefulness and reliability of ADCPs as a tool to improve numerical and conceptual hydrodynamic models through field-based calibration and validation (Acuña & Ávila, 2015; Andersson et al., 2012; Lalander et al., 2013; Piper et al., 2015; Williams et al., 2013).

Some of the techniques proposed in the PhD research contribute to an improved accuracy and availability of ADCP data for applications beyond hydrodynamic mapping. For example, the ADCP-IMU integration offers an effective low-cost solution useful in ADCP applications, such as discharge measurements and bathymetric surveying, at sites potentially affected by temporary magnetic interference (Gaeuman & Jacobson, 2005; Mueller & Wagner, 2009). Likewise, ADCP positioning in GNSS-denied locales (e.g. under bridges or in forests) has been a common problem in ADCP applications relying on spatial data referencing or accurate boat velocity references to substitute BT signals biased by a non-stationary channel bed or lacking due to weed growth on the river bed or large turbulence and turbidity (see Section 3.4.3).

The PhD research also highlighted the large potential of some techniques from the domain of mobile robotics for innovations in river research. While the visual odometry algorithms assessed in this research require further enhancements to increase their accuracy, floating survey vessels equipped with cameras create opportunities in river monitoring that go beyond localisation. In previous research, optical imagery from aerial vehicles has been shown to enable the efficient, automated characterisation of physical in-stream and riparian ecosystem features (Casado et al., 2015; Flynn & Chapra, 2014; Kaneko & Nohara, 2014). The imagery collected from cameras on survey vessels might complement such analyses and allow for detailed, ground-based monitoring of erosion, vegetation and hydraulic patterns. The integration of data simultaneously collected from an ADCP and cameras on a single monitoring vessel can contribute to more holistic physical assessments of river ecosystems, capturing the environments below and above the water surface.

8.5 Future research

In this final section, requirements for further research to improve and validate the developed methodology have been highlighted.

8.5.1 Real-time data processing

There has been a lack of sampling guidelines for the ADCP-based hydrodynamic river characterisation, making it complicated to *a priori* determine efficient sampling strategies. In the research presented here and previous studies (e.g. Muste et al., 2004b; Petrie et al., 2013b; Szupiany et al., 2007; Vermeulen et al., 2014) the number of transects required per section to capture the temporally averaged velocity has been determined during post-processing. The findings from these studies have been valuable to reveal information that is valid across sites (see Section 7.3.1) and have contributed towards the formulation of sampling guidelines. However, the post-processing approach relies on conservative sampling strategies with potentially redundant transects.

This is not suitable for practical river management, because at the time the results are obtained, the sampling strategy cannot be corrected anymore.

Software enabling the real-time processing of ADCP data for the estimation of mean water velocities would increase the efficiency of such ADCP application. The software could, for example, provide an estimate of the change in the mean velocity caused by including another transects (see Section 7.3.1), report the number of radial velocities already available per mesh cell (when using the method by Vermeulen et al., 2014; see Section 4.3.2) and highlight sub-sections requiring further sampling. The approach is, in principle, the same as for ADCP discharge measurements, where general guidelines for the number of transects required per section are available from research (e.g. Mueller & Wagner, 2009), but the manufacturer-provided ADCP software (e.g. SonTek, 2014a; Teledyne RDI, 2014a) complements these guidelines by indicating the need for further measurements to the ADCP user in the field. Thereby, site-specific variation from the general guidelines can be taken into account.

8.5.2 Improvements to spatial velocity interpolation

Ordinary kriging was implemented as a frequently used method for interpolating moving-vessel ADCP data (e.g. Jamieson et al., 2011, 2013; Rennie & Church, 2010; Rennie, 2012; Venditti et al., 2014), but was found to introduce relatively strong data smoothing and interpolation artefacts (see Sections 7.3.3 and 7.3.5.3). While the former bears the risk of underestimating the maximum water velocities near fish passes (and thus bias the comparison of these velocities with known fish swimming speeds), the latter affects the derivation of metrics based on spatial velocity variation. Future research is recommended to reduce the uncertainty introduced by the spatial interpolation of water velocities. This might be achieved by amendments to the implementation of ordinary kriging interpolation. For example, the proposed methodology involves the separate interpolation of the streamwise, cross-stream and vertical velocity components, the direction of which was defined based on channel geometry in the studies presented here. The definition of the stream coordinate system has been shown

to significantly affect the interpretation of velocity components, particularly the cross stream component (Lane et al., 2000; Petrie et al., 2013b). Further research could explore, whether and how it affects the spatial correlation of the respective velocity components identified in kriging and the resulting interpolation. The interpolation artefacts may be reduced through continuity correction (see Section 7.3.5.3) subsequent to kriging interpolation. Finally, future research might also involve the assessment of interpolation techniques other than kriging (e.g. Tsubaki et al., 2012).

8.5.3 Methodology validation

While the individual techniques and equipment developed as part of the PhD research have been subject to detailed quantitative evaluation and validation, the validation of the proposed ADCP-based methodology as a whole requires further research.

The methodology can be validated in terms of:

(i) the accuracy of the estimated 3D mean velocity distribution and hydrodynamic metrics derived from it, or

(ii) the validity of the derived hydrodynamic indicators for fish pass attractiveness.

The former could be achieved through comparison of the ADCP-derived hydrodynamics with those from reference measurements. In previous field-based studies, the mean velocity profiles from moving-vessel ADCP measurements have been compared against those from fixed-vessel ADCP data (e.g. Jamieson et al., 2011; Muste et al., 2004b; Petrie et al., 2013b; Szupiany et al., 2007). This approach quantifies the effect of the number of transects or the spatial velocity interpolation, but does not involve validation of the velocity data prior to averaging. These “raw” velocity data have previously been compared against ADV measurements in the laboratory (e.g. Nystrom et al., 2007). ADV deployment in the environmental conditions associated with in-channel structures involves potential data quality issues, such as decorrelation

of the acoustic signals due to small-scale turbulence or effects of instrument motion during measurements (Chanson, 2008; Macvicar et al., 2007). The identification of the best available instrument and procedure against which to compare the ADCP-based near-pass hydrodynamics is subject to further research. Additionally, techniques from uncertainty analysis and error propagation can be used to quantify the overall uncertainty in the ADCP-based 3D flow maps and the hydrodynamic features as emphasised in Section 8.3.1.2.

The suitability of the methodology to quantify near-pass hydrodynamics with biological relevance can be validated in a biological study involving the simultaneous measurement of near-pass hydrodynamics and position of fish approaching the fish pass entrance (e.g. Nestler et al., 2008; Piper et al., 2015).

8.5.4 Further research opportunities

In addition to those outlined above, the following research opportunities have been identified:

- The processing technique suggested in Vermeulen et al. (2014) could be adapted to allow for 3D velocity estimation on a non-linear mesh. This would relax the requirement for sampling along a straight section, which, near in-channel structures, can be difficult to achieve (see Section 4.3.2).
- In the research presented here, the effect of the spatio-temporal sampling strategy on the near-pass hydrodynamics quantification has been evaluated through field-based studies at three sites (see Chapter 7). Further research covering a larger number and variety of sites is required to enable the establishment of a quantitative relationship between the uncertainty in 3D flow maps and the spatio-temporal sampling strategy, while accounting for the hydraulic site conditions. This will support the formulation of effective and efficient sampling guidelines for ADCP-based hydrodynamic mapping applications. The field-based studies could be complemented by numerical simulations of ADCP surveys using a virtual ADCP model to extract samples from the output of hydrodynamic models quantifying the hydrodynamics near fish

passes. This approach has previously been illustrated as useful to quantify the performance of ADCPs within a controlled setting (e.g. Richmond et al., 2015; Tokyay et al., 2009; Tsubaki et al., 2012).

- Future research could explore the usefulness of complementary measurements using other technologies to account for some of the shortcomings of the ADCP-based methodology. For example, LS-PIV might be suitable to obtain surface velocity data, where the ADCP cannot measure, as well as data in areas with velocities too fast for ADCP deployment (Jodeau et al., 2008; Muste et al., 2008). Complementary ADV measurements at high spatial and temporal resolutions could be taken to characterise the hydrodynamics in areas identified to be particularly relevant (based on the coarser scale ADCP data; e.g. Jamieson et al., 2013).
- The methodology for near-pass hydrodynamics quantification defined in this thesis requires testing in the context of downstream fish passage. This could involve an assessment of the methodology suitability to implement the SVP-hypothesis for predicting swim path selection of downstream migrants based on hydrodynamic metrics derived from the temporally-averaged flow field (Nestler, 2008; see Section 2.4.4).
- Based on the findings of the research presented here, stereo visual odometry requires further improvement to increase the reliability and accuracy of the positioning technique in vessel-based river monitoring. Specifically, future developments can extend the algorithm to include loop-closure detection and integrate a low-cost IMU, as suggested in Section 5.4.2.3. The integration of platform velocity information from BT might provide further reliability at no additional equipment cost. Further visual odometry evaluations covering longer trajectories as well as faster flowing and more turbulent hydraulic conditions are required.
- The PhD research presented here has illustrated the integration of a micro-controller and position-logging SBC on an RC ADCP platform and

thereby established the hardware required for a platform with autonomous features. Future research can build on this by developing navigation software for autonomous platform operation features, such as active heading hold or the capability for following a pre-defined track. These features can support the accurate implementation of ADCP data sampling strategies.

REFERENCES

Acuña, G. & Ávila, H. (2015). An experimental design based methodology for calibrating 2D hydromorphodynamic numerical models for rivers. In: *Proceedings of the World Environmental and Water Resources Congress*, Austin, TX, USA, 17-21 May 2015, pp. 1419–1431.

Andersson, A.G., Lindberg, D.-E., Lindmark, E.M., Leonardsson, K., Andreasson, P., Lundqvist, H. & Lundström, T.S. (2012). A study of the location of the entrance of a fishway in a regulated river with CFD and ADCP. *Modelling and Simulation in Engineering*, 2012, pp. 1–12.

Von Appen, W.-J. (2015). Correction of ADCP compass errors resulting from iron in the instrument's vicinity. *Journal of Atmospheric and Ocean Technology,* 32, pp. 591–603.

Arduino (2015). Arduino Uno. Available from: https://www.arduino.cc/en/Main/ArduinoBoardUno (last accessed: 25 December 2015).

Armstrong, G.S., Aprahamian, M.W., Fewings, G.A., Gough, P.J., Reader, N.A. & Varallo, P. V. (2010). Environment Agency fish pass manual. Guidance notes on the legislation, selection and approval of fish passes in England and Wales. Environment Agency, Bristol.

Arnekleiv, J.V. & Kraabol, M. (1996). Migratory behaviour of adult fast-growing brown trout (Salmo Trutta, L.) in relation to water flow in a regulated Norwegian river. *Regulated Rivers: Research & Management,* 12, pp. 39–49.

Atmel (2009). 8-bit AVR microcontroller with 4/8/16/32K bytes in-system programmable flash, Atmel Corporation. Available from: http://www.atmel.com/Images/doc8161.pdf (last accessed: 25 December 2015).

Audras, C., Comport, A.I., Meilland, M.& Rives, P. (2011). Real-time dense appearance-based SLAM for RGB-D sensors. In: *Proceedings of the Australian Conference on Robotics and Automation (ACRA)*, Melbourne, Australia, 7-9 December 2011.

Azenha, A., Peneda, L. & Carvalho, A. (2010). Error analysis in indoors localization using ZigBee wireless networks. In: *Proceedings of the 36th IEEE Annual Conference on Industrial Electronics (IECON)*, Glendale, AZ, USA, 7-10 November 2010, pp. 2193–2197.

Baek, K.O. & Kim, Y. Do (2014). A case study for optimal position of fishway at low-head obstructions in tributaries of Han River in Korea. *Ecological Engineering*, 64, pp. 222–230.

Bainbridge, R. (1958). The speed of swimming of fish as related to size and to the frequency and amplitude of the tail beat. *The Journal of Experimental Biology*, 35, pp. 109–133.

Baras, E., Lambert, H. & Philippart, J.-C. (1994). A comprehensive assessment of the failure of Barbus barbus spawning migrations through a fish pass in the canalized River Meuse (Belgium). *Aquatic Living Resources,* 7, pp. 181–189.

Barua, D.K. & Rahman, K.H. (1998). Some aspects of turbulent flow structure in large alluvial rivers. *Journal of Hydraulic Research,* 36 (2), pp. 235–252.

Bayoud, F.A. (2006). Leica's pinpoint EDM technology with modified signal processing and novel optomechanical features. In: *Proceedings of the XXII FIG Congress: Shaping the Change*, Munich, Germany, 8-13 October 2006, pp. 1–16.

Beach, M.H. (1984). *Fish pass design - criteria for the design and approval of fish passes and other structures to facilitate the passage of migratory fish in rivers*.UK Ministry of Agriculture, Fisheries and Food, Lowestoft, UK.

Beamish, F.W. (1978). Swimming capacity. In: W. S. Hoar & D. J. Randall (eds.). *Locomotion*. Academic Press, pp. 101–187.

Bekkali, A., Sanson, H. & Matsumoto, M. (2007). RFID indoor positioning based on probabilistic RFID map and Kalman filtering. In: *Proceedings of the third IEEE International Conference on Wireless and Mobile Computing, Networking and Communications (WiMOB)*, White Plains, NY, USA,8-10 October 2007.

Bell, M.C. (1990). *Fisheries handbook of engineering requirements and biological criteria*. 3rd Ed., U.S. Army Corps of Engineers, North Pacific Division, Portland, Oregon, USA.

Bendat, J. & Piersol, A. (2000). *Random data*. 3rd Ed., Wiley, New York, USA.

Bertram, V. (2000). *Practical ship hydrodynamics*. 1st Ed., Butterworth-Heinemann, Oxford, UK.

Bleckmann, H. (1986). Role of the lateral line in fish behaviour. In: T. J. Pitcher (ed.). *The behaviour of teleost fishes*. Croom Helm, pp. 177–202.

Borenstein, J., Everett, H.R. & Feng, L. (1996). *Where am I? Sensors and methods for mobile robot positioning*. University of Michigan.

Brett, J.R. (1964). The respiratory metabolism and swimming performance of young sockeye salmon. *Journal of the Fisheries Research Board of Canada*, 21 (5), pp. 1183–1226.

Bunt, C.M., Castro-Santos, T. & Haro, A. (2012). Performance of fish passage structures at upstream barriers to migration. *River Research and Applications*, 28, pp. 457–478.

Bunt, C.M., Katopodis, C. & Mckinley, R.S. (1999). Attraction and passage efficiency of White Suckers and Smallmouth Bass by two Denil fishways. *North American Journal of Fisheries Management*, 19, pp. 793–803.

Burnett, N.J., Hinch, S.G., Donaldson, M.R., Furey, N.B., Patterson, D., Roscoe, D.W. & Cooke, S.J. (2014). Alterations to dam-spill discharge influence sex-specific activity, behaviour and passage success of migrating adult sockeye salmon. *Ecohydrology,* 7, pp. 1094–1104.

Casado, M.R., Gonzalez, R.B., Kriechbaumer, T. & Veal, A. (2015). Automated identification of river hydromorphological features using UAV high resolution aerial imagery. *Sensors,* 15 (11), pp. 27969–89.

Castro-Santos, T., Cotel, A. & Webb, P. (2009). Fishway evaluations for better bioengineering: an integrative approach. In: *Proceedings of the International Symposium Challenges for Diadromous Fishes in a Dynamic Global Environment,* Halifax, Nova Scotia, Canada,18-21 June 2007, pp. 557–575.

Castro-Santos, T. & Haro, A. (2003). Quantifying migratory delay : a new application of survival analysis methods. *Canadian Journal of Fisheries and Aquatic Sciences,* 60, pp. 986–996.

Caudill, C.C., Daigle, W.R., Keefer, M.L., Boggs, C.T., Jepson, M.A., Burke, B.J., Zabel, R.W., Bjornn, T.C. & Peery, C.A. (2007). Slow dam passage in adult Columbia River salmonids associated with unsuccessful migration: delayed negative effects of passage obstacles or condition-dependent mortality? *Canadian Journal of Fisheries and Aquatic Sciences,* 64, pp. 979–995.

Chambers, A., Achar, S., Nuske, S., Rehder, J., Kitt, B., Chamberlain, L., Haines, J., Scherer, S. & Singh, S. (2011). Perception for a river mapping robot. In: *Proceedings of the IEEE/RSJ International Conference on Intelligent Robots and Systems (IROS)*, San Francisco, CA, USA, 25-30 September 2011, pp. 227–234.

Chanson, H. (2008). Acoustic Doppler Velocimetry (ADV) in the field and in laboratory: practical experiences. In: *Proceedings of the International Meeting on Measurements and Hydraulics of Sewers IMMHS'08, Summer School GEMCEA/LCPC,* Bouguenais, France, 19-21 August 2008, pp. 49–66.

Chapman, S.J. (2005). *Electric machinery fundamentals*. 4th Ed., McGraw-Hill.

Chiang, K.-W., Duong, T.T. & Liao, J.-K. (2013). The performance analysis of a real-time integrated INS/GPS vehicle navigation system with abnormal GPS measurement elimination. *Sensors,* 13 (8), pp. 10599–622.

Clay, C.H. (1995). *Design of fishways and other fish facilities*. 2nd Ed., CRC Press.

Clough, S.C. & Turnpenny, A.W.H. (2001). Swimming speeds in fish: phase 1. Environment Agency, Bristol, UK.

Comport, A.I., Malis, E. & Rives, P. (2007). Accurate quadrifocal tracking for robust 3D visual odometry. In: *Proceedings of the IEEE International Conference on Robotics and Automation (ICRA)*, Rome, Italy, 10-14 April 2007, pp. 40–45.

Comport, A.I., Malis, E.& Rives, P. (2010). Real-time quadrifocal visual odometry. *International Journal of Robotics Research,* 29 (2-3), pp. 245–266.

Cook, C.B., Richmond, M.C. & Serkowski, J.A. (2007). Observations of velocity conditions near a hydroelectric turbine draft tube exit using ADCP measurements. *Flow Measurement and Instrumentation*, 18 (3-4), pp. 148–155.

Cooke, S.J. & Hinch, S.G. (2013). Improving the reliability of fishway attraction and passage efficiency estimates to inform fishway engineering, science, and practice. *Ecological Engineering,* 58, pp. 123–132.

Coutant, C.C. (1998). Turbulent attraction flows for juvenile salmonid passage at dams. Report ORNL/TM-13608, Oak Ridge National Laboratory, Oak Ridge, TN, USA.

Coutant, C.C. & Whitney, R.R. (2000). Fish behavior in relation to passage through hydropower turbines : a review. *Transactions of the American Fisheries Society,* 129, pp. 351–380.

Cowley, J. (2011). Salmon spawning report 2010. Midlands Region, West. April 2011, Environment Agency, Bristol, UK.

Crowder, D.W. & Diplas, P. (2000). Evaluating spatially explicit metrics of stream energy gradients using hydrodynamic model simulations. *Canadian Journal of Fisheries and Aquatic Sciences*, 57, pp. 1497–1507.

Crowder, D.W. & Diplas, P. (2002). Vorticity and circulation: spatial metrics for evaluating flow complexity in stream habitats. *Canadian Journal of Fisheries and Aquatic Sciences,* 59 (4), pp. 633–645.

Cummins, M. & Newman, P. (2010). Appearance-only SLAM at large scale with FAB-MAP 2.0. *The International Journal of Robotics Research*, 30 (9), pp. 1100–1123.

Demers, S., Buffin-Bélanger, T. & Roy, A.G. (2013). Macroturbulent coherent structures in an ice-covered river flow using a pulse-coherent Acoustic Doppler Profiler. *Earth Surface Processes and Landforms,* 38 (9), pp. 937–946.

Dijkgraaf, S. (1963). The functioning and significance of the lateral-line organs. *Biological Reviews,* 38 (1), pp. 51–105.

Dinehart, R.L. & Burau, J.R. (2005a). Averaged indicators of secondary flow in repeated Acoustic Doppler Current Profiler crossings of bends. *Water Resources Research,* 41 (9), pp. 1–18.

Dinehart, R.L. & Burau, J.R. (2005b). Repeated surveys by Acoustic Doppler Current Profiler for flow and sediment dynamics in a tidal river. *Journal of Hydrology,* 314 (1-4), pp. 1–21.

Domenici, P. & Blake, R.W. (1997). The kinematics and performance of fish fast-start swimming. *The Journal of Experimental Biology*, 200, pp. 1165–1178.

Drucker, E.G. & Lauder, G. V. (1999). Locomotor forces on a swimming fish: three-dimensional vortex wake dynamics quantified using digital particle image velocimetry. *The Journal of Experimental Biology,* 202, pp. 2393–2412.

Durrant-Whyte, H. & Bailey, T. (2006). Simultaneous Localisation and Mapping (SLAM): part I the essential algorithms. *IEEE Robotics & Automation Magazine,* 13 (2), pp. 99–110.

El-Rabbany, A. (2006). *Introduction to GPS: the Global Positioning System*. 2nd Ed., Artech House.

Enders, E.C., Boisclair, D. & Roy, A.G. (2003). The effect of turbulence on the cost of swimming for juvenile Atlantic salmon (Salmo salar). *Canadian Journal of Fisheries and Aquatic Sciences*, 60, pp. 1149–1160.

Enders, E.C., Gessel, M.H., Anderson, J.J. & Williams, J.G. (2012). Effects of decelerating and accelerating flows on juvenile salmonid behavior. *Transactions of the American Fisheries Society*, 141 (2), pp. 357–364.

Enders, E.C., Gessel, M.H. & Williams, J.G. (2009). Development of successful fish passage structures for downstream migrants requires knowledge of their behavioural response to accelerating flow. *Canadian Journal of Fisheries and Aquatic Sciences,* 66 (12), pp. 2109–2117.

Engel, J., Sturm, J. & Cremers, D. (2013). Semi-dense visual odometry for a monocular camera. In: *Proceedings of the IEEE International Conference on Computer Vision (ICCV)*, Sydney, Australia, 1-8 December 2013, pp. 1449–1456.

Environment Agency (2009). Modernisation of salmon and freshwater fisheries legislation; new regulatory order to address the passage of fish (for WFD and EU Eel Regulation). Response to Defra consultation. Available from: http://goo.gl/vD4qPi (last accessed: 14 March 2016).

Environment Agency (2013). National standard contract and specification for surveying services. Version 3.2, Standard Technical Specifications, Environment Agency, Bristol, UK.

ESA - European Space Agency (2009). EGNOS: European Geostationary Navigation Overlay Service, Available from: http://www.egnos-pro.esa.int/Publications/ESA_EGNOS_br284_2009.pdf (last accessed: 14 March 2016).

EC - European Commission (2000). Directive 2000/60/EC of the Parliament and of the Council establishing a framework for community action in the field of water policy. *Official J. Eur. Communities*, L327, pp. 1–72.

EC - European Commission (2007). Council Regulation (EC) No 1100/2007 of 18 September 2007 establishing measures for the recovery of the stock of European eel. *Official J. Eur. Union*, L248. pp. 17–23.

EC – European Commission (2015). Communication from the Commission to the European Parliament and the Council. The Water Framework Directive and the Floods Directive: actions towards the “good status” of EU water and to reduce flood risks.

Evans, S.D., Adams, N.S., Rondorf, D.W., Plumb, J.M. & Ebberts, B.D. (2008). Performance of a prototype surface collector for juvenile salmonids at Bonneville Dam’s first powerhouse on the Columbia River, Oregon. *River Research and Applications,* 24, pp. 960–974.

Fang, Z. &Zhang, Y. (2015). Experimental evaluation of RGB-D visual odometry methods. *International Journal of Advanced Robotic Systems,* 12 (26), pp. 1–16.

FAO (2002). Fish passes - Design, dimensions and monitoring. FAO, Rome, Italy.

Fischler, M.A. & Bolles, R.C. (1981). Random Sample Consensus: a paradigm for model fitting with applications to image analysis and automated cartography. *Communications of the ACM,* 24 (6), pp. 381–395.

Fleming, D.F. & Reynolds, J.B. (1991). Effects of spawning-run delay on spawning migration of arctic grayling. In: *Proceedings of the American Fisheries Society Symposium 10*, Bethesda, MD, USA, pp. 299–305.

Flener, C., Wang, Y., Laamanen, L., Kasvi, E., Vesakoski, J.-M. & Alho, P. (2015). Empirical modeling of spatial 3D flow characteristics using a remote-controlled ADCP system: monitoring a spring flood. *Water,* 7 (1), pp. 217–247.

Floyd, E.Y., Churchwell, R. & Cech, J.J. (2007). Effects of water velocity and trash rack architecture on juvenile fish passage and interactions: a simulation. *Transactions of the American Fisheries Society,* 136 (5), pp. 1177–1186.

Flynn, K. & Chapra, S. (2014). Remote sensing of submerged aquatic vegetation in a shallow non-turbid river using an unmanned aerial vehicle. *Remote Sensing,* 6 (12), pp. 12815–12836.

Forsberg (2015). ReACT: Receiver Antenna Compact Technology, Forsberg Services Ltd., Available from: http://goo.gl/7IxOpH (last accessed: 14 March 2016).

Gaeuman, D. & Jacobson, R.B. (2005). Aquatic habitat mapping with an Acoustic Doppler Current Profiler: considerations for data quality. United States Geological Survey (USGS), Reston, VA, USA.

García, C.M., Cantero, M.I., Nino, Y. & García, M.H. (2005). Turbulence measurements with Acoustic Doppler Velocimeters. *Journal of Hydraulic Engineering*, 131 (12), pp. 1062–1073.

Gartner, J.W. & Ganju, N.K. (2002). A preliminary evaluation of near-transducer velocities collected with low-blank Acoustic Doppler Current Profiler. In: *Proceedings of the ASCE Conference, Hydraulic Measurements and Experimental Methods*, Estes Park, CO, USA,25 October 2002,pp. 1–13.

Geiger, A., Lenz, P. & Urtasun, R. (2012). Are we ready for autonomous driving? The KITTI vision benchmark suite. In: *Proceedings of the IEEE Conference on Computer Vision and Pattern Recognition (CVPR)*, Providence, RI, USA,16-21 June 2012, pp. 3354–3361.

Geiger, A., Ziegler, J. & Stiller, C. (2011). StereoScan : dense 3D reconstruction in real-time. In: *Proceedings of the IEEE Intelligent Vehicles Symposium (IV)*, Baden-Baden, Germany, 5-9 June 2011, pp. 963–968.

González-Castro, J.A. & Muste, M. (2007). Framework for estimating uncertainty of ADCP measurements from a moving boat by standardized uncertainty analysis. *Journal of Hydraulic Engineering,* 133 (12), pp. 1390–1410.

González-Castro, J.A., Oberg, K. & Duncker, J.J. (2000). Effect of temporal resolution on the accuracy of ADCP measurements. In: *Proceedings of the Joint Conference on Water Resource Engineering and Water Resources Planning and Management 2000: Building Partnerships*, Minneapolis, MN, USA, 30 July – 2 August 2000.

Goodwin, R.A. (2004). Hydrodynamics and juvenile salmon movement behavior at Lower Granite Dam: decoding the relationship using 3-D space-time (CEL Agent IBM) simulation. PhD Thesis, Cornell University, Ithaca, NY, USA.

Gordon, R.L. (1996). Acoustic Doppler Current Profiler. Principles of operation. A practical primer. RD Instruments, San Diego, CA, USA.

Gowans, A.R.D., Armstrong, J.D. & Priede, I.G. (1999). Movements of adult Atlantic salmon in relation to a hydroelectric dam and fish ladder. *Journal of Fish Biology,* 54, pp. 713–726.

Gridling, G. & Weiss, B. (2007). Introduction to microcontrollers. Courses 182.064 & 182.074. February 26, 2007, Institute of Computing Engineering, Vienna University of Technology. Available from: https://goo.gl/Ue8fbw (last accessed: 14 March 2016).

Griffiths, A.M., Ellis, J.S., Clifton-Dey, D., Machado-Schiaffino, G., Bright, D., Garcia-Vazquez, E. & Stevens, J.R. (2011). Restoration versus recolonisation: the origin of Atlantic salmon (Salmo salar L.) currently in the River Thames. *Biological Conservation,* 144 (11), pp. 2733–2738.

Grimes, M. & LeCun, Y. (2009). Efficient off-road localization using visually corrected odometry. In: *Proceedings of the IEEE International Conference on Robotics and Automation (ICRA)*, Kobe, Japan, 12-17 May 2009, pp. 2649–2654.

Groves, P.D. (2008). *Principles of GNSS, inertial, and multisensor integrated navigation systems*. Artech House, London.

Gunawan, B., Sterling, M. & Knight, D.W. (2010). Using an Acoustic Doppler Current Profiler in a small river. *Water and Environment Journal,* 24 (2), pp. 147–158.

Hamilton, O.K., Breckon, T.P., Bai, X. & Kamata, S.-I. (2013). A foreground object based quantitative assessment of dense stereo approaches for use in automotive environments. In: *Proceedings of the 20th IEEE International Conference on Image Processing (ICIP)*, Melbourne, Australia, 15-18 September 2013, pp. 418–422.

Haro, A., Odeh, M., Noreika, J. & Castro-Santos, T. (1998). Effect of water acceleration on downstream migratory behavior and passage of Atlantic salmon smolts and juvenile American shad at surface bypasses. *Transactions of the American Fisheries Society,* 127, pp. 118–127.

Hasan, A.M., Samsudin, K., Ramli, A.R., Azmir, R.S. & Ismaeel, S.A. (2009). A review of navigation systems (integration and algorithms). *Australian Journal of Basic and Applied Sciences,* 3 (2), pp. 943–959.

Hatry, C., Binder, T.R., Thiem, J.D., Hasler, C.T., Smokorowski, K.E., Clarke, K.D., Katopodis, C. & Cooke, S.J. (2013). The status of fishways in Canada: trends identified using the national CanFishPass database. *Reviews in Fish Biology and Fisheries,* 23 (3), pp. 271–281.

Hinch, S.G., Standen, E.M., Healey, M.C. & Farrell, A.P. (2002). Swimming patterns and behaviour of upriver-migrating adult pink (Oncorhynchus gorbuscha) and sockeye (O. nerka) salmon as assessed by EMG telemetry in the Fraser River, British Columbia, Canada. *Hydrobiologia*, 483, pp. 147–160.

Hinze, J.O. (1975). *Turbulence*. McGraw-Hill, New York.

Hirschmuller, H. (2008). Stereo processing by semiglobal matching and mutual information. *IEEE Transactions on Pattern Analysis and Machine Intelligence,* 30 (2), pp. 328–341.

Hockley, F.A., Wilson, C.A.M.E., Brew, A. & Cable, J. (2014). Fish responses to flow velocity and turbulence in relation to size, sex and parasite load. *Journal of the Royal Society Interface*, 11, pp. 1-11.

Horn, B.K.P. (1987). Closed-form solution of absolute orientation using unit quaternions. *Journal of the Optical Society of America A*, 4 (4), pp. 629–642.

Horowitz, P. & Hill, W. (1989). *The art of electronics*. 2nd Ed. Cambridge University Press.

HR Wallingford (2015). ARC-Boat. Available from: http://goo.gl/pWeh6R (last accessed on 8 June 2015).

Jacobsaquatic (2006). SWIMIT 3.3. Environment Agency, Southampton, UK.

Jamieson, E.C., Rennie, C.D., Jacobson, R.B. & Townsend, R.D. (2011). 3-D flow and scour near a submerged wing dike: ADCP measurements on the Missouri River. *Water Resources Research,* 47 (7), pp. 1–20.

Jamieson, E.C., Ruta, M.A., Rennie, C.D. & Townsend, R.D. (2013). Monitoring stream barb performance in a semi-alluvial meandering channel: flow field dynamics and morphology. *Ecohydrology*, 6, pp. 611–626.

Jodeau, M., Hauet, A., Paquier, A., Le Coz, J. & Dramais, G. (2008). Application and evaluation of LS-PIV technique for the monitoring of river surface velocities in high flow conditions. *Flow Measurement and Instrumentation,* 19 (2), pp. 117–127.

Johnson, G.E., Richmond, M.C., Hedgepeth, J.B., Ploskey, G.R., Anderson, M.G., Deng, Z., Khan, F., Mueller, R.P., Rakowski, C.L., Sather, N.K., Serkowski, J.A. & Steinbeck, J.R. (2009). Smolt responses to hydrodynamic conditions in forebay flow nets of surface flow outlets, US Army Corps of Engineers, Portland, OR, USA.

Kaneko, K. & Nohara, S. (2014). Review of effective vegetation mapping using the UAV (Unmanned Aerial Vehicle) method. *Journal of Geographic Information System,* 6, pp. 733–742.

Karppinen, P., Mäkinen, T.S., Erkinaro, J., Kostin, V. V, Sadkovskij, R. V, Lupandin, A.I. & Kaukoranta, M. (2002). Migratory and route-seeking behaviour of ascending Atlantic salmon in the regulated River Tuloma. *Hydrobiologia*, 483, pp. 23–30.

Katopodis, C. & Williams, J.G. (2012). The development of fish passage research in a historical context. *Ecological Engineering*, 48, pp. 8–18.

Keefer, M.L., Peery, C. a., Lee, S.R., Daigle, W.R., Johnson, E.L. & Moser, M.L. (2011). Behaviour of adult Pacific lamprey in near-field flow and fishway design experiments. *Fisheries Management and Ecology,* 18 (3), pp. 177–189.

Kelly, A. (1994). *Modern inertial and satellite navigation systems*. Pittsburgh, PA, USA.

Kemp, P.S., Gessel, M.H., Sandford, B.P. & Williams, J.G. (2006). The behaviour of Pacific salmonid smolts during passage over two experimental weirs under light and dark conditions. *River Research and Applications,* 22 (4), pp. 429–440.

Kemp, P.S., Gessel, M.H. & Williams, J.G. (2005). Fine-scale behavioral responses of Pacific salmonid smolts as they encounter divergence and acceleration of flow. *Transactions of the American Fisheries Society*, 134 (2). pp. 390–398.

Kemp, P.S. & O'Hanley, J.R. (2010). Procedures for evaluating and prioritising the removal of fish passage barriers: a synthesis. *Fisheries Management and Ecology,* 17, pp. 297–322.

Kemp, P.S., Russon, I.J., Vowles, S. & Lucas, M.C. (2011). The influence of discharge and temperature on the ability of upstream migrant adult river lamprey (Lampetra fluviatilis) to pass experimental overshot and undershot weirs. *River Research and Applications,* 27, pp. 488–498.

Kerl, C., Sturm, J. & Cremers, D. (2013). Robust odometry estimation for RGB-D cameras. In: *Proceedings of the IEEE International Conference on Robotics and Automation (ICRA)*, Karlsruhe, Germany, 6-10 May 2013. 2013, pp. 3748–3754.

Kim, D. & Muste, M. (2012). Multi-dimensional representation of river hydrodynamics using ADCP data processing software. *Environmental Modelling & Software*, 38, pp. 158–166.

Kirschner, H. & Stempfhuber, W. (2008). The kinematic potential of modern tracking total stations - a state of the art report on the Leica TPS1200+. In: *Proceedings of the 1st International Conference on Machine Control & Guidance*, Zurich, Switzerland, 24-26 June 2008.

Kitt, B., Geiger, A. & Lategahn, H. (2010). Visual odometry based on stereo image sequences with RANSAC-based outlier rejection scheme. In: *Proceedings of the IEEE Intelligent Vehicles Symposium (IV)*, San Diego, CA, USA, 21-24 June 2010, pp. 486–492.

Knights, B. & White, E.M. (1998). Enhancing immigration and recruitment of eels: the use of passes and associated trapping systems. *Fisheries Management and Ecology,* 5, pp. 459–471.

Koletschka, T., Puig, L. & Daniilidis, K. (2014). MEVO : multi-environment stereo visual odometry. In: *Proceedings of the IEEE/RSJ International*

Conference on Intelligent Robots and Systems (IROS), Chicago, IL, USA, 14-18 September 2014, pp. 4981–4988.

Konolige, K., Agrawal, M. & Sol, J. (2007). Large scale visual odometry for rough terrain. In: *Proceedings of the 13th International Symposium of Robotics Research*, Hiroshima, Japan, 26-29 November 2007.

Konolige, K., Bowman, J., Chen, J.D., Mihelich, P., Calonder, M., Lepetit, V. & Fua, P. (2010). View-based maps. *International Journal of Robotics Research,* 29 (8), pp. 941–957.

Kriechbaumer, T., Blackburn, K., Everard, N. & Rivas-Casado, M. (2016). Acoustic Doppler Current Profiler measurements near a weir with fish pass: assessing solutions to compass errors, spatial data referencing and spatial flow heterogeneity. *Hydrology Research*, 47 (3), pp. 591-605.

Lacey, J.R.W., Neary, V.S., Liao, J.C., Enders, E.V.A.C. & Tritico, H.M. (2012). The IPOS framework: linking fish swimming performance in altered flows from laboratory experiments to rivers. *River Research and Applications*, 28, pp. 429–443.

Laine, A. (1995). Fish swimming behaviour in Finnish fishways. In: *Proceedings of the International Symposium on Fishways '95*, Gifu, Japan, 24-26 October 1995, pp. 323–328.

Lalander, E., Thomassen, P. & Leijon, M. (2013). Evaluation of a model for predicting the tidal velocity in fjord entrances. *Energies,* 6 (4), pp. 2031–2051.

Lane, S.N., Biron, P.M., Bradbrook, K.F., Butler, J.B., Chandler, J.H., Crowell, M.D., McLelland, S.J., Richards, K.S. & Roy, A.G. (1998). Three-dimensional measurement of river channel flow processes using Acoustic Doppler Velocimetry. *Earth Surface Processes and Landforms,* 23, pp. 1247–1267.

Lane, S.N., Bradbrook, K.F., Richards, K.S., Biron, P.M. & Roy, A.G. (2000). Secondary circulation cells in river channel confluences: measurement artefacts or coherent flow structures? *Hydrological Processes,* 14, pp. 2047–2071.

Larinier, M. (2001). Environmental issues, dams and fish migration. In: G. Marmulla (ed.). *Dams, fish and fisheries. Opportunities, challenges and conflict resolution*. FAO, Rome, pp. 45–89.

Larinier, M. (1998). Upstream and downstream fish passage experience in France. In: M. Jungwirth, S. Schmutz, & S. Weiss (eds.). *Fish migration and fish bypasses*. Wiley, pp. 127–145.

Larinier, M. (2002a). Location of fishways. *Bull. Fr. Pêche Piscic.*, 364 suppl., pp. 39–53.

Larinier, M. (2002b). Fishways - general considerations. *Bull. Fr. Pêche Piscic,* 364 suppl., pp. 21–27.

Larsson, L. & Baba, E. (1996). Ship resistance and flow computations. In: M. Ohkusu (ed.). *Advances in Marine Hydrodynamics*. Comp. Mech. Publ.

Leica Geosystems (2015a). Leica Nova MS50. Available from: http://goo.gl/pAEO1e (last accessed: 24 April 2015).

Leica Geosystems (2015b). Leica Viva TS15. Available from: http://goo.gl/p7zFlf (last accessed: 8 June 2015).

Leica Geosystems (2015c). Leica Nova MS60 data sheet. Available from: http://goo.gl/EOJC6T (last accessed: 14 March 2016).

Lemaire, T., Berger, C., Jung, I.-K. & Lacroix, S. (2007). Vision-based SLAM: stereo and monocular approaches. *International Journal of Computer Vision,* 74 (3), pp. 343–364.

Li, J. & Allinson, N.M. (2008). A comprehensive review of current local features for computer vision. *Neurocomputing,* 71 (10-12), pp. 1771–1787.

Liao, J.C. (2007). A review of fish swimming mechanics and behaviour in altered flows. *Philosophical Transactions of the Royal Society of London. Series B, Biological sciences,* 362 (1487), pp. 1973–1993.

Liao, J.C., Beal, D.N., Lauder, G. V & Triantafyllou, M.S. (2003a). Fish exploiting vortices decrease muscle activity. *Science,* 302 (5650), pp. 1566–1569.

Liao, J.C., Beal, D.N., Lauder, G.V. & Triantafyllou, M.S. (2003b). The Kármán gait: novel body kinematics of rainbow trout swimming in a vortex street. *Journal of Experimental Biology,* 206 (6), pp. 1059–1073.

Lindberg, D.-E., Leonardsson, K., Andersson, A.G., Lundström, T.S. & Lundqvist, H. (2013). Methods for locating the proper position of a planned fishway entrance near a hydropower tailrace. *Limnologica - Ecology and Management of Inland Waters,* 43 (5), pp. 339–347.

Lovett, T. (2004). Roll stability calculator. Available from: http://goo.gl/6EJoAV (last accessed: 25 December 2015).

Lucas, M.C. & Baras, E. (2001). *Migration of freshwater fishes*. Blackwell Science, Oxford, UK.

Lundqvist, H., Rivinoja, P., Leonardsson, K. & McKinnell, S. (2008). Upstream passage problems for wild Atlantic salmon (Salmo salar L.) in a regulated river and its effect on the population. *Hydrobiologia,* 602 (1), pp. 111–127.

Lupandin, A.I. (2005). Effect of flow turbulence on swimming speed of fish. *Biology Bulletin,* 32 (5), pp. 558–565.

Macvicar, B.J., Beaulieu, E., Champagne, V. & Roy, A.G. (2007). Measuring water velocity in highly turbulent flows: field tests of an electromagnetic current meter (ECM) and an Acoustic Doppler Velocimeter (ADV). *Earth Surface Processes and Landforms,* 32, pp. 1412–1432.

Madgwick, S.O.H., Harrison, A.J.L. & Vaidyanathan, R. (2011). Estimation of IMU and MARG orientation using a gradient descent algorithm. In: *Proceedings of the IEEE International Conference on Rehabilitation Robotics (ICORR)*, Zurich, Switzerland, 29 June – 1 July 2011.

Magnabosco, M. & Breckon, T.P. (2013). Cross-spectral visual simultaneous localization and mapping (SLAM) with sensor handover. *Robotics and Autonomous Systems,* 61 (2), pp. 195–208.

MAN (2011). Basic principles of ship propulsion. MAN, Copenhagen, Denmark.

Marsden, R., Huang, H., Song-Sheng, C., De-Xun, Y. & Jin-Chun, W. (2003). Yangtze River ADCP discharge measurement using multiple external sensor inputs. In: *Proceedings of the IEEE/OES 7th Working Conference on Current Measurement Technology*, San Diego, CA, USA, 13-15 March 2003.

MEA - Millennium Ecosystem Assessment (2005). Ecosystems and human well-being: wetlands and water. Synthesis. Washington, DC, USA.

Mei, C., Sibley, G., Cummins, M., Newman, P. & Reid, I. (2009). A constant-time efficient stereo SLAM system. In: *Proceedings of the 20th British Machine Vision Conference (BMVC)*, London, UK, 7-10 September 2009.

Meyer, J.L., Strayer, D.L., Wallace, J.B., Eggert, S.L., Helfman, G.S. & Leonard, N.E. (2007). The contribution of headwater streams to biodiversity in river networks. *JAWRA Journal of the American Water Resources Association*, 43 (1), pp. 86–103.

Moore, C.S. (2010). *The principles of naval architecture series: intact stability*. Society of Naval Architects, Jersey City, NJ, USA.

Moser, M.L., Matter, A.L., Stuehrenberg, L.C. & Bjornn, T.C. (2002). Use of an extensive radio receiver network to document Pacific lamprey (Lampetra tridentata) entrance efficiency at fishways in the Lower Columbia River, USA. *Hydrobiologia,* 483, pp. 45–53.

Mroz, F. & Breckon, T.P. (2012). An empirical comparison of real-time dense stereo approaches for use in the automotive environment. *EURASIP Journal on Image and Video Processing*, 13, pp. 1–19.

Mueller, D.S. (2013). Extrap: software to assist the selection of extrapolation methods for moving-boat ADCP streamflow measurements. *Computers & Geosciences,* 54, pp. 211–218.

Mueller, D.S., Abad, J.D., García, C.M., Gartner, J.W., García, M.H. & Oberg, K.A. (2007). Errors in Acoustic Doppler Profiler velocity measurements caused by flow disturbance. *Journal of Hydraulic Engineering,* 133 (12), pp. 1411–1420.

Mueller, D.S. &Wagner, C.R. (2009). Measuring discharge with Acoustic Doppler Current Profilers from a moving boat. Techniques and Methods 3-A22. United States Geological Survey (USGS), Reston, VA, USA.

Mueller, D.S. & Wagner, C.R. (2007). Correcting Acoustic Doppler Current Profiler discharge measurements biased by sediment transport. *Journal of Hydraulic Engineering*, 133 (12), pp. 1329–1336.

Mueller, D.S., Wagner, C.R., Rehmel, M.S., Oberg, K.A. & Rainville, F. (2013). Measuring discharge with Acoustic Doppler Current Profilers from a moving boat. Techniques and Methods 3-A22, Version 2. United States Geological Survey (USGS), Reston, VA, USA.

Muste, M., Fujita, I. & Hauet, A. (2008). Large-scale particle image velocimetry for measurements in riverine environments. *Water Resources Research*, 44 (4), pp. 1–14.

Muste, M., Kim, D. & González-Castro, J.A. (2010). Near-transducer errors in ADCP measurements: experimental findings. *Journal of Hydraulic Engineering,* 136 (5), pp. 275–289.

Muste, M., Kim, D. & Merwade, V. (2012). Modern digital instruments and techniques for hydrodynamic and morphologic characterization of river channels. In: M. Church, P. M. Biron, & A. G. Roy (eds.). *Gravel-bed rivers: processes, tools, environments*. John Wiley & Sons, pp. 315–341.

Muste, M., Yu, K., Pratt, T. & Abraham, D. (2004a). Practical aspects of ADCP data use for quantification of mean river flow characteristics Part II: fixed-vessel measurements. *Flow Measurement and Instrumentation,* 15 (1), pp. 17–28.

Muste, M., Yu, K. & Spasojevic, M. (2004b). Practical aspects of ADCP data use for quantification of mean river flow characteristics Part I: moving-vessel measurements. *Flow Measurement and Instrumentation*, 15 (1). pp. 1–16.

NASCO - North Atlantic Salmon Conservation Organisation (2015). Maintaining and improving river connectivity: the current position and experience in England. NASCO, Available from: http://goo.gl/J3wW2T (last accessed: 14 March 2016).

NASCO - North Atlantic Salmon Conservation Organisation (2009). Protection, restoration and enhancement of salmon habitat focus area report, EU-UK (England & Wales). NASCO, Edinburgh, UK, Available from: http://goo.gl/wrlJCb (last accessed: 14 March 2016).

Neary, V.S., Gunawan, B., Hill, C. & Chamorro, L.P. (2013). Near and far field flow disturbances induced by model hydrokinetic turbine: ADV and ADP comparison. *Renewable Energy,* 60, pp. 1–6.

Nestler, J.M., Goodwin, R.A., Smith, D.L., Anderson, J.J. & Li, S. (2008). Optimum fish passage and guidance designs are based in the hydrogeomorphology of natural rivers. *River Research and Applications,* 24, pp. 148–168.

Neubeck, A. & Van Gool, L. (2006). Efficient non-maximum suppression. In: *Proceedings of the 18th International Conference on Pattern Recognition (ICPR)*, Hong Kong, China, 20–24 August 2006, pp. 850–855.

Nezu, I. & Nakagawa, H. (1993). *Turbulence in open channel flows*. IAHR Monograph, Rotterdam, Netherlands.

Nikora, V.I., Aberle, J., Biggs, B.J.F., Jowett, I.G. & Sykes, J.R.E. (2003). Effects of fish size, time-to-fatigue and turbulence on swimming performance: a case study of Galaxias maculatus. *Journal of Fish Biology*, 63, pp. 1365-1382.

Nikora, V. & Roy, A.G. (2012). Secondary flows in rivers: theoretical framework, recent advances, and current challenges. In: M. Church, P. M. Biron, & A. G. Roy (eds.). *Gravel-bed rivers: processes, tools, environments*. John Wiley & Sons, pp. 3–22.

Nilsson, C., Reidy, C., Dynesius, M. & Revenga, C. (2005). Fragmentation and flow regulation of the world's large river systems. *Science,* 308 (5720), pp. 405–408.

Nistér, D., Naroditsky, O. & Bergen, J. (2004). Visual odometry. In: *Proceedings of the 2004 IEEE Computer Society Conference on Computer Vision and Pattern Recognition (CVPR)*, Washington, DC, USA, 27 June – 2 July 2004, pp. 652–659.

Noonan, M.J., Grant, J.W.A. & Jackson, C.D. (2012). A quantitative assessment of fish passage efficiency. *Fish and Fisheries*, 13 (4), pp. 450–464.

Northcote, T.G. (1998). Migratory behaviour of fish and its significance to movement through riverine fish passage facilities. In: M. Jungwirth, S. Schmutz, & S. Weiss (eds.). *Fish migration and fish bypasses*. Wiley, pp. 3–18.

Nystrom, E.A., Oberg, K.A. & Rehmann, C.R. (2002). Measurement of turbulence with Acoustic Doppler Current Profilers - sources of error and laboratory results. *Proceedings of the Hydraulic Measurements and Experimental Methods Specialty Conference (HMEM)*, Estes Park, CO, USA, 28 July – 1 August 2002.

Nystrom, E.A., Rehmann, C.R. & Oberg, K.A. (2007). Evaluation of mean velocity and turbulence measurements with ADCPs. *Journal of Hydraulic Engineering*, 133 (12), pp. 1310–1318.

Oberg, K. (2002). In search of easy-to-use methods for calibrating ADCP's for velocity and discharge measurements. *Proceedings of the Hydraulic Measurements and Experimental Methods Specialty Conference (HMEM)*, Estes Park, CO, USA, 28 July – 1 August 2002.

Oberg, K. & Mueller, D.S. (2007). Validation of streamflow measurements made with Acoustic Doppler Current Profilers. *Journal of Hydraulic Engineering*, 133 (12), pp. 1421–1432.

Oceanscience (2011a). Q-Boat 1550T. Available from: http://goo.gl/i3slML (last accessed: 7 November 2012).

Oceanscience (2011b). Q-Boat 1800. Available from: http://goo.gl/6W8Uk6 (last accessed: 14 March 2016).

Oceanscience (2011c). Riverboat SP. Available from: http://goo.gl/G19ZyJ (last accessed: 7 November 2012).

Oceanscience (2011d), High-Speed Riverboat. Available from: http://goo.gl/CkxpIJ (last accessed: 7 November 2012).

Oceanscience (2011e), Riverboat. Available from: http://goo.gl/luwXqt (last accessed: 7 November 2012).

Odeh, M., Noreika, J.F., Haro, A., Maynard, A., Castro-Santos, T. & Cada, G.F. (2002). Evaluation of the effects of turbulence on the behavior of migratory fish. Report for the U.S. Department of Energy, Bonneville Power Administration, & Division of Fish and Wildlife, Report Number DOE/BP-00000022-1.

Odeh, M. & Orvis, C. (1998). Downstream fish passage design considerations and developments at hydroelectric projects in the north-east USA. In: M. Jungwirth, S. Schmutz, & S. Weiss (eds.). *Fish migration and fish bypasses*. Blackwell Science, pp. 267–280.

Omnisense (2013). Series 500 Cluster Geolocation System. Available from: http://goo.gl/A4In4h (last accessed: 14 March 2016).

Ovidio, M. & Philippart, J.-C. (2002). The impact of small physical obstacles on upstream movements of six species of fish. *Hydrobiologia,* 483, pp. 55–69.

OXTS - Oxford Technical Solutions (2015). RT Inertial and GNSS measurement systems. User manual. Oxford Technical Solutions Ltd., Available from: http://goo.gl/kMZP54 (last accessed: 14 March 2016).

Parsons, D.R., Best, J.L., Lane, S.N., Orfeo, O., Hardy, R.J. & Kostaschuk, R. (2007). Form roughness and the absence of secondary flow in a large confluence-diffluence, Rio Paraná, Argentina. *Earth Surface Processes and Landforms,* 32, pp. 155–162.

Parsons, D.R., Best, J.L., Orfeo, O., Hardy, R.J., Kostaschuk, R. & Lane, S.N. (2005). Morphology and flow fields of three-dimensional dunes, Rio Paraná, Argentina: Results from simultaneous multibeam echo sounding and Acoustic Doppler Current Profiling. *Journal of Geophysical Research,* 110, pp. 1–9.

Parsons, D.R., Jackson, P.R., Czuba, J.A., Engel, F.L., Rhoads, B.L., Oberg, K.A., Best, J.L., Mueller, D.S., Johnson, K.K. & Riley, J.D. (2012). Velocity Mapping Toolbox (VMT): a processing and visualization suite for moving-vessel ADCP measurements. *Earth Surface Processes and Landforms,* 38 (11), pp. 1244–1260.

Paull, L., Saeedi, S., Seto, M. & Li, H. (2014). AUV navigation and localization: a review. *IEEE Journal of Oceanic Engineering,* 39 (1), pp. 131–149.

Pavlov, D.S. (1989). Structures assisting the migrations of non-salmonid fish: USSR. FAO Fisheries Technical Paper. FAO, Rome.

Pavlov, D.S., Mikheev, V.N., Lupandin, A.I. & Skorobogatov, M. A. (2008). Ecological and behavioural influences on juvenile fish migrations in regulated rivers: a review of experimental and field studies. *Hydrobiologia,* 609 (1), pp. 125–138.

Peneda, L., Azenha, A. & Carvalho, A. (2011). Indoors localization using mobile communications radio signal strength. In: M. Khatib (ed.), *Advanced trends in wireless communications*. InTechOpen, pp. 265-280.

Petrie, J., Diplas, P., Gutierrez, M. & Nam, S. (2013a). Data evaluation for Acoustic Doppler Current Profiler measurements obtained at fixed locations in a natural river. *Water Resources Research,* 49 (2), pp. 1003–1016.

Petrie, J., Diplas, P., Gutierrez, M. & Nam, S. (2013b). Combining fixed- and moving-vessel Acoustic Doppler Current Profiler measurements for improved characterization of the mean flow in a natural river. *Water Resources Research,* 49, pp. 5600–5614.

Petrie, J., Diplas, P., Nam, S. & Gutierrez, M.S. (2010). Boat and bed load motion effects on velocity profiles measured with an acoustic Doppler current profiler. In: *Proceedings of the 6th International Symposium on Environmental Hydraulics,* Athens, Greece, 23-25 June 2010, pp. 845–850.

Piper, A.T., Manes, C., Siniscalchi, F., Marion, A., Wright, R.M. &Kemp, P.S. (2015). Response of seaward-migrating European eel (Anguilla anguilla) to manipulated flow fields. *Proceedings of the Royal Society B,* 282, pp. 1–9.

Piper, A.T., Wright, R.M. & Kemp, P.S. (2012). The influence of attraction flow on upstream passage of European eel (Anguilla anguilla) at intertidal barriers. *Ecological Engineering,* 44, pp. 329–336.

Point Grey Research (2015). Bumblebee2 1394a. Available from: http://goo.gl/FsjDc4 (last accessed: 8 June 2015).

Queensland Government (2009). Standards for hydrographic surveys within Queensland Waters. Revision 1.3.Brisbane, Australia, Available from: http://goo.gl/Sh3RJZ (last accessed: 14 March 2016).

R Core Team (2015). R: a language and environment for statistical computing. R Foundation for Statistical Computing, Vienna, Austria.

Radspinner, R.R., Diplas, P., Lightbody, A.F. & Sotiropoulos, F. (2010). River training and ecological enhancement potential using in-stream structures. *Journal of Hydraulic Engineering,* 136 (12), pp. 967–980.

Raspberry Pi Foundation (2015a). Raspberry Pi 1 Model B+. Available from: https://www.raspberrypi.org/products/model-b-plus/ (last accessed: 25 December 2015).

Raspberry Pi Foundation (2015b). Raspberry Pi 2 Model B. Available from: https://www.raspberrypi.org/products/raspberry-pi-2-model-b/ (last accessed: 23 February 2016).

Redeker, M. & Morgenschweis, G. (2007). Application of ADCP flow measurements in fish pass design. In: *Proceedings of the 32nd IAHR World Congress,* Venice, Italy, 1-6 July 2007.

Rehder, J., Gupta, K., Nuske, S. & Singh, S. (2012). Global pose estimation with limited GPS and long range visual odometry. In: *Proceedings of the IEEE International Conference on Robotics and Automation (ICRA)*, Saint Paul, MN, USA, 14-18 May 2012, pp. 627–633.

Remo, J.W.F., Khanal, A. & Pinter, N. (2013). Assessment of chevron dikes for the enhancement of physical-aquatic habitat within the Middle Mississippi River, USA. *Journal of Hydrology,* 501, pp. 146–162.

Rennie, C.D. (2012). Mapping water and sediment flux distributions in gravel-bed rivers using ADCPs. In: M. Church, P. M. Biron, & A. G. Roy (eds.). *Gravel-bed rivers: processes, tools, environments*. John Wiley & Sons, pp. 342–350.

Rennie, C.D. & Church, M. (2010). Mapping spatial distributions and uncertainty of water and sediment flux in a large gravel bed river reach using an Acoustic Doppler Current Profiler. *Journal of Geophysical Research,* 115, pp. 1–27.

Rennie, C.D., Millar, R.G. & Church, M. A. (2002). Measurement of bed load velocity using an Acoustic Doppler Current Profiler*. Journal of Hydraulic Engineering*, 128 (5), pp. 473–483.

Rennie, C.D. & Rainville, F. (2006). Case study of precision of GPS differential correction strategies: influence on ADCP velocity and discharge estimates. *Journal of Hydraulic Engineering,* 132 (3), pp. 225–234.

Rennie, C.D. & Rainville, F. (2008). Improving precision in the reference velocity of ADCP measurements using a Kalman filter with GPS and bottom track. *Journal of Hydraulic Engineering*, 134 (9), pp. 1257–1266.

Rennie, C.D., Rainville, F. & Kashyap, S. (2007). Improved estimation of ADCP apparent bed-load velocity using a real-time Kalman filter. *Journal of Hydraulic Engineering*, 133 (12), pp. 1337–1344.

Retscher, G. & Fu, Q. (2010). Continuous indoor navigation with RFID and INS. In: *Proceedings of the IEEE/ION Position Location and Navigation Symposium (PLANS)*, Indian Wells, CA, USA,4-6 May 2010, pp. 102–112.

Richmond, M., Harding, S. & Romero-Gomez, P. (2015). Numerical performance analysis of Acoustic Doppler Velocity Profilers in the wake of an axial-flow marine hydrokinetic turbine. *International Journal of Marine Energy,* 11, pp. 50–70.

Roscoe, D.W. & Hinch, S.G. (2010). Effectiveness monitoring of fish passage facilities: historical trends, geographic patterns and future directions. *Fish and Fisheries,* 11 (1), pp. 12–33.

Rowe, F.D. & Young, J.W. (1979). An ocean current profiler using Doppler sonar. In: *Proceedings of OCEANS '79*, San Diego, CA, USA,17-19 September 1979, pp. 292–297.

Russon, I.J. & Kemp, P.S. (2011). Advancing provision of multi-species fish passage: Behaviour of adult European eel (Anguilla anguilla) and brown trout (Salmo trutta) in response to accelerating flow. *Ecological Engineering*, 37 (12), pp. 2018–2024.

Salychev, O.S. (2012). *MEMS-based inertial navigation: expectations and reality*. BMSTU Press, Moscow, Russia.

Scaramuzza, D. & Fraundorfer, F. (2011). Visual odometry. Part I: the first 30 years and fundamentals. *IEEE Robotics & Automation Magazine,* 18 (4), pp. 80–92.

Scherer, S., Rehder, J., Achar, S., Cover, H., Chambers, A., Nuske, S. & Singh, S. (2012). River mapping from a flying robot: state estimation, river detection, and obstacle mapping. *Autonomous Robots,* 33 (1-2), pp. 189–214.

Schmutz, S., Giefing, C. & Wiesner, C. (1998). The efficiency of a nature-like bypass channel for pike-perch (Stizostedion lucioperca) in the Marchfeldkanalsystem. *Hydrobiologia,* 371/372, pp. 355–360.

Schneekluth, H. & Bertram, V. (1998). Ship design for efficiency and economy. 2nd Ed., Butterworth-Heinemann, Oxford, UK.

Scruton, D.A., Booth, R.K., Pennell, C.J., Cubitt, F., McKinley, R.S. & Clarke, K.D. (2007). Conventional and EMG telemetry studies of upstream migration and tailrace attraction of adult Atlantic salmon at a hydroelectric installation on the Exploits River, Newfoundland, Canada. *Hydrobiologia,* 582 (1), pp. 67–79.

Scruton, D.A., Mckinley, R.S., Kouwen, N., Eddy, W. & Booth, R.K. (2002). Use of telemetry and hydraulic modeling to evaluate and improve fish guidance efficiency at a louver and bypass system for downstream-migrating Atlantic salmon (Salmo salar) smolts and kelts. *Hydrobiologia,* 483, pp. 83–94.

Scruton, D.A., Pennell, C.J., Bourgeois, C.E., Goosney, R.F., King, L., Booth, R.K., Eddy, W., Porter, T.R., Ollerhead, L.M.N. & Clarke, K.D. (2008). Hydroelectricity and fish: a synopsis of comprehensive studies of upstream and downstream passage of anadromous wild Atlantic salmon, Salmo salar, on the Exploits River, Canada. *Hydrobiologia,* 609 (1), pp. 225–239.

Shields, F.D., Knight, S.S., Testa, S.I. & Cooper, C.M. (2003). Use of Acoustic Doppler Current Profilers to describe velocity distributions at the reach scale. *Journal of the American Water Resources Association,* 39 (6), pp. 1397–1408.

Shields, F.D. & Rigby, J.R. (2005). River habitat quality from river velocities measured using Acoustic Doppler Current Profiler. *Environmental Management,* 36 (4), pp. 565–575.

Shih, H.H., Payton, C., Sprenke, J. & Mero, T. (2000). Towing basin speed calibration of acoustic Doppler current profiling instruments. In: *Proceedings of the Joint Conference on Water Resource Engineering and Water Resources Planning and Management 2000: Building Partnerships*, Minneapolis, MN, USA, 30 July – 2 August 2000.

Simpson, M.R. (2001). Discharge measurements using a broad-band acoustic Doppler current profiler. Open-File Report 01-1, United States Geological Survey (USGS), Sacramento, CA, USA.

Simpson, M.R. & Oltmann, R.N. (1993). Discharge measurement using an Acoustic Doppler Current Profiler, United States Geological Survey (USGS), Denver, CO, USA.

Skorobogatov, M.A., Pavlov, D.S. & Lupandin, A.I. (1996). Effect of current velocity and turbulence intensity on the distribution of the roach Rutilus rutilus in a water stream. *Journal of Ichthyology,* 36, pp. 687–692.

Smith, I.P., Johnstone, A.D.F. & Smith, G.W. (1997). Upstream migration of adult Atlantic salmon past a fish counter weir in the Aberdeenshire Dee, Scotland. *Journal of Fish Biology,* 51, pp. 266–274.

Sokal, R.R. (1994). *Biometry: the principles and practices of statistics in biological research*. 3rd Ed., W.H.Freeman and Co, New York, NY, USA.

Sokoray-Varga, B., Weichert, R. & Lehmann, B. (2011). Flow investigations for fish pass Lauffen/Neckar in field and laboratory. In: *Proceedings of the 34. Dresdner Wasserbaukolloquium 2011: Wasserkraft - mehr Wirkungsgrad + mehr Ökologie = mehr Zukunft*, Dresden, Germany, 10-11 March 2011, pp. 87–94.

SonTek (2014a). RiverSurveyor S5/M9 system manual, SonTek, San Diego, CA, USA.

SonTek (2014b). RiverSurveyor. Available from: http://goo.gl/BkMEPi (last accessed: 14 May 2014).

Sotiropoulos, F. (2005). Introduction to statistical turbulence modelling for hydraulic engineering flows. In: P. D. Bates, S. N. Lane, & R. I. Ferguson (eds.). *Computational Fluid Dynamics: Applications in Environmental Hydraulics*. John Wiley & Sons, pp. 91–120.

Sprankle, K. (2005). Interdam movements and passage attraction of American shad in the Lower Merrimack River main stem. *North American Journal of Fisheries Management,* 25 (4), pp. 1456–1466.

Stacey, M.T., Monismith, S.G. & Burau, J.R. (1999). Measurements of Reynolds stress profiles in unstratified tidal flow. *Journal of Geophysical Research,* 104 (C5), pp. 933–949.

Steinbrucker, F., Sturm, J. & Cremers, D. (2011). Real-time visual odometry from dense RGB-D images. In: *Proceedings of the IEEE International Conference on Computer Vision Workshops (ICCV Workshops)*, Barcelona, Spain, 6-13 November 2011, pp. 719–722.

Stone, M.C. & Hotchkiss, R.H. (2007). Evaluating velocity measurement techniques in shallow streams. *Journal of Hydraulic Research,* 45 (6), pp. 752–762.

Strasdat, H., Montiel, J.M.M. & Davison, A.J. (2012). Visual SLAM: why filter? *Image and Vision Computing,* 30 (2), pp. 65–77.

Sukhodolov, A.N. (2015). Field-Based research in fluvial hydraulics: potential, paradigms and challenges. *Journal of Hydraulic Research*, 53 (1), pp. 1–19.

Svendsen, J.C., Eskesen, A.O., Aarestrup, K., Koed, A. & Jordan, A.D. (2007). Evidence for non-random spatial positioning of migrating smolts (salmonidae) in a small lowland stream. *Freshwater Biology,* 52 (6), pp. 1147–1158.

Szupiany, R.N., Amsler, M.L., Best, J.L. & Parsons, D.R. (2007). Comparison of fixed- and moving-vessel flow measurements with an ADP in a large river. *Journal of Hydraulic Engineering,* 133 (12), pp. 1299–1309.

Szupiany, R.N., Amsler, M.L., Hernandez, J., Parsons, D.R., Best, J.L., Fornari, E. & Trento, A. (2012). Flow fields, bed shear stresses, and suspended bed sediment dynamics in bifurcations of a large river. *Water Resources Research,* 48 (11), pp. 1–20.

Szupiany, R.N., Amsler, M.L., Parsons, D.R. & Best, J.. (2009). Morphology, flow structure, and suspended bed sediment transport at two large braid-bar confluences. *Water Resources Research,* 45 (5).

Takasu, T. (2013). RTKLIB: an open source program package for GNSS positioning. Available from: http://www.rtklib.com/ (last accessed: 23 December 2015).

Takasu, T. & Yasuda, A. (2008). Evaluation of RTK-GPS performance with low-cost single-frequency GPS receivers. In: *Proceedings of the International Symposium on GPS/GNSS*, Tokyo, Japan, 11-14 November 2008, pp. 852-861.

Taylor, D. (2015). The Raspberry Pi as a Stratum-1 NTP Server. Available from: http://www.satsignal.eu/ntp/Raspberry-Pi-NTP.html (last accessed: 28 December 2015).

Taylor, J.R. (1996). *An Introduction to Error Analysis: the Study of Uncertainties in Physical Measurements.* 2nd Ed., University Science Books.

Teledyne RDI (2007). WorkHorse Rio Grande Acoustic Doppler Current Profiler. Technical manual. November 2007, Teledyne RDI, San Diego, CA, USA.

Teledyne RDI (2009a). PlanADCP - WorkHorse deployment configuration planning software package 2.06. Teledyne RDI, San Diego, CA, USA.

Teledyne RDI (2011). Acoustic Doppler Current Profiler. Principles of operation. A practical primer. Teledyne RDI, San Diego, CA, USA.

Teledyne RDI (2010). ADCP coordinate transformation. Formulas and calculations. P/N 951-6079-00 (January 2010), Teledyne RDI, San Diego, CA, USA.

Teledyne RDI (2002a). RD Instruments Application Note FSA-019: ADCP beam clearance area, Teledyne RDI, San Diego, CA, USA.

Teledyne RDI (2014a). WinRiver II. Software user's guide. Teledyne RDI, San Diego, CA, USA.

Teledyne RDI (2006a). Workhorse RioGrande ADCP. Available from: http://goo.gl/LjxYoR (last accessed: 5 February 2016).

Teledyne RDI (2013). StreamPro ADCP guide. May 2013 Teledyne RDI, San Diego, CA, USA.

Teledyne RDI (2009b). RiverRay ADCP. Available from: http://goo.gl/ANZlxR (last accessed: 5 February 2016).

Teledyne RDI (2014b). RiverPro ADCP. Available from: http://goo.gl/xYK2rY (last accessed: 5 February 2016).

Teledyne RDI (2002b). High resolution water profiling Water Mode 11 FSA-013 (March 2002), Teledyne RDI, San Diego, CA, USA.

Teledyne RDI (2006b). StreamPro ADCP. Available from: http://goo.gl/Eje3V2 (last accessed: 5 February 2016).

Tesch, F.-W. (2003). *The eel*. 3rd Ed., Blackwell Science, Oxford, UK.

Thorstad, E.B., Økland, F., Kroglund, F. & Jepsen, N. (2003). Upstream migration of Atlantic salmon at a power station on the River Nidelva, Southern Norway. *Fisheries Management and Ecology*, 10, pp. 139–146.

Thrun, S., Burgard, W. & Fox, D. (2005). *Probabilistic robotics*. MIT Press, Cambridge, MA, USA.

Ting, S.L., Kwok, S.K., Tsang, A.H.C. & Ho, G.T.S. (2011). The study on using passive RFID tags for indoor positioning. *International Journal of Engineering Business Management,* 3 (1), pp. 9–15.

Tokyay, T., Constantinescu, G. & Gonzalez-Castro, J.A. (2009). Investigation of two elemental error sources in boat-mounted Acoustic Doppler Current Profiler measurements by large eddy simulations. *Journal of Hydraulic Engineering,* 135 (11), pp. 875–887.

Travade, F. & Larinier, M. (2002). Monitoring techniques for fishways. *Bull. Fr. Pêche Piscic.,* 364 suppl, pp. 166–180.

Trimble Navigation (2015). GNSS planning online. Available from: https://www.trimble.com/GNSSPlanningOnline/ (last accessed: 20 November 2015).

Tritico, H.M. & Cotel, a J. (2010). The effects of turbulent eddies on the stability and critical swimming speed of creek chub (Semotilus atromaculatus). *The Journal of Experimental Biology,* 213, pp. 2284–2293.

Tsubaki, R., Kawahara, Y., Muto, Y. & Fujita, I. (2012). New 3-D flow interpolation method on moving ADCP data. *Water Resources Research,* 48, pp. 1–15.

Venditti, J.G., Rennie, C.D., Bomhof, J., Bradley, R.W., Little, M. & Church, M. (2014). Flow in bedrock canyons. *Nature,* 513, pp. 534–537.

Vermeulen, B., Hoitink, J.F. & Sassi, M.G. (2011). Coupled ADCPs can yield complete Reynolds stress tensor profiles in geophysical surface flows. *Geophysical Research Letters,* 38, pp. 1–6.

Vermeulen, B., Hoitlink, A.J.F. & Labeur, R.J. (2015). Flow structure caused by a local cross-sectional area increase and curvature in a sharp river bend. *Journal of Geophysical Research: Earth Surface,* 120 (9). pp. 1771–1783.

Vermeulen, B., Sassi, M.G. & Hoitlink, A.J.F. (2014). Improved flow velocity estimates from moving-boat ADCP measurements. *Water Resources Research*, 50, pp. 4186-4196.

Vowles, A.S., Eakins, L.R., Piper, A.T., Kerr, J.R. & Kemp, P. (2013). Developing realistic fish passage criteria: an ecohydraulics approach. In: I. Maddock, A. Harby, P. Kemp, & P. Wood (eds.). *Ecohydraulics. An integrated approach*. Wiley Blackwell, pp. 143–156.

Vowles, A.S. & Kemp, P.S. (2012). Effects of light on the behaviour of brown trout (Salmo trutta) encountering accelerating flow: application to downstream fish passage. *Ecological Engineering,* 47, pp. 247–253.

Wagner, C.R. & Mueller, D.S. (2011). Comparison of bottom-track to global positioning system referenced discharges measured using an Acoustic Doppler Current Profiler. *Journal of Hydrology,* 401 (3-4), pp. 250–258.

Walton, S.E., Bolland, J.D. & Cowx, I.G. (2012). Investigating fish passage: acoustic fish tracking project - Yorkshire Esk, Ruswarp. HIFI final draft, 19 April 2012.

Warren, M., Mckinnon, D., He, H. & Upcroft, B. (2010). Unaided stereo vision based pose estimation. In: *Proceedings of the Australasian Conference on Robotics and Automation*, Brisbane, Australia, 1-3 December 2010.

Webb, J. (1990). The behaviour of adult Atlantic salmon ascending the rivers Tay and Tummel to Pitlochry dam. Scottish Fisheries Research Report Number 48, Department of Agriculture and Fisheries for Scotland in association with the Atlantic Salmon Trust.

Webster, R. & Oliver, M.A. (2007). *Geostatistics for environmental scientists*. 2nd Ed., Wiley, Chichester, UK.

Wilkes, M.A., Maddock, I., Visser, F. & Acreman, M.C. (2013). Incorporating hydrodynamics into ecohydraulics: The role of turbulence in the swimming performance and habitat selection of stream-dwelling fish. In: Maddock, I., Harby, A., Kemp, P. &Wood, P. (eds.). *Ecohydraulics. An integrated approach*. John Wiley & Sons, pp. 9–30.

Williams, J.G., Armstrong, G., Katopodis, C., Larinier, M. & Travade, F. (2012). Thinking like a fish: A key ingredient for development of effective fish passage facilities at river obstructions. *River Research and Applications,* 28, pp. 407–417.

Williams, R.D., Brasington, J., Hicks, M., Measures, R., Rennie, C.D. & Vericat, D. (2013). Hydraulic validation of two-dimensional simulations of braided river flow with spatially continuous ADCP data. *Water Resources Research,* 49, pp. 5183–5205.

Wisniewski, B., Bruniecki, K. & Moszynski, M. (2013). Evaluation of RTKLIB's positioning accuracy using low-cost GNSS receiver and ASG-EUPOS. *TransNav, The International Journal on Marine Navigation and Safety of Sea Transportation,* 7 (1), pp. 79–85.

Woodgate, R. & Holroyd, A.E. (2011). Correction of Teledyne Acoustic Doppler Current Profiler (ADCP) bottom-track range measurements for instrument pitch and roll. University of Washington Technical Report, Available from: http://psc.apl.washington.edu/BeringStrait.html (last accessed: 14 March 2016).

Woodman, O.J. (2007). An introduction to inertial navigation. Technical Report Number 696. Computer Laboratory, University of Cambridge.

WWAP - United Nations World Water Assessment Programme (2015). The United Nations World Water Development Report 2015: Water for a Sustainable World. UNESCO, Paris, France.

x-io Technologies (2012). x-IMU. Available from: http://www.x-io.co.uk/products/x-imu/ (last accessed: 8 June 2015).

x-io Technologies (2013). x-IMU user manual 5.2. Available from: http://www.x-io.co.uk/products/x-imu/ (last accessed: 8 June 2015).

Xylem Analytics UK (n.d.). R2V2 River robot for velocity and volume. Available from: http://goo.gl/uz1aGl (last accessed: 3 January 2013).

Yang, J., Rao, D., Chung, S. & Hutchinson, S. (2011). Monocular vision based navigation in GPS-denied riverine environments. In: *Proceedings of the AIAA Infotech@ Aerospace Conferenc*e, St. Louis, MO, USA, 29-31 March 2011.

Zhang, H., Liu, Y. & Tan, J. (2015). Loop closing detection in RGB-D SLAM combining appearance and geometric constraints. *Sensors,* 15 (6), pp. 14639–14660.

Zhao, J., Chen, Z. & Zhang, H. (2014). A robust method for determining the heading misalignment angle of GPS compass in ADCP measurement. *Flow Measurement and Instrumentation,* 35, pp. 1–10.

Zug, G.R. (2015). Lateral line system. Available from: http://www.britannica.com/science/lateral-line-system (last accessed: 23 December 2015).

APPENDICES

Appendix A Supplementary material

A.1 Selected categories of fish swimming speeds and measures of water velocities traditionally used in the design of fish passes (supplement to Chapter 2)

Category	Definition	Source
Cruising	A speed that can be maintained for long periods of time (hours)	Bell, 1990
Sustained swimming	A speed that can be maintained for long periods (> 200 minutes) without muscular fatigue	Beamish, 1978
	A speed that can be maintained for minutes	Bell, 1990
Prolonged swimming	A speed that can be maintained for 20 seconds to 20 minutes and results in fatigue	Beamish, 1978
Critical swimming speed, V_{crit}	V_{crit} is derived from flume experiments, where fish are forced to swim at incremental water velocity levels for pre-defined time intervals Δt until exhaustion: $V_{crit} = V_1 + [\Delta V(t_1/\Delta t)]$ V_1…highest water velocity levels maintained for the entire time interval ; ΔV… velocity increment; t_1… duration for which the water velocity of exhaustion was maintained	Brett, 1964
Burst swimming (also darting)	A single swimming effort, not sustainable	Bell, 1990
	The highest swimming speeds that fish are capable of; they can be maintained for less than 20 seconds.	Beamish, 1978
Fast start or sprint swimming	A form of burst swimming lasting for less than approx. one second and used by fish during predator–prey encounters	Domenici & Blake, 1997
Threshold current velocity	The minimum current velocity leading to an orientation reaction against the current[a]	Pavlov, 1989
Critical velocity	The minimum current velocity at which fish begin to be carried away by the water flow[a]	

[a] These are measures of water velocities rather than categories of swimming speeds and are relevant mainly to juvenile fish (Clay, 1995)

A.2 Platform propulsion system components and specifications (supplement to Chapter 6)

Units	Component	Specifications
Forward jet propulsion		
2	Graupner jet drive 2340	Impeller diameter: 40 mm
2	Energ C50-20 brushless DC motor	Working current: 40-80 A, peak 85 A Voltage: 18.5-22.2 V (5 or 6 series LiPo batteries) Revs: 670 Kv
2	EnergPro Marine 60 water cooled electronic speed controller	Output: 60 A continuously, 80 A burst (10 s) BEC output: 5.5 V / 3 A
4	S3003 Standard Futaba servo	Torque: 3.2 kg^{-cm} Voltage: 4.8 V
Tail thruster		
1	Raboesch Bow Thruster	Flat pedal impeller 22mm internal pipe diameter
1	Raboesch Power 400 brushed DC motor	Operational voltage: 6 - 7.2 V Revs (idle): 17,000 RPM
1	SyRen 10 A electronic speed controller	Output: 10 A continuously, 15 A burst (for 18 V input)

Appendix B Publications arising from the PhD research (by March 2016)

B.1 Peer-reviewed journal articles

Kriechbaumer, T., Blackburn, K., Everard, N. & Rivas Casado, M. (2016). Acoustic Doppler Current Profiler measurements near a weir with fish pass: assessing solutions to compass errors, spatial data referencing and spatial flow heterogeneity. *Hydrology Research*, 47 (3), pp. 591-605.

Kriechbaumer, T., Blackburn, K., Breckon, T.P., Hamilton, O. & Rivas Casado, M. (2015). Quantitative evaluation of stereo visual odometry for autonomous vessel localisation in inland waterway sensing applications. *Sensors*, 15, pp. 31869-31887.

Rivas Casado, M., Ballesteros Gonzales, R., **Kriechbaumer, T**. & Veal, A. (2015). Automated identification of river hydromorphological features using UAV high resolution aerial imagery. *Sensors*, 15, pp. 27969-27989.

B.2 Conference proceedings

Kriechbaumer, T. Blackburn, K. Gill, A., Breckon, T., Everard, N., Wright, R. & Rivas Casado, M. (2014). Fish pass assessment by remote control: a novel framework for quantifying the hydraulics at fish pass entrances, EGU General Assembly 2014, 27 April – 2 May, Vienna, *Geophysical Research Abstracts*, 16, p. 13906.

Kriechbaumer, T. Blackburn, K., Breckon, T., Gill, A., Everard, N., Wright, R. & Rivas Casado, M. (2014). A novel sensor platform for the rapid hydraulic characterisation of freshwater ecosystems, EGU General Assembly 2014, 27 April – 2 May, Vienna, *Geophysical Research Abstracts*, 16, p. 13730.

B.3 Invited talks and poster presentations

Environment Agency River Science Workshop (**Wallingford**, 17 September **2015**), Invited speaker: ‘Using ADCPs on radio control platforms to map the hydraulics near river engineering structures’

British Hydrological Society (BHS) National Symposium 2014 (**Birmingham**, 2-4 September **2014**), Poster presentation: ‘Towards simultaneous mapping of 3D water velocities, bathymetry and the river bank environment with a single remote control sensor platform’

SET FOR BRITAIN Engineering Sciences Exhibition (Westminster Palace, **London**, 17 March **2014**), Poster presentation: ‘Fish and chips: a robotic sensor platform to support fish migration in UK rivers’

Cranfield University Doctoral Training Centre Annual Conference (**Cranfield**, 5 February **2014**), Poster presentation: ‘A novel remote control sensor platform for the rapid assessment of fish passes’

Environment Agency Anglian Fisheries Technical Workshop (**Brampton**, 20 November **2013**), Invited speaker: ‘Using ADCP technology to assess fish pass attractivity’

WaterDiss2.0 Summer School 2013, Increasing sustainability in river basin planning and management: concepts and tools for river Restoration (**Venice**, 5-11 August **2013**), Oral presentation: ‘Using ADCP technology to develop indicators for fish passage assessment’

British Hydrological Society (BHS) National Meeting 2013 (**Birmingham**, 17 April **2013**), Poster presentation: ‘Enhancing ADCP technology for aquatic habitat research: the example of fish passage assessment’

Environment Agency Annual Fisheries Technical Workshop (**Great Malvern**, 20-21 March **2013**), Invited speaker: ‘Using ADCP technology to develop indicators for fish passage assessment’